Mesoscale Convection Associated with a Polar Cap Arc Event: Multi-Instrument and Regional Data Assimilation Results

Amalie Øie Hovland

Master's Thesis in Space Physics

Department of Physics and Technology

University of Bergen

August 2021

Abstract

This thesis characterises and quantifies the two-dimensional mesoscale ionospheric flows surrounding a long-lasting auroral arc in the polar cap during a five-hour interval on 14-15 December 2014. The polar cap arc was observed around 80° magnetic latitude in the northern hemisphere dusk-sector. The interplanetary magnetic field (IMF) underwent multiple turnings during the event, but was dominated by positive B_Y and B_Z components. It allows for investigations of the ionospheric convection during variable solar wind.

A regional model of the F-region ionospheric convection surrounding the arc is developed through assimilation of densely distributed plasma drift observations from ground-based SuperDARN radars and DMSP spacecraft. No external solar wind or geomagnetic conditions are required as inputs. The model reproduces high altitude ionospheric convection in two dimensions and on small spatial scales of $\sim$100 km. The resulting mesoscale convection pattern often showed turbulent and structured flows, with up to four adjacent channels of flow in alternating zonal directions. The mesoscale flows frequently deviated from the global average convection patterns typically presented in textbooks.

The regional model was compared to optical data and particle measurements. A channel of anti-sunward flow was consistently located on the edge of the polar cap arc. Towards the end of the observation period, a channel of reversed flow was identified at 15-19 magnetic local time. Although this is far from magnetic noon, the reversed flow channel resembles characteristics that are similar to events that have been reported in the literature for the cusp region. It opens up the intriguing question of whether all such events are generated on the dayside, or if some of the reversed flow events can map to the magnetospheric flanks or further into the nightside.

An abrupt northward IMF turning during the observation period allowed the ionospheric response to be quantified. From the time evolution of the mesoscale flow patterns produced by the regional model, the ionospheric response time was estimated. It took 15$\pm$2 minutes from the IMF turning northward near the bow shock before reconfiguration became visible in the convection in the polar ionosphere. Another 13$\pm$2 minutes pass before the northward IMF reconfiguration is complete and a lobe cell is fully developed.

These results are a contribution to the investigation of convection in the dark ionosphere. Our new modelling technique offers better spatial resolution than empirical statistical models, without their inherent ambiguities of solar wind input.

Acknowledgements

First and foremost, I would like to thank my supervisor, Professor Kjellmar Oksavik, for giving me an excellent start to this project, for continual support, and for keeping me inspired throughout the process. I would also like to thank my co-supervisor, Dr Jone P. Reistad, for keeping me on track and always bringing my focus back to the physics questions. Thank you both for all of our long discussions, your good ideas, patience, and guidance in the process of scientific writing.

Writing a master's thesis during a global pandemic has brought on additional challenges. I want to thank the Institute for Physics and Technology staff for actively working to secure the interests of the students through the challenges of these past 1.5 years.

A big thanks to the people at the Birkeland Centre for Space Science (BCSS) for providing a great learning environment and for making these last two years a positive experience. A special thanks to Katie Herlingshaw and Nina K. Eriksen at UNIS for helping me access and extract data. Thank you to all the members of the Dynamics of the Asymmetric Geospace (DAG) group in Bergen for sharing their expertise, code, and time with me. No office door (or slack inbox) was ever closed to my questions. You have all contributed to this thesis in your own ways, and it has been a joy working with you all. A special thanks to group leader Dr Karl M. Laundal for inviting me to participate in ongoing research projects funded by the Norwegian Research Council (Contract 300844) and through the Trond Mohn Foundation. It has been a highly motivating and unique learning experience.

I want to extend a special thanks to Dr Marc R. Hairston at The University of Texas at Dallas for insightful discussions and DMSP SSIES data necessary for the research conducted in this thesis. I thank Dr Marina Schmidt at The University of Saskatchewan for providing access to SuperDARN data.

A big thanks to the many people who acted as 'reviewers' on this thesis. To Simon, Andy, Oline, and the rest, I am grateful for your efforts.

I thank my fellow students for the good discussions, long lunch breaks, late-night laughs, and (pre-covid) hugs.

I also want to thank my family, friends, and my amazing partner Nikolai, for providing endless support and encouragement. Thank you for putting up with my lengthy ramblings on space physics and this project. You are all irreplaceable.

Lastly, I acknowledge the following agencies and institutions:

- The DMSP SSJ particle data was obtained through the online spectrograph viewer and auroral boundary lists at the Johns Hopkins University Applied Physics Laboratory (JHU/APL) website.
- The National Oceanic and Atmospheric Administration National Centers for Environmental Information (NOAA NCEI) provided improved DMSP spacecraft trajectories.
- Dr Larry Paxton at JHU/APL and the SSUSI team for SSUSI auroral image data.

– The SuperDARN Data Analysis Working Group provided the pyDARNio software toolkit.

– Global SuperDARN map potential plots were obtained through the SuperDARN website at Virginia Polytechnic Institute and State University.

– All-sky imager data was provided by the Redline Geospace Observatory (REGO) and the University of Calgary data portal. REGO is a joint Canada Foundation for Innovation and Canadian Space Agency project developed by the University of Calgary.

– The National Aeronautics and Space Administration (NASA) Goddard Space Flight Center's Coordinated Data Analysis Web (CDAWeb) service for providing solar wind and IMF conditions, ACE and Geotail spacecraft trajectories and geomagnetic indices.

Amalie Øie Hovland
Bergen, 15 August 2021

List of abbreviations

AACGM	Altitude-adjusted corrected geomagnetic
ACE	Advanced Composition Explorer
BPS	Boundary plasma sheet
BSN	Bow shock nose
DMSP	Defense Meterological Satellite Program
FAC	Field-aligned current
FC	Flow channel
FOV	Field of view
FTE	Flux transfer event
FUV	Far-ultraviolet
GSM	Geocentric solar magnetic system
HF	High-frequency
IGRF	International Geomagnetic Reference Field
IMF	Interplanetary magnetic field
ISR	Incoherent scatter radar
LEO	Low Earth orbit

LOS	Line-of-sight	
MHD	Magnetohydrodynamic	
MLAT	Magnetic latitude	
MLT	Magnetic local time	
OCB	Open-closed boundary	
PCA	Polar cap arc	
PC	Polar cap	
REGO	Redline Geospace Observatory	
RFE	Reverse flow event	
SECS	Spherical Elementary Current Systems	
SuperDARN	Super Dual Auroral Radar Network	
SW-M-I-T	Solar wind-magnetosphere-ionosphere-thermosphere	
SW	Solar wind	
TPA	Transpolar arc	
TRINNI	Tail reconnection during IMF northward non-substorm intervals	
UT	Universal time	
LBHS	Lyman-Birge-Hopfield short (wavelength band)	140−160 nm
R_E	Earth's radius (average)	6371.2×10^{-3} m

Contents

Chapter 1

Introduction

Background and motivation

A fundamental feature of Earth's interaction with space is ionospheric convection, i.e. large-scale circulation in the upper polar atmosphere. The ionosphere is the portion of the upper atmosphere that is populated by low-density ionised gasses called a plasma. The ionospheric convection is commonly seen on a large scale (>500 km), where it is observed as laminar flows in circulation patterns that show strong dependence on external solar wind driving. On the other hand, observations of convection on mesoscale ($\sim$30$-$500 km; *Gabrielse et al.*, 2018) often reveal highly structured and turbulent ionospheric flows. The detailed characteristics, physical generation mechanisms, and overall implications of mesoscale convection events remain to be resolved.

Meso and small-scale processes are important for the deposition of energy and momentum from the polar ionosphere. Enhanced flows may cause localised heating through collisions between the ionised and neutral constituents. Increased upwelling of the heated gas leads to increased drag for spacecraft in low Earth polar orbit (*Lühr et al.*, 2004). Ionospheric convection also plays a major role in the transport and structuring of ionospheric plasma. Flow shears associated with mesoscale convection have been related to structuring and production of irregularities in ionospheric plasma (e.g. *Oksavik et al.*, 2011). Plasma irregularities can disrupt radio signals used for communication and navigation, including Global navigation satellite system (GNSS) signals. Therefore, understanding the characteristics and behaviour of mesoscale convection is a key step in developing robust space weather applications. By studying mesoscale convection, we also gain deeper insight into the physical mechanisms driving the large-scale processes.

A wide range of auroral forms have been linked to mesoscale ionospheric convection (e.g. *Moen et al.*, 2008; *Lyons et al.*, 2016), including polar cap auroral arcs. Historically, a large void of ground-based observations from within the central polar cap has constrained the quantification of polar cap arcs primarily to space-based imaging, which has often lead to erroneous conclusions of the origin and behaviour of these arcs (*Hosokawa et al.*, 2020).

High-resolution observations have in recent years become increasingly available in the central polar cap through expansion of radar networks such as the Super Dual Auroral Radar Network (SuperDARN; *Nishitani et al.*, 2019) and the deployment of incoherent scatter radars, ground-based imagers, and a fleet of new spacecraft in low polar orbits. As a result, the spatio-temporal data coverage in some regions of the high-latitude ionosphere now allows for detailed multi-instrument regional investigations that

were impossible just a few years ago.

Simultaneously, there is an increasing need for computational tools to process and analyse these huge and complex data sets. A renewed initiative for the development of regional modelling techniques using data assimilation has emerged (e.g. *Amm et al.*, 2010; *Laundal et al.*, 2021). Regional analysis is currently a key topic of interest in the Dynamics of the Asymmetric Geospace (DAG) group at the Birkeland Centre for Space Science (BCSS), with multiple projects focusing on regional analysis of various processes in the ionosphere. The current thesis is a key contribution within that framework.

Earlier studies of mesoscale convection have most commonly been focusing on areas and topics close to magnetic noon or magnetic midnight in the ionosphere (e.g. *Gabrielse et al.*, 2018). The current thesis focuses on some characteristics of mesoscale convection in the central polar cap during a period of good data coverage from multiple instrumentations both on the ground and in space.

Thesis objectives

The main objective of this thesis is to characterise and quantify the two-dimensional mesoscale ionospheric flows surrounding auroral arcs in the high latitude central polar cap. It includes a regional multi-instrument event study, with the following sub-objectives:

* Develop a technique for assimilative regional modelling of ionospheric convection for the high-latitude central polar cap. This model should resolve mesoscale convection features.
* Place observed mesoscale convection features into a global context.
* Determine and quantify the relationship between mesoscale convection and polar auroral arcs.
* Characterise how the mesoscale convection responds to variations in the external solar wind driver.
* Determine the response and reconfiguration time of the mesoscale convection during a northward turning of the interplanetary magnetic field.

Methodology

The research questions will be addressed through literature review, multi-instrument analysis, and assimilative modelling. Data from northern hemisphere ground-based radars and imagers will be combined with space-based observations to obtain a comprehensive picture of the convection in the local region surrounding a long-lived polar cap auroral arc on 14-15 December 2014 at 21:00-02:00 UT. Simultaneous solar wind observations will also be presented, and the Spherical Elementary Current Systems (SECS; *Amm*, 1997) technique will be utilised to obtain a regional model of the ionospheric convection.

Outline

The thesis is structured in the following way. Chapter 2 gives an introduction to some key concepts in space physics and presents an overview of the current understanding of

ionospheric convection at the mesoscale and auroral features in the polar cap. Chapter 3 describes the instrumentation that was used to collect the observational data, and Chapter 4 details the principles and method of the modelling technique. Chapter 5 presents the findings of this thesis. Chapter 6 is a discussion, followed by the conclusions in Chapter 7. Some suggestions for future work are outlined in Chapter 8. Appendix A presents some relevant coordinate frames.

Chapter 2

Theory

This chapter introduces the three main regions in the coupled solar wind-magnetosphere-ionosphere system (Sections 2.1, 2.2 and 2.3). The connection between these regions is explained with a focus on how the solar wind interacts with the magnetosphere-ionosphere system (Sections 2.4 and 2.5) leading to the ionospheric signatures studied in this thesis; ionospheric convection and auroras (Sections 2.6 and 2.7). The chapter ends with a summary of the current knowledge of ionospheric convection in relation to auroral forms (Section 2.8).

2.1 The Sun and the solar wind

The Sun influences the magnetosphere-ionosphere system through the solar wind and radiation. The solar plasma is continuously flowing out from the outer layer of the Sun's atmosphere, the corona, populating the interplanetary space with charged particles. This near radial outflow of particles is the solar wind. The solar wind plasma is a gas of negatively charged electrons and positively charged ions - mainly protons (H^+), but also about 4% alpha particles (He^{2+}) and trace amounts of heavier ions (*Wurz*, 2005). The number of ions and electrons are the same and the net charge of the solar wind is zero. Within the plasma, the high conductivity keeps the charge fairly uniformly distributed and the solar wind plasma is said to be quasi-neutral (on spatial scales larger than 10 meters, which is the Debye length in the solar wind; *Tonks and Langmuir*, 1929; *Thorne and Blandford*, 2017).

The average solar wind speed is about 400 km/s, but it is highly variable depending on many factors. It can normally range from 'slow' speeds of 300 km/s to as high as 800 km/s, with some recorded speeds being almost 1850 km/s (*Li et al.*, 2016; *Skoug et al.*, 2004). The Earth orbits the Sun at an average distance of 1 AU $\approx 1.5 \cdot 10^8$ km. Light from the Sun reaches the Earth in only 8 minutes, while the solar wind will reach the Earth's magnetosphere in 2−5 days depending on its speed. The solar wind plasma is not very dense, with typical densities of 3−10 particles/cm^3 (*Ma et al.*, 2020), but this also varies. The solar wind carries with it a magnetic field, dubbed the interplanetary magnetic field (IMF), which is discussed in section 2.4.

Coronal holes, sunspots and explosive activity on the surface of the Sun, like coronal mass ejections (CME), affect solar wind speeds and densities (and the IMF), which in turn affects the Earth's magnetosphere-ionosphere system. The occurrence of these phenomena varies with the 11-year solar cycle (*Li et al.*, 2016).

2.1.1 Frozen-in magnetic field

Electric and magnetic fields of the solar wind plasma are often observed in reference frames in which the plasma is moving with a bulk speed $\mathbf{v}$. For example, a reference frame fixed to the Earth or a satellite in orbit. $\mathbf{E}$ and $\mathbf{B}$ are the electric and magnetic fields observed from such a reference frame, S. The electric and magnetic fields observed in the reference frame that is moving with the plasma, S', can then be written as:

$$\mathbf{E}' = \mathbf{E} + \mathbf{v} \times \mathbf{B} \tag{2.1}$$

$$\mathbf{B}' = \mathbf{B} + \frac{\mathbf{v} \times \mathbf{E}}{c^2} \tag{2.2}$$

from transformation between the two reference frames. Relativistic effects on the fields are ignored as $|\mathbf{v}| \ll c$, where $c = 3.0 \cdot 10^8$ m/s is the speed of light. With this approximation the second term in Equation (2.2) can be neglected, which means that the magnetic field is not frame-dependent, and remains the same when observed in the different reference frames: $\mathbf{B}' = \mathbf{B}$. This is, however, not true for the electric field, as the $\mathbf{v} \times \mathbf{B}$ term in Equation (2.1) is of the same order of magnitude as $\mathbf{E}$, and the electric field is frame-dependent.

When the space plasmas can be approximated to be collisionless, the only forces acting on the plasma particles are electromagnetic forces (gravitational forces are usually neglected). If no other forces are acting to stop the plasma particles (charges) from moving, the plasma has infinite conductivity. Any possible charge-build up occurs on spatial scales smaller than the Debye length and is quickly cancelled out. Therefore no large-scale electric fields are present in the plasma reference frame: $\mathbf{E}' = 0$. From Equation (2.1) the electric field observed from reference frame S can then be written as:

$$\mathbf{E} = -\mathbf{v} \times \mathbf{B} \tag{2.3}$$

This also leads to the magnetic field and the plasma being bound together; the magnetic field is said to be *frozen-in* (*Alfvén*, 1942). The magnetic field must follow the movement of the plasma perpendicular to the magnetic field lines. One can also consider it as the plasma being stuck to the magnetic field lines (gyrating around them due to magnetic forces), not being able to move between the field lines (diffuse). The frozen-in assumption usually holds in the solar wind, the magnetosphere, and even in the upper ionosphere (see Section 2.3). It does, however, break down in regions where magnetic reconnection occurs (see Section 2.4) and the lower ionosphere where collisions occur (see Section 2.6). For further information, see *Baumjohann and Treumann* (2012).

2.2 The magnetosphere

The Earth is surrounded by a protective magnetosphere, a region where the geomagnetic field has an influence on charged particles. The influence of the geomagnetic field extends to around 15 Earth radii ($R_E \approx 6371$ km) on the Sun-facing side and some hundred Earth radii on the side facing away from the Sun (*Laundal and Richmond*, 2017). The magnetosphere shields the Earth by deflecting most solar particles away.

The geomagnetic field is a superposition of fields from many sources. The most

significant contribution comes from generation mechanisms in the Earth's outer core, often referred to as the main field. The geomagnetic field is not static, as the 'stable' sources can move around slowly, and external fields can induce currents at Earth that act as additional time-varying sources of magnetic fields (*Olsen et al.*, 2010). Modelling the total geomagnetic field is useful not only to separate the different sources but also to investigate space weather events. Making these models is, however, not an easy task, and various main field models exist (*Laundal and Richmond*, 2017). One of these magnetic field models is introduced in Appendix A.

Despite the variation in the geomagnetic field, the large-scale features of the magnetosphere are generally as depicted in the schematic in Figure 2.1. On the Earth's surface, magnetised material in the crust, ocean currents, and other local sources make the magnetic field a complex, multipole one (*Olsen et al.*, 2010) (not shown in the schematic). Moving some distance away from the Earth's surface, the geomagnetic field is approximately dipolar, as depicted in the figure. The magnetic field points out from the southern hemisphere and into the northern hemisphere (black arrow lines), and the magnetic field strength, the magnitude, falls off with $1/r^3$ with the distance r from the Earth's centre. At some distance from the Earth, the effects of the solar wind can be seen, as its dynamic pressure distorts the dipolar field geometry by compressing the dayside field (on the left) and pulling the nightside field (on the right) into a tail-like shape, the magnetotail (*Ness*, 1965). A cleft near the magnetic poles, the cusp, separates the dayside and nightside magnetosphere. The magnetospheric lobes are located on the tailward side of the cusp on either side of the central part of the magnetotail.

The magnetosphere is an obstacle to the supersonic solar wind flow, and the solar wind is decelerated to subsonic speeds at a region upstream of the magnetosphere called the bow shock (the bold dashed line to the left in Figure 2.1). The bow shock location varies but is on average situated at $\sim$13 R_E in the equatorial plane (*Fairfield*, 1971). The magnetopause (the narrow dashed line in Figure 2.1) is the outer boundary of

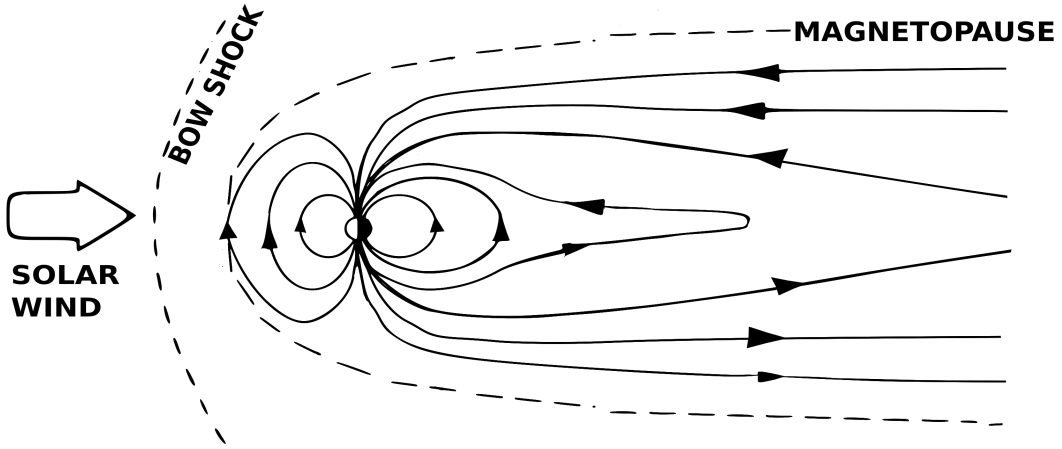

Figure 2.1: Schematic of the Earth's magnetosphere. The Sun is to the left in the figure, with the large arrow indicating the solar wind flow direction. The bold dashed line depicts the bow shock location upstream of the magnetopause (thin, dashed line). The magnetic field lines in the magnetosphere are solid arrow lines indicating their direction (adapted from *Borovsky*, 2017).

the magnetosphere, separating field lines connected to the Earth from field lines in the IMF. The region between the bow shock and the magnetopause, where the deceleration has altered the plasma properties and IMF configuration, is called the magnetosheath (*Borovsky and Valdivia*, 2018).

A large number of different plasma populations exist within the magnetosphere. Magnetic fields trap plasma, and different magnetospheric regions can be identified by investigating the plasma populations. Measuring properties like temperature, composition and density of plasma can be used to identify the different regions of the magnetosphere and reveal information about energy transfer in the solar wind-magnetosphere-ionosphere (SW-M-I) system.

The major sources of magnetospheric plasma are the ionosphere and the solar wind (*Borovsky and Valdivia*, 2018). Interaction with the solar wind is also the main driver of convection and electrical current systems within the magnetosphere (and in the ionosphere). This is further described in Sections 2.4-2.6.

2.3 The ionosphere

The ionosphere is a weakly ionised region in the Earth's upper atmosphere. Understanding the production and loss of plasma in the ionosphere and how it depends on altitude is crucial for understanding ionospheric dynamics. It is also essential for some ground-based observational methods as the ionospheric electron density affects radio signals (see Section 3.2). The neutral atmosphere and the ionosphere are interconnected via collisions and chemical reactions. To understand the origin and behaviour of the ionospheric plasma, one has to understand the neutral atmosphere.

Figure 2.2a shows average pressure and temperature profiles of the neutral atmosphere (from models; *Lente and Ősz*, 2020). The atmospheric pressure profile (black line) is decreasing exponentially with altitude. In the lower atmosphere, where the density is high, the collisions between the neutral gas particles keep them evenly mixed. Moving upwards, the density and consequently the collisions decrease. The mixing of species becomes less even, and the number density of heavier gas particles declines with altitude. This behaviour is shown in Figure 2.2b, where the number density of heavier species like Ar, O_2 and N_2 fall off more rapidly than the lighter species H, He and O (*Cottin et al.*, 2017).

In contrast to the pressure and number density profiles, the atmospheric temperature profile fluctuates with altitude. The profile shown in Figure 2.2a (blue line) has several regions of local minima and maxima. The fluctuations in temperature are due to variations in the absorption of sunlight at different altitudes, which depends on the atmosphere's chemical composition. For instance, the number density of ozone (O_3) is essential for where the solar radiation deposits its energy. The neutral atmosphere is divided into layers based on this temperature profile (*Rees*, 1989).

The ionosphere is the part of the upper atmosphere where we see plasma (>60 km altitude; *Richmond*, 2007). Figure 2.3 shows the ionospheric density for different times of the day and solar activity (typical mid-latitude profiles; *Richmond*, 2007). The ionosphere is divided into layers depending on the density of free electrons, n_e. The ionospheric layers are traditionally set to the approximate altitude ranges $\sim$60$-$90 km (D-region), $\sim$90$-$150 km (E-region) and $\gtrsim$150 km (F-region) centred around regions of

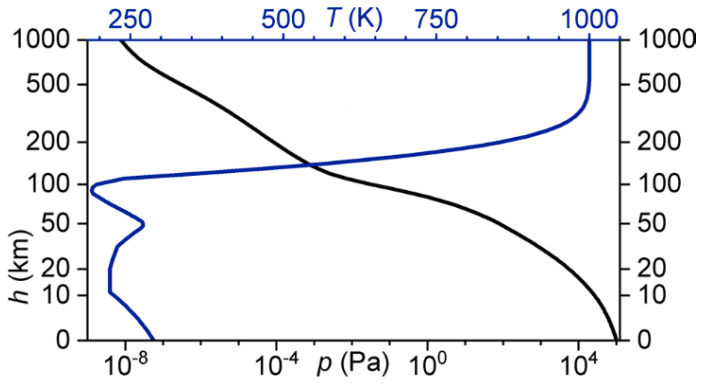

(a)

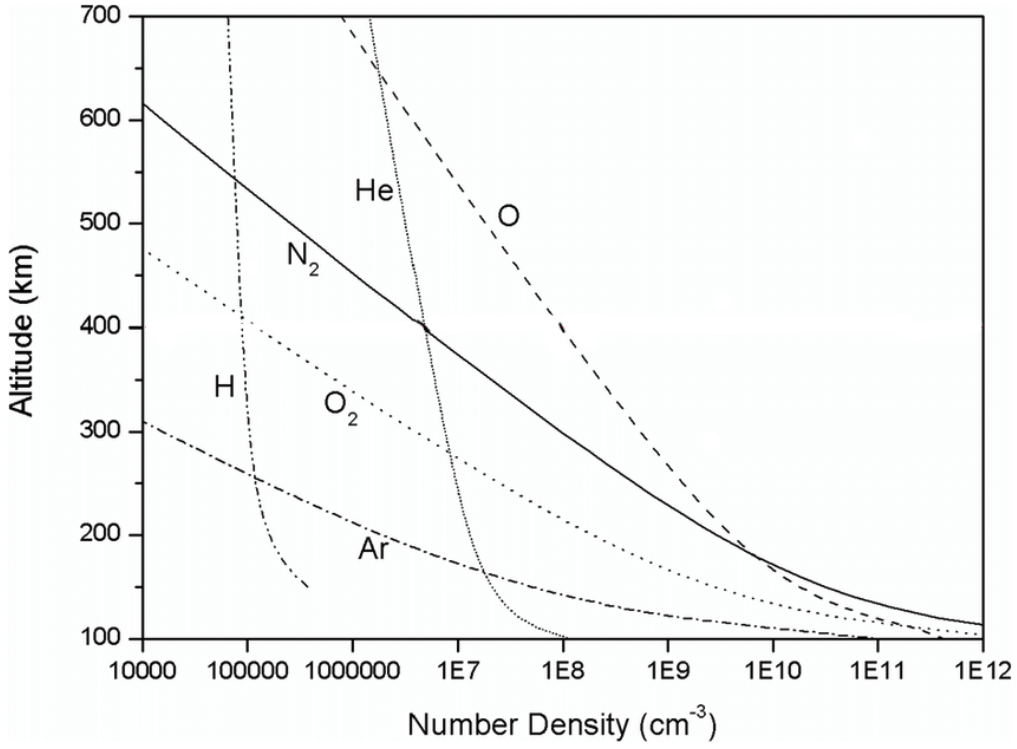

(b)

Figure 2.2: (a) Atmospheric pressure (black) and temperature (blue) profiles based on models (adapted from *Lente and Ősz*, 2020). (b) The average atmospheric number density of neutral species in the upper atmosphere (adapted from *Cottin et al.*, 2017).

local maxima in electron density (*Kelley*, 2009).

The primary production mechanism for the ionospheric plasma is solar radiation that ionises particles in the atmosphere. Earth's rotation around its axis and the orbit around the Sun affects which part of the atmosphere is sunlit. In addition, the intensity of the solar radiation varies with distance from the Sun and solar activity. The height and density of the ionosphere (and neutral atmosphere) therefore varies diurnally, seasonally and with the solar cycle (*Liu et al.*, 2011). In Figure 2.3 the dependence on solar activity is seen in the difference between the solar minimum (solid) and solar maximum (dashed) curves. Noon and midnight differences are indicated, showing no

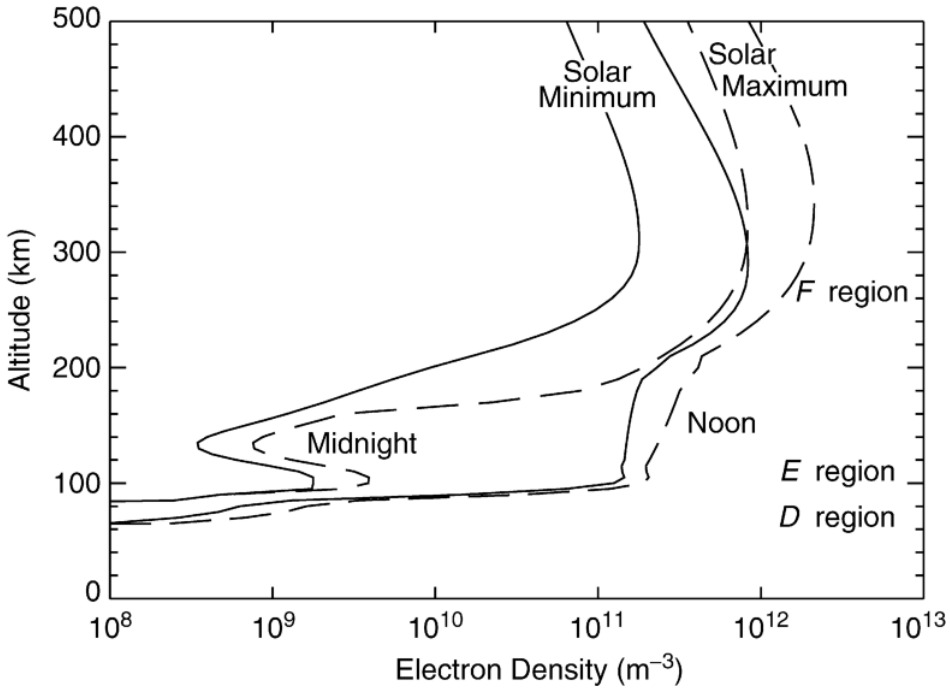

Figure 2.3: Typical electron density-altitude profiles for the mid-latitude ionosphere at September equinox with D, E and F-regions indicated. Ionospheric profiles for solar maximum and minimum are distinguished by dashed and solid lines, respectively. Noon and midnight differences in electron densities are also shown (from *Richmond*, 2007).

D-region and a significantly lower electron density at low altitudes (E and lower F-region) when the atmosphere is not sunlit.

The other major production mechanism of ionospheric plasma is particle precipitation. Figure 2.4 shows ionisation rates for different production mechanisms at different altitudes. Solar radiation is shown in orange. Particles deposit their energy differently from photon radiation, and the altitude of maximum energy deposited is highly dependent on the energy of the precipitating particles. In general, more energetic particles deposit maximum ionisation at lower altitudes (*Mironova et al.*, 2015). The ionisation due to particle precipitation depends on the solar activity as the solar wind is a major source of ionising particle precipitation, and magnetospheric responses to solar activity cause plasma from the magnetosphere to precipitate (*Sinnhuber et al.*, 2012; *Mironova et al.*, 2015). These contributions are shown in green and pink, respectively. Cosmic rays are a form of very energetic particle precipitation and is shown in grey. Cosmic rays mainly create D-region and lower altitude plasma. High energy particles originating from the Sun (solar protons, blue) also cause ionisation. Solar protons are very dependent on solar activity (*Buchvarova et al.*, 2003; *Mironova et al.*, 2015).

Loss of plasma happens through chemical processes and collisions that lead to the recombination of ions and electrons. The loss rate is complex and depends on the physical and chemical properties of the ionosphere and atmosphere. The type of ions present in the plasma is important for the recombination rate, as dissociative recombination (a loss process for molecular ions) is more rapid than recombination processes for monoatomic ions. The recombination processes are also dependent on the neutral densities, as interactions between monoatomic ions and neutrals through charge ex-

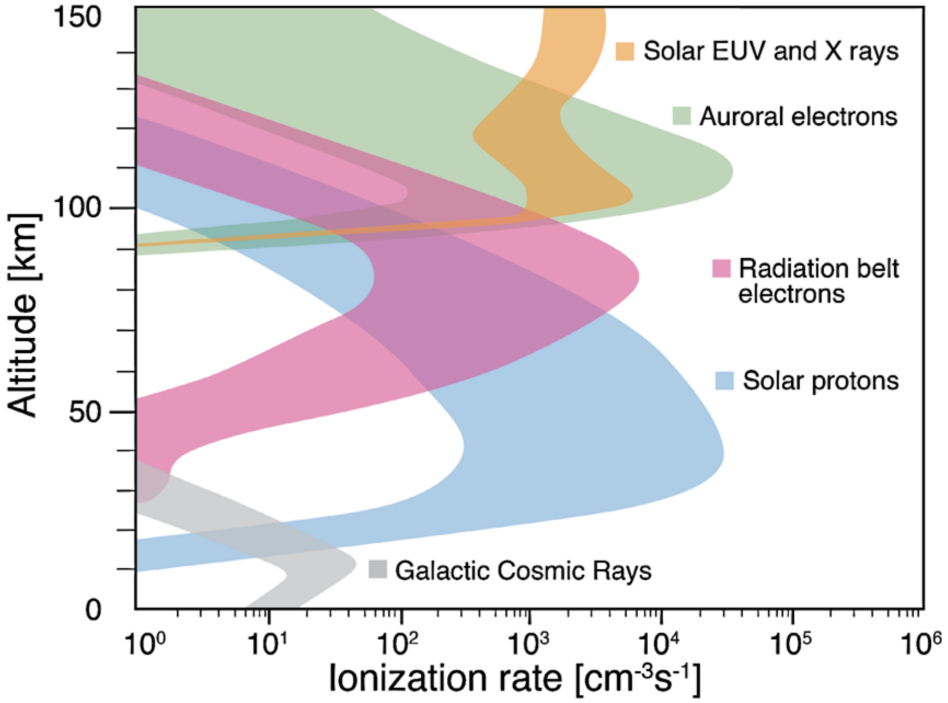

Figure 2.4: Ionisation rates at different altitudes for solar radiation (orange) and particle precipitation (green, pink, blue and grey) in the Earth's atmosphere (from *Mironova et al.*, 2015).

change leave molecular ions that can undergo dissociative recombination (*Bates*, 1950). These dependencies lead to lower altitude plasma being depleted faster than plasma in the upper ionosphere. In other words, the lower ionosphere plasma is short-lived. It virtually disappears when plasma is not being continuously produced, reflected in the diurnal variations in Figure 2.3. On the other hand, the upper ionosphere plasma is long-lived and can have a lifetime of several hours (*Kelley*, 2009).

2.4 The interplanetary magnetic field and magnetic reconnection

As described in Section 2.2, the solar wind and accompanying IMF flow past the magnetosphere while compressing and stretching the geomagnetic field. The IMF orientation at the magnetopause varies depending on the conditions on the Sun and where the Earth is located in its orbit. Similar to the solar wind flowing out from the Sun like an extension of its corona, IMF is the solar magnetic field extending out into interplanetary space. The IMF field lines connect to the Sun, and due to its rotation, the field forms a spiral shape as shown in the illustration in Figure 2.5, called the Parker spiral (a shape predicted by *Parker*, 1958).

Although some solar wind energy can transfer to the magnetosphere by the dynamic pressure from the solar wind alone (*Russell et al.*, 1994), a process called magnetic reconnection allows the solar wind to couple to the magnetosphere in a more direct way. Reconnection of magnetic field lines is an energy conversion process where built-up

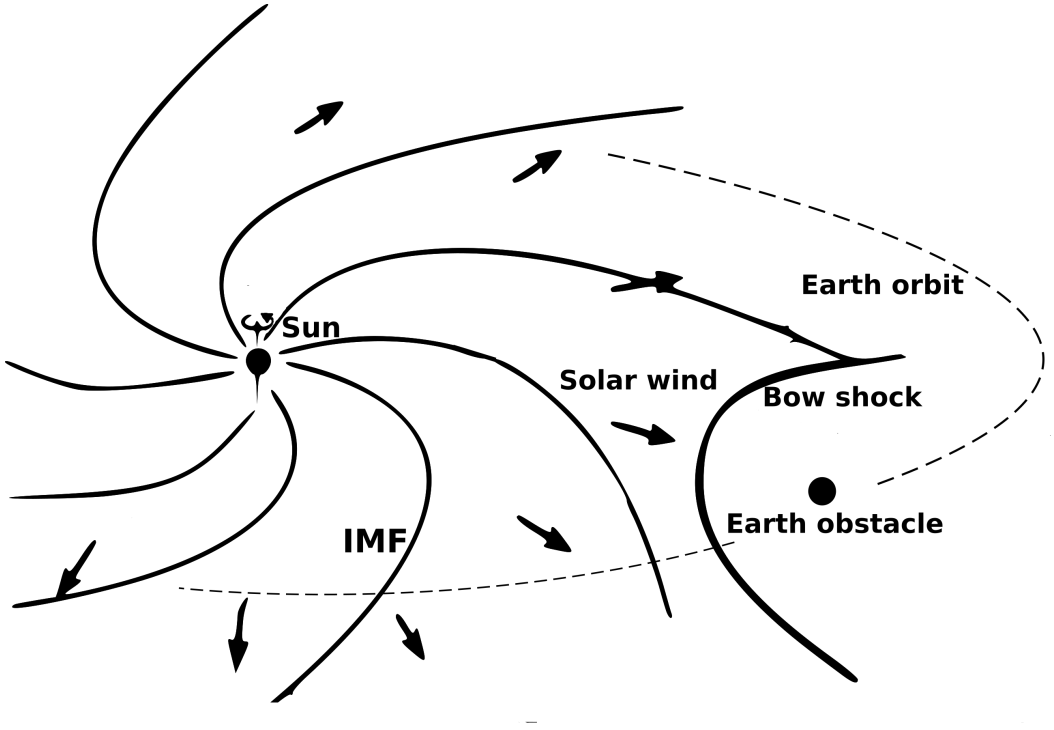

Figure 2.5: Illustration of the Parker spiral (adapted from *ThoughSF*, 2020).

magnetic energy is converted into heat and kinetic energy of charged particles. Magnetic reconnection is not unique to the solar wind-magnetosphere system near Earth. In fact, it can happen wherever magnetic field lines of opposite polarity are pushed together with sufficient pressure, like on the Sun, in laboratory plasma, or near neutron stars (*Burch and Drake*, 2009). In the solar wind-magnetosphere system, reconnection is vital as it transfers plasma particles, momentum and energy from the solar wind across the magnetopause (*Borovsky and Valdivia*, 2018). Plasma particles cannot diffuse across magnetic field lines when the frozen-in condition holds (see Section 2.1.1), and the solar wind plasma (mass) cannot cross the magnetopause and enter the magnetosphere system without reconnection.

Reconnection between the solar wind and the geomagnetic field is dependent on the IMF field geometry and solar wind plasma properties (*Ma et al.*, 2020), which both can vary on time scales of minutes (*Milan*, 2015). Two reconnecting magnetic field lines do not have to be strictly anti-parallel, but they must have anti-parallel components (*Cowley*, 1976). The orientation of IMF with respect to the geomagnetic field is therefore important for the rate of solar wind energy transfer to the magnetosphere. The coupling also depends on the dipole tilt of the Earth relative to the Sun (season). We use the geocentric solar magnetic (GSM) coordinate system to represent the IMF orientation relative to the geomagnetic field (see Appendix A). The IMF orientation specified in the GSM system is: $\mathbf{B}_{\mathrm{SW}} = B_X\hat{\mathbf{x}}_{\mathrm{GSM}} + B_Y\hat{\mathbf{y}}_{\mathrm{GSM}} + B_Z\hat{\mathbf{z}}_{\mathrm{GSM}}$. Where the subscript SW stands for the solar wind.

The IMF clock angle is often used to express the IMF orientation:

$$\theta_{\mathrm{CA}} = \tan^{-1}\left(\frac{B_Y}{B_Z}\right) \tag{2.4}$$

It is the angle between IMF projected into the GSM YZ-plane and the Z-axis. The magnitude of the transverse component of IMF (B_Y and B_Z) is often denoted B_T. The IMF B_T is mostly preserved even as the solar wind enters the magnetosheath, while the (parallel) B_X-component is modified as IMF drapes over the magnetosphere (*Frey et al.*, 2019).

The two major sites of reconnection in the solar wind-magnetosphere system are at the dayside magnetopause and in the magnetotail (*Dungey*, 1961). Other reconnection sites are possible depending on the IMF orientation (*Crooker*, 1979), with northward IMF (B_Z+) being related to high-latitude dayside reconnection in the magnetosphere lobes (e.g. *Luhmann et al.*, 1984; *Russell*, 1972; *Li et al.*, 2008). Sections 2.5 and 2.6 will discuss how the reconnection leads to magnetospheric and ionospheric convection of magnetic field and plasma (*Milan et al.*, 2017), and how different reconnection geometries affect the patterns of convection.

2.5 Magnetospheric dynamics

Convection of plasma and magnetic field in the magnetosphere leads to circulation in the ionosphere as the two systems are interconnected. The current picture of SW-M-I coupling is built on the work of *Dungey* (1961). He proposed a model of the system where the large-scale dynamics of the SW-M-I system could be explained in terms of an open magnetosphere. The following section outlines his model and introduces the expanding contracting polar cap (ECPC) paradigm (*Lockwood et al.*, 1990; *Cowley and Lockwood*, 1992) for explaining the time-dependence of the M-I dynamics.

Dungey (1961) described a cycle of magnetospheric (and ionospheric) convection that is driven by the opening of the magnetosphere by dayside reconnection and the closing of the magnetosphere by nightside (tail) reconnection. This is the Dungey cycle. Following the simplified schematic in Figure 2.6, a purely southward IMF (1) hits the magnetopause where it reconnects with the geomagnetic field in the equatorial plane (red X). The reconnection opens the magnetospheric field line at the magnetopause (2). Open magnetic field lines are connected to IMF in one end and the geomagnetic field (Earth) in the other. The newly opened field line convects anti-sunward as it is dragged by the solar wind towards the nightside, where it forms the lobes (3-4). The open field lines are closed by reconnection in the equatorial plane in the magnetotail (blue X). Closed magnetic field lines are connected to the Earth in both ends. The energy released by nightside reconnection causes the newly closed field line to convect sunward (6), where it ends up as part of the dayside geomagnetic field once again (7). The boundary between open and closed field lines is called the open-closed boundary (OCB), and the region in the ionosphere where the open field lines have their footpoints is called the polar cap (PC).

Expanding on the Dungey cycle framework, *Lockwood et al.* (1990) and *Cowley and Lockwood* (1992) explained how bursts of reconnection (either opening or closing of magnetic flux) excite flows in the magnetosphere. In Figure 2.7, the arrow lines show the convection in the magnetosphere excited by a deformation of the magnetopause. The dashed line is the new magnetosphere configuration after the excited plasma flows bring the magnetosphere to a new force balance (equilibrium) with the solar wind. The top view (left) of the magnetosphere shows how the burst of dayside reconnection

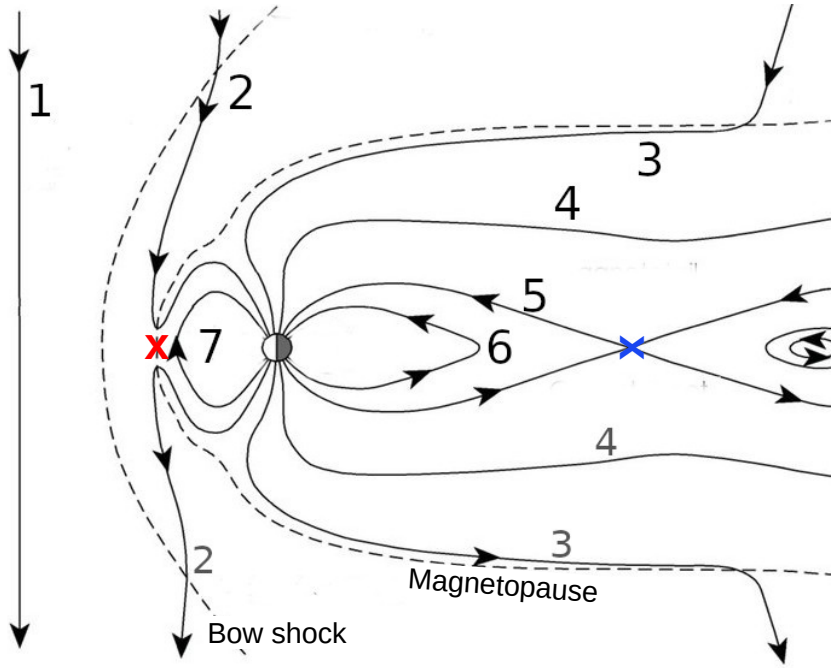

Figure 2.6: The Dungey cycle. A cross-section of the magnetosphere as seen from the dusk-side of the Earth with the Sun to the left. The numbers indicate the different steps of the cycle. The X markers are the locations of (subsolar) dayside reconnection (red) and night-side reconnection (blue) (adapted from *Cowley et al.*, 2003).

makes an indent on the OCB as magnetic field lines are opened. A cross-section of the magnetotail seen from the nightside of the Earth (right) shows how the magnetosphere tail is deformed in both the north and south as the newly opened field lines are added to the lobes.

As described in Section 2.4, the opening of magnetic flux by dayside reconnection depends on interplanetary conditions. The closing of magnetic flux by nightside reconnection depends on conditions in the magnetotail. A balance in the dayside and nightside reconnection leads to a stable convection where the total amount of open magnetic flux (polar cap flux, F_{PC}) is constant. In reality, the magnetospheric convection is not smooth and steady as the dayside and nightside reconnection varies on different time scales. The time variation in these drivers leads to a highly dynamic magnetosphere, with the change in the total amount of open magnetic flux:

$$\frac{dF_{\mathrm{PC}}}{dt} = \Phi_D - \Phi_N \tag{2.5}$$

where Φ_D (unit Wb/s) is the rate of opening of flux (dayside reconnection rate), and Φ_N (unit Wb/s) is the rate of closing of flux (nightside reconnection rate). The total amount of open flux is variable ($\frac{dF_{\mathrm{PC}}}{dt} \neq 0$) on minute to hour time scales but on time scales longer than two to three hours, the amount of open magnetic flux is constant ($\frac{dF_{\mathrm{PC}}}{dt} = 0$) (*Milan*, 2015).

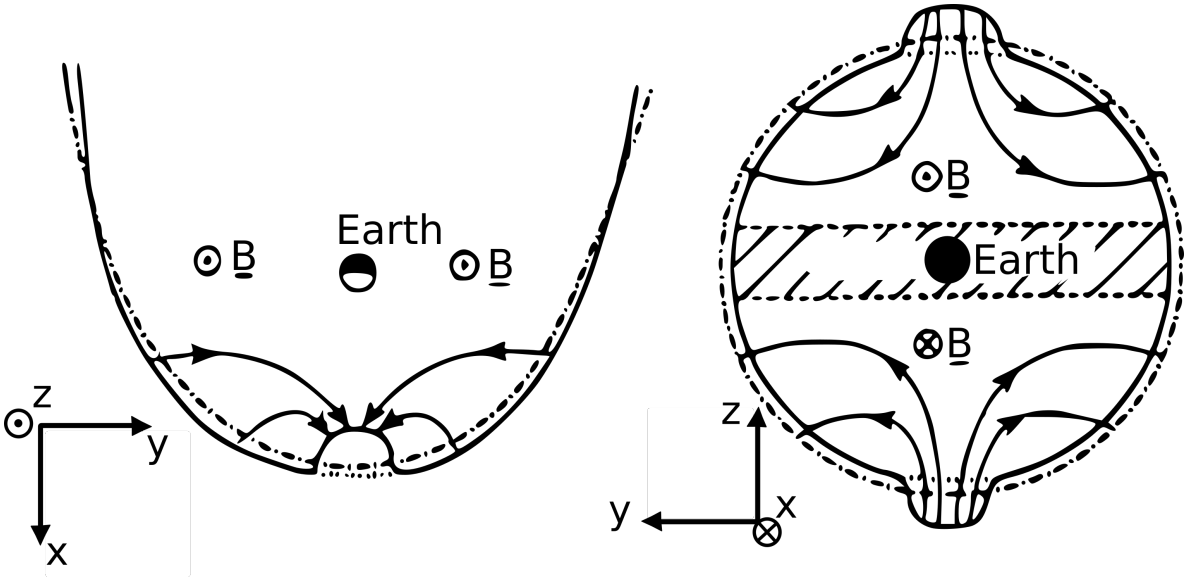

Figure 2.7: Illustration of the magnetospheric convection due to dayside reconnection. The left-hand panel is a cross-section of the magnetopause in the equatorial plane as seen from above the northern hemisphere. The right-hand panel is a cross-section of the magnetotail as seen from the nightside of the Earth. The direction of the geomagnetic field (**B**) in the plane is indicated by the dotted (out of) and crossed (into) circles. The arrow lines are the flows inside the magnetosphere excited by the deformation of the magnetosphere (solid black lines). The dot-dashed lines are the magnetopause after the new equilibrium has been reached (adapted from *Cowley and Lockwood*, 1992).

2.6 Ionospheric dynamics

The magnetospheric convection introduced in Section 2.5 is communicated to the ionosphere along the convecting magnetic field lines (*Cowley*, 2000). This transmission of stress from the magnetosphere to the ionosphere keeps the ionospheric plasma in near-continuous motion. The link between the SW-M coupling and the plasma motion in the ionosphere can be exploited, and studying plasma convection in the high-latitude ionosphere can give important insight into the interaction between the solar wind and Earth systems. The vast distances at the magnetopause and variations in interaction sites make in-situ studies of SW-M coupling challenging. Studying the ionospheric convection is less complicated, as distances are considerably shorter and observational coverage is denser.

2.6.1 Global convection patterns

Figure 2.8 shows the ionospheric response to a sudden impulse of reconnection as described by *Cowley and Lockwood* (1992) (the ionospheric equivalent to the schematic shown in Figure 2.7). As discussed in Section 2.5, the dayside reconnection opens magnetic flux. This excites a flow of plasma to obtain a new equilibrium, a new force balance between the solar wind and the M-I system (*Lockwood et al.*, 1990; *Cowley and Lockwood*, 1992).

In Figure 2.8, the ionosphere is depicted from above the pole in a magnetic latitude

(MLAT) and magnetic local time (MLT) coordinate system where noon is up, and dusk is to the left (see Appendix A). The black line is the OCB marking the boundary between the footpoints of the open magnetic field lines in the PC and the footpoints of the closed magnetic field lines at lower latitudes. Before the dayside reconnection occurs (t_1), the amount of open flux is F. The reconnection perturbs the OCB as it opens an amount dF of magnetic flux (t_2), and the flow pattern indicated by arrows (t_3) is excited in order to obtain the new OCB configuration (dot-dashed line in t_2). At t_4 a new force balance has been reached, the PC has expanded (green arrows),

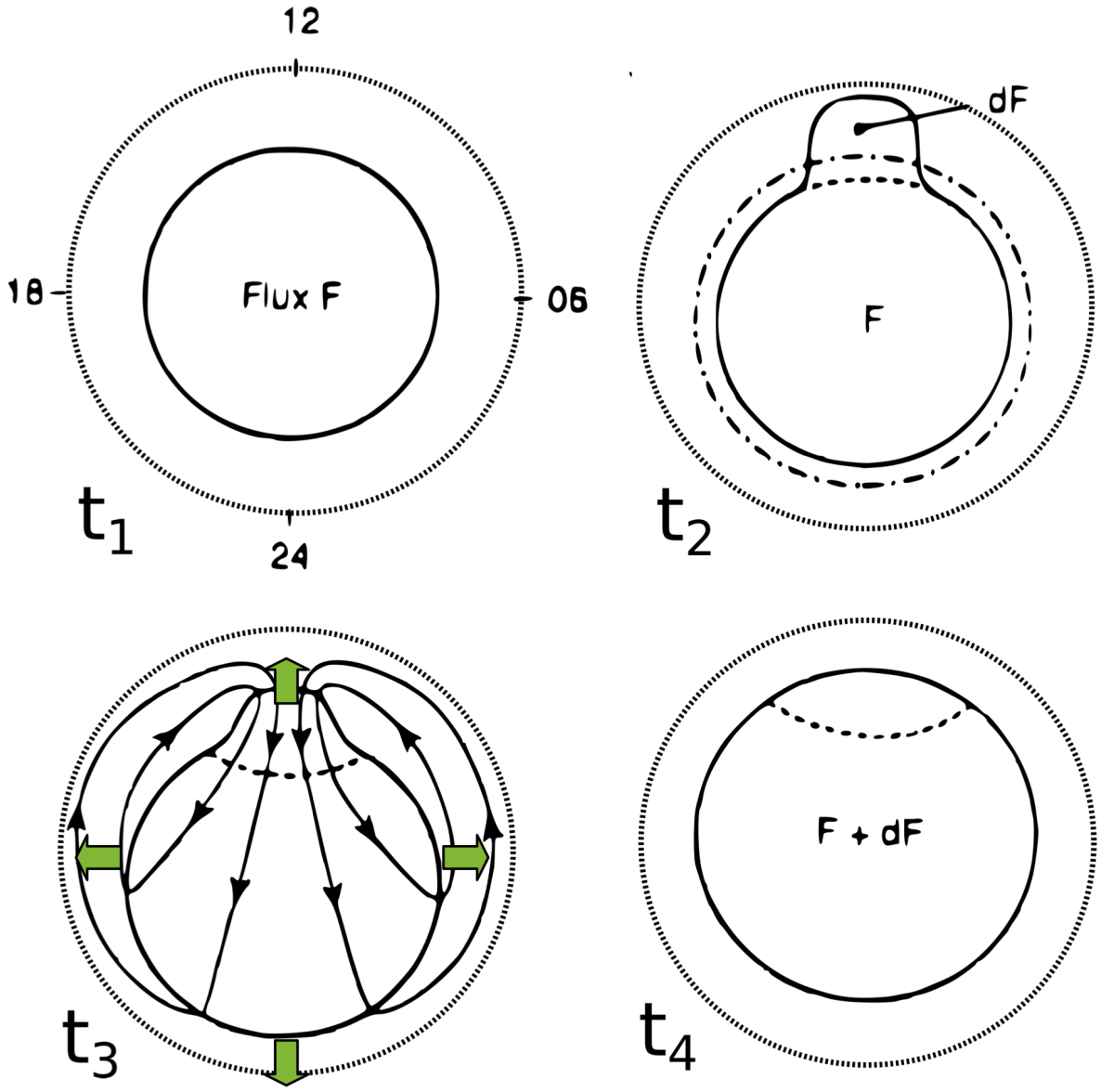

Figure 2.8: Illustration of the ionospheric convection resulting from unbalanced dayside reconnection. The solid line is the open-closed boundary. At t_1 the polar cap contains the open magnetic flux F. At t_2 dayside reconnection has added an amount of magnetic flux dF to the polar cap. The excited ionospheric convection (arrow lines) causes an expansion of the polar cap (green arrows) at t_3. At t_4 a new equilibrium (dot-dashed line in t_2) has been reached (adapted from *Cowley and Lockwood*, 1992).

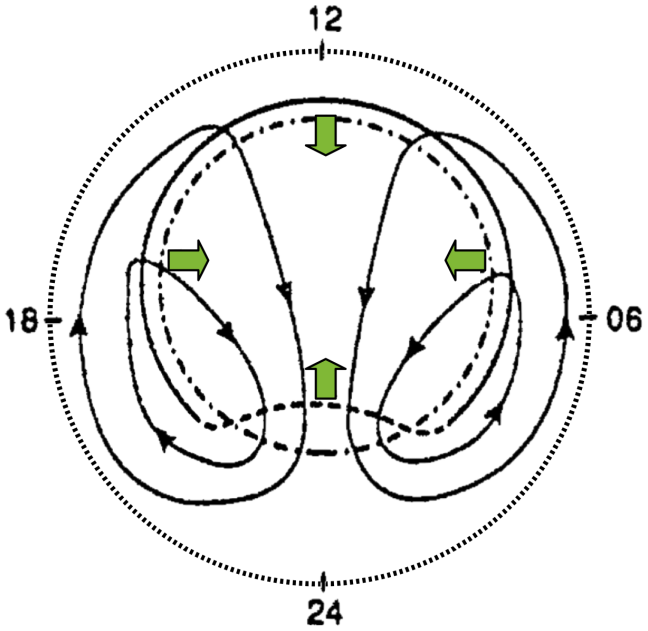

Figure 2.9: Illustration of the ionospheric convection resulting from unbalanced nightside reconnection. Nightside reconnection closes flux (dashed line) and the resulting ionospheric convection (arrow lines) causes a contraction (green arrows) of the polar cap from its original size (black line) to a new equilibrium (dot-dashed line) (adapted from *Cowley and Lockwood*, 1992).

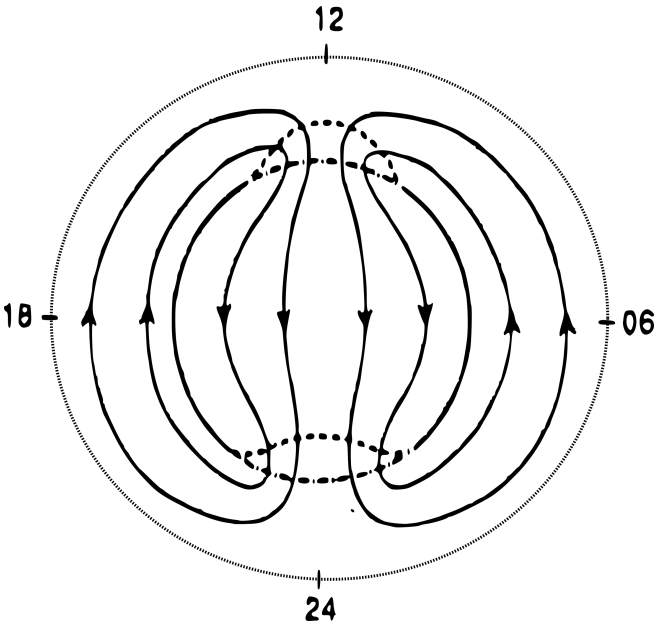

Figure 2.10: Illustration of the two-cell ionospheric convection pattern resulting from a balance in dayside and nightside reconnection. The black arrow lines are convection streamlines, the black solid line is the open-closed boundary (OCB), while the dashed lines show perturbations of the OCB due to magnetic reconnection. The dot-dashed line is the equlibrium OCB (adapted from *Cowley and Lockwood*, 1992).

and the amount of open flux is $F + dF$. The ionospheric flows are excited almost immediately after the reconnection impulse, with a delay of only ∼2 minutes (*Lockwood et al.*, 1989; *Freeman et al.*, 1990a).

The convection in Figure 2.8 is the ionospheric convection excited by unbalanced dayside reconnection, causing an expanding PC. Figure 2.9 shows the ionospheric convection due to unbalanced nightside reconnection causing a contraction (green arrows) of the PC (from solid to dot-dashed lines). The total convection pattern in the ionosphere will be a combination of the flows excited by both dayside and nightside reconnection, as the total amount of open flux (the size of the PC) changes according to Equation (2.5). The 'twin-cell' pattern in Figure 2.10 is the convection that would result from a balance in (subsolar) dayside reconnection and nightside reconnection (*Dungey*, 1961; *Cowley and Lockwood*, 1992). The pattern shows anti-sunward convection within the PC and a sunward return flow at lower latitudes (outside the PC).

As discussed in Section 2.4, the conditions in the solar wind and orientation of the IMF affects the location of dayside reconnection and thus changes the induced convection in the M-I system. Figure 2.11 is an illustration of different ionospheric flow patterns (bottom row) thought to be induced by different types of dayside reconnection (top row). Note that the figure does not depict any nightside contributions.

In Figure 2.11a, subsolar reconnection is illustrated, with the blue arrows indicating the flow direction of the newly opened field lines in the GSM XZ-plane. The resulting ionospheric convection (black arrow lines) is shown in panel d (the same pattern is shown in Figure 2.8 at t_3). The green arrows indicate an expansion of the polar cap (solid red line), and the dashed red line is the footprint of the magnetopause reconnection site. Subsolar reconnection happens when IMF is southward oriented (B_Z-). Still, dayside reconnection that opens closed geomagnetic field lines on at the magnetopause can occur for orientations with B_Z+ as long as the B_Y component is significant (clock angles within the 40°−240° range; e.g. *Neudegg et al.*, 2000). Note that 'subsolar reconnection' will be used throughout this thesis to refer to all such dayside reconnection, even when the reconnection site is shifted away from the magnetopause nose.

Figures 2.11b and c depict reconnection scenarios for northward oriented IMF (B_Z+). IMF field lines reconnect to already open field lines in the magnetosphere lobes and cannot add more open flux to the PC. This type of reconnection is also called high-latitude reconnection. Single-lobe reconnection is shown in panel b and does not change the total amount of magnetic flux in the PC. Still, it can excite convection, as tension forces on the field lines cause movement in the direction indicated by the blue arrows. For a strongly northward IMF (B_Z+ and $B_Y \approx 0$ nT), the same IMF field line can reconnect to open lobe field lines in both hemispheres, closing the magnetic field lines and reducing the amount of open flux in the PC. This is called dual-lobe reconnection and is illustrated in panel c.

The ionospheric convection resulting from lobe reconnection has a direction opposite of the pattern excited by subsolar reconnection. Figure 2.11e shows the 'stirring' of ionospheric plasma due to single-lobe reconnection. Note how the footprint of the magnetopause reconnection (dashed red line) is poleward of the OCB (solid red line). No expansion or contraction of the PC is observed. The reverse convection cells, or lobe cells, are asymmetric depending on the sign of B_Y, as this IMF component adds tension forces in the dawn-dusk direction. Panel e depicts how the dawn-side lobe cell

is larger in the northern hemisphere for B_Y+ (e.g. *Milan et al.*, 2020). The closing of flux by dual-lobe reconnection leads to a PC contraction, as shown by the green arrows in panel f. Here the ionospheric convection has a direction opposite of the convection in panel a.

It is now clear how the shape of the large-scale ionospheric convection (the global convection pattern) is dependent on the IMF orientation. Many statistical models of the ionospheric convection sorted by IMF orientation have been constructed using different observational methods and modelling techniques. Examples of observational methods that are used for making climatological models of global convection are ground-based coherent and incoherent scatter radars (e.g. *Thomas and Shepherd*, 2018; *Zhang et al.*, 2007), ground-based magnetometers (e.g. *Friis-Christensen et al.*, 1985), and in-situ observations from low-altitude spacecraft (e.g. *Weimer*, 2005) and high-altitude

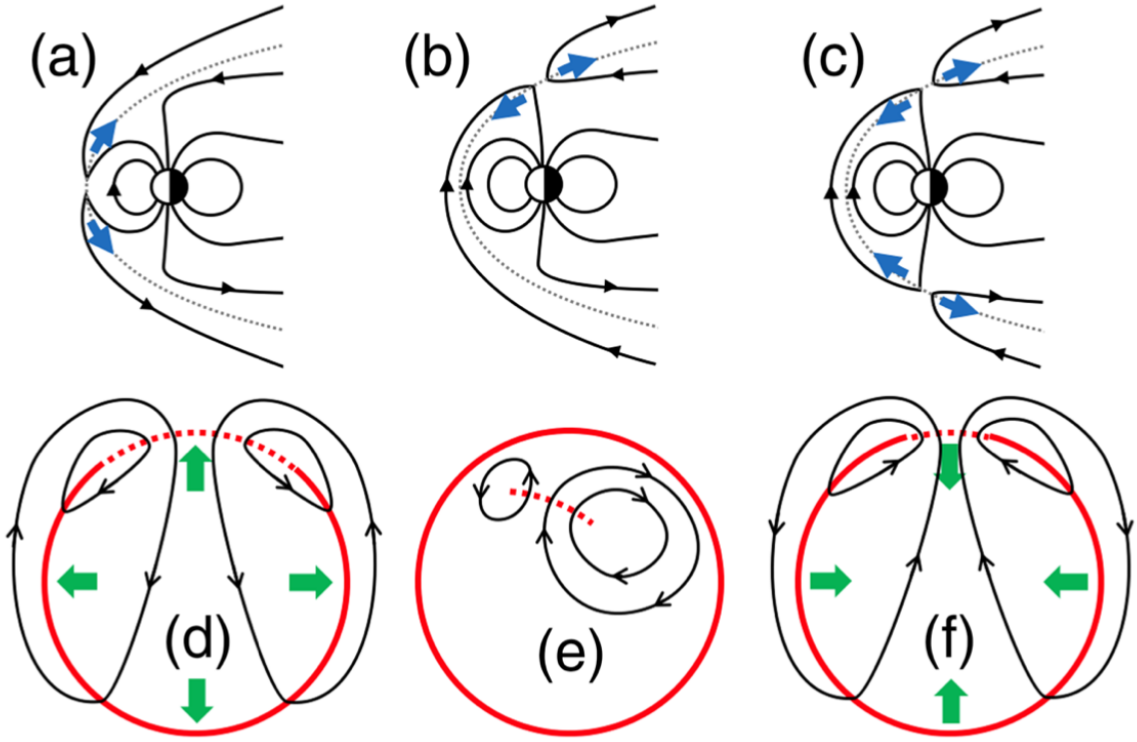

Figure 2.11: Illustration of different types of magnetopause reconnection (top row) and resulting ionospheric convection patterns (bottom row). The top row panels show cross sections of the magnetosphere in the GSM XZ-plane. The Sun is to the left. The solid arrow lines are magnetic field lines. Dashed lines are the magnetopause. Blue arrows indicate flow direction of the field lines after reconnection. In the bottom row panels, magnetic noon is up and dusk is to the left. Black arrow lines are convection streamlines. Solid red lines are the open-closed boundary. Dashed red lines show the location of newly reconnected field lines. The green arrows indicate expansion or contraction of the polar cap. (a and d) Subsolar reconnection opens magnetic field lines resulting in an expansion of the polar cap. (b and e) Single-lobe reconnection results in lobe reverse convection cells in the polar cap. The depicted convection is in the northern hemisphere for IMF B_Y+. (c and f) Dual-lobe reconnection closes open magnetic flux in the lobes and results in a contraction of the polar cap (from *Milan et al.*, 2020).

spacecraft (e.g. *Förster and Haaland*, 2015).

An example of convection patterns sorted by different IMF clock angles is shown in Figure 2.12. The panels show average (statistical) convection patterns inferred from more than ten years of observations of electron drifts from the high-altitude Cluster spacecraft (*Förster and Haaland*, 2015). The patterns are presented in MLAT/MLT coordinates. Although the contours are lines of equal electric potentials, they can be interpreted as convection streamlines. Black arrows are added to show the direction of the convection. The closer these curves are spaced, the stronger the convection is. The centre panel indicates the IMF clock angle.

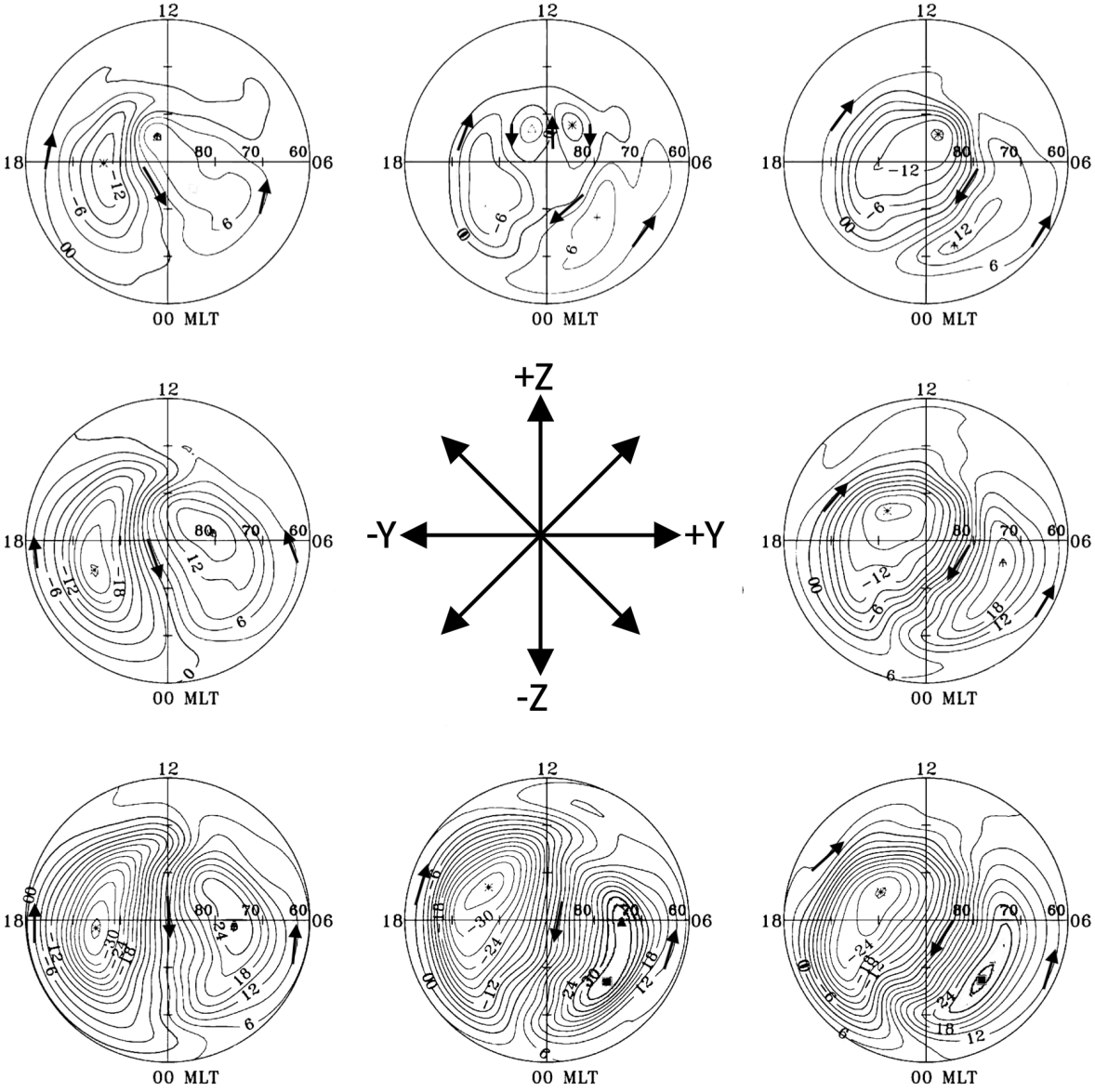

Figure 2.12: Statistical patterns for electric potential in the polar ionosphere based on observations from high-altitude spacecraft. The patterns are sorted for the different orientations of the IMF given in the central panel. The curves can be interpreted as convection streamlines where the small arrows show the direction of the flow (adapted from *Förster and Haaland*, 2015).

The pattern for southward IMF in the centre panel at the bottom of Figure Figure 2.12 shows a twin-cell convection pattern similar to the one in Figure 2.10. When comparing the convection patterns on the right and the left, the dawn-dusk tension forces introduced by the IMF B_Y component is visible as they lead to asymmetries in the pattern. B_Y+ makes the dusk-cell rounder, and B_Y- makes the dawn-cell rounder. The patterns for northward IMF (top row) have some sunward convection inside the PC, reflecting the lobe convection cells from Figure 2.11e. The patterns for northward IMF show weaker convection in areas restricted to higher latitudes, as for a contracted PC, while the patterns for southward IMF show generally stronger convection that ex-

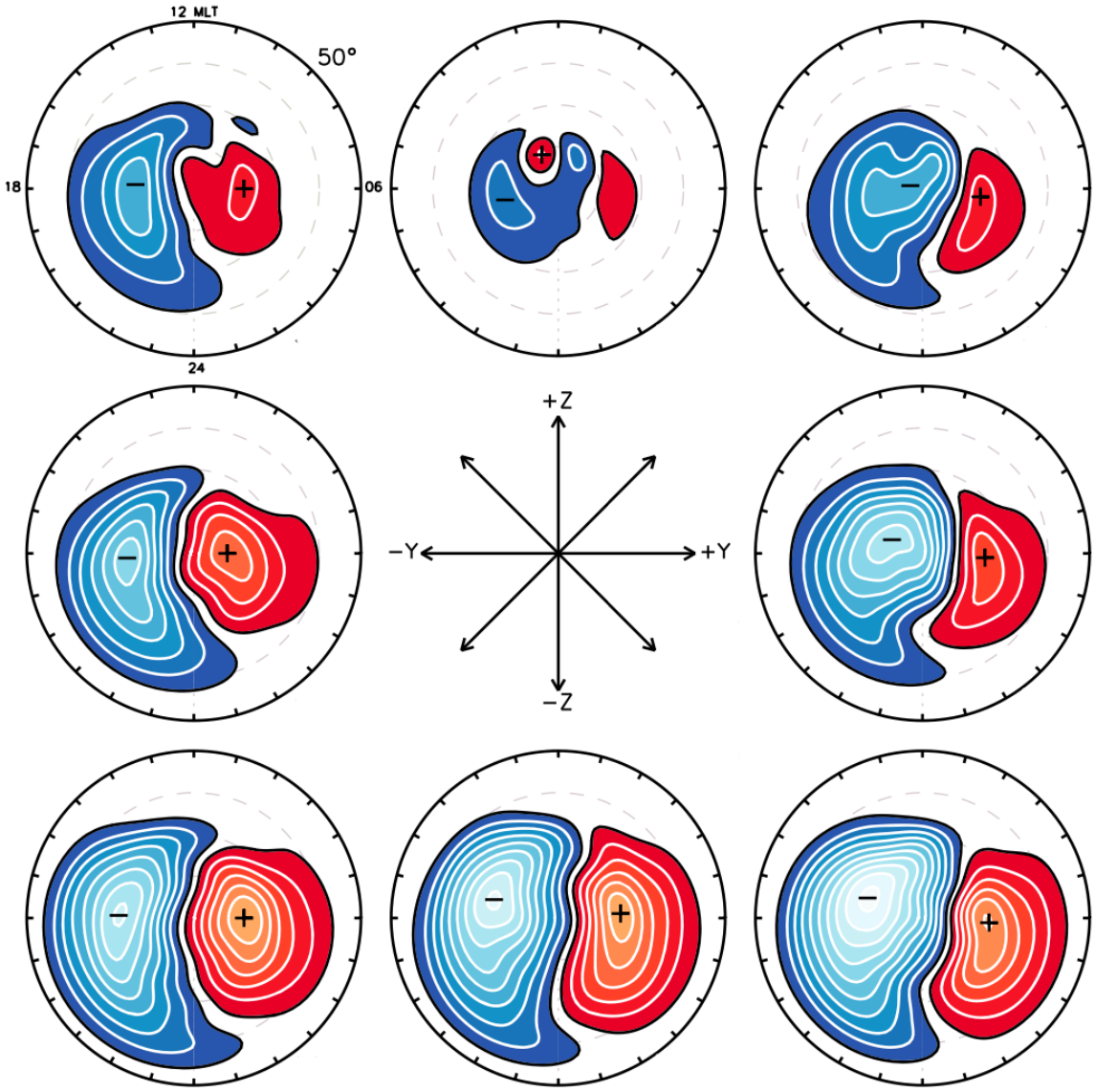

Figure 2.13: Statistical patterns for electric potential in the polar ionosphere based on observations from ground-based radars. The patterns are sorted for the different orientations of the IMF given in the central panel. The curves can be interpreted as convection streamlines where blue (red) contours have convection in the clockwise (counter-clockwise) direction (adapted from *Thomas and Shepherd*, 2018).

tends to lower latitudes reflecting an expanded PC. The contribution from the nightside reconnection can be seen in the global convection patterns for all IMF orientations as the sunward return flow on the lower latitudes.

Several new convection models have emerged over the years as more data of large-scale convection becomes available. Figure 2.13 presents one of the newest examples; a set of statistical convection patterns sorted on IMF clock angle that are made from seven years of observations of plasma drifts from all northern hemisphere radars in the SuperDARN network (mid, high and polar-latitude radars; *Thomas and Shepherd*, 2018, see Section 3.2). Convection follows the blue (red) contours in the clockwise (counter-clockwise) direction. Despite the advances in the global statistical convection models, they continue to show the same main convection features as described for Figure 2.12.

2.6.2 Mesoscale convection in the ionosphere

As presented in the previous Section 2.6.1, the average high-latitude ionospheric convection is seen as a continuous laminar flow on a global scale. However, on the mesoscale ($\sim$30$-$500 km; *Gabrielse et al.*, 2018), the ionospheric flows are more turbulent when looking at specific time intervals (e.g. *Herlingshaw et al.*, 2019). The mesoscale flows are important for how magnetic flux and plasma is transported across the PC and have also been linked to the formation of plasma structures (density irregularities) in the ionosphere (e.g. *Oksavik et al.*, 2011; *Spicher et al.*, 2016). However, the formation of mesoscale flows and their effect on the coupled SW-M-I-thermosphere system is not well understood. (The thermosphere is the upper region of the neutral atmosphere.)

Rockets, low-altitude satellites, and ground-based radars, like incoherent scatter radars (ISR) and the radars in the SuperDARN array, have been used to study flow structures on this scale. The mesoscale convection phenomena are classified based on speeds, locations, and temporal and spatial scales. Some classifications are based on the observational method used, and multiple terms are used in the literature to describe observations of what is possibly the same phenomena. The flow structures observed are often narrow, transient channels of enhanced or reversed flow embedded within the large-scale convection.

Most studies of mesoscale flows have been focused on the dayside, as transient convection structures have been related to bursty (subsolar) dayside reconnection - flux transfer events (FTE; *Russell and Elphic*, 1978). Examples of dayside convection phenomena thought to be ionospheric responses to FTEs are flow channel events (FCE; *Pinnock et al.*, 1993) and pulsed ionospheric flows (PIF; *Provan et al.*, 1998). FCE are longitudinally extended channels of fast flows ($2-3$ km/s) in the same direction as the background convection. PIF also refers to channels of enhanced flow and have been named due to their repetitive (pulsed) behaviour.

Another type of regularly observed mesoscale convection structure is reverse flow events (RFE; *Rinne et al.*, 2007). Unlike the flow transients described so far, RFEs are channels of enhanced convection that oppose the background flow. They are long and narrow channels with lengths of >400 km and widths in the range $\sim$50$-$250 km. The RFE are a common feature in the dayside ionosphere and are observed 16% of the time in the cusp (*Rinne et al.*, 2007). RFEs are mainly observed during B_Y-dominated IMF conditions (*Rinne et al.*, 2007; *Moen et al.*, 2008). RFEs have also been linked to FTE,

but their exact driving mechanism is not yet resolved.

RFEs have primarily been studied using the European Incoherent Scatter (EISCAT) Svalbard Radar (e.g. *Oksavik et al.*, 2004, 2005; *Rinne et al.*, 2007; *Moen et al.*, 2008). However, *Oksavik et al.* (2011) showed that RFE could also be resolved in observations by the SuperDARN radars. Figure 2.14 shows an example of an RFE observed on the dayside by a SuperDARN radar during winter. The RFE is indicated by a pink arrow and is seen as a narrow channel of flow anti-sunward flow (red colour) is embedded in a sunward flow (blue colour). The large-scale background convection similar to the patterns in Figure 2.13 is overlaid with solid or dashed back curves.

The term flow channel (FC) is used to refer to latitudinally extended, narrow (a few 100 km) channels of enhanced convection (>900 m/s). FCs have been shown to play a significant role in the overall transport of magnetic flux over the PC. Though FCs were first studied in the cusp region, they are also observed at other MLTs (even at the nightside) with a slight dawn-side preference (*Herlingshaw et al.*, 2019).

FCs are often presented in the framework of *Sandholt and Farrugia* (2009), where they are divided into four categories based on location. FC 1 and FC 2 are observed on the dayside and have been related to dayside processes. FC 3 and FC 4 are observed on the nightside and have been linked to activity in the magnetosphere lobes or tail (*Andalsvik et al.*, 2011; *Gallardo-Lacourt et al.*, 2014; *Gabrielse et al.*, 2018; *Herlingshaw et al.*, 2019, 2020). Figure 2.15a and b shows the predicted MLT location of the types of FC in the polar ionosphere. The dashed line is the OCB, and FC 1 (red), FC 2 (blue), and FC 3 (green) are thought to occur on open magnetic field lines. The FC 4 (yellow) are thought to occur on closed field lines. FC 0 (purple) are channels observed on closed magnetic field lines in the return flow.

Similar to the RFEs, FCs are observed during periods where the IMF is B_Y-

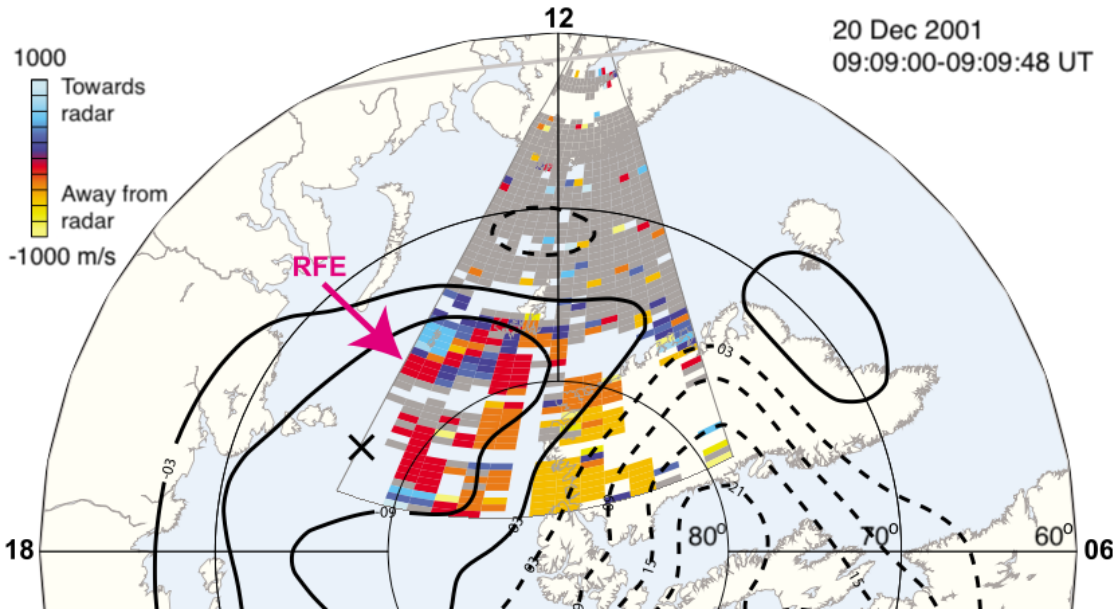

Figure 2.14: Example of a reversed flow event observed by a SuperDARN radar on an MLAT/MLT grid. The pink arrow indicates the narrow channel of flow opposing the direction of the surrounding convection (adapted from *Oksavik et al.*, 2011).

dominated, and their location on the dawn or dusk side depends on the sign of B_Y. This dependence is summarised in Figure 2.15, where panels a and b show a dusk-side preference for B_Y+, and a dawn-side preference for B_Y-. Panels c and d are occurrence distributions of all FC for the different signs of B_Y (*Herlingshaw*, 2021).

The mesoscale flows in the high-latitude ionosphere are commonly studied in relation to auroral forms. Nightside flow transients are, in fact, mainly studied in relation to auroral streamers (namely FC 4; e.g. *Herlingshaw et al.*, 2019; *Gallardo-Lacourt et al.*, 2014). (Streamers are narrow, equatorward moving auroral forms observed on the nightside.) The relation between mesoscale convection and auroral forms will be discussed in Section 2.8.

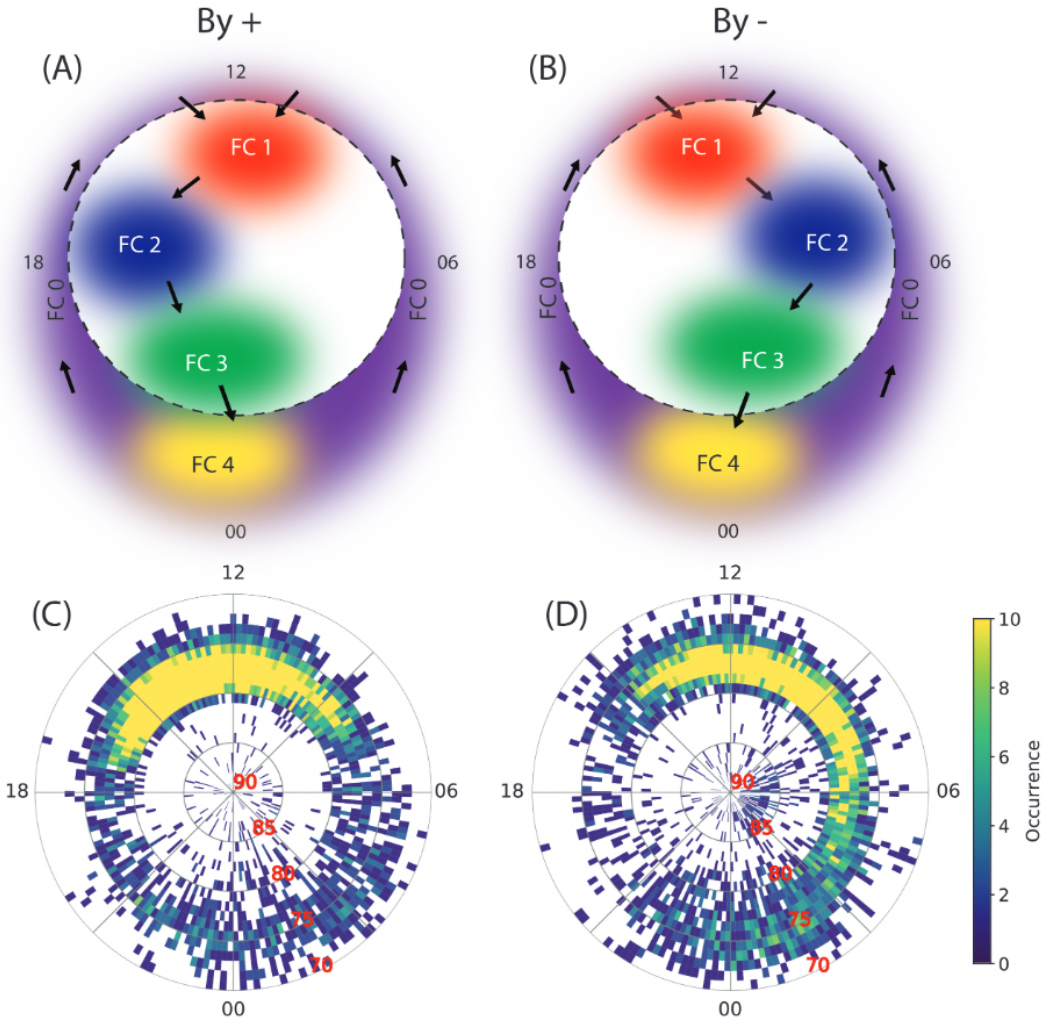

Figure 2.15: Distribution of flow channels (FC) in the polar ionosphere on an MLAT/MLT grid. (a) Preferred location of the different categories of flow channels for B_Y+. The dashed line is the open-closed boundary. (b) Same as panel a but for B_Y-. (c) Occurrence of all flow channels for B_Y+. (d) Same as panel c, but for B_Y- (from *Herlingshaw*, 2021).

2.6.3 Currents in the polar ionosphere

The M-I coupling sets up currents in the ionosphere. The currents are measurable as magnetic disturbances on ground or in space. On time scales longer than a few tens of seconds, the ionospheric electrodynamics can be said to be steady-state (*Milan*, 2013), and the currents flowing in the M-I system must flow in closed loops according to Ampere-Maxwell's law. On steady-state time scales the displacement current vanishes ($\epsilon_0\mu_0\frac{\partial \mathbf{E}}{\partial t} \approx 0$) and taking the divergence of Ampere-Maxwell's law yields $\nabla\cdot\mathbf{j} = 0$, as the divergence of a curl is zero. Hence, the current density in the M-I system is divergence free.

The ionospheric Ohm's law can be used to relate the ionospheric current density, $\mathbf{j}$, and the ionospheric electric fields, $\mathbf{E} = \mathbf{E}_\perp + \mathbf{E}_{||}$:

$$\mathbf{j} = \sigma_P\mathbf{E}_\perp + \sigma_H\hat{\mathbf{b}} \times \mathbf{E}_\perp + \sigma_{||}\mathbf{E}_{||} \tag{2.6}$$

where $\hat{\mathbf{b}}$ is a unit vector pointing along the main geomagnetic field. σ_P, σ_H and $\sigma_{||}$ are the Pedersen, Hall and parallel conductivities, respectively. The perpendicular ($\perp$) and parallel ($||$) directions are with respect to the geomagnetic field lines (*Baumjohann and Treumann*, 2012).

Equation (2.6) describes the three-dimensional structure of the ionospheric current system. On the right-hand side, the terms from left to right correspond to the horizontal Pedersen and Hall current densities ($\mathbf{j}_P$ and $\mathbf{j}_H$), and a parallel current density ($\mathbf{j}_{||}$). The Pedersen currents flow parallel to the horizontal electric field ($\mathbf{j}_P \parallel \mathbf{E}$, $\mathbf{j}_P \perp \mathbf{B}$), while the Hall currents have horizontal flow perpendicular to the electric field ($\mathbf{j}_H \perp \mathbf{E}$ and $\mathbf{B}$). The parallel currents are called field-aligned currents (FAC), or Birkeland currents after *Birkeland* (1908) who proposed their existence.

In Figure 2.16, the direction of the Hall and Pedersen currents are given by green and orange arrows, respectively. The convection electric field is presented as short black arrows (Equation (2.3)). The large-scale convection pattern for southward IMF (e.g. Figure 2.10) is shown by the arrow lines in Figure 2.16. The direction of the FACs into and out of the ionosphere is given by the red dotted circles and blue crossed circles, respectively.

The plasma in the ionosphere can interact with neutral particles through collisions. If the collisions are frequent and efficient enough, they affect the movement of the plasma, particularly the ions. It is this frictional coupling between the plasma and the neutral atmosphere that is reflected in the conductivities. In the F-region ionosphere (>150 km, see Section 2.3) the conductivities are usually low and both ions and electrons are moving with the $\mathbf{E} \times \mathbf{B}$ drift velocity:

$$\mathbf{v}_\perp = \frac{\mathbf{E} \times \mathbf{B}}{|\mathbf{B}|^2} \tag{2.7}$$

At E-region altitudes (90−150 km, see Section 2.3), collisions with neutrals modify the ion movement to a larger degree, and at these altitudes, the conductivity can be significant (*Ieda et al.*, 2014). The Hall and Pedersen currents in the ionosphere flow where the ionosphere is conductive, and it is common to assume the horizontal ionospheric currents flow in a thin layer of the ionosphere between $\sim 100 - 120$ km

altitude where the horizontal conductivities are the highest (*Laundal et al.*, 2021).

The electrons are very mobile along the magnetic field lines. Therefore the parallel conductivity is very high, and the parallel electric field ($\mathbf{E}_{||}$) must be small, often assumed to be zero. The electric field due to plasma motions perpendicular to the magnetic field ($\mathbf{E}_{\perp}$) is conserved along the magnetic field lines: $\mathbf{E}_{\perp}(h_1) = \mathbf{E}_{\perp}(h_2)$. Thus one can integrate the horizontal components of Equation (2.6) over the height of the ionosphere:

$$\mathbf{J}_{\perp} = \Sigma_P \mathbf{E} + \Sigma_H \hat{\mathbf{b}} \times \mathbf{E} \tag{2.8}$$

where Σ_P and Σ_H are the height integrated Pedersen and Hall conductivities called conductances. $\mathbf{J}$ is capitalised to indicate that is it the height integrated current density. This equation relates the horizontal current densities to the ionospheric electric field.

As $\nabla \cdot \mathbf{j} = 0$, any divergence in the height integrated horizontal current density in Equation (2.8) must be balanced by currents flowing into or out of the ionosphere, the FACs:

$$J_{||} = \nabla \cdot \mathbf{J}_{\perp} = \Sigma_P \nabla \cdot \mathbf{E} + \hat{\mathbf{b}} \cdot (\mathbf{E} \times \nabla \Sigma_H) + \mathbf{E} \cdot \nabla \Sigma_P \tag{2.9}$$

where $\nabla \cdot \mathbf{J}_{\perp} < 0$ correspond to upwards FAC, and $\nabla \cdot \mathbf{J}_{\perp} > 0$ correspond to downwards FAC. The first term on the right-hand side is the relationship between the FACs and

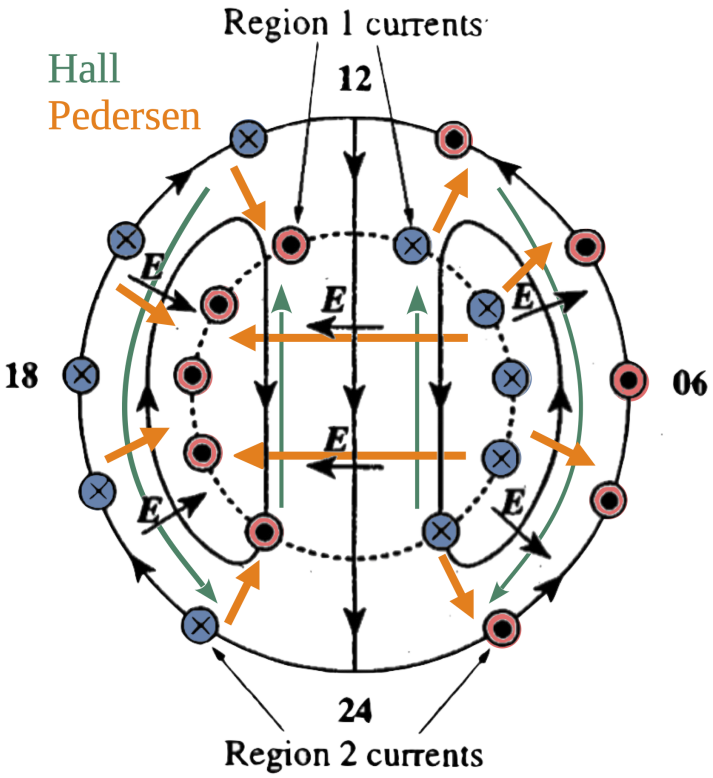

Figure 2.16: Schematic of the current system for the northern hemisphere. The black arrow lines show a two-cell convection pattern. The short black arrows are the convection electric field ($\mathbf{E}$). The orange arrows shows the direction of the Pedersen currents, and the green arrows show the direction of the Hall currents. The region 1 field-aligned currents (FACs) are at the open-closed boundary (OCB; dashed line) and the region 2 FACs are at lower latitudes. The FACs flow out of (dotted circles, red) and into (crossed circles, blue) the ionosphere (adapted from *Cowley*, 2000).

the divergence of the convection electric field. The second term is related to spatial gradients in the Pedersen conductance. The third term is related to spatial gradients in the Hall conductance. The terms containing conductivity gradients are in many cases assumed to be negligible as gradients in conductance often are very small compared to $\Sigma_P \nabla \cdot \mathbf{E}$. An example of when the gradient terms are not negligible are in regions with a high degree of localised ionisation of the lower ionosphere.

Global maps of the large-scale FACs show that the currents flow in two main regions,

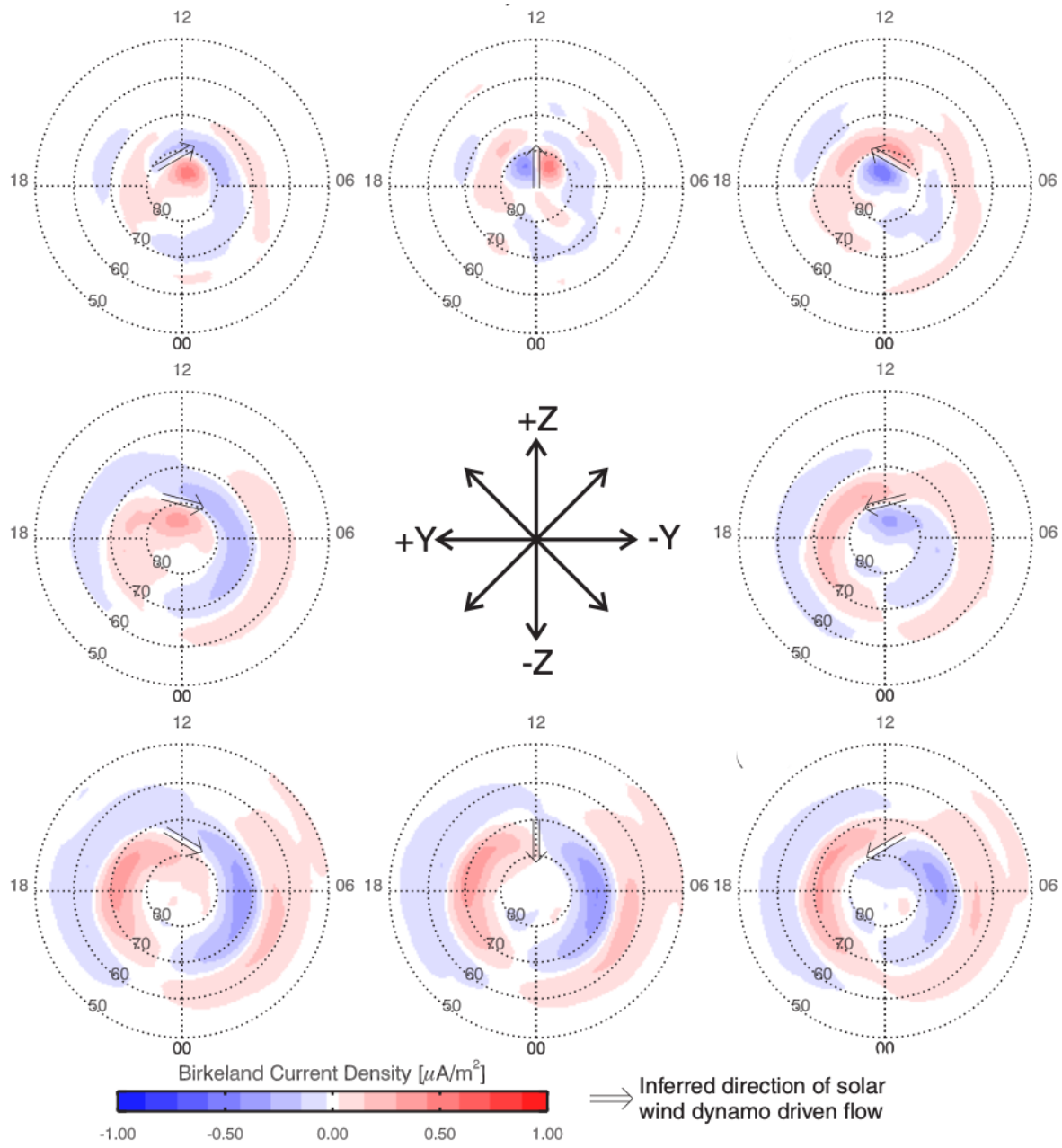

Figure 2.17: Statistical maps of field-aligned current density (FAC) based on satellite observations. The patterns are sorted by IMF orientations which are shown in the centre panel. The red (blue) contours are upwards (downwards) FAC. The arrows show the direction of flow inferred from the most poleward FACs (from *Anderson et al.*, 2008).

Region 1 (R1) and Region 2 (R2) (*Iijima and Potemra*, 1976). R1 and R2 coincide with regions of flow shears in the 'traditional' two-cell convection pattern. In Figure 2.16, R1 FACs are on the boundary between the anti-sunward and sunward convection, the OCB (dashed line). The R2 FACs are on the boundary between the sunward return flow and the region at lower latitudes where there is no convection.

Figure 2.17 shows large-scale statistical patterns of the FAC sorted on IMF orientation. The patterns are inferred from observations from low Earth orbit (LEO) satellites (magnetometer observations; *Anderson et al.*, 2008). The centre panel indicates the IMF clock angle. The R1 and R2 currents are visible in the patterns as red and blue 'half moons' matching the schematic in Figure 2.16. Note how the R1 currents are, in general, stronger than the R1 currents. The patterns also look similar to the global convection patterns in Figures 2.12 and 2.13. The regions of FAC at high latitudes in the top row panels (specifically in the centre top panel) are the northward B_Z currents (NBZ currents; *Anderson et al.*, 2008).

The relation between FACs and velocity shears means that observations of the vorticity in the ionospheric convection can be used to study FAC (e.g. *Freeman et al.*, 1990b; *Sofko et al.*, 1995; *Chisham et al.*, 2009; *Milan*, 2013). The relationship between diverging electric fields, convection and FACs is discussed further in Section 4.6.

2.7 Aurora

Aurora is a visible consequence of the SW-M-I coupling. The stress transfer from the magnetosphere to the ionosphere to put ionospheric plasma into motion (convection) is communicated by the FACs and thus accompanied by flows of charged particles along the magnetic field lines. The aurora is caused by precipitating particles hitting the atmosphere. Particles with sufficient energy will excite neutrals, and as the neutrals fall back to their ground state, they emit light. The precipitating particles also cause plasma production through impact ionisation, locally enhancing the ionospheric conductivity (*Borovsky and Valdivia*, 2018).

Main oval

Auroras are commonly observed in an approximately circular belt surrounding the magnetic poles, the auroral oval, or the main oval. The main oval encircles the PC and is primarily situated on what is believed to be closed magnetic field lines. The oval size and width vary considerably with geomagnetic activity, as its shape, brightness, and size reflect processes in the magnetosphere. The main oval auroras are, on average, located around $\sim 70^\circ$ MLAT (*Akasofu*, 1981). Most of the bright aurora is produced by the impact of precipitating electrons, though precipitating ions can also excite neutrals (*Zhu et al.*, 1997; *Borovsky and Valdivia*, 2018). Aurora is therefore seen in regions where FACs flow (R1 and R2 FAC; see Section 2.6.3), primarily where the currents flow out of the ionosphere (upwards FACs are associated with precipitating electrons).

Figure 2.18 shows the average location of the main oval in the northern hemisphere for typical levels of geomagnetic activity (*Loewe and Prölss*, 1997). Panel a shows the main oval region (hatched) constructed from a collection of ground-based all-sky imager observations by *Feldstein and Starkov* (1967). *Milan et al.* (2010) observed the same

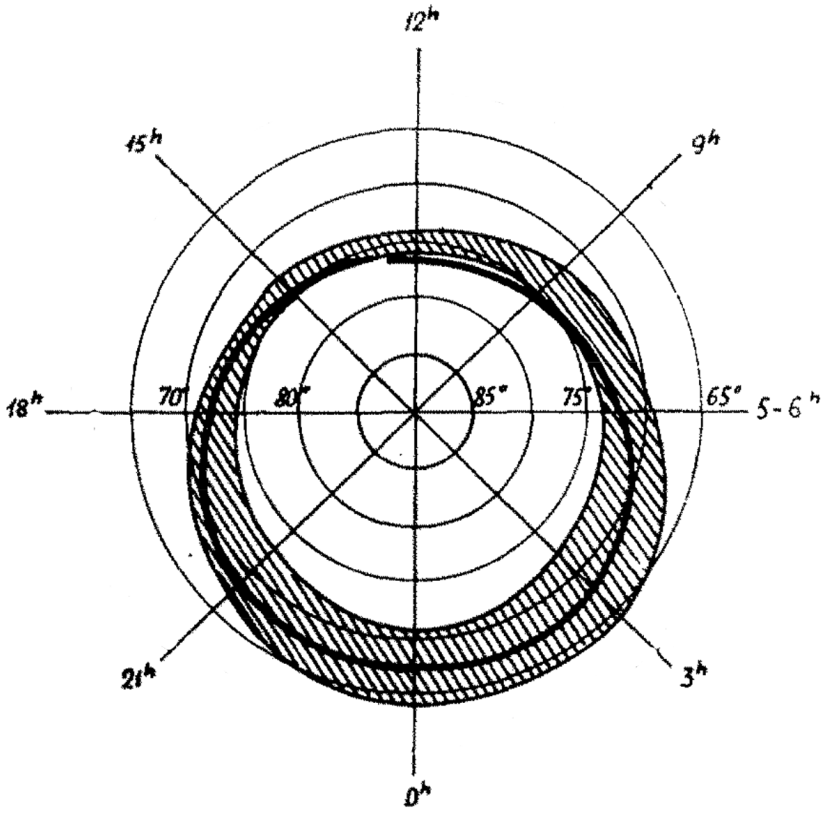

(a)

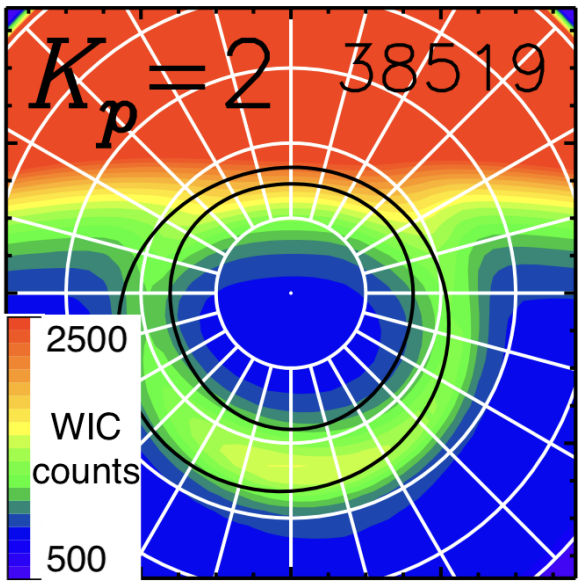

(b)

Figure 2.18: Location of the main oval auroras in the northern hemisphere. (a) Pattern (hatched region) determined from ground-based observations (adapted from *Feldstein and Starkov*, 1967). (b) Averaged observations of the auroras in the northern hemisphere observed by space-based global imagers. The higher counts towards the dayside is due to dayglow (adapted from *Milan et al.*, 2010).

general location of the main oval auroras with observations from space-based global imagers. Panel b shows the average counts from two years of images with the oval shape from panel a superimposed (black curves). The high counts towards the dayside are dayglow (emissions due to sunlight).

Auroral emissions

The aurora's emission altitude depends on the particle precipitation's energy, as this energy is related to the penetration depth — high energy auroral precipitation cause auroral emissions at lower altitudes than lower energy auroral precipitation. The emission altitude range is typically from 105−400 km (*Akasofu*, 1981) but auroral emissions are sometimes also observed outside this range.

The auroral emissions have different wavelengths (colours) depending on what molecule or atom is excited. The colours of the aurora also have different altitude ranges, partly due to the altitude ranges of the concentration of different species in the neutral atmosphere. The atmospheric density decreases with increasing altitude, and the density of heavier species decreases more rapidly than that of the lighter species (see Figure 2.2b). The altitudes of three major optical auroral emission lines reflect this. Lower altitude (∼80−120 km; *Sandholt et al.*, 2002) optical aurora is emitted by molecular nitrogen, N_2, and has wavelengths of 427.8 nm ('blue-line'). The often most dominating optical aurora are 'green-line' emissions (577.7 nm) from atomic oxygen, O, at altitudes from 150−230 km (*Sandholt et al.*, 2002). At even higher altitudes, the 'red-line' (630.0 nm) aurora is observed (*Gillies et al.*, 2017).

The red-line emissions are caused by the transition of atomic oxygen from the excited state $O(^1D)$ to the ground state. The initial excitation of the atomic oxygen is caused by precipitating auroral electrons. The excitation energy of the $O(^1D)$ excited state is low and makes this emission sensitive to lower energy precipitation (*Liang et al.*, 2016).

The red-line emissions can exist in a broad altitude range (150−400 km) where the concentration of atomic oxygen is abundant. The $O(^1D)$ excited state has a long radiative lifetime, ∼110 seconds, which partly explains the lower limit of the altitude range of the red-line aurora. Looking at Figure 2.2b, atomic oxygen is still abundant at altitudes below 150 km. Still, at lower altitudes where the density of the atmosphere is higher, quenching by gases (especially N_2) suppresses the emissions before they happen. The red-line is more extended in altitude than other auroral emissions, making the emissions more challenging to study through auroral imaging. This will be further discussed in Section 3.4.

Auroral emissions also occur outside the visible part of the spectrum. Additional auroral emission lines can be observed using cameras sensitive to X-ray and far-ultraviolet (FUV, wavelengths <170 nm) radiation. There is a range of wavelengths that are seen in FUV images of the aurora. Some of the more distinct lines are emissions from hydrogen (Lyman-α; 121.6 nm) and from atomic oxygen (130.4 nm and 135.6 nm), while a range of other FUV wavelengths is related to emissions from N_2. The N_2 FUV emissions are known as the Lyman-Birge-Hopfield (LBH) band, which is divided into LBHS (short, ∼140−160 nm) and LBHL (long, ∼160−180 nm). The N_2 FUV emissions are prompt and are assumed to come from lower ionospheric altitudes (∼80−120 km) (*Lee et al.*, 2010).

Airglow

Emissions of light from gases in the atmosphere can also be due to other processes than particle precipitation. When ionised particles recombine (see Section 2.3), they emit electromagnetic radiation observed as airglow. The airglow from recombination of atomic oxygen ions at high altitudes has the same wavelengths as red-line aurora (630.0 nm). The plasma at these altitudes is long-lived, and the airglow from the recombination can be used to locate and track regions of high plasma density (like polar cap patches) or regions void of plasma (depletion regions) in the ionosphere (*Gillies et al.*, 2017).

Diffuse and discrete aurora

The aurora can be divided into the diffuse or discrete aurora. Diffuse aurora is usually weaker emissions with little internal structure. The diffuse aurora is usually spread over a wide area on the equatorward edge of the main oval. The discrete aurora has a more structured, often curtain-like form. Auroral arcs are discrete auroral forms. Discrete auroral forms are most often observed on the poleward side in the main oval, where multiple arcs can be observed close together (*Akasofu*, 1981).

From ground-based optical observations, structures in the main oval can be distinguished from each other, especially when viewing from below, as shown in the all-sky image in Figure 2.19. The image shows an example of when multiple curtains of au-

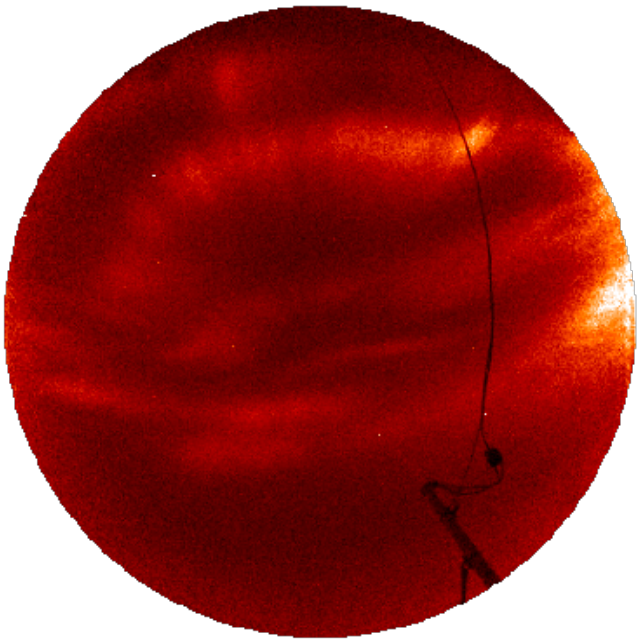

Figure 2.19: Example of multiple discrete auroral forms within the main auroral oval. The image shows 630.0 nm emissions from a ground-based all-sky camera.

rora are visible in the 630.0 nm emissions. Other optical observational methods (like space-based imagers) with poorer spatial resolution can rarely distinguish between the individual arcs and structures comprising the main oval but rather sees one bright band of auroral emissions.

2.7.1 Aurora poleward of the main oval

Most auroras are found in the main auroral oval, but auroral features can also be observed elsewhere. On the poleward side of the main oval (inside the PC), a variety of auroral features have been reported, either in the form of discrete auroral arcs or spots of auroral emissions (see reviews by *Zhu et al.*, 1997; *Newell et al.*, 2009; *Frey et al.*, 2019; *Hosokawa et al.*, 2020).

FUV images of the aurora from high-altitude satellites are used to observe the large-scale aurora over time as they give a global view of the entire hemisphere with good temporal resolution. However, they are limited to studying brighter and wider polar cap auroral features due to lower spatial resolution and higher intensity thresholds. LEO satellites can also observe aurora inside the PC, usually through UV imagers. These satellites have a better spatial resolution and lower intensity threshold than the global imagers. They can thus see thinner and dimmer auroral forms, but they have the disadvantage of a more limited observational coverage in both space and time. Imagers onboard LEO satellites only provide snapshots of the aurora as the satellites traverse the polar regions and are therefore not suited to study the temporal evolution of the aurora. All-sky imagers and LEO satellite images are further discussed in Sections 3.4 and 3.3.3, respectively. Another observational method is ground-based all-sky imagers that have a limited field of view (FOV) but high spatial resolution.

Polar auroral arcs

Auroral arcs poleward of the main auroral oval have routinely been observed from the ground since the early 1900s (*Mawson*, 1925). Polar auroral arcs are generally seen during times of northward IMF and low geomagnetic activity. Small-scale arcs with lengths of a few 100 km reaching into the poleward side of the main oval are discerned from large-scale arcs that can cross the entire PC (with lengths >1000 km; *Kullen et al.*, 2002). All polar auroral arcs disappear if the IMF turns persistently southward or if large substorms (periods of substantial tail reconnection) occur (*Kullen and Janhunen*, 2004).

The polar auroral arcs are referred to by many terms, some of which relate to specific types of polar auroral arc forms, while others are more general 'umbrella terms' for polar arc features. In order to avoid confusion, the term polar cap arc (PCA) will be used throughout this thesis to refer to general auroral arc forms observed poleward of the main oval. *Kullen et al.* (2002) studied large-scale PCA and sorted them into five categories: 'oval-aligned,' 'moving,' 'bending,' 'midnight,' and 'multiple'. The *Kullen et al.* (2002) classifications were based on observations from global imagers, and do in general, not relate to specific formation mechanisms. This is the case for many of the names used for PCA, as they historically are a result of the different observational methods that are used to study them (*Zhu et al.*, 1997). Lately, PCA terminology has been aimed at possible causal relationships between the different arc forms, though

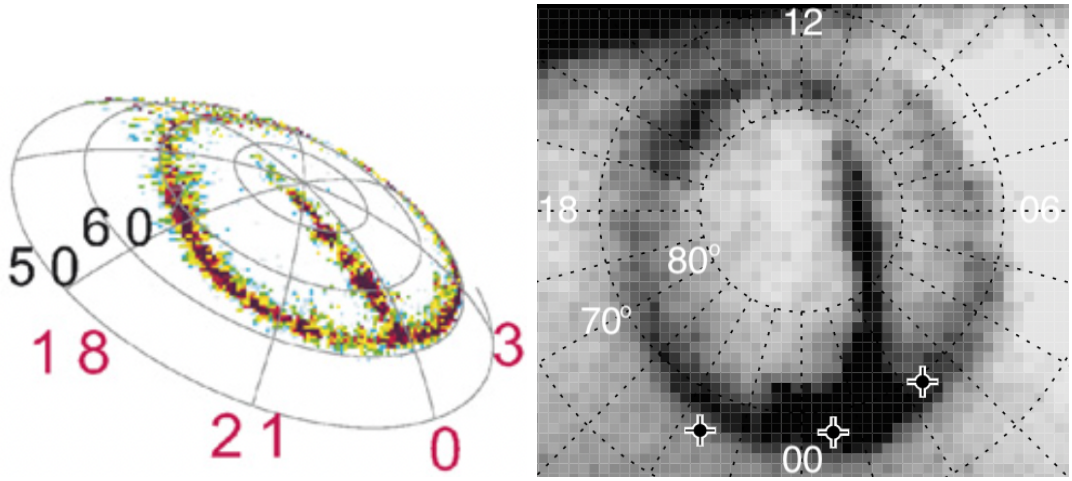

(a) (b)

Figure 2.20: Examples of transpolar arcs observed from global imagers (a) The global aurora is theta shaped (from *Østgaard et al.*, 2007). (b) A transpolar arc that has formed during IMF B_Y- (adapted from *Milan et al.*, 2005).

different names are still used in the literature. In this section, four terms used to refer to different types of PCA are introduced: *transpolar arcs*, *bending arcs*, *sun-aligned arcs*, and *horse-collar aurora*. Several of these PCA types can also be observed simultaneously (*Hosokawa et al.*, 2020).

The large-scale *transpolar arcs* (TPA) were first observed by *Frank et al.* (1982) who dubbed them 'theta aurora' due to the shape of the global auroral pattern during these events resembling the Greek letter theta. The TPA usually develop from a bulge on the nightside main oval and stretch towards the dayside. The TPA can be observed crossing the PC from midnight to midday regions, like the classic theta aurora, or they are observed only partially reaching into the PC (similar to the 'midnight arcs' described by *Kullen et al.*, 2002). TPAs have been shown to appear closer to the dawn or dusk side of the PC, with a preference depending on the sign of IMF B_Y (dawn-side preference for B_Y- and a dusk-side preference for B_Y+ in the northern hemisphere; e.g. *Fear and Milan*, 2012a; *Kullen et al.*, 2002). Some TPA will move across the PC during their lifetime ('moving arcs'; *Kullen et al.*, 2002). The direction of the movement has also been related to IMF B_Y polarity, where the TPA moves in the direction of the B_Y; duskward for B_Y+ and dawnward for B_Y- (in the northern hemisphere). A similar movement has been reported for some other types of PCA (*Hosokawa et al.*, 2020). Figure 2.20 shows examples of TPA observed from global imagers. The TPA often has a brightness similar to the main oval (*Hosokawa et al.*, 2020).

Milan et al. (2005) suggested that the TPA form as a consequence of tail reconnection during IMF northward non-substorm intervals (TRINNI). In their description, the TPA is located on closed magnetic field lines in the tail that protrude into the PC as a TRINNI occurs during IMF conditions with a significant B_Y component. Others propose that TPAs are formed as a consequence of lobe reconnection or by IMF B_Y sign changes causing twists in the magnetospheric tail (*Hosokawa et al.*, 2020).

The *bending arcs* observed by *Kullen et al.* (2002) are PCA that separate from the dawn or dusk-side main oval and become hook-shaped as they bend polewards while still

being connected on the anti-sunward end. Figure 2.21a shows an example of a bending arc observed from a global UV imager. The statistical IMF dependence of bending arcs was re-investigated by *Kullen et al.* (2015), who find some significant differences between bending arcs and other PCA. The B_Y dependence of bending arc location was opposite to that of the other PCA, and the bending arcs were most often observed shortly (within 20 minutes) after the IMF turned southward. They also observed that bending arcs were fainter and shorter-lived than other PCA.

Carter et al. (2015) proposed that bending arcs have a formation mechanism similar to that of poleward moving auroral forms (PMAFs; these will be described shortly). They explain that the bending arc is located on the poleward side of a region of newly opened flux on the dayside that is pushed into the PC as dayside reconnection occurs (for southward IMF with a significant B_Y component). Figure 2.21b shows a schematic of the suggested formation mechanism.

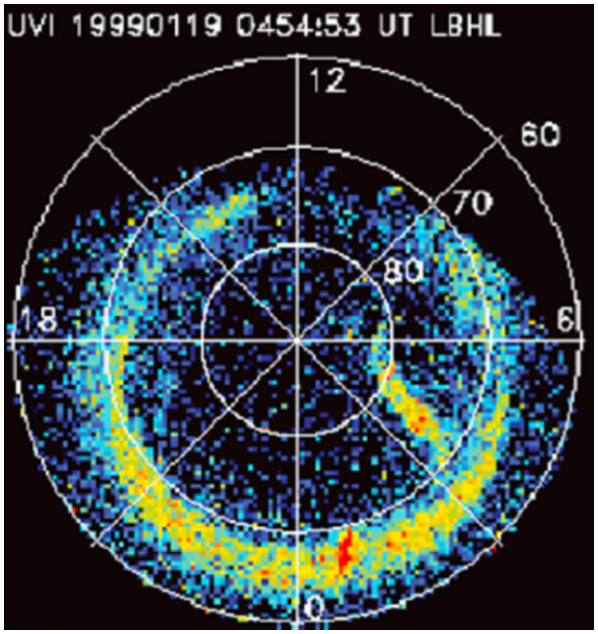

(a)

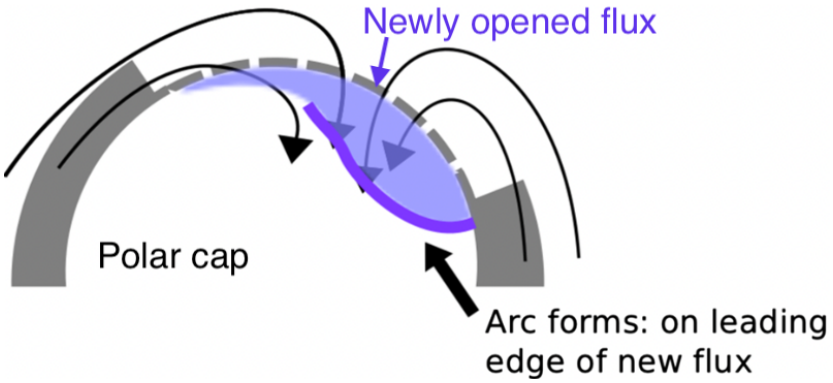

(b)

Figure 2.21: Example of a bending arc observed from a global FUV imager (from *Kullen et al.*, 2015). (b) Schematic of a suggested formation mechanism for bending arcs under IMF B_Y+ conditions (adapted from *Carter et al.*, 2015).

Faint *sun-aligned arcs* (or cusp-aligned arcs; *Zhang et al.*, 2016) are frequently observed during northward IMF (*Newell et al.*, 2009). These arcs are often grouped with TPA as they have a similar appearance but are usually thinner and possibly due to a different formation mechanism (*Hosokawa et al.*, 2020). Figure 2.22 shows multiple PCA aligned with the cusp (marked with a red circle) observed from a LEO satellite.

Sun-aligned arcs have been related to FACs associated with flow shears in the PC convection (on open magnetic field lines; *Carlson and Cowley*, 2005). *Zhang et al.* (2016) attribute sun-aligned arcs to flow shears due to instability processes on the low latitude magnetopause. *Zhang et al.* (2020) observed multiple cusp-aligned PCA at the same time. They showed through magnetohydrodynamic (MHD) simulations how multiple sheets of FAC could arise from Kelvin-Helmholtz instabilities (KHI) at the magnetopause and cause the multiple arcs aligned with the cusp.

Another PCA phenomenon where arcs are seen as sun-aligned is an auroral configuration called *horse-collar aurora* (*Hones et al.*, 1989). During strongly northward IMF conditions, the dawn- and dusk-side of the PC boundaries move poleward so that the polar cap gets a teardrop-shape, where weak auroras are seen at high latitudes on the dawn- and dusk sides. *Hones et al.* (1989) noted that brighter 'bars' of emissions (discrete arcs) are observed at the poleward edge of the horse-collar pattern. An example of horse-collar aurora is seen in Figure 2.23. *Milan et al.* (2020) attributes the horse-collar aurora to dual-lobe reconnection.

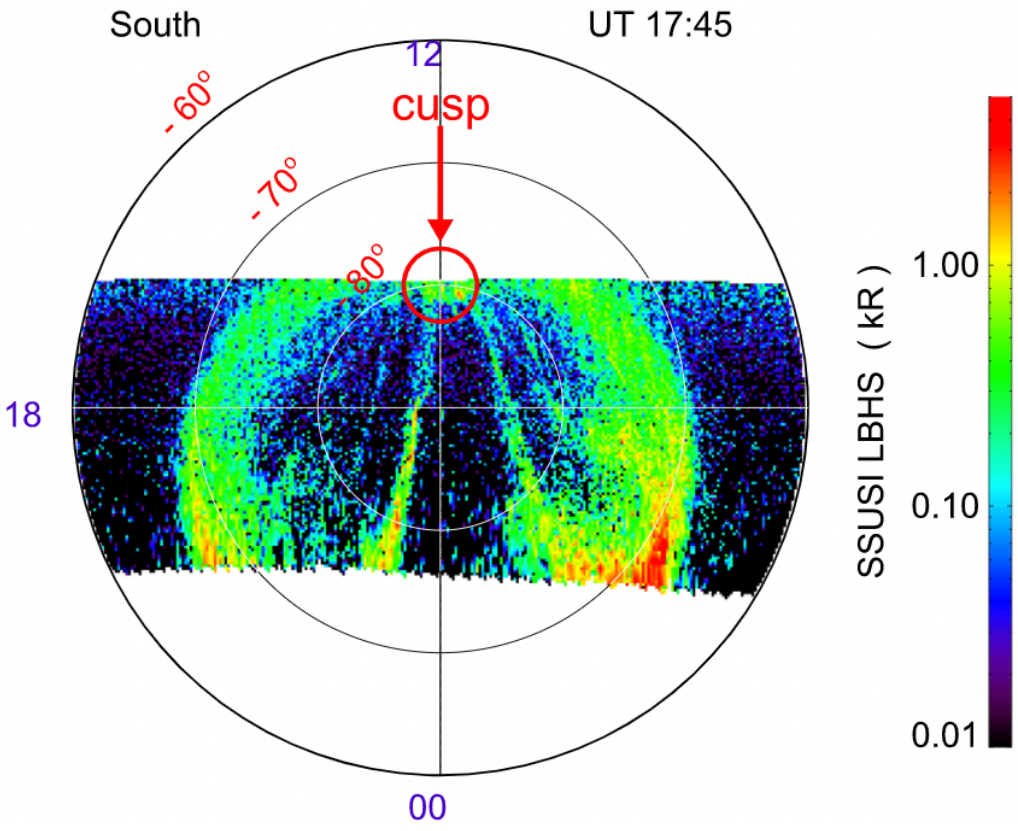

Figure 2.22: Example of multiple sun-aligned arcs observed from an FUV imager on board a low Earth orbit spacecraft (from *Zhang et al.*, 2016).

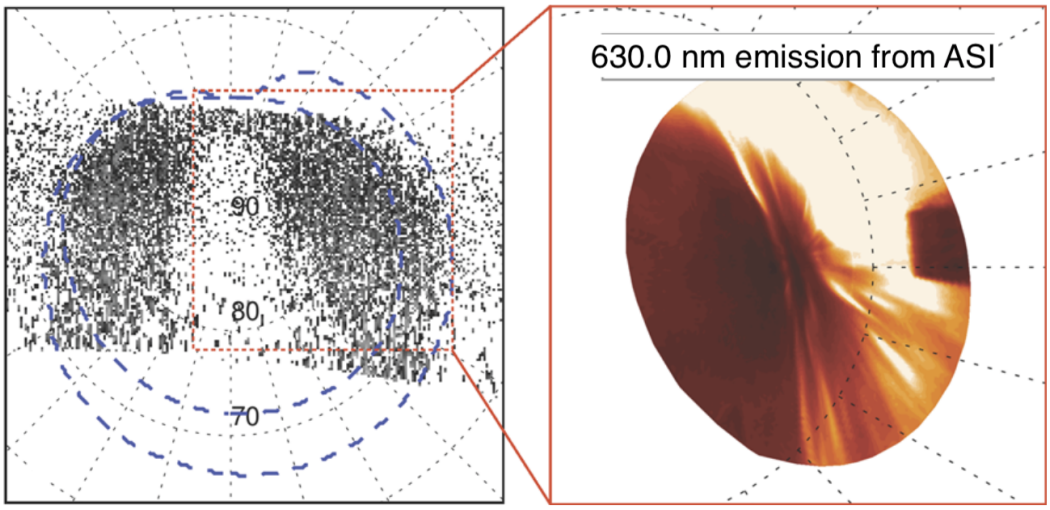

Figure 2.23: Example of simultaneous observations of horse-collar aurora observed by an FUV imager on board a low Earth orbit spacecraft (left) and from an 630.0 nm all-sky imager (right) (adapted from *Hosokawa et al.*, 2020).

Non-PCA aurora at high-latiudes

Other auroral features observed at high latitudes during northward IMF are, for instance, PMAFs, cusp spots, and High Latitude Dayside Aurora (HiLDA). PMAFs are auroral forms that split off from the main oval completely and move poleward for some minutes before they fade. PMAFs are thought to be a signature of FTEs or dynamic pressure pulses in the solar wind (*Frey et al.*, 2019). Cusp spots are also a signature of reconnection on the dayside and are observed at the main oval for southward IMF. They are associated with downwards FAC (ion precipitation; *Frey et al.*, 2019). During northward IMF, the cusp spots are seen at latitudes poleward of the main oval emissions and are thought to be the footprint of single-lobe reconnection (*Carter et al.*, 2020). HiLDAs are localised spots of aurora with hour lifetimes observed deep within an otherwise dark PC in the summer (sunlit) hemisphere. They are observed during periods of B_Y dominated IMF (B_Y+ for northern hemisphere summer) and low solar wind density and are associated with upwards FAC (electron precipitation; *Frey et al.*, 2019). HiLDAs are often seen at the same time as cusp spots and are possibly also related to single-lobe reconnection (*Frey et al.*, 2019).

In a recent paper, *Zhang et al.* (2021b) present observations of a cyclone-shaped auroral feature located in the centre of the PC. The large auroral spot had a diameter of >1000 km and multiple spiral arms and was dubbed a 'space hurricane'. The feature was observed in the northern hemisphere summer ionosphere during a period of persistently northward IMF (more than 8 hours) and quiet geomagnetic conditions. The IMF had a significant B_Y+ component, and the solar wind had low densities. They propose that the space hurricane could be the same phenomenon as HiLDA, and that the spiral shape developed due to the very prolonged period (several hours) of single-lobe reconnection. Nevertheless, it clearly illustrates that phenomena in the central PC are currently a hot topic in the international scientific community.

Auroral arc precipitation

There is still debate about which magnetic field line topology PCA occur on. Studies of PCA often include observations of particle precipitation, as energy spectral properties of the precipitating electrons and ions can be used to determine a likely magnetospheric source region (e.g. *Newell and Meng*, 1992) and may help determine if the PCA are located on open or closed magnetic field lines. Based on particle precipitation characteristics, *Newell et al.* (2009) group PCA into three types; one type residing on open field lines, and two which are on closed field lines.

Inverted-V type electron precipitation is often observed in relation to discrete auroral arcs. The nearly monoenergetic electron fluxes that increase to an energy peak and then decrease as the spacecraft moves through the precipitation region forms an upside-down V-shape in energy spectra (*Lin and Hoffman*, 1982). Inverted-Vs are associated with field-aligned acceleration of plasma due to quasi-steady field-aligned electric potential drops.

2.8 Summary of auroral forms and mesoscale convection

Most of the PCA phenomena described in Section 2.7.1 are known to be related to localised regions of enhanced plasma flows (*Hosokawa et al.*, 2020). Similarly, many of the mesoscale convection phenomena from Section 2.6.2 are studied in relation to auroral forms. Figure 2.24 shows an overview of the different auroral forms that are related to mesoscale flow structures in the polar ionosphere. The black arrows are mesoscale convection enhancements, and the black circle is the OCB.

PMAFs and their radar echo counterpart, poleward moving radar auroral forms (PMRAFs; *Wild et al.*, 2001), are signatures often seen in the vicinity of dayside convection transients, like FC 1 and RFE (e.g. *Milan et al.*, 2000; *Oksavik et al.*, 2004, 2005, 2011). *Moen et al.* (2008) showed that a discrete auroral feature was always present at the clockwise flow reversal of RFEs observed by EISCAT (in all cases where optical observations were available).

The schematic in Figure 2.25 shows how a PMAF starts as an auroral equatorward boundary intensification (EBI) at the OCB. In the figure, magnetic noon is down, and dusk is to the right. A poleward burst of convection is also observed, and the auroral feature and associated flow channel move into the PC as indicated by the grey arrows. The location and motion of the PMAFs and localised channels of convection depend on the sign of IMF B_Y. PMAFs have been shown to decay into polar cap patches (see Section 2.7) as illustrated in the schematic. As discussed in Section 2.6.2, transient convection features likely play a role in creating such plasma irregularities.

The patches have been used to study convection across the PC. *Nishimura et al.* (2014) used optical data to track a polar cap patch as it traversed the entire PC. They showed through simultaneous SuperDARN radar observations that a narrow channel of enhanced anti-sunward flow was aligned with the trajectory of the polar cap patch. *Nishimura et al.* (2014) proposed that the patch was transported from the dayside to the nightside by the mesoscale flow transient and not the slower large-scale convection. This

is evidence that mesoscale flows can propagate over large distances without diffusing away, though it is unclear what may cause them to move across the PC.

Multiple studies of convection surrounding PCA show that they are associated with strong flow shears or reversals on the edges of localised regions of enhanced anti-sunward convection (*Hosokawa et al.*, 2020). For instance, FC 2 are often seen in conjunction with PCA (*Herlingshaw et al.*, 2019). As illustrated in Figure 2.24, the PCAs are often observed on the poleward side of anti-sunward flow enhancements, consistent with the relation between FACs and diverging electric fields in Equation (2.8) (also see Section 4.6). PCA that traverse the PC must have associated channels of enhanced flows that also traverse the PC (*Lyons et al.*, 2016).

On the nightside, flow enhancements are sometimes observed as approaching the OCB. These are seen at the bottom of Figure 2.24. Poleward boundary intensifications (PBIs) and streamers are auroral phenomena that have been linked to such convection

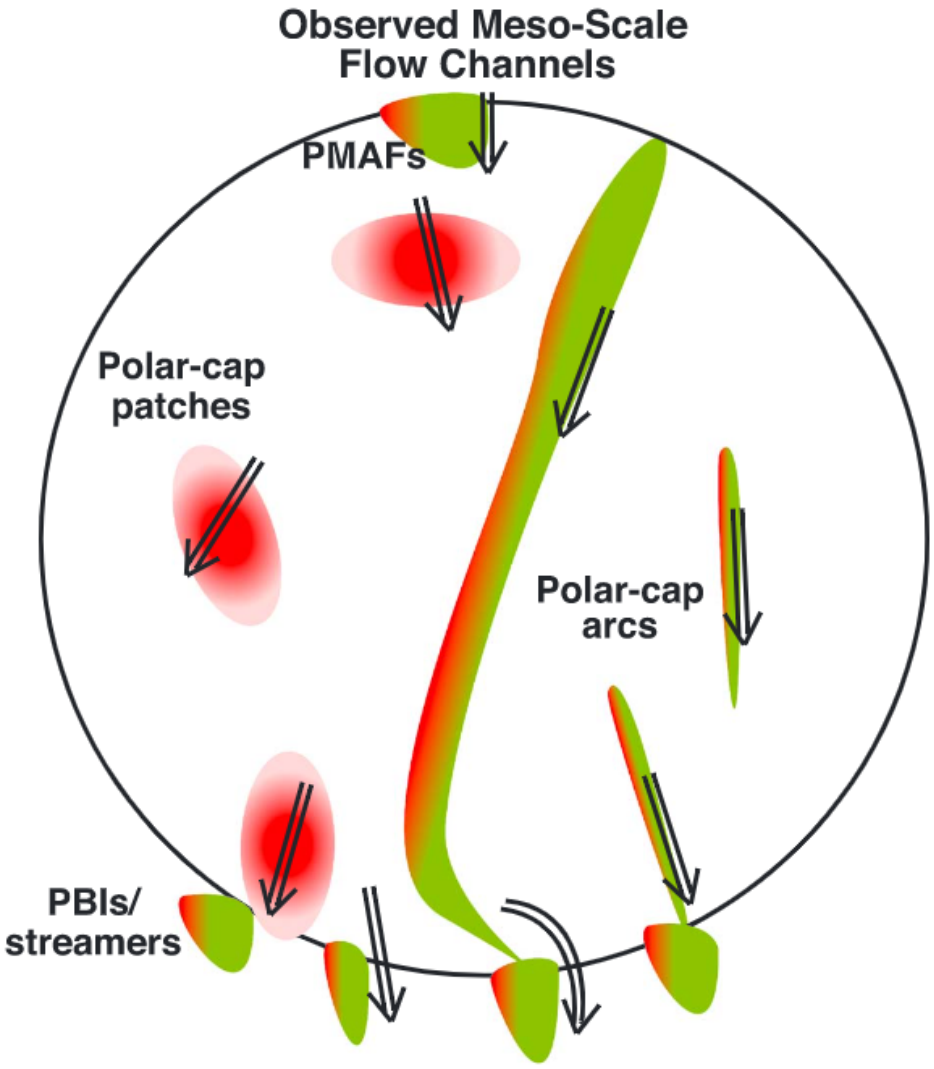

Figure 2.24: Overview of mesoscale convection enhancements and optical emissions in the polar ionosphere. The black circle is the open-closed boundary. The features are presented on an MLAT/MLT grid where noon is up and dusk is to the left (from *Lyons et al.*, 2016).

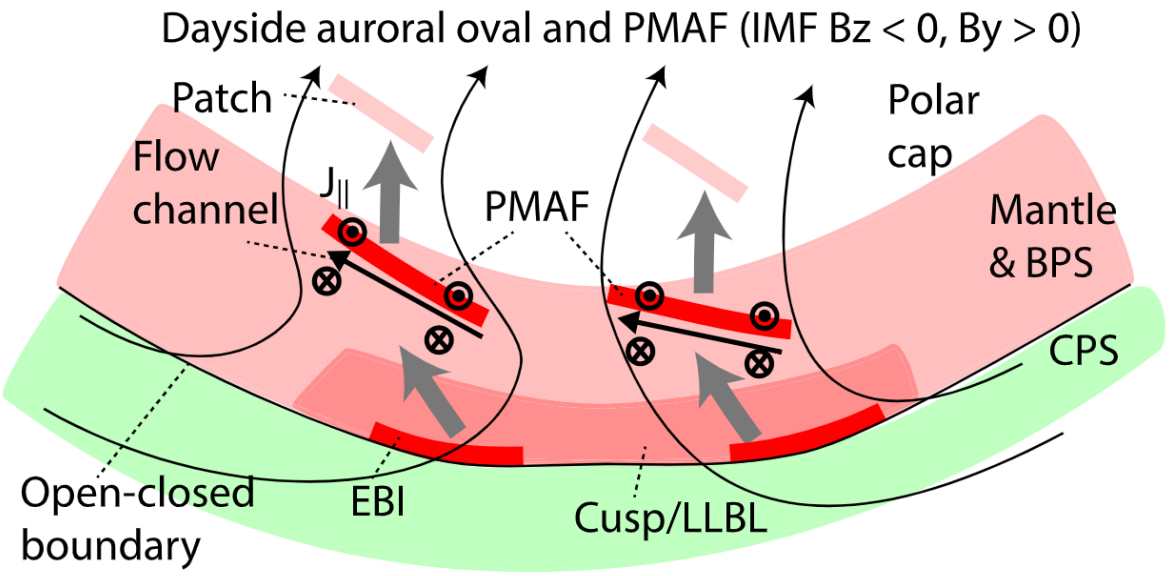

Figure 2.25: A schematic of how poleward moving auroral forms (PMAF) develop at the dayside auroral oval and traverse into the polar cap. Magnetic noon is down and dusk is to the right (from *Frey et al.*, 2019).

enhancements (*Lyons et al.*, 2016).

Chapter 3

Instrumentation and Data

This chapter describes the instrumentation and data products used for this thesis. Under each observational method, an outline of the limitations and possible sources of error is given. In Section 3.1, two satellites measuring the solar wind and interplanetary magnetic field (IMF) are introduced. Instrumentation for studying the ionosphere from ground and space are presented in Sections 3.2, 3.3, and 3.4. Sections 3.4.1 and 3.5 describe some additional complexities related to the observational methods.

3.1 Solar wind data

The IMF and solar wind conditions largely control the dynamics of the ionosphere (see Section 2.6). This section presents two spacecraft that can monitor the IMF and solar wind upstream of the Earth's magnetosphere.

3.1.1 ACE

The first Lagrange point (L1) is at a distance of ~ 230 R_E from the Earth, approximately 1/100 of the distance between the Earth and the Sun. At this location, the solar wind and IMF (SW/IMF) is monitored by the Advanced Composition Explorer (ACE). ACE was launched in 1997 by The National Aeronautics and Space Administration (NASA) and has since then provided observations of the particles and magnetic fields in the solar wind. ACE's payload contains magnetometers that observe the IMF in three dimensions (MAG) and instruments for observing particles and solar wind plasma parameters such as speed, density, temperature, and dynamic pressure (SWEPAM) (*Stone et al.*, 1998).

The ACE data presented in this thesis are from the high-resolution OMNI data set (HRO; 1 minute time resolution) is downloaded through the NASA Goddard Space Flight Center's Coordinated Data Analysis Web (CDAWeb) service (`https://cdaweb.gsfc.nasa.gov/sp_phys/data/omni/`). The HRO data set contains near-continuous observations of the SW/IMF and is constructed from observations from multiple spacecraft. An index is provided in the HRO data set, specifying which spacecraft is used for observations of IMF and solar wind parameters. All HRO data presented in this thesis are from the ACE spacecraft. The HRO data contains a one minute average of the original data product from ACE (containing IMF data for every 16 seconds and plasma data for every 64 seconds; *King and Papitashvili*, 2005, 2021). The HRO data product also contains geomagnetic indices obtained from the World Data Center (WDC)

for Geomagnetism Kyoto (`http://swdcwww.kugi.kyoto-u.ac.jp/aeasy/`), and polar cap (PC) definitive indices from WDC Copenhagen (`https://ftp.space.dtu.dk/WDC/indices/pcn/PCN_definitive/`).

In the HRO data product, the SW/IMF observations have been time-shifted to the predicted bow shock nose (BSN) location (based on models from *Shue et al.*, 1997; *Farris and Russell*, 1994). The BSN is just upstream of the dayside magnetopause, and representing the SW/IMF at this location is useful for studying solar wind-magnetosphere interactions (*King and Papitashvili*, 2005). The IMF components presented in this thesis are given in the GSM coordinate system (see Appendix A).

Limitations and sources of error

When calculating the time shift from the observation location (at the L1 point) to the predicted BSN, it is assumed that variations in the SW/IMF are organised in plane fronts, 'phase fronts'. During ACE's ∼180 day orbit around the L1 point, it will have an offset from the Sun-Earth line of some tens of R_E which must be considered when time-shifting the observations. Any variations in the SW/IMF perpendicular to the solar wind flow direction are disregarded. In cases where ACE is significantly offset from the Sun-Earth line, it may be observing a part of the solar wind that is not geoeffective (*King and Papitashvili*, 2005, 2021).

The time shift is based on assumptions that the phase fronts move towards the magnetosphere with the solar wind flow speed. The fact that some structures can move with different velocities and 'overtake' SW/IMF structures that passed ACE at an earlier time is ignored. It leads to errors in the time shift when there are significant variations in the solar wind flow speed. In addition, the predicted BSN location is not always accurate, especially during periods with significant variability in the SW/IMF (*King and Papitashvili*, 2021). The estimated errors for the time shift are provided in the HRO data set. For the data used in this study, time-shift errors vary from ±1 second to ±10 minutes and are most commonly smaller than ±1 minute.

3.1.2 Geotail

The Geotail spacecraft was launched in 1992 as a joint program of NASA and the Institute of Space and Astronautical Science (ISAS) in Japan. The mission's main objective was to study the geomagnetic tail. Onboard Geotail, there is instrumentation for monitoring both magnetospheric and solar wind plasma, as well as magnetometers that study the geomagnetic field and IMF (MGF; *Nishida*, 1994). The Geotail orbit was adjusted multiple times after launch, but since 1997 the orbit has remained such that for some months of the year, parts of the five-day Geotail orbit is upstream of the bow shock (*King and Papitashvili*, 2021).

In this thesis, Geotail observations of the SW/IMF are of interest. The Geotail data products are downloaded from the CDAWeb service (`https://cdaweb.gsfc.nasa.gov/index.html/`; GE_SW_CPI for plasma data; GE_K0_MGF for magnetometer data). The data sets contain key parameters from Geotail instruments with 64 second cadence. Vector quantities in the Geotail data sets are oriented in a Geocentric Solar Ecliptic (GSE) system, and the SpacePy python package (*Niehof et al.*, 2020) was used

to transform the IMF components into GSM coordinates. The Geotail observations are not time-shifted relative to the bow shock.

Limitations and sources of error

Geotail's ability to study the SW/IMF is limited by its orbit, as the spacecraft is located Earthward of the bow shock for most of its orbit. Orbital information is combined with plasma particle parameters to determine if the spacecraft monitors the SW/IMF outside the bow shock. This process does not eliminate any contributions from foreshock effects (*Zhang et al.*, 2021a; *King and Papitashvili*, 2021). Therefore Geotail observations of the SW may not always be comparable to other spacecraft monitoring the SW/IMF (e.g. ACE).

The key parameter plasma and magnetometer data sets contain flags indicating data quality. The flags are related to instrument errors and to the time averaging done when constructing the key parameter data sets ("Geotail KP Magnetic Field Data," 2021; "Geotail CPI," 2021). All Geotail data presented in this thesis are flagged as 'good quality'.

3.2 SuperDARN

Ground-based radars can be used to study ionospheric convection. This section introduces the Super Dual Auroral Radar Network (SuperDARN) and the SuperDARN data products used in this thesis. The physical principles that are the basis of the radar function are explained, and the limitations of the observational method and data products are discussed. The section is based on the reviews by *Greenwald et al.* (1995), *Chisham et al.* (2007), and *Nishitani et al.* (2019).

SuperDARN is a global network of coherent scatter radars. The network consists of over 35 radars located in the northern and southern hemispheres at mid, high, and polar latitudes. SuperDARN utilises radio waves to monitor ionospheric parameters from electron density irregularities in a plasma volume. They primarily observe upper ionosphere (F-region) plasma convection (line-of-sight (LOS) Doppler velocity). The plasma irregularities in the F-region ionosphere are most abundant at higher latitudes and are produced by instability processes, mainly gradient drift instabilities.

One of the main research objectives of SuperDARN is studying the structure and dynamics of the global convection as the radars cover a wide area of the high and polar-latitude regions and have several overlapping fields of view (FOVs). The radars are also useful for studying mesoscale convection.

A SuperDARN radar consists of the main antenna array, with transmitters that send pulses of radio waves with a stable phase relationship and receivers that sample the backscattered signal. There is also a smaller receive-only interferometer array around 100 meters away from the main array. The altitude and ground range of a backscatter volume can be determined by the phase difference of the received signals of the main and interferometer arrays.

The radars operate in the high-frequency (HF) range of $8-20$ MHz. It allows for flexibility to select the optimal frequency for obtaining F-region backscatter for varying ionospheric conditions. The radar frequency is a limiting factor in the scale size of

the irregularities that can be resolved. At the common frequencies, one can resolve irregularities of around 10 m size. At these spatial scales, the plasma in the F-region ionosphere behaves more as a fluid than a collection of particles, and the SuperDARN radars observe the bulk plasma velocity (electrons and ions move together with the $\mathbf{E} \times \mathbf{B}$ drift velocity; see Section 2.6.3).

An advantage of the SuperDARN radars is large FOVs and nearly continuous observation of the ionosphere. In the standard operating mode, a radar scans 16 consecutive beams with an azimuthal separation of $\sim$3.2°. Range gates separate the beams into 75 intervals in the LOS direction with a range gate separation of 45 km. In the standard mode, a total radar FOV covers an azimuthal area of $\sim$52° and a region from $\sim$200 km to more than $\sim$3300 km in the LOS direction. The integration period per beam is usually 3−7 seconds, with a complete scan in 1−2 minutes.

The FOV of the SuperDARN radars used in this thesis is shown in Figure 3.1. They are plotted in a magnetic latitude (MLAT) and magnetic local time (MLT) grid. The magnetic latitudes and longitudes used throughout the thesis are Modified Apex coordinates unless specified otherwise (see Appendix A). The three Canadian radars are located at Rankin Inlet (RKN; blue), Inuvik (INV; green) and Clyde River (CLY; orange). Table 3.1 lists the three radars, their radar code, year of the first operation, and the geographic and magnetic coordinates of each radar site.

The SuperDARN parameters (LOS Doppler velocity, spectral width and backscatter power) are obtained by processing the sampled return signal to get multi-lag complex autocorrelation functions (ACF). The raw ACF data files are produced at the radar sites and distributed to users. The data can be further processed and fitted using the standard SuperDARN data analysis software, the Radar Software Toolkit (RST; *SuperDARN Data Analysis Working Group,* 2021a). There are several ways of processing the raw ACF files. The current standard fitting algorithm is FITACF 2.5.

For this thesis, FITACF 2.5 data files were downloaded from Globus (University of Saskatchewan SuperDARN mirror). The latest SuperDARN data visualisation software called pyDARNio (*SuperDARN Data Analysis Working Group,* 2021b) was used to read the downloaded files. The radar range gate locations of each beam are also retrieved from the pyDARNio software. In the modelling technique described in Chapter 4, the centre of each range gate is used as the 'observation location' for the SuperDARN measurements. The assumed altitude of the measurements is 300 km.

Table 3.1: Radar code, first year of operation and location in geographic- and magnetic coordinates for three Canadian SuperDARN radars (adapted from *Nishitani et al.*, 2019).

Radar name	**Code**	**Year**	**Geo. lat.**	**Geo. lon.**	**Mag. lat.**	**Mag. lon.**
Rankin Inlet	RKN	2007	62.8°	-92.1°	71.7°	-22.6°
Inuvik	INV	2008	68.4°	-133.8°	71.0°	-82.1°
Clyde River	CLY	2012	70.5°	-68.5°	77.7°	18.3°

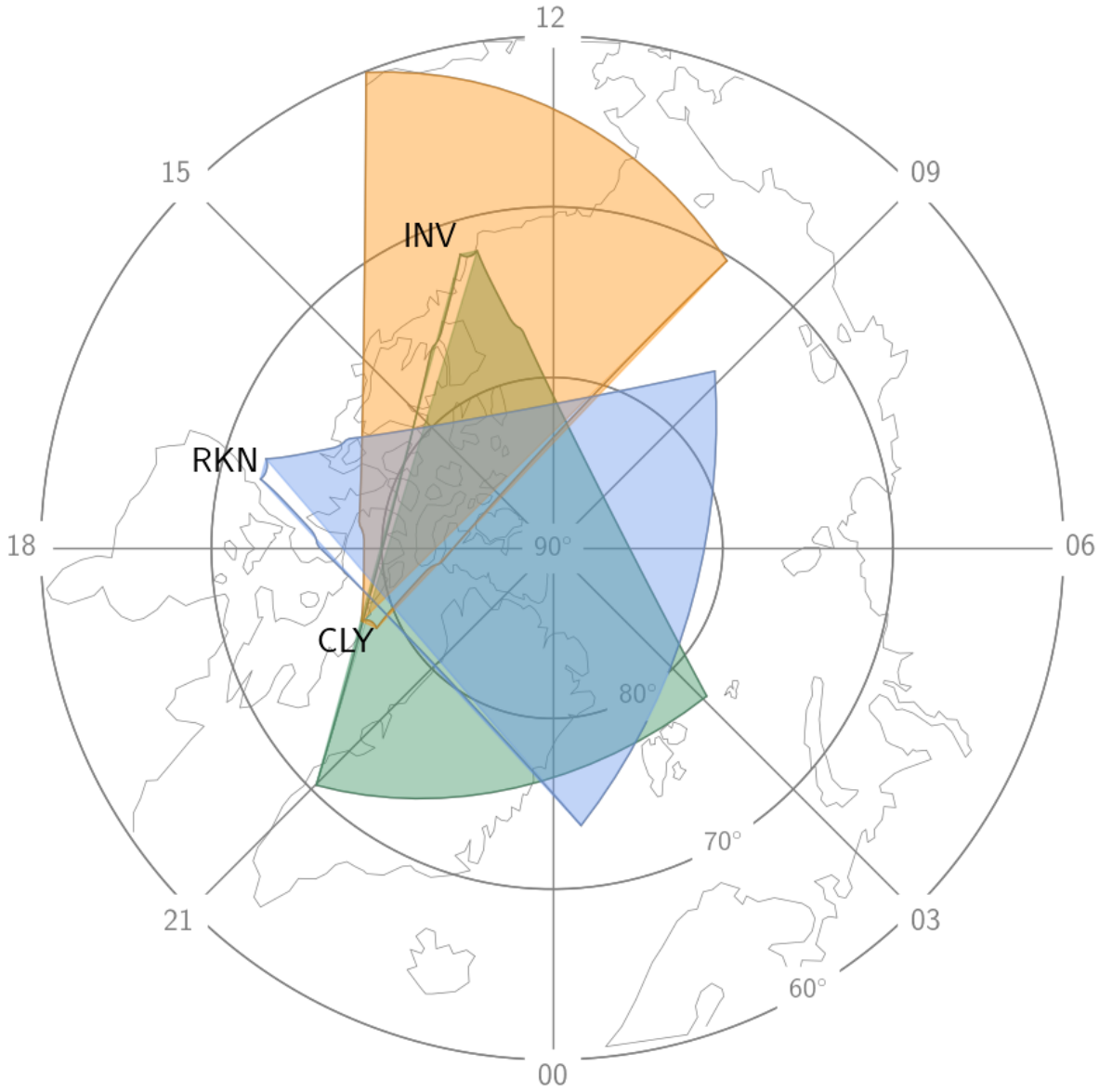

Figure 3.1: Field of view for three polar SuperDARN radars on an MLAT/MLT grid. Noon is up and dusk is to the left. Rankin Inlet (RKN) is in blue, Inuvik (INV) in green, and Clyde River (CLY) in orange.

HF radar backscatter

The SuperDARN radars are sensitive to signals which have experienced Bragg-scattering. The Bragg-scattered signal is amplified by constructive interference and produces a Bragg-peak if Bragg's condition is satisfied:

$$2d \sin\theta = n\lambda$$

where n is an integer, and θ is the glancing angle of incidence. SuperDARN radars receive a detectable echo of coherent backscatter when plasma irregularities are present in the backscatter volume, the transmitted signal has a wavelength λ that is two times the scale length d of the ionospheric irregularities, and both the transmitted and returned

signal are able to propagate between the radar site and the backscatter volume.

The transmitted signal must have an incident angle approximately perpendicular to the magnetic field lines to get coherent backscatter from plasma irregularities that are aligned with the geomagnetic field. The observed plasma drift is thus always measured perpendicular to the geomagnetic field lines. This orthogonality is hard to achieve at high latitudes, as the magnetic field lines are nearly vertical. The SuperDARN radars operate at frequencies that utilise ionospheric refraction of the radio wave in order to obtain backscatter echoes far beyond the local horizon. The refraction varies with the ionospheric density, which increases with altitude. The backscattered echo is returned approximately along the same ray path as the transmitted signal.

Any transmitted signals that do not meet the criteria will pass through the ionosphere and be lost. In cases where there are high plasma densities in the D-region, the radar signal is severely attenuated by absorption, and no return signal can be detected. However, the D-region is generally weak in the dark winter polar ionosphere (see Section 2.3).

Figure 3.2 shows a schematic of how SuperDARN radars typically observe the ionosphere (blue region) through echoes from plasma irregularities (darker blue shading). The black arrows are geomagnetic field lines. The solid red line shows a simplified ray path. The dashed red line shows a transmitted signal that is lost into space because of insufficient refraction.

As is illustrated in Figure 3.2, there can be multiple backscatter regions. F-region observations near the radar site where the backscatter criteria are first met are called the '$\frac{1}{2}$ hop' signal (shaded blue). A second region of ionospheric backscatter is sometimes observed due to the transmitted signal taking a new hop to the ionosphere after a reflection via the ground or sea surface ('$1\frac{1}{2}$ hop' signal, shaded blue). Signals can also

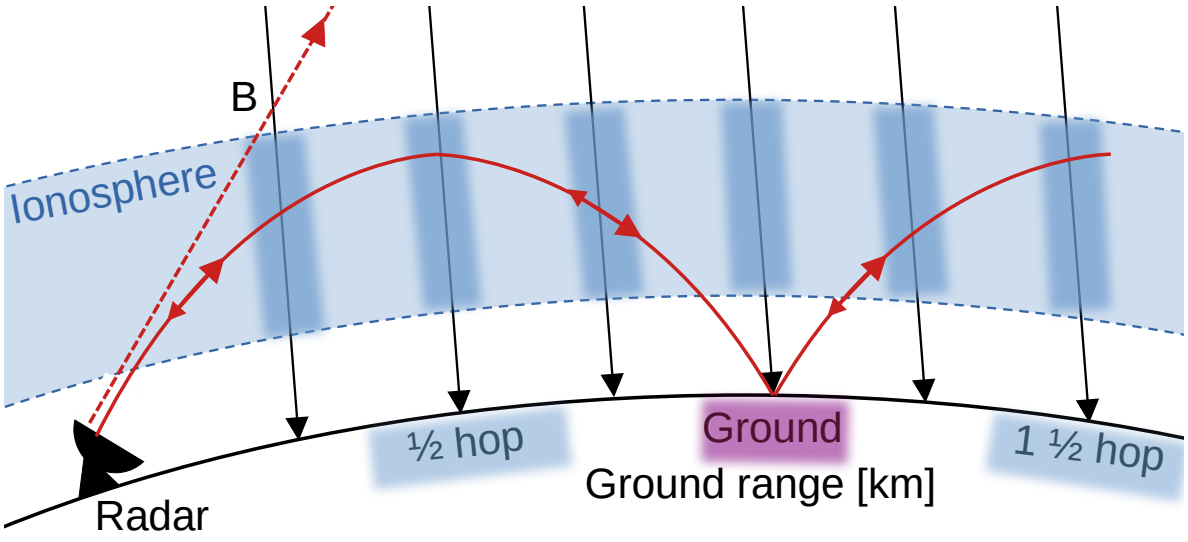

Figure 3.2: Schematic of backscatter regions for a SuperDARN radar. The solid red line shows how a signal can be returned from the ionosphere (blue) and from the ground (purple). The dashed red line shows a transmitted signal that is not returned to the radar site, but passes through the ionosphere into space. Ionospheric irregularities are darker blue regions surrounding the magnetic field lines (**B**).

be reflected by roughness on the ground or sea surface. This is ground backscatter (shaded purple).

Limitations and sources of error

Compared to other observational methods, the SuperDARN radars have large FOVs, but a single radar can never make global observations of the ionosphere. In addition, the data coverage within a radar FOV can vary on time scales of minutes. Though the frequency transmitted by the SuperDARN radars is adjusted to fit the ionospheric conditions, a very low ionospheric plasma density or high rate of ionisation at low altitudes can still lead to the reduction or loss of backscatter signal. Whether or not the absence of backscatter is due to a lack of ionospheric plasma or absorption is not always discernible. Entire scans are sometimes omitted if there are issues with the hardware or software of the radar.

Another limitation is that the SuperDARN radars only monitor one of the two components of the perpendicular plasma convection. Convection structures that are oriented perpendicular to the radar LOS are not observed. It is common to 'merge' observations from radars with overlapping FOVs to obtain two-dimensional vectors of convection, but such common volume observations are often sparse.

The Doppler velocity obtained from a SuperDARN observation in one range gate is the average within an ionospheric volume. The determined Doppler velocity for the volume, therefore, has uncertainties related to it. Error estimates are given in the FITACF 2.5 files. In this thesis, observations with errors $\geq$150 m/s are removed from the analysis.

Determining the backscatter volume's ground range (geographic location) is difficult, especially for the far ranges. The signal's exact ray path is unknown, and electron density profiles of the ionosphere needed for ray tracing are rare, especially in polar regions, so it is common to use empirical models of the electron density. The location of the backscatter volume can therefore have significant uncertainties (ground-range location typically has errors of >16 km; *Yeoman et al.*, 2001; *Chisham et al.*, 2008). The fitting algorithm for the ACF files determines the ground range of the backscattered signal, and the observation location in the FOV grid is provided in the FITACF 2.5 data files.

SuperDARN observations can be contaminated by non-F-region backscatter (*Chisham and Pinnock*, 2002). Examples are the aforementioned ground backscatter, backscatter from lower altitude plasma (E-region), ionisation trails from meteors, or other processes that can cause density irregularities. E-region backscatter is often observed closest to the radar site, and some studies discard observations near the radar site to avoid this contamination (e.g. *Thomas and Shepherd*, 2018). The ground backscatter is identified when processing the raw ACF data, and flags for ground backscatter are provided in the FITACF 2.5 data files. Observations flagged as ground backscatter are removed from the analysis in this thesis.

The refraction of the transmitted signals will also cause the propagation speeds of the radio waves to change, which can lead to underestimates of the ionospheric plasma drift velocity. *Gillies et al.* (2009) found that this effect could cause a 10-20% reduction of the LOS Doppler velocities observed by SuperDARN radars. They describe how the underestimation can be corrected by having complete electron density profiles in

the backscatter volume or using the interferometer array to obtain a proxy for the refractive index in the ionosphere. These methods are currently not applied, but the velocity underestimates due to refraction are generally small within the polar cap (PC) (*Gillies et al.*, 2009).

3.3 DMSP spacecraft

All space-based observations of the ionosphere utilised in this thesis are from the US Air Force Defense Meteorological Satellite Program (DMSP) spacecraft. A major advantage of these satellites is the simultaneous observation of several key parameters in geophysics and solar-terrestrial physics (*Kilcommons et al.*, 2017).

The DMSP satellites are sun-synchronous, with polar orbits that are roughly dusk to dawn oriented (in the northern hemisphere). A complete orbit takes ∼1.5 hours. At an average altitude of around 850 km, the low Earth orbit (LEO) spacecraft observe the topside ionosphere in-situ (*Hardy et al.*, 2008).

Data from the DMSP F16, F17 and F18 satellites were selected for the study in this thesis. The satellites are part of the most recent series of DMSP spacecraft, the block 5D-3 series, and all carry the same payload (*Kilcommons et al.*, 2017). This is preferential when comparing the observations, as all three spacecraft can give the same parameters from similar instrument systems.

Table 3.2 lists the three satellites used in this thesis, their year of deployment and the version of the relevant instrument systems; the Special Sensor for Ions, Electrons, and Scintillation (SSIES) for measuring bulk plasma properties, Special Sensor J (SSJ) for detecting precipitating particles, and the Special Sensor Ultraviolet Spectrographic Imager (SSUSI) for imaging of the Earth's atmosphere (*Redmon et al.*, 2017). The instrument systems and related data products are presented in the following Sections 3.3.1, 3.3.2, and 3.3.3. Some challenges and sources of error are also discussed.

The three DMSP spacecraft have been operating for different periods of time and have experienced different levels of degradation of the instrumentation. Differences in instrumentation sensitivities (calibration) between the spacecraft apply to all three instrument systems.

A general limitation of in-situ observations from the DMSP spacecraft is that the obtained parameters are point measurements. SSIES and SSJ measure ionospheric parameters along the spacecraft trajectory. The satellite may be located within a region of interest only for brief periods and will thus only capture snapshots of what is happening in the upper ionosphere.

Table 3.2: Satellite ID, year of deployment and version of relevant instrument systems for three DMSP satellites (adapted from `https://directory.eoportal.org/web/eoportal/satellite-missions/d/dmsp-block-5d`).

Satellite ID	**Year**	**SSIES**	**SSJ**	**SSUSI**
F16	2003	3	5	1
F17	2006	3	5	1
F18	2009	3	5	1

The DMSP spacecraft trajectories given in the instrumental data files are estimates made onboard the satellites. These often disagree with trajectories calculated in retrospect using ground-tracking information (*Redmon et al.*, 2017). Improved location of the F16, F17 and F18 spacecraft were obtained from the National Oceanic and Atmospheric Administration (NOAA) National Centers for Environmental Information (NCEI) and applied to the data to specify a more accurate spacecraft trajectory (*Kilcommons et al.*, 2017, downloaded from `https://satdat.ngdc.noaa.gov/dmsp/data_cal/`).

3.3.1 Ion drifts (SSIES)

As presented in Table 3.2, the DMSP F16, F17 and F18 spacecraft all carry the 3rd version of the SSIES system. SSIES-3 contains four instruments that monitor in-situ plasma parameters like bulk ion velocities (drifts), ion/electron temperatures, electron density, and density of different ion species (H^+, He^+ and O^+).

For this thesis, the ion drift meter (IDM) and retarding potential analyser (RPA) are used. The IDM data contains cross-track ion drifts, giving the ion velocities in the vertical (up) direction and in the horizontal direction perpendicular to the spacecraft trajectory. The RPA observes the horizontal ion velocity in the along-track direction. The ion drift data set used in this thesis was provided by Dr M. R. Hairston at The University of Texas at Dallas and is referred to as the Hairston data set. The following description of the SSIES-3 data is based on personal communication with M. R. Hairston in the spring of 2021.

The Hairston data set has been corrected for corotation in order to use the Earth's rotating system (see Section 3.5). For every observation, a velocity corresponding to Earth's rotational speed at the latitude of the spacecraft is calculated through Equation (3.1) and subtracted from the east-west components of the ion drift observations. This is done for both the cross-track and along-track ion drifts. The along-track observations are also corrected for the spacecraft velocity.

Limitations and sources of error

Plasma measurements from spacecraft are subject to several sources of errors, including sensitivity thresholds, noise or 'ringing' from the instruments, and errors in the fitting of electrical signals to physical parameters.

The accuracy of the measurements of the IDM instrument depends on ionospheric conditions, namely the ion density. The IDM instrument has two operational modes depending on ionospheric conditions. In normal mode, the output data has a one-second cadence and contains the average of six observations and corresponding standard deviations. When the ion density is lower than $3.0 \cdot 10^4$ ions/cm^3, the IDM operates in a slow mode to avoid self-noise or 'ringing'. This mode yields a poorer temporal resolution, as each cross-track direction is monitored every other second. Slow mode observations are repeated twice (same value for two consecutive seconds) in the Hairston data set.

The Hairston data set contains quality flags for all parameters. It is important to emphasise that even the determination of the quality flags can have embedded errors. However, the data presented in this thesis has been thoroughly double-checked and seems reasonable. The four tiers of quality in the Hairston data set are:

1 - good quality data that can be used with high confidence.

2 - fair quality data that can probably be used with confidence.

3 - data that should only be used with caution.

4 - data that is bad and should not be used.

5 - data of uncertain quality.

The quality flags are most accurate in polar regions. Note that special flags are placed in the F17 IDM data as this instrument has shown anomalous behaviour after 2009. Data from this instrument is consequently less reliable than the IDM data values from F16 and F18. For F17, the IDM data flags are 6 - good, 7 - fair, and 8 - caution. Only entries flagged as 'good quality' are included in our results.

3.3.2 Precipitating particles (SSJ)

As listed in Table 3.2, the three DMSP spacecraft all carry the SSJ5 instrument system. D. A. Hardy designed the SSJ particle detectors at Air Force Research Laboratory. They measure the in-situ particle precipitation. SSJ5 detects and analyses electron and ion precipitation in the 0.3−30 keV energy range with full spectra every second (*Hardy et al.*, 2008). Precipitation in this energy range can produce auroral emissions (see Section 2.7).

From the SSJ5 observations, energy-versus-time spectrograms are made (*Hardy et al.*, 2008). The spectrograms show the characteristic energies and energy fluxes of the precipitating electrons and ions. These parameters are useful for determining the acceleration mechanism of precipitating auroral particles, their magnetospheric source region, and the location and altitude of the resulting ionisation or auroral emissions. The energy-versus-time spectrograms are obtained through the interactive interface of The Johns Hopkins University Applied Physics Laboratory (JHU/APL) (spectrograms available at `http://sd-www.jhuapl.edu/Aurora/spectrogram/`). In the spectrograms, background signals (noise) have been removed (*Redmon et al.*, 2017).

JHU/APL also provides a database of magnetospheric source regions of the precipitating particles (avaliable at `http://sd-www.jhuapl.edu/Aurora/dayside/`). An automated boundary detection program determines the type of precipitation observed by the DMSP spacecraft (*Newell et al.*, 2004). Based on principles introduced in *Newell et al.* (1991) (and references therein), the dayside automated identifications database divides the precipitation on the dayside into eight different types: central plasma sheet (*CPS*), boundary plasma sheet (*BPS*), low latitude boundary layer (*LLBL*), *cusp*, *mantle*, *polar rain*, and *void* (precipitation at or below noise levels). For explanations of the different precipitation types, see *Newell and Meng* (1992) and *Newell et al.* (2004). There is also an *unclassified* type for particle precipitation that does not fit into any of the classifications.

Limitations and sources of error

Aside from possible degradation of the SSJ5 instruments and errors associated with the removal of background signals, there is a limitation to the accuracy of the automatic

detection of dayside precipitation. As pointed out by *Lockwood and Smith* (1993), mapping the observed precipitation at the ionospheric altitudes to a magnetospheric source region is not straight forward. The mapping may only apply to a static scenario, where there is no convection in the magnetosphere. As the system is in near constant motion, the particle populations observed can be a combination of many different magnetospheric source regions. The fact that the names of the different classifications elude to a magnetospheric region can therefore be misleading. Still, the automated dayside boundaries can give hints towards the expected magnetospheric source regions, though they should be used with caution.

3.3.3 UV aurora (SSUSI)

The Block 5D-3 spacecraft (F16 and after) were the first spacecraft in the DMSP mission to carry the SSUSI instrument (*Paxton et al.*, 1992). It is therefore listed as the first version in Table 3.2, though other missions have previously used nearly identical instrumentation. SSUSI observes far-ultraviolet (FUV) radiation from the Earth's atmosphere and visible radiation like airglow and terrestrial albedo. SSUSI has a scanning imaging spectrometer (SIS) and a nadir photometer system (NPS).

The SIS is of interest for this study, as it can observe auroras. The SIS performs cross-track scans horizon-to-horizon as the spacecraft follows the dusk-dawn trajectory. It has a 11.8° wide FOV along the spacecraft track and a cross-track FOV of 134.4° (*Paxton et al.*, 1992). One cross-track scan takes ∼22 seconds. It takes ∼20 minutes to complete one scan of the polar ionosphere. The instrument is slightly angled towards the nightside of the Earth to avoid sunlight contamination in the disk image and to study the Earth limb at the nightside. This is seen in Figure 3.3, where the spacecraft trajectory is the dotted line located towards the dayside of the SSUSI image.

SIS records emissions in five FUV wavelength bands. The result is five simultaneous 'monochromatic' images. FUV emissions are distinguishable from the dayglow background (e.g. *Frey et al.*, 2019). In this thesis, the LBHS (140−160 nm; see Section 2.7) observations from SSUSI are used to study the auroras.

The SSUSI images are calibrated (adjusted for different sensitivities of the pixels and self-noise), background-corrected (noise from dayglow and energetic particles are removed), and geolocated with an assumed emission altitude of 110 km ("SSUSI Data," 2013).

Limitations and sources of error

As described in Section 2.7.1, LEO satellites have the advantage of being able to image a large area with relatively high spatial resolution and sensitivity thresholds. However, the temporal resolution is limited, and the images are only snapshots of the aurora.

Towards the edges of the SSUSI FOV, the imagers observe the atmosphere at an angle, and auroral forms can get distorted and smeared out (see discussion in Section 3.4.1). If the auroras move while SIS makes its cross-track scans, the aurora may look warped in the final image. It may be hard to distinguish between artificial morphologies due to this warping and the true shapes of the aurora.

The emission intensity may also be attenuated between the emission site and the

spacecraft, as the topside neutral atmosphere can absorb some FUV photons. In addition, the background correction or calibration may remove faint auroral emissions.

The geolocation of the SSUSI images is done by assuming a common emission altitude for the FUV emissions, but the emissions can occur over an altitude range (∼80−120 km; see Section 2.7). The geolocation of the auroral emissions may be slightly off if the assumed emission altitude is wrong. Any inaccuracy of the spacecraft trajectories will affect the uncertainty in the geolocation of the emissions. However, both of these sources of error are expected to be minor.

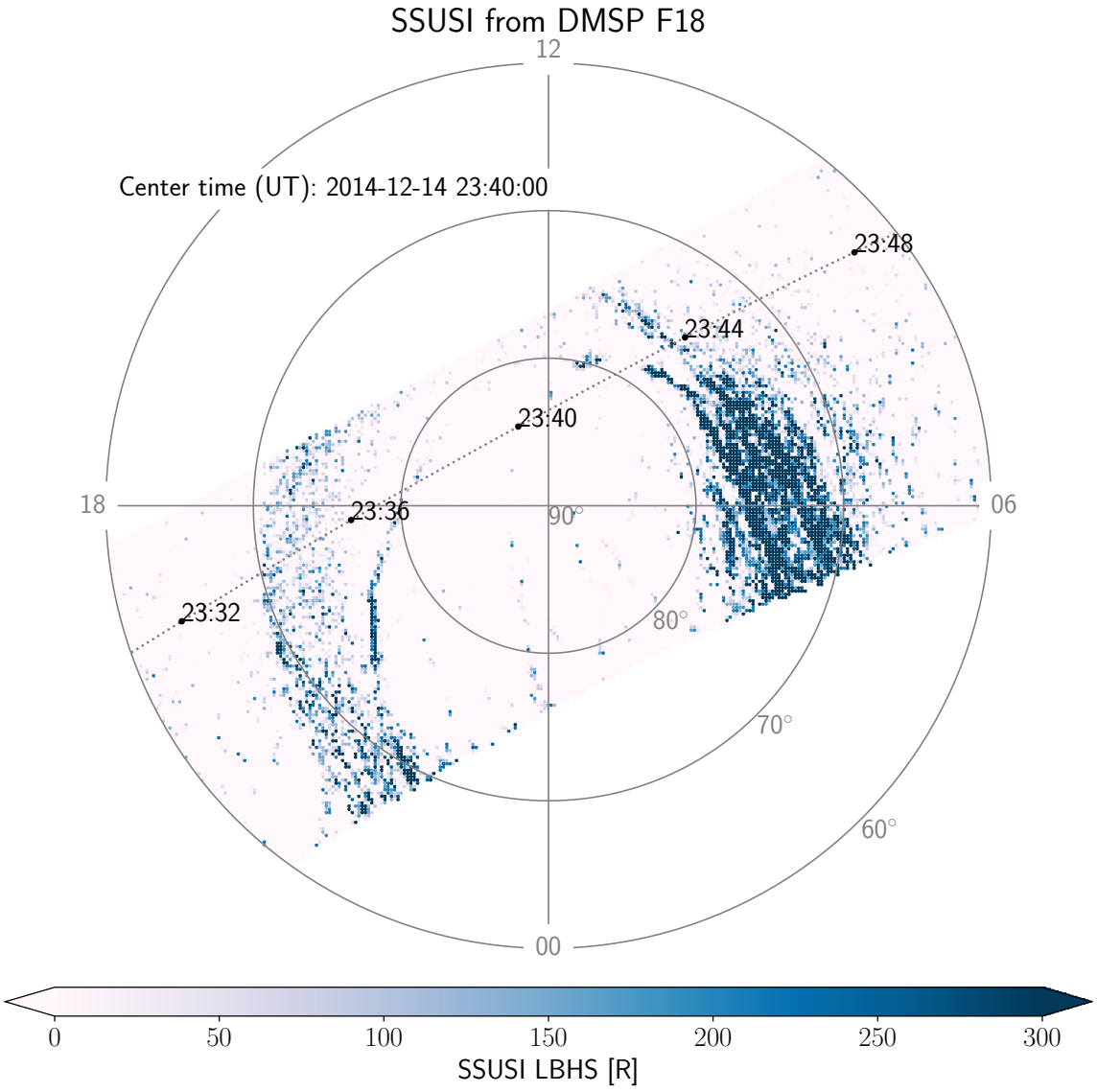

Figure 3.3: Example of a SSUSI FUV LBHS image for a northern hemisphere DMSP F18 satellite pass projected on an MLAT/MLT grid. The intensity of the LBHS emissions is shown in the colour bar.

3.4 REGO all-sky imagers

All-sky imagers are commonly used to observe auroral emissions from the ground. The Redline Geospace Observatory (REGO) is an array of 'monochromatic' all-sky imagers that observe 630.0 nm (red-line) emissions (see Section 2.7). This section presents the REGO all-sky imager array and the raw all-sky images obtained from that array. The post-processing of the images is described, and limitations of the observational method and the data product are introduced.

The REGO array has been deployed since late 2014 and consists of around nine all-sky imagers distributed across Canada and Alaska. The imagers have overlapping FOVs, and together they can monitor auroras from sub-auroral latitudes to within the PC (*Gillies et al.*, 2017). The REGO imagers are colocated with other all-sky systems to obtain complementary observations at different wavelengths.

The REGO imagers are highly sensitive and can detect emissions of only a few 10 s of Rayleigh. The exposure times are short (∼2 seconds), and images are obtained with a 3 second cadence (up to 20 images per minute; *Liang et al.*, 2016). *Liang et al.* (2016) performed an instrumental check and concluded that the REGO array observes red-line emissions with minimal leakage ($< 0.2\%$) of light from other wavelengths passing through the filtering.

Figure 3.4 shows the FOV of the two REGO all-sky imagers used in this thesis. The imagers at Resolute Bay (RESU, green) and Taloyoak (TALO, orange) in northern Canada have a common FOV around 72°−88° MLAT and across several MLT sectors. Table 3.3 lists information about the two REGO imagers, including their abbreviation code, number, the first year of operation, and location in geographic and magnetic coordinates.

Table 3.3: Imager code and number, first year of operation, and location in geographic and magnetic coordinates for two Redline Geospace Observatory (REGO) all-sky imagers located in northern Canada. (The information is extracted from the raw data files at `https://data.phys.ucalgary.ca/sort_by_project/GO-Canada/REGO/`.)

Imager name	Code	Nr.	Year	Geo. lat.	Geo. lon.	Mag. lat.	Mag. lon.
Resolute Bay	RESU	655	2014	74.7°	-94.9°	82.3°	-33.4°
Taloyoak	TALO	653	2014	69.5°	-93.6°	77.8°	-27.0°

The REGO data are provided by the University of Calgary (UCalgary; available at `https://data.phys.ucalgary.ca/sort_by_project/GO-Canada/REGO/`). One raw image frame is 512×512 pixels, and each data file contains up to 20 raw frames (one minute of observations). For the all-sky images presented in this thesis, the first frame of each raw data file is extracted, usually an image of the first 2 seconds of the minute.

In this study, corrections and conversions to the raw frames are done according to the "REGO Calibration," (2015). Each REGO imager has unique calibration files. The files are updated yearly to account for changes in the instrumentation performance. The site-specific calibration files are downloaded from the UCalgary website. The following list summarises the steps to obtain a processed image:

1. Dark frame correction: The data points in the corners of the raw image do not contain any observations, only a dark frame surrounding the actual image. One of

these dark corners (25×25 pixels) is used for dark frame correction. The average value in the corner area is subtracted from the rest of the image to correct for baseline detector noise.

2. Flat-field correction: The all-sky imagers use a wide-angle (fisheye) lens to capture a wide area of the sky. This will affect the radiation intensity measured in different pixels of the all-sky image. Flat-field correction accounts for the geometrical variations across the FOV and pixel sensitivity variation in the imager. We apply this correction to the dark frame corrected images.

3. Rayleigh conversion: Converting the image counts to the unit Rayleigh is done by multiplying each image with a calibration factor. The factor is normalised to 1 second exposure, but as the imagers typically have exposure times of about 2 seconds, the factor is divided by the exposure time provided in the raw image files.

The coordinates of the all-sky image are needed to project the observed emissions onto a geographic map. Skymap files (downloaded from the UCalgary website) contain

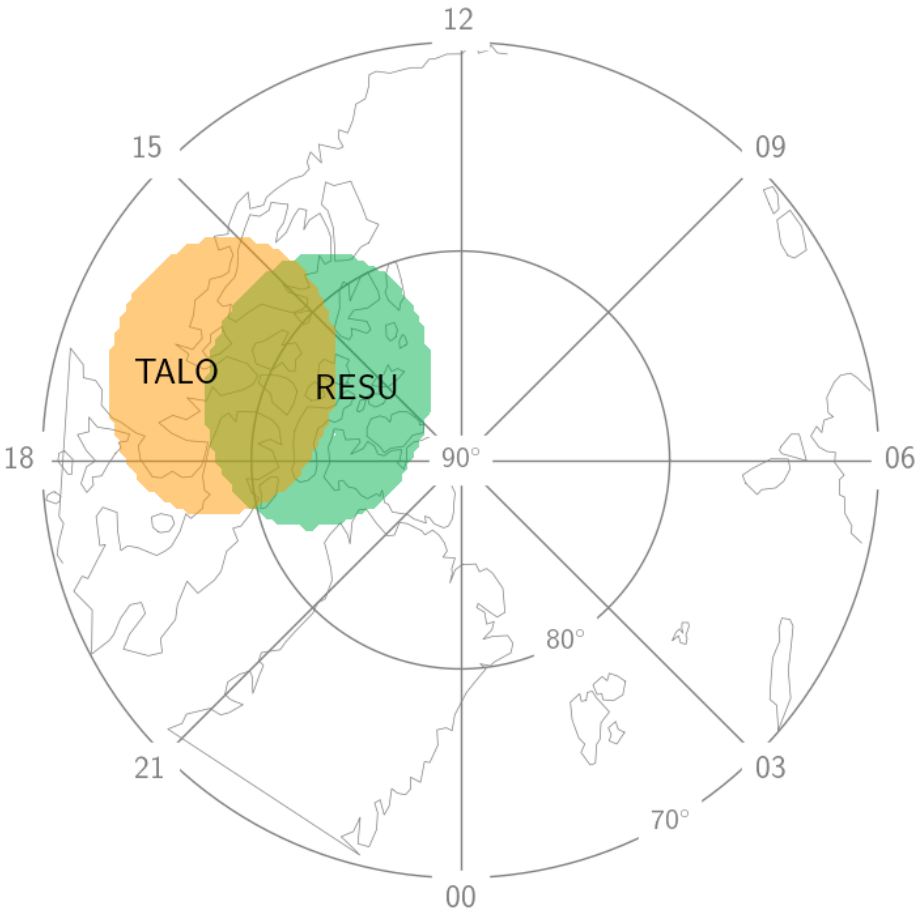

Figure 3.4: Field of view for two Redline Geospace Observatory (REGO) all-sky imagers shown on an MLAT/MLT grid. Noon is at the top and dusk is to the left. The fields of view have been cut at 15° elevation. Resolute Bay (RESU) is in green, and Taloyoak (TALO) is in orange.

information about each pixel's look angles and geographic coordinates in the FOV. The geographic locations are determined using stars. The sky maps are updated yearly, as calibrations of the all-sky imager can alter the FOV. Three different sets of geographic coordinates, corresponding to three different emission altitudes (110 km, 150 km, and 230 km), are provided in the sky maps. The 230 km coordinates are used in this thesis (a standard emission altitude for 630.0 nm emissions; see Section 2.7).

Limitations and sources of error

All-sky imagers require clear skies and darkness to observe the aurora. This limits the REGO imager's operational times to nighttime and winter. Scattered light in clouds also needs to be distinguished from auroral emissions and airglow (see Section 2.7). The difference in brightness of airglow and auroras can be used to distinguish between the two. Airglow intensity is typically weaker than 100 R, while auroras have intensities in the 0.1−1 kR range. The imagers are also sensitive to other sources of light contamination, for instance, moonlight or headlight from cars.

A considerable limitation of the all-sky imagers is their restricted FOV (as described in Section 2.7.1). The all-sky imagers can only observe parts of large-scale auroral features. Historically, this has lead to misinterpretations of aurora observed from the ground (*Zhu et al.*, 1997).

The geolocation of the pixels in the imager FOV can have significant uncertainties. The geolocation depends on assumed emission altitude, and *Gillies et al.* (2017) argue that an emission altitude of 200 km may sometimes be the most accurate for the red-line aurora. The peak emission altitude can also change with time.

The intensity of the auroral emissions observed by the all-sky imagers is highly dependent on the viewing geometry. The flat-field correction corrects for intensity differences due to the fisheye lens, but the extended altitude range of the red-line emissions (∼150−400 km; see Section 2.7) and the viewing geometry also affects the measured intensity. If the aurora moves from the zenith (centre of the FOV) to the edge of the image, it can cause an apparent decrease in the observed intensity. This could be misinterpreted as dimming of the aurora. Similarly, there will be an apparent brightening if the aurora moves the other way. There is also a related limitation associated with the Rayleigh conversion, as the raw data files only contain information about *requested* exposure time for the images. Interpretation of auroral emission intensities from the REGO all-sky images must therefore be made with caution.

Distortion of auroral forms towards the edges of the FOV also affects the interpretation of the all-sky images. The distortion is illustrated in Figure 3.5, where the 630.0 nm emissions are depicted as a diffuse red region extending along the magnetic field line. The horizontal red line is the extent of the emissions when projected onto a single altitude. In addition, the emitters have long radiative lifetimes (∼110 seconds; see Section 2.7), and can move with the $\mathbf{E} \times \mathbf{B}$ drift before they emit light. This can cause additional smearing of the red-line aurora images. The all-sky images get further distorted when projected on a flat MLAT/MLT grid. The all-sky images are cut off at 15° elevation to minimise the distortion effect.

3.4.1 Comparing ground-based and space-based images of the aurora

In this thesis, images from the ground-based all-sky imagers and the space-based SSUSI are utilised to study the auroras. The high temporal coverage of the all-sky imagers is combined with the large FOV of the SSUSI images. Besides temporal and spatial resolution, the two observational methods differ. The most important difference is related to the viewing geometries. Even though the two observation methods see signatures of the same magnetospheric dynamics, the projection of the auroras to the two-dimensional geographic reference frame can cause disagreement in the geolocation of the emissions.

Figure 3.5 shows a schematic of how the space-based SSUSI instruments onboard DMSP and the ground-based REGO imagers can observe aurora caused by precipitation along the same magnetic field lines. The 630.0 nm emissions are depicted in red colour, and LBHS emissions are depicted in blue colour. The emissions extend along the same magnetic field line, but the LBHS emissions are observed at lower altitudes and over a narrower altitude range than the red-line emissions.

The distortion towards the edges in the SSUSI images is less prominent than for

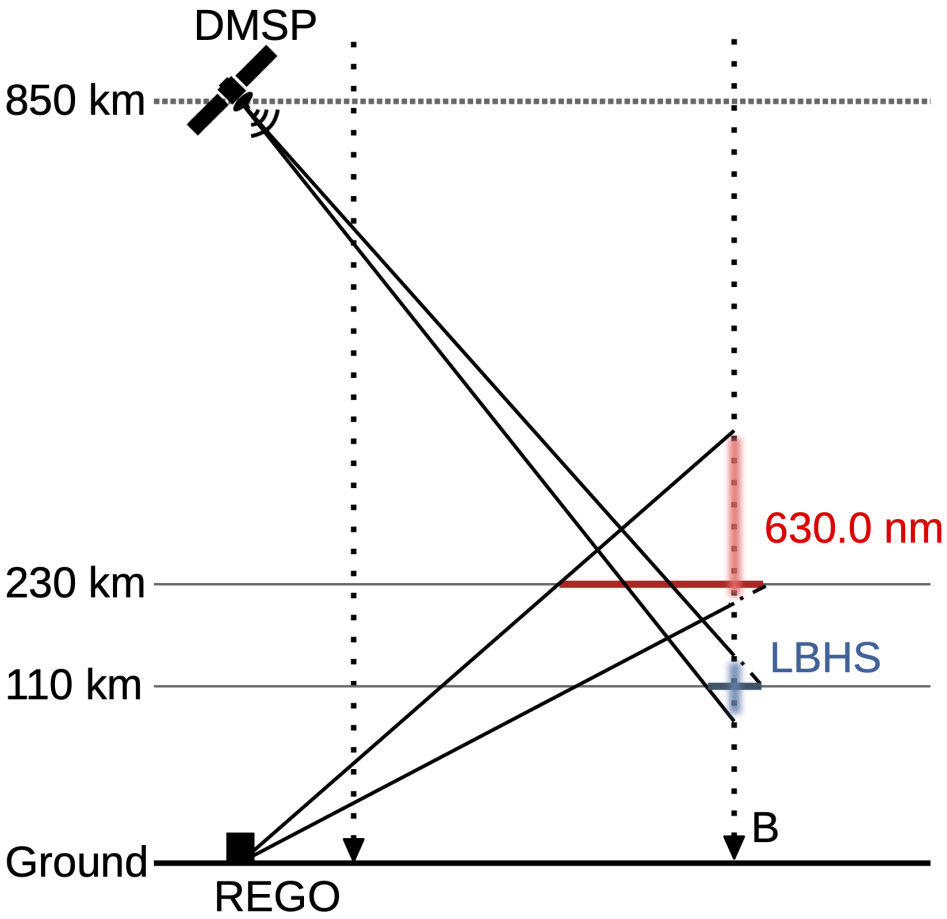

Figure 3.5: Schematic of how different viewing geometry and assumed emission altitudes affect the projection of observations from ground-based 630.0 nm imagers (REGO) and space-based imagers (DMSP) observing LBHS emissions.

the all-sky imagers. This is partly due to the FUV emissions having a smaller extent in altitude than the red-line emissions and partly because the DMSP spacecraft are located further away from the auroral emissions and have a better viewing geometry. The horizontal blue line shows the LBHS emissions projected to a plane at 110 km altitude.

Lastly, it is noted that the two emission bands are excited by different energy of the precipitating particles. The 630.0 nm emissions are caused by lower energy precipitation than LBHS the emissions, and the two types of emissions may not occur simultaneously (see Section 2.7).

3.5 Effect of corotation

The rotation of the Earth adds to the complexity of combining different observational methods for observing the ionospheric phenomena, namely convection. The rotational speed of the Earth is given by:

$$\mathbf{v}_{\text{rot}} = \frac{\pi \mathrm{R_E}}{24 \text{ hr}} \cos(\theta) \tag{3.1}$$

where θ is the geographic latitude.

The neutral atmosphere follows the Earth's rotation, and the ionosphere and a portion of the inner magnetosphere will follow the rotational motion as it is coupled to the neutral atmosphere via collisions (corotation; *Rees*, 1989; *Borovsky and Valdivia*, 2018). Note that the corotation speeds along a magnetic latitude circle are not constant.

The DMSP spacecraft are crossing the northern hemisphere as the Earth rotates below them. Thus, they are in a different frame of reference than the ground-based instrumentation (SuperDARN), which is rotating with the Earth. In Section 3.3.1, it was described how the DMSP observations were corrected in order to transform them into Earth's rotating frame. This correction is an essential step in the model technique described in the following chapter, where data from the two observational methods are combined to construct a regional model.

3.6 Remarks on instrumentation and data

As is evident from Sections 3.1-3.4, limitations are an inherent property of all sorts of instrumentation used in space science. In this work, instrumental errors are avoided by only using data with good quality flags or small error measures, and uncertainties in the timing and location of the measurements are attempted reduced by combining observations from multiple instruments. The limitations and possible sources of error listed in this chapter are kept in mind through the analysis and interpretation of the data.

Chapter 4

Modelling

This chapter presents how the Spherical Elementary Current Systems (SECS) technique is used to obtain a regional model of the ionospheric convection. Section 4.1 introduces the SECS technique, while Section 4.2 describes how it is applied for electric fields and potentials. Section 4.3 moves on to discuss the challenge associated with the inherent singularities of the SECS basis functions and how they can be corrected. Subsequently, Section 4.4 outlines how we can adjust the model region to avoid this challenge, as well as introducing how the model region is selected with respect to the observational data. The modelling technique is outlined in Section 4.5, and Section 4.6 discusses the interpretation of the model output. Section 4.7 presents how the observational data is prepared before it is used as input data for modelling. In Section 4.8, the spatial coverage of the input data is discussed, and a test is performed to investigate the effect of changing data coverage. Finally, Section 4.9 discusses the methodology and techniques used to solve the SECS inverse problem.

4.1 Spherical Elementary Current Systems (SECS)

Spherical Elementary Current Systems (SECS) is a technique developed by *Amm* (1997) and *Amm and Viljanen* (1999) to describe any sufficiently smooth two-dimensional vector field on a spherical surface. The technique was initially developed to describe the ionospheric current system and accompanying ground magnetic field disturbances but has since been applied to other ionospheric vector fields such as convection velocity fields (*Amm et al.*, 2010) and convection electric fields (*Reistad et al.*, 2019).

According to the Helmholtz theorem, a sufficiently smooth vector field, such as a magnetic field or a velocity field, can be uniquely described as a superposition of two vector fields, one curl-free (CF) and one divergence-free (DF) field: $\mathbf{u} = \mathbf{u}_{CF} + \mathbf{u}_{DF}$. This decomposition is known as Helmholtz decomposition, and formed the basis of *Amm* (1997) developing the SECS technique, which describes a smooth vector field reconstructed on a spherical shell with radius R, using elementary field sources, or nodes, placed on the sphere. Each node is associated with either a curl-free or a divergence-free vector field. The functional form of the basis functions for the vector

field of each node is given by:

$$\begin{aligned} \mathbf{u}_{CF,j}(\mathbf{r}_i) &= \frac{A_j}{4\pi R} \cot\left(\frac{\theta_{ij}}{2}\right) \hat{\theta}_{ij} \\ \mathbf{u}_{DF,j}(\mathbf{r}_i) &= \frac{A_j}{4\pi R} \cot\left(\frac{\theta_{ij}}{2}\right) \hat{\phi}_{ij} \end{aligned} \tag{4.1}$$

where $\mathbf{r}_i$ is the location where the vector field is evaluated, A_j is the amplitude of a node j, and θ_{ij} is the angular distance between the location of a node j and a given location i. $\hat{\theta}_{ij}$ and $\hat{\phi}_{ij}$ are unit vectors in a local spherical reference frame pointing away from the node along the surface (co-latitude unit vector) and perpendicular to the direction away from the node (azimuthal direction unit vector), respectively. A_j will have units determined by the modelled vector field.

Since Equations (4.1) only describe contributions from a single node j at location i, the linear combination of the contributions from all the n nodes will represent the total curl-free and divergence-free part of the vector field at the location $\mathbf{r}_i$, as represented by the SECS nodes:

$$\begin{aligned} \mathbf{u}_{CF}(\mathbf{r}_i) &= \sum_{j=1}^{n} \left(\frac{A_j}{4\pi R} \cot\left(\frac{\theta_{ij}}{2}\right) \hat{\theta}_{ij} \right)_t \\ \mathbf{u}_{DF}(\mathbf{r}_i) &= \sum_{j=1}^{n} \left(\frac{A_j}{4\pi R} \cot\left(\frac{\theta_{ij}}{2}\right) \hat{\phi}_{ij} \right)_t \end{aligned} \tag{4.2}$$

However, before the sum from all the nodes can be evaluated, the elementary fields in Equations (4.1) have to be converted to a common coordinate system, since the elementary field from each node is expressed in its own local frame of reference. This is noted by the subscript t.

The SECS technique has some important advantages over other spherical representations of ionospheric vector fields. One advantage is the flexibility in deciding the size and shape of the region to be investigated. Another advantage is the behaviour of the SECS basis functions in Equations (4.1), since they decrease with distance from the node location, leading to the ionospheric parameters being determined locally and allowing for high spatial resolution. The method also does not require fixed boundary conditions to be specified and can thus be constrained by observations only.

4.2 Application of SECS technique to describe convection electric fields and potentials

In this thesis, the SECS technique is applied to model convection electric fields and corresponding electrostatic potentials in a local region in the F-region ionosphere. These parameters are related to ionospheric convection and are useful in describing local ionospheric dynamics.

By assuming that the magnetic field has no rapid variations over the time period for which the technique is applied, the convection electric field can be approximated to

be curl-free. This is evident from Faraday's law, where: $\frac{\partial \mathbf{B}}{\partial t} = 0 \implies \nabla \times \mathbf{E} = 0$. In this application, the electrodynamics are modelled on minute time scales, making the assumption well-founded since ignoring inductive effects is valid on time scales longer than a few tens of seconds (*Milan*, 2013).

As a consequence, the convection electric field can be expressed solely by the curl-free SECS basis function from Equations (4.2). At a given location i, the convection electric field is given by the superposition of the curl-free electric field contribution from each of the n SECS nodes:

$$\mathbf{E}(\mathbf{r}_i) = \mathbf{E}_{CF}(\mathbf{r}_i) = \sum_{j=1}^{n} \left(\frac{A_j}{4\pi R_I} \cot\left(\frac{\theta_{ij}}{2}\right) \hat{\theta}_{ij} \right)_t \tag{4.3}$$

In our application, the nodes are placed on a spherical shell at 300 km (F-region) altitude using the method described in Section 4.4, making $R_I = \mathrm{R_E} + 300$ km. At this altitude, the frozen-in assumption holds (see Section 2.1.1), which is important in this specific application of the SECS technique. The electric field has units of volts per meter (V/m), giving the SECS node amplitudes, A_j, units of volts.

Additionally, the SECS node amplitudes can be used to describe the electrostatic potential (Φ). When ignoring inductive effects, the electric field can be expressed as:

$$\mathbf{E} = -\nabla\Phi \tag{4.4}$$

The electrostatic potential in a location $\mathbf{r}_i$ can then be found by integrating Equation (4.3):

$$\Phi(\mathbf{r}_i) = \sum_{j=1}^{n} \frac{-A_j}{2\pi} \ln\left(\sin\frac{\theta_{ij}}{2}\right) \tag{4.5}$$

(*Reistad et al.*, 2019). Note the missing subscript t as Φ is a scalar quantity, and coordinate conversion is unnecessary. The equation is multiplied by R_I as the integration is done along the direction $\hat{\theta}_{ij}$, at a distance R_I from the centre of the Earth (origin). The electrostatic potential has units of V.

4.3 Singularities

The SECS basis functions in Equation (4.1) are singular - they go to infinity at the node location since $\cot\left(\frac{\theta_{ij}}{2}\right) \to \infty$ when $\theta_{ij} \to 0$. This may lead to numerical problems, especially when studying the SECS vector fields close to a node. To correct for the effects of the singularities in the basis function, *Vanhamäki and Juusola* (2020) introduced modifications to Equation (4.1):

$$\begin{aligned}
\mathbf{u}_{CF,j}(\mathbf{r}_i) &= \frac{A_j}{4\pi R}\hat{\theta}_{ij} \begin{cases} \cot\left(\frac{\theta_{ij}}{2}\right)\tan\left(\frac{\theta_{ij}}{2}\right) & \theta_{ij} < \theta_0 \\ \cot\left(\frac{\theta_{ij}}{2}\right) & \theta_{ij} \geq \theta_0 \end{cases} \\
\mathbf{u}_{DF,j}(\mathbf{r}_i) &= \frac{A_j}{4\pi R}\hat{\phi}_{ij} \begin{cases} \cot\left(\frac{\theta_{ij}}{2}\right)\tan\left(\frac{\theta_{ij}}{2}\right) & \theta_{ij} < \theta_0 \\ \cot\left(\frac{\theta_{ij}}{2}\right) & \theta_{ij} \geq \theta_0 \end{cases}
\end{aligned} \tag{4.6}$$

which go to zero within a specified distance θ_0 from the node. An interpretation of this modification is that the modified node represents a source of finite size (θ_0) rather than placing the source at a single point.

In some cases, choosing the node and evaluation locations carefully so that there is no need to evaluate the SECS vector field too close to a node can avoid the singularity effect altogether (*Vanhamäki and Juusola*, 2020). The grid placement that avoids overlapping node and evaluation locations is discussed further in Section 4.4 but the singularity correction described in Equation (4.6) was also required in this thesis due to variations in the input data resulting in possible overlap between observation points and nodes. We set the threshold θ_0 in the singularity correction to half the grid cell resolution.

4.4 Choosing the grid

An advantage of using the SECS technique is the flexibility in positioning the model region which allows for a localised region of analysis. Both the node and evaluation locations - the grids - are adjustable and are not predefined to a specific shape or resolution. The placement of the node grid can be tuned depending on the data coverage, and spatial resolution and accuracy of the input measurements.

In this thesis, the node and evaluation grid is placed using the cubed sphere projection (*Ronchi et al.*, 1996; *Laundal et al.*, 2021). The grid is constructed using the *secsy* Python code (*Laundal*, 2021). A cubed sphere grid is chosen as it allows for easy calculation of gradients. A drawback of a cubed sphere grid is the presence of minor distortion towards the edges of the cube face. However, the region chosen for this analysis is centred on one of the cube faces and is small compared to the size of the entire cube face. Thus, the grids are very regular with negligible distortion.

Placing the grid relative to the locations of the ground-based instruments introduced in Chapter 3 is essential for two reasons. Firstly, we want to investigate the ionospheric dynamics in relation to the auroras. The grids are placed in a region where we have optical data from the all-sky cameras. The centre of the grid (centre of the cube face) is placed at the approximate location of the REGO imager at Resolute Bay at 73°N, 98°W geographic coordinates. Secondly, the modelling method requires observational input which mainly consists of SuperDARN line-of-sight (LOS) Doppler-velocity measurements. The grids are oriented and scaled such that the data coverage is as even as possible. The grid resolution is set to 70 km to fit the resolution of the SuperDARN observations with the uncertainties in geolocation (see Section 3.2). Figure 4.1 shows the location of the grid with respect to the ground-based observation fields of view (FOVs). The location of the SECS nodes are given as blue dots, while orange dots represent the evaluation locations. The SuperDARN FOVs are shaded grey and the REGO FOVs are shaded green. The grids are fixed in geographic coordinates, and follow the ground-based instruments.

To avoid the singularity problem introduced in Section 4.3, the evaluation locations must be placed sufficiently far away from the nodes. A common strategy is to evaluate the SECS model on a grid of the same spatial resolution as the node grid, but shifted to the mid-point between the nodes. The nodes are placed in the centre of the cubed sphere grid cells, and the evaluation locations are selected to be evenly displaced in the corners of the cubed sphere grid cells. The node grid is 1900×1900 km with a

total of $n = 676$ nodes. To avoid boundary effects, we set the size of the evaluation grid to be smaller than the node grid by twice the grid resolution (*Vanhamäki and Juusola*, 2020). The evaluation grid therefore covers a smaller region of 1620×1620 km. There are $m = 529$ evaluation locations in total. Observations within twice the grid resolution outside the node grid are included as input data to the SECS inversion, to further improve the solutions of the exterior nodes.

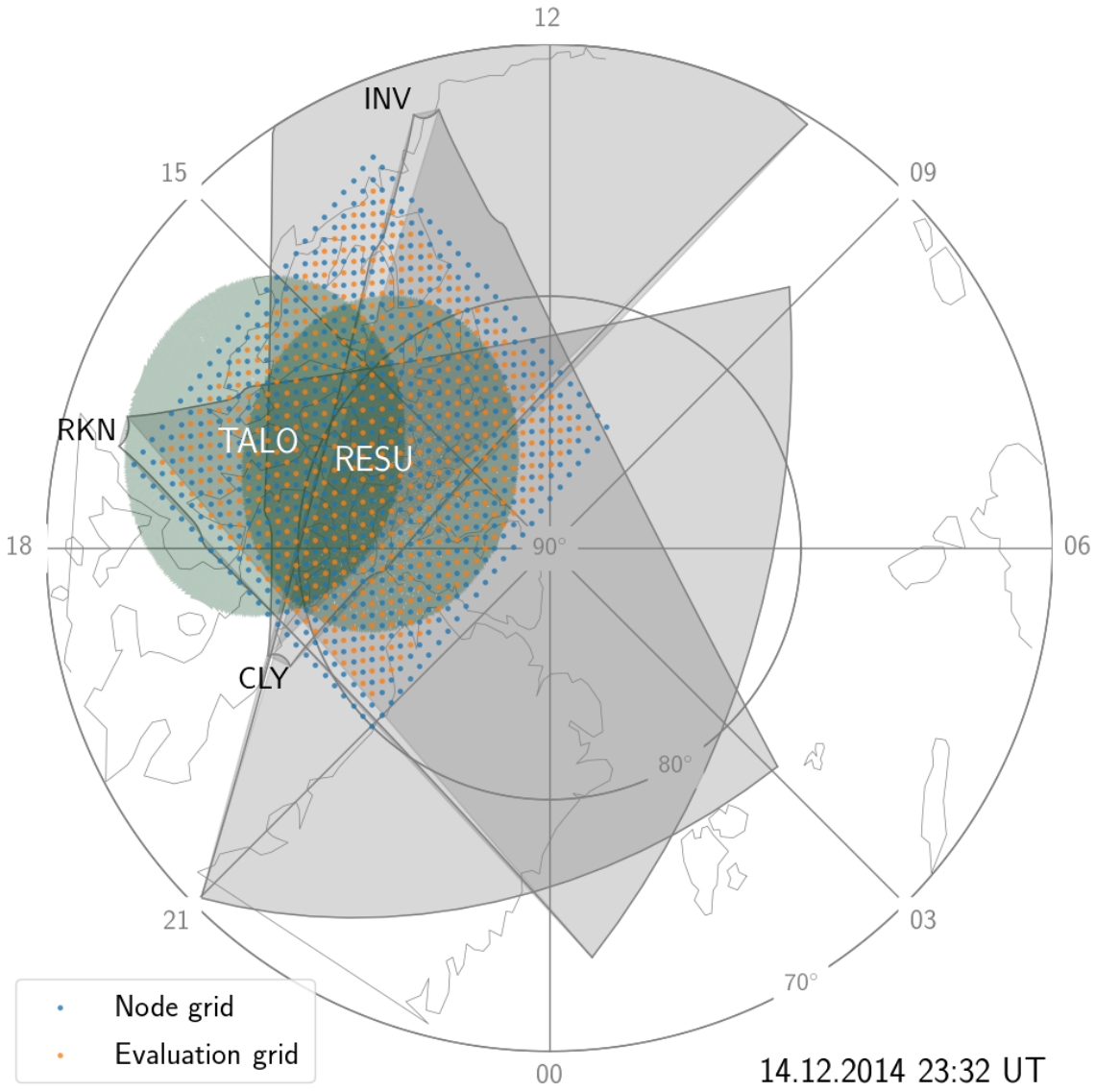

Figure 4.1: SECS grids in relation to the ground-based instrument fields of view plotted on an MLAT/MLT grid. The blue markers are the node locations and the orange markers are the evaluation locations. Fields of view of the SuperDARN polar radars at Inuvik (INV), Rankin Inlet (RKN) and Clyde River (CLY) are shaded in grey. Fields of view of the REGO imagers at Taloyoak (TALO) and Resolute Bay (RESU) are shaded in green.

4.5 Construction/evaluation of the model

The SECS technique is used to produce an observation-based model that describes the convection electric field ($\mathbf{E}$) and electrostatic potential (Φ) within the entire model region, even in areas where there is sparse or no observational data. The model is constructed by determining the SECS node amplitudes (A_j) from observational data. The SECS node amplitudes describe $\mathbf{E}$ and Φ at any location in the model region through Equations (4.3) and (4.5), respectively.

The observed plasma velocities, $\mathbf{v}_{\text{LOS}}$, are from SuperDARN observations and the DMSP spacecraft. The subscript LOS is used to denote either the SuperDARN observations, or each of the horizontal components of the convection observed by DMSP SSIES (cross-track or along-track drift measurements; see Section 3.3.1). The DMSP observations are mapped to the 300 km altitude of the SECS nodes, and weights are determined, as described in Section 4.7. For each model, four minutes of observational data is included to achieve a sufficient number of observations to constrain the model. This time window also accounts for a periodic variability in the transmission frequency of the SuperDARN radars. Note that we define the *model time* to be the start time of the four-minute interval.

The $\mathbf{v}_{\text{LOS}}$ at F-region altitudes is related to $\mathbf{E}$ through Equation (2.3). The magnetic field ($\mathbf{B}$) at the observation locations is obtained from the IGRF model (see Appendix A). The magnetic field is assumed to be vertical across the model region defined in Section 4.4. This approximation was tested and proved to be sufficiently accurate. Within the model region, >99% of the (IGRF) magnetic field strength is contained in the vertical component. For an observation i at observation location $\mathbf{r}_i$, the 'observed' convection electric field is given by: $\mathbf{E}_{\text{obs}}(\mathbf{r}_i) = -\mathbf{v}_{\text{LOS},\,i} \times \mathbf{B}_{\text{IGRF}}(\mathbf{r}_i)$.

We calculate $\mathbf{E}_{\text{obs}}$ for each of the m observations. As can be seen from Equation (4.3), $\mathbf{E}$ and A_j are linearly dependent. Thus, a set of m linear equations must be solved in order to estimate the amplitudes of the n SECS nodes. The set of equations can be written in matrix algebra form as:

$$G\mathbf{m} = \mathbf{d} \tag{4.7}$$

where $\mathbf{d}$ is an $m \times 1$ matrix containing the observed convection electric field magnitudes. $\mathbf{m}$ is an $n \times 1$ matrix of SECS node amplitudes, referred to as the solution, or model. G is an $m \times n$ matrix describing the geometry. An element in the G matrix for the electric field is on the form:

$$G_{ij} = \left(\frac{1}{4\pi R_I} \cot\left(\frac{\theta_{ij}}{2}\right) \hat{\theta}_{ij} \right)_t \cdot \hat{\mathbf{k}}_i \tag{4.8}$$

where each element of the matrix represents the effect of a curl-free SECS node j of unity amplitude on an observation location $\mathbf{r}_i$ in the $\hat{\mathbf{k}}_i$ direction. $\hat{\mathbf{k}}_i$ is the direction of the convection electric field in a common reference frame: $\mathbf{E}_{\text{obs}}(\mathbf{r}_i) = E_i\hat{\mathbf{k}}_i$ (east, north). The subscript t denotes the conversion of $\hat{\theta}_{ij}$ from a local node reference frame to the common reference frame. With this definition, G can be computed if the node grid and locations and orientations of the velocity observations are known. The *secsy* Python code (*Laundal*, 2021) is used to compute G. Note that the corrections for singularity effects in Equations (4.6) are included in the matrix.

To obtain the regional model, Equation (4.7) must be solved for $\mathbf{m}$. How the solution to this inverse problem is calculated is discussed in Section 4.9. The solutions to the linear equations should give the SECS node amplitudes that produce a modelled convection electric field that matches the observational data and at the same time is realistic in terms of the physics in the ionosphere, and the nature of the observations, e.g. the spatial resolution of the instrumentation used. For this, we use Tikhonov regularisation, also discussed in Section 4.9.

Equation (4.7) is general. If the model $\mathbf{m}$ is known, Equation (4.7) describes the forward problem of computing the model value corresponding to the design of G, referred to as evaluating the model. When evaluating, $\mathbf{d}$ is the quantity described by the model, either $\mathbf{E}$ or Φ depending on the choice of G matrix. When evaluating, we build the G matrix based on the n node locations and the m locations of the points of evaluation. When evaluating for $\mathbf{E}$, $\mathbf{d}$ will represent the component of the electric field described by $\hat{\mathbf{k}}$ in Equation 4.8. To get the full vector $\mathbf{E}$ we must build the G matrix for the modelled east and north components separately. The modelled $\mathbf{E}$ can also be used to calculate the model $\mathbf{E} \times \mathbf{B}$ drift velocity of the ionospheric plasma through Equation (2.7). When evaluating for the scalar field Φ, the G matrix will have elements corresponding to Equation (4.5).

The method for constructing a model $\mathbf{m}$ can be summarised as follows:

1. Specify a SECS node grid at 300 km altitude.
2. Obtain four minutes of horizontal $\mathbf{v}_{\text{LOS}}$ from SuperDARN and the DMSP spacecraft and convert the data into a common reference frame.
3. Calculate $\mathbf{E}_{\text{obs}}(\mathbf{r}_i)$ from $\mathbf{v}_{\text{LOS}}$ and $\mathbf{B}_{\text{IGRF}}$. This is $\mathbf{d}$ in Equation (4.7).
4. Construct the G matrix that relates the observation locations and node locations.
5. Solve the inverse problem in Equation (4.7) for $\mathbf{m}$ (the SECS node amplitudes). This step involves applying weights to the data and regularisation.

The following steps summarise how the model is evaluated once $\mathbf{m}$ is obtained:

6. Specify an evaluation grid at 300 km altitude.
7. Construct the G matrix for either $\mathbf{E}$ or Φ, relating the evaluation locations and node locations.
8. Solve Equation (4.7) for $\mathbf{d}$ (the modelled parameter).
9. Use the modelled $\mathbf{E}$ (and $\mathbf{B}_{\text{IGRF}}$) to find the $\mathbf{E} \times \mathbf{B}$ drift velocities through Equation (2.7).

4.6 Interpreting the SECS node amplitude

The SECS node amplitudes have a physical interpretation. *Amm* (1997) used the SECS technique to describe the height-integrated ionospheric current density field $\mathbf{J}_{\perp}$ (see Section 2.6.3) with the unit Ampere per meter. In their application, the SECS node

amplitudes have units of Ampere and can be interpreted as line currents intersecting the spherical shell at the node locations (the field-aligned currents; FACs) in the case of curl-free elementary functions. In our application, we describe $\mathbf{E}$ which has units of V/m, while the SECS node amplitudes have units of V. Here, the node amplitude A_j is proportional to $\nabla \cdot \mathbf{E}$ in the grid cell occupied by node j (a detailed description is found in *Reistad et al.*, 2019).

$\mathbf{E}$ is related to plasma convection through Equation (2.3), and the divergence of the electric field can be written as:

$$\nabla \cdot \mathbf{E} = -\nabla \cdot (\mathbf{v} \times \mathbf{B}) = \mathbf{v} \cdot \nabla \times \mathbf{B} - \mathbf{B} \cdot \nabla \times \mathbf{v} \tag{4.9}$$

where $\mathbf{v}$ is the velocity field and $\mathbf{B}$ is the magnetic field. By using the steady-state Ampere-Maxwell's law (see Section 2.6.3) to substitute for $\nabla \times \mathbf{B}$, we get:

$$\nabla \cdot \mathbf{E} = \mathbf{v} \cdot \mu_0 \mathbf{J}_\perp - \mathbf{B} \cdot \nabla \times \mathbf{v} \tag{4.10}$$

where μ_0 is a constant. The first term on the right-hand side of the equation is negligible in the upper ionosphere (*Freeman et al.*, 1990b). The divergence of the convection electric field at the SECS node altitude can then be expressed as:

$$\nabla \cdot \mathbf{E} = -\mathbf{B} \cdot \nabla \times \mathbf{v} \tag{4.11}$$

where the curl of the velocity field, $\nabla \times \mathbf{v}$, is called the *vorticity*.

There is vorticity in regions where there are spatial gradients in the convection speed (shears), and in regions where the direction of the convection rotates (rotation). The vorticity increases with sharper changes in flow speeds and direction of flow. Figure 4.2 shows a schematic of how changes in the plasma flows cause either positive or negative vorticity (in northern hemisphere where up is defined as the positive direction).

The SECS node amplitudes can thus be used to describe spatial changes in the F-region convection. They are also related to FACs through Equation (2.9), provided the gradients of the conductance in the ionosphere can be considered negligible. Under these assumptions, the node amplitudes can be related to multiple parameters:

$$A_j \propto \nabla \cdot \mathbf{E} \propto \nabla \times \mathbf{v} \propto J_{||} \tag{4.12}$$

where A_j<0 corresponds to upwards FAC, and A_j>0 corresponds to downwards FAC.

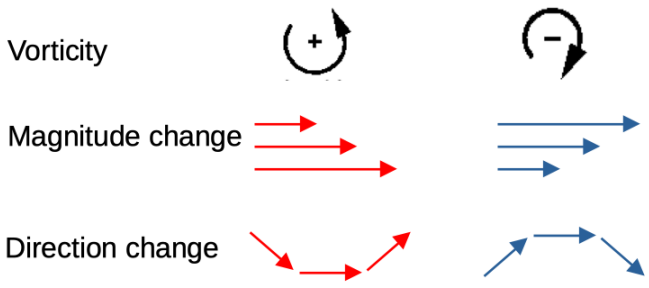

Figure 4.2: The sign of $\nabla \times \mathbf{v}$ (vorticity) for different types and directions of flow shears as seen when looking down from above the northern hemisphere.

4.7 Mapping and weights

In addition to the SuperDARN observations of convection, measurements of convection from the DMSP spacecraft were useful input data to the model when available. However, observations from the two sets of measurements could not be directly compared. This section outlines the preparation of the data sets required before constructing the regional model.

Firstly, we avoid large errors inherent in the observational data by removing 'bad' measurements from the data sets, as described in Sections 3.2 and 3.3.1. Still, the large differences in spatial and temporal coverage of the two methods need to be taken into account. The SuperDARN observations are averages over a larger region of approximately 45×45 km during the integration time of ∼3 seconds. DMSP observations, on the other hand, have one second cadence and obtain up to two (along-track and cross-track) in-situ measurements every ∼7 km. In a four-minute period there may be as many as 240×2 DMSP measurements concentrated along the satellite track, while the amount and locations of SuperDARN measurements in this time period is variable, and the observations are further apart. DMSP observations can outnumber the SuperDARN observations seven to one for every 45 km. Even though there are typically more SuperDARN measurements in total, the DMSP measurements will dominate the solution in the region around the spacecraft trajectory and may lead to unphysical models. To avoid this effect, weights of $7/45 \approx 0.16$ are applied to the DMSP observations, while no weights are applied to the SuperDARN observations.

The DMSP observations are taken at the spacecraft altitude of ∼850 km. Hence, these observations are not directly comparable to the drifts at 300 km observed by SuperDARN. In order to include the DMSP observations as input to the model, the observed velocity vector must be scaled to fit the corresponding velocity at 300 km altitude. ApexPy (*van der Meeren et al.*, 2021) is used to do the mapping of the horizontal ion drift observations along the magnetic field lines. The ApexPy python wrapper for the Fortran code presented in *Emmert et al.* (2010) uses modified Apex base vectors to map the drift velocity along the magnetic field (*Richmond*, 1995; *Emmert et al.*, 2010, see Appendix A). The orientation and magnitude of the velocity will change as the vector quantity is mapped along the geomagnetic field line, to the corresponding footpoint at 300 km altitude. In this work, the magnitude of the DMSP ion drift velocity is typically reduced with ∼13%.

4.8 Effect of data coverage

4.8.1 A measure of data coverage

How the observation locations are distributed across the model region relative to the SECS node locations affects the model. SECS nodes with many observations in their vicinity are well defined by data. We define the coverage quality as a metric quantifying the distribution of input data across the model region, allowing us to compare the observational coverage between different model times. The measure is accompanied by a coverage plot, showing how the data is distributed over the model region.

For the coverage quality measure, we sort the SECS nodes into two categories based

on coverage: 'good' (j_{good}) and 'poor' (j_{poor}). Three observations are set as the lower limit for when a node is well defined by data. A SECS node is 'good' if there are >3 observation points within the distance range 7−180 km from the node location. We do not include observations <7 km from a node as the modified basis functions in Equation (4.6) goes to zero close to the node. SECS nodes that do not meet the criterion are considered 'poor'. The coverage quality measure is then given as:

$$\text{coverage quality} = \frac{\sum j_{\text{good}}}{n}$$

where n is the total number of nodes. The coverage quality will always lie between 0 and 1, where a higher number indicates more evenly distributed data coverage.

The coverage quality metric does not provide information regarding the total number of observations or their locations; it only expresses how well they are distributed across the grid. The coverage plots are suited for identifying areas in the SECS model region that are poorly constrained by data. They are constructed by assigning an observation point to the closest SECS node, leaving each SECS node with a finite number of observations. Figure 4.3 shows an example of a coverage plot. The contours show the number of observations assigned to each SECS node, where a lighter colour indicates a higher number of observations. In this example, the northwestern part and the southern edge of the model region have a very low density of observations. The coverage plots also include the coverage quality measure and the total number of observations, printed below the model region.

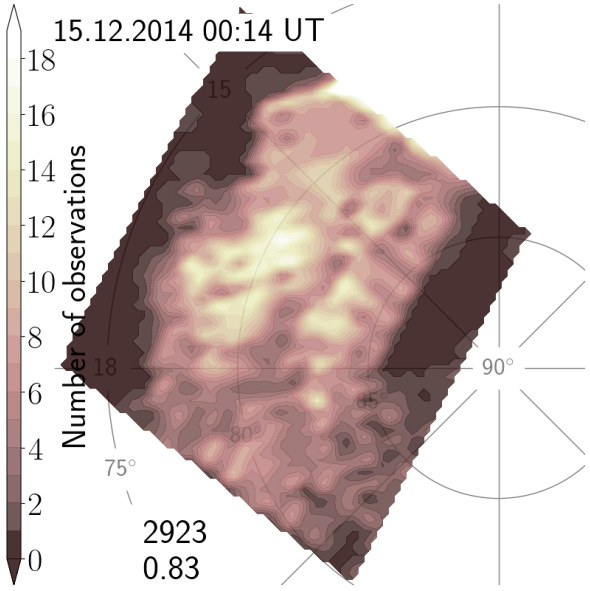

Figure 4.3: Example of a SECS coverage plot for a common distribution of observation points. The colour scale is the number density of observations over the SECS model region. The total number of observations and the coverage quality measure is written in the lower left-hand corner.

4.8.2 Validation with a synthetic data set

The nonuniform data coverage is an obstacle when using the SECS technique with coherent scatter radar observations as the main data input. The LOS velocities from SuperDARN radars have varying coverage depending on the ionospheric conditions and radar transmitter frequency (see Section 3.2). The changing coverage leads to a new geometry in the construction of the model for each model time (new G matrix). Additionally, the total number of observation locations that are provided as input for the model varies from minute to minute.

In order to investigate the effect of the changing data coverage on the model set up, a coverage test similar to the virtual experiment presented in *Amm et al.* (2010) is performed. A synthetic model is to be reconstructed. A model electric field ($\mathbf{E}_{\text{orig}}$) is used as the 'synthetic' input reality. This model is constructed from real observational data on 14 December 2014 at 23:43-23:47 UT, but the chosen time is arbitrary and any synthetic data could be used. We gather observation locations and LOS unit vectors ($\hat{\mathbf{k}}_{LOS}$) that correspond to real coverage scenarios. The modelled $\mathbf{E}\times\mathbf{B}$ drift velocity at observation location i is obtained ($\mathbf{v}_{\text{m},i}$). The LOS-component of these synthetic model velocities is then found through:

$$\mathbf{v}_{\text{m,LOS},i} = \mathbf{v}_{\text{m},i} \cdot \hat{\mathbf{k}}_{\text{LOS},i}$$

where the subscript m indicates that the velocity originates from a model. Figure 4.4 shows an example of $\mathbf{v}_{\text{m}}$ (red vectors) and the corresponding $\mathbf{v}_{\text{m,LOS}}$ (black vectors) for observation locations in the Clyde River (CLY) SuperDARN radar FOV. All the $\mathbf{v}_{\text{m,LOS}}$ are then used as input data to construct a new model of the convection electric field

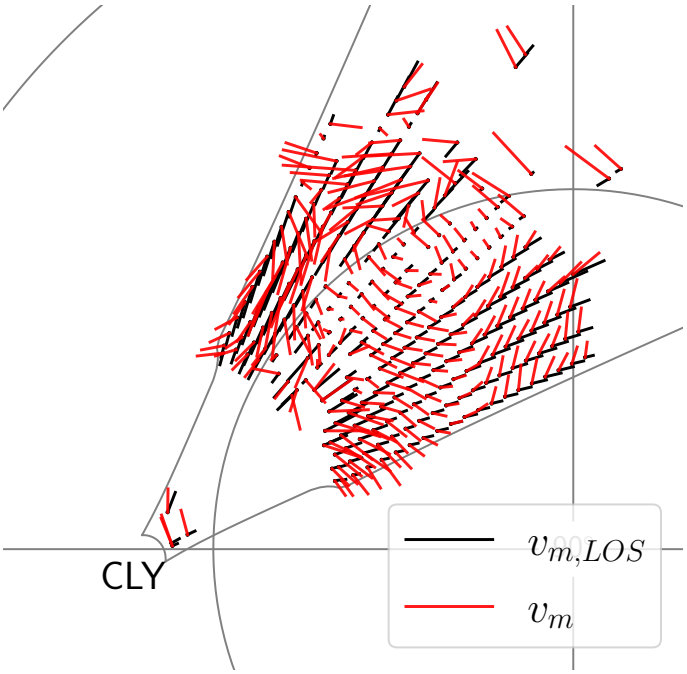

Figure 4.4: Modelled $\mathbf{E}\times\mathbf{B}$ drift velocities ($\mathbf{v}_{\text{m},}$, red) and their components in the SuperDARN Clyde River (CLY) radar line-of-sight direction ($\mathbf{v}_{\text{m,LOS}}$, black).

following the steps in Section 4.5.

The relative error of $\mathbf{E}_{\text{orig}}$ and the reconstructed electric field, $\mathbf{E}_{\text{recon}}$, from the simulated data input is defined as:

$$\text{error} = \frac{\sum_{k=1}^{m} |\mathbf{E}_{\text{recon},k} - \mathbf{E}_{\text{orig},k}|}{\sum_{k=1}^{m} |\mathbf{E}_{\text{orig},k}|} \tag{4.13}$$

where m is the number of evaluation points in the evaluation grid (see Section 4.4). The result is a measure of how well the technique is able to reproduce the synthetic data with the given data coverage situation. The test is performed for five hours of realistic data coverage scenarios (14-15 December 2014 21:00-02:00 UT), yielding a total of 295 coverage scenarios with corresponding relative errors.

Figure 4.5 presents reconstructions for three different coverage scenarios. The corresponding coverage plots are shown in Figure 4.6. The original solution, i.e. the synthetic data set, is shown in Figure 4.5a. Panel b is a reconstruction for a good coverage scenario, panel c is a poor coverage scenario, and panel d is a typical coverage scenario corresponding to the model time of the synthetic data set. Each panel shows three different model parameters. On the left-hand side, the model electrostatic potential, Φ, is plotted as equipotential curves with contour intervals of 1 kV. The arrows are modelled $\mathbf{E} \times \mathbf{B}$ drift velocity unit vectors. At the bottom, the maximum potential difference across the model region (between the black X markers) is written. The magnitude of the modelled electric field is shown in the middle, with the maximum magnitude

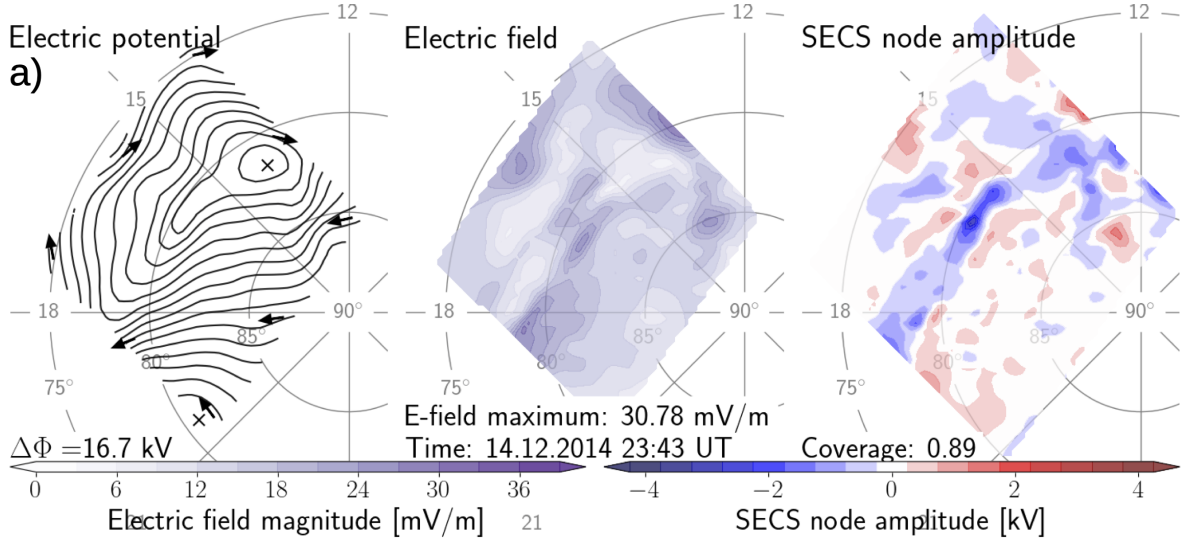

Figure 4.5: Reconstruction of a synthetic data set for three different coverage scenarios. All panels show (from left to right) lines of equal potential with contour intervals 1 kV, convection electric field strength with magnitudes shown in the purple colour bar, and solution node amplitudes with magnitudes as shown in the blue to red colour bar. The black arrows in the left-hand panel are $\mathbf{E} \times \mathbf{B}$ drift velocity unit vectors. See text for details. (a) The synthetic data set that is reconstructed in panels b-d.

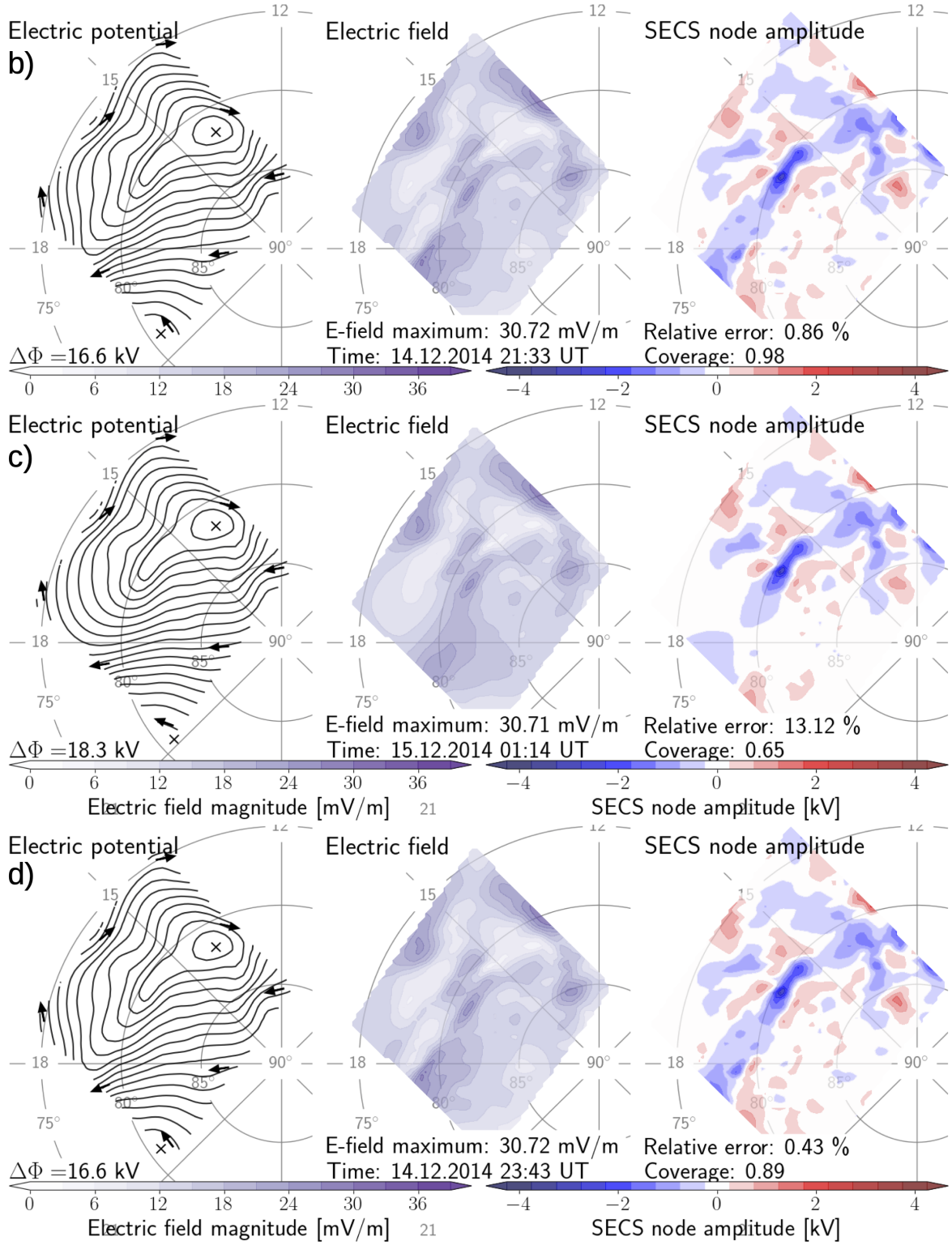

Figure 4.5: Continued. (b) Reproduction of the synthetic data set for a high density of observations. (c) Same as panel b but for a low density of observations. (d) Same as panel b but for a coverage scenario that is observed frequently.

written below. The time of the coverage scenario is also written here. On the right-hand side, the SECS node amplitudes are shown. The relative error and the coverage quality measure is written below. Note that the model region on the MLAT/MLT grid is set consistently at the location for 23:43 UT for easier comparison.

Figure 4.5 shows that the main features of the solutions remain fairly constant for all three levels of coverage. Even for the poor coverage density scenario in panel c, the reconstructed models on the westward part of the model region are remarkably similar to the original model in panel a. The poor coverage density model does, however, show a significant difference in the eastward part of the region. The potential curves are smoother in that area, and both the electric field magnitude and node amplitude plots show less fine structure than the other solutions. This is explained by a lack of observation points in the area, as can be seen from the corresponding coverage plot in

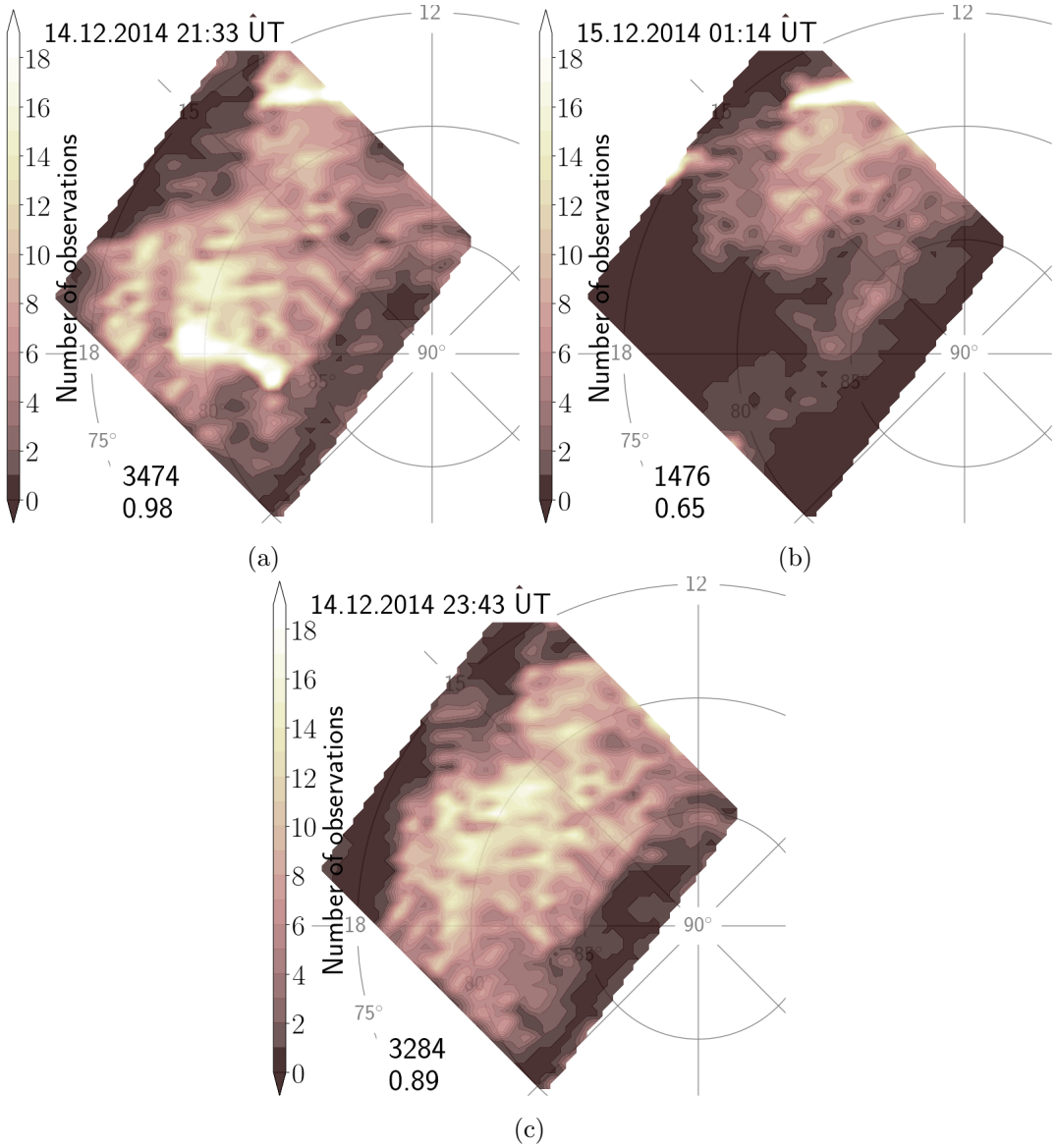

Figure 4.6: Coverage plots for different coverage scenarios corresponding to Figure 4.5. (a) Good data coverage. (b) Poor data coverage. (c) Data coverage used for simulated data set.

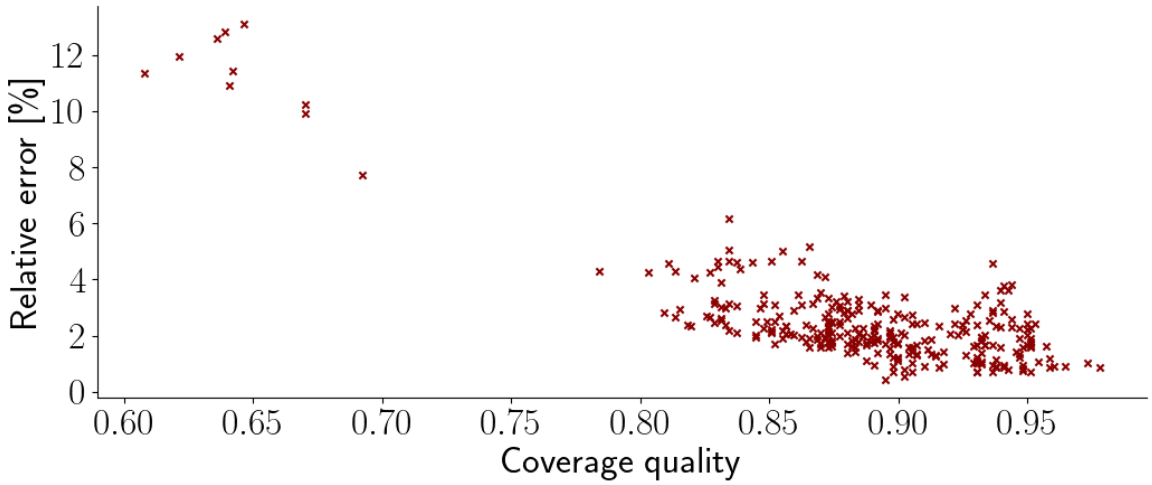

Figure 4.7: The effect of spatial coverage on the ability of the SECS technique to reconstruct a synthetic model of the convection electric field.

Figure 4.6b. The relative error of 13.12% for this coverage scenario is the highest of all the coverage scenarios tested. The remaining two coverage scenarios in panels b and d are almost indistinguishable from the original solution in panel a, with both having relative errors <1%.

The results of the validation test can be summarised by Figure 4.7. The figure shows the relative error depending on the coverage quality measure for all coverage scenarios tested. From the distribution in the scatter plot, it is clear that scenarios with lower coverage quality measures perform worse in recreating the synthetic data set, which was to be expected. However, the relative error never has values >13.12%, even for a poor coverage scenario. On average, the relative error is $2.54 \pm 1.91\%$. The majority of the realistic data coverage scenarios (>89%) can reproduce the synthetic data set with relative errors <4%.

Still, some of the high coverage quality solutions have relative errors >4%. This could be due to a low total number of observations that often causes sporadic behaviour of the SECS models. In order to quickly identify models that may be unreliable, we choose lower limits of 0.84 for the coverage quality measure and 2800 for the total number of observations.

4.9 Inverse problems

As described in Section 4.5, the SECS technique involves solving a set of linear equations since the relationship between the electric field at a specified location and a SECS node amplitude at a known location is linear (from Equation (4.3)). Evaluating Equation (4.7) for $\mathbf{d}$ is straightforward when $\mathbf{m}$ and G are known, while solving the equation for $\mathbf{m}$ is an inverse problem and is thus more complicated. This section describes how the inverse problem is solved.

An exact solution $\mathbf{m}$ that satisfies Equation (4.7) is unlikely to exist. A least squares regression, or L_2 regression, is a method of finding a model that best fits the data

based on specific criteria. When evaluating the model at the same location as it was constrained by data, there will be a misfit between the data ($\mathbf{d}$) and model predictions ($G\mathbf{m}$), called the residual vector: $\mathbf{r} = \mathbf{d} - G\mathbf{m}$. The least-squares solution, $\mathbf{m}_{L_2}$, is a model that minimises the squared length of the residual vector:

$$\min ||G\mathbf{m} - \mathbf{d}||_2^2 = \min \sum_{i=1}^{n} ((G\mathbf{m})_i - d_i)^2 \tag{4.14}$$

where $|| \cdot ||_2$ indicates the euclidean norm, or the length of a vector: $||\mathbf{x}||_2 = \sqrt{\mathbf{x}^T\mathbf{x}}$. Note that the model minimises the *square* of this length, which implies that data points inconsistent with the rest of the data set (outliers) have significant effects on the solution (*Aster et al.*, 2013).

An example of a simple least-squares solution to a set of randomly generated data points is shown in Figure 4.8. The grey line is the linear least-squares solution to the data points shown as blue dots. The red lines mark the residual vectors.

Another common way of writing the least squares condition is in terms of minimising a cost function. The general least squares cost function is given as:

$$f_0 = ||G\mathbf{m} - \mathbf{d}||_2^2 = (G\mathbf{m} - \mathbf{d})^T(G\mathbf{m} - \mathbf{d}) \tag{4.15}$$

where the superscript T denotes the transpose of a matrix.

In this thesis, Tikhonov regularisation (*Aster et al.*, 2013) is used to limit the model's degree of freedom. A regularisation term is added to the cost function in Equation (4.15). The damped cost function is then given as:

$$f = f_0 + \lambda ||I_n \mathbf{m}||_2 \tag{4.16}$$

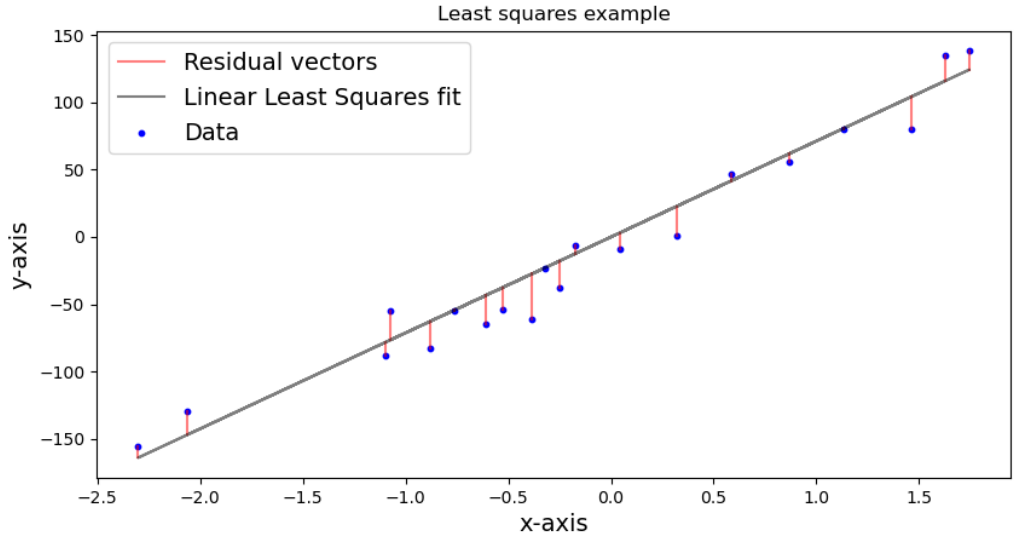

Figure 4.8: Least squares solution plot made with randomly generated data from scikit-learn (*Pedregosa et al.*, 2011). The grey line is the linear least-squares solution to the blue data points. The red lines are the residual vectors.

where f_0 is the original cost function from Equation (4.15). I_n is an identity matrix and $\mathbf{m}$ is the solution. λ is the damping parameter, found through the method described in Section 4.9.1.

The regularised least squares solution to the set of equations will then be given by a minimum in the total cost function shown in Equation (4.16). This is when the partial derivative of the cost function f with respect to $\mathbf{m}$ is zero:

$$\frac{\partial f}{\partial \mathbf{m}} = \frac{\partial f_0}{\partial \mathbf{m}} + \lambda \frac{\partial}{\partial \mathbf{m}} ||I_n \mathbf{m}||_2 = 0 \tag{4.17}$$

The solution of the first term in Equation (4.17), the derivative of Equation (4.15), is:

$$\frac{\partial f_0}{\partial \mathbf{m}} = \frac{\partial}{\partial \mathbf{m}} (G\mathbf{m} - \mathbf{d})^T (G\mathbf{m} - \mathbf{d}) = 2 \cdot G^T (G\mathbf{m} - \mathbf{d}) \tag{4.18}$$

and the solution of the second term in Equation (4.17), the term related to the regularisation, is:

$$\lambda \frac{\partial}{\partial \mathbf{m}} ||I_n \mathbf{m}||_2 = \frac{\partial}{\partial \mathbf{m}} (I_n \mathbf{m})^T (I_n \mathbf{m}) = 2 \cdot \lambda I_n \mathbf{m} \tag{4.19}$$

Equations (4.18) and (4.19) can then be inserted back into Equation (4.17):

$$\begin{aligned} & 2 \cdot G^T (G\mathbf{m} - \mathbf{d}) + 2 \cdot \lambda I_n \mathbf{m} = 0 \\ \iff & G^T (G\mathbf{m} - \mathbf{d}) + \lambda I_n \mathbf{m} = 0 \\ \iff & (G^T G + \lambda I_n)\mathbf{m} - G^T \mathbf{d} = 0 \\ \iff & (G^T G + \lambda I_n)\mathbf{m} = G^T \mathbf{d} \end{aligned} \tag{4.20}$$

From Equation (4.20), the solution that minimises the regularised cost function in Equation (4.16) is

$$\mathbf{m} = (G^T G + \lambda I_n)^{-1} G^T \mathbf{d} \tag{4.21}$$

where the inverse of $(G^T G + \lambda I_n)$ (indicated by the superscript -1) is found through singular value decomposition (SVD; *Eckhart and Young*, 1939) using the NumPy linear algebra least squares solver (*Harris et al.*, 2020).

4.9.1 Regularisation parameter

Most real inverse problems are ill-posed, as they do not fulfil the conditions required for inverse problems to be well-posed; their solutions are not unique, nor do the solutions depend continuously on the data (*Hadamard*, 2003). Regularisation is a technique used to overcome this problem. Multiple regularisation schemes exist.

Tikhonov regularisation is used in this thesis as described in Section 4.9. The regularisation is applied to avoid over-fitting, where the model is fitted too precisely to the data. Over-fitting can lead to unphysical solutions if the data coverage is limited. We seek the solution that both fits the data and is physically meaningful. In the damped cost function in Equation (4.16), the value of the damping parameter λ decides the extent to which large SECS node amplitudes are penalised. This is why Tikhonov regularisation is called damping. The damping parameter is $\lambda = \alpha^2$, where α is the regularisation parameter.

Several methods have been developed to help select the ideal regularisation parameter. In this thesis, the method of Generalised cross-validation (GCV; *Craven and Wahba*, 1978) is used to determine α. The GCV method is a computationally effective way to test for the best regularisation parameter (*Aster et al.*, 2013). Multiple regularisation parameters are tested, and each is assigned a GCV score, $g(\alpha)$, depending on the prediction error, i.e. how well the regularised solution can reproduce the data.

In this thesis, 50 regularisation parameters in the range 10^{-7}–10^{-1} are tested for each SECS model. Figure 4.9 shows an example of a typical GCV curve for the SECS models constructed in this thesis. For this specific model, the $g(\alpha)$ minimum corresponds to $\alpha = 9.103 \cdot 10^{-6}$ (red dot). This is the regularisation parameter for which the model best reproduces the data.

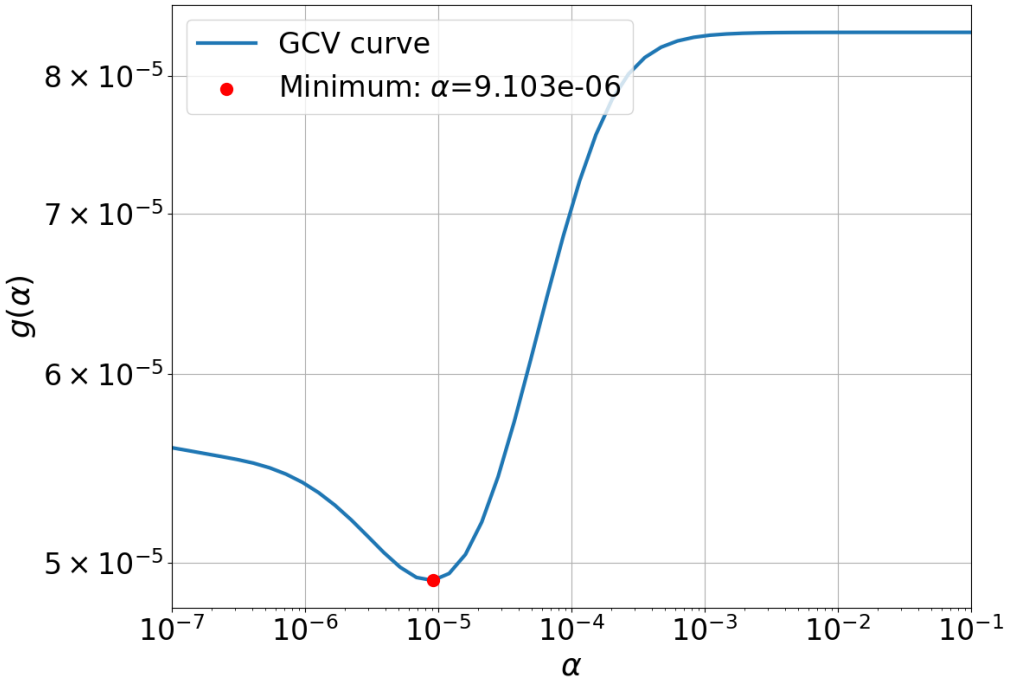

Figure 4.9: Example of a GCV curve. The minimum is marked with a red dot.

Chapter 5

Results

This chapter presents the results from the case study centred around a polar cap auroral arc (PCA) event in the northern hemisphere on 14-15 December 2014. The focus of this chapter is the five hour time interval from 21:00-02:00 UT, hereafter called the observation period. The electrodynamics surrounding the arc is investigated using multi-instrument ground-based and space-based observations in collaboration with the regional model described in Chapter 4. This chapter is divided into ten parts. Sections 5.1-5.5 present observational data of the interplanetary magnetic field (IMF) and solar wind, ionospheric plasma convection, and auroral emissions. An overview of the ionospheric convection from the assimilation model results is presented in Section 5.6. In Sections 5.7 and 5.8, the model convection is compared to independent observations of auroral emissions from ground and space. Section 5.8 also investigates details of the PCA from DMSP satellite passes. In Section 5.9, the model is applied to study the response of the ionospheric convection to a northward turning of the IMF. Finally, the results are summarised in Section 5.10.

5.1 Geophysical context

Geomagnetic indices

The observation period studied in this thesis is a period of relatively quiet geomagnetic conditions. Values for three geomagnetic indices during the observation period are presented in Table 5.1. The Kp index is a measure of geomagnetic disturbances on a global scale (*Matzka et al.*, 2021a). The AE index represents the overall activity of the auroral electrojets, while the SYM-H index describes the geomagnetic disturbances at mid-latitudes (*Iyemori et al.*, 2010).

Table 5.1: Lowest and highest values of geomagnetic indices for 14-15 December 2014 at 21:00-02:00 UT. Kp indices are retrieved from the *Matzka et al.* (2021b) dataset. SYM-H and AE indices are obtained from the CDAWeb HRO dataset (see Section 3.1).

Index	**Value**
Kp	2^-
Sym-H	-13 to $+5$ nT
AE	24 to 169 nT

The three geomagnetic indices presented in Table 5.1 all show values indicating low

geomagnetic activity. Both at mid (SYM-H index) and high (AE index) latitudes, low disturbance levels are measured (*Loewe and Prölss*, 1997).

Solar wind

The solar wind and IMF data products consist of observations from the ACE (HRO data set) and Geotail spacecraft (see Section 3.1). Figure 5.1 shows the spacecraft locations in the GSM system during the observation period (see Appendix A). The orange crosses are ACE locations in the GSM XY (panel a), XZ (panel b), and YZ (panel c) planes as the spacecraft orbits the L1 point. ACE is located at approximately $(x_{\mathrm{GSM}}, y_{\mathrm{GSM}}, z_{\mathrm{GSM}}) = (240, 15, 27)\mathrm{R_E}$, upstream in the solar wind and is somewhat offset from the Sun-Earth line. The blue lines and star markers are the Geotail locations in the same system, with the star indicating the spacecraft location at 02:00 UT. Geotail is approximately located at $(16, -1, 4)\mathrm{R_E}$. This is outside the predicted location of the Earth's bow shock nose (BSN) given in the HRO dataset. The values of the solar wind parameters and IMF strength observed from Geotail presented in Figure 5.2 also point to the spacecraft being located in the solar wind upstream of the bow shock for most

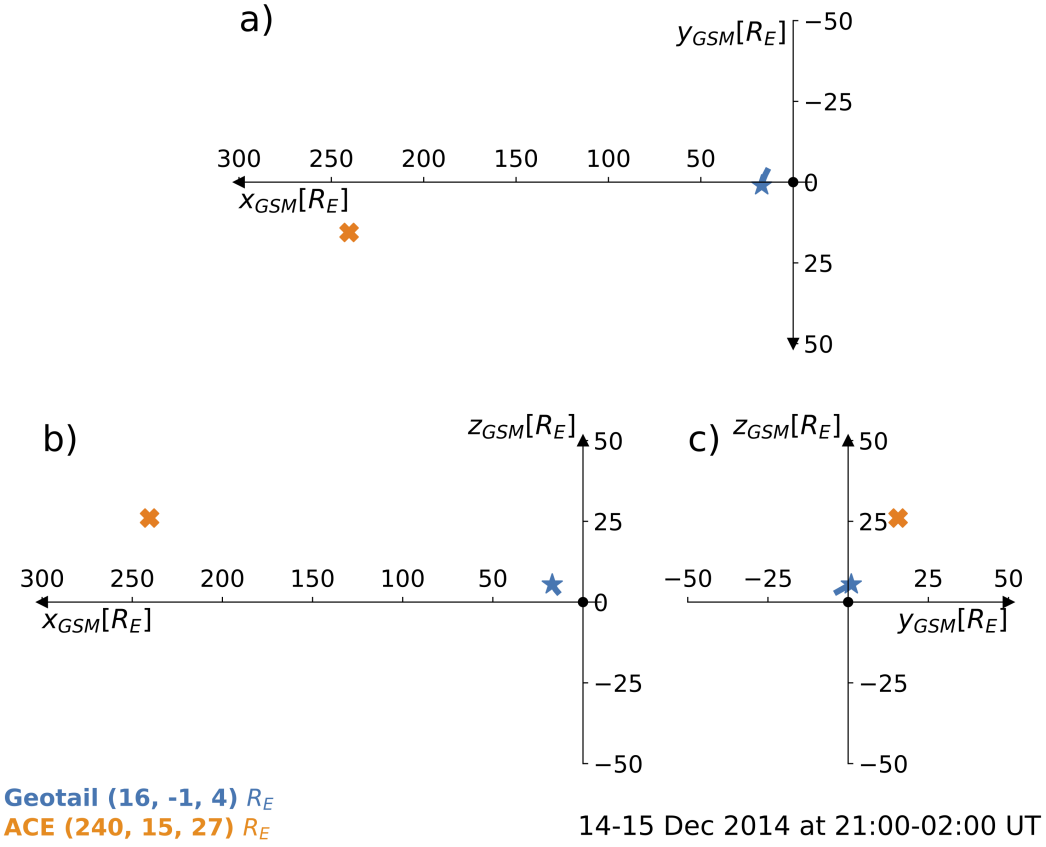

Figure 5.1: Locations of the ACE (orange crosses) and Geotail (blue star markers) spacecraft in the GSM coordinates during 14-15 December 2014 at 21:00-02:00 UT. The approximate locations of the spacecraft in GSM (x, y, z) coordinates is written in the lower left hand corner. Earth's location is indicated with a black dot at origin. (a) GSM XY-plane as viewed from over the northern hemisphere. (b) GSM XZ-plane as viewed from the dusk-side. (c) GSM YZ-plane as viewed from the Sun.

of the observation period.

Data from ACE show that the IMF had a fairly steady southward component with IMF clock angles, θ_{CA}, in the range $110°-180°$ before the observation period (not shown). The southward IMF persisted for ∼3.5 hours before a gradual northward turning at ∼21:00 UT. During the period of southward IMF, the B_Y-component switched signs rapidly but was on average positive. B_X remained negative for many hours before the observation period. Geotail was located inside or at the bow shock before the observation period and could not study solar wind (SW)/IMF conditions.

Figure 5.2 shows an overview of the SW/IMF conditions observed from ACE (orange) and Geotail (blue). Note that the ACE data has been time-shifted to the predicted BSN location. Both ACE and Geotail observe frequent fluctuations in IMF B_Y and B_Z. Systematic differences of ∼10 minutes between the large scale structures observed from the different spacecraft are seen, as expected from the propagation of ACE observations to the BSN. However, some structures are not seen by both spacecraft, even if time-shifting is altered. Geotail's location close to the Earth's bow shock makes it better suited for observing the SW/IMF near Earth, and Geotail data is thus preferred over ACE when interpreting observations in the ionosphere in relation to the solar wind and IMF. We choose to refer to observations from Geotail when SW/IMF data is presented in the following sections.

Figure 5.2a shows a negative IMF B_X component during the observation period in both ACE and Geotail datasets. Negative values for the IMF components from Geotail observations are indicated with shading. Panel b shows that IMF B_Y generally stays positive during the observation period with some short-term fluctuations and one short term departure towards negative values at ∼00:00 UT. Panel c shows $B_Z > 0$ nT for most of the event, with some short periods of negative values. The absolute value of the IMF clock angle in panel d has periods with values $|\theta_{\mathrm{CA}}| > 90°$ corresponding to southward IMF (indicated by shading for Geotail observations). The solar wind density, temperature and speed (panels e, f, and g) were rather constant, with Geotail observing generally higher ion densities than ACE. Geotail observes the largest fluctuations in ion density when the IMF turns southward. The higher ion temperature and lower velocity observed from Geotail at the start of the observation period indicate that the spacecraft possibly was located quite close to the bow shock before ∼21:30 UT.

Temporal data coverage

In addition to the ACE and Geotail spacecraft, observational data has been obtained from SuperDARN radars, REGO all-sky imagers, and DMSP satellites (see Chapter 3). Figure 5.3 shows the temporal coverage of the different instruments during the observation period. The SuperDARN radars (orange colour) at Rankin Inlet, Inuvik and Clyde River were operating nearly continuously, with some data gaps in the Rankin Inlet radar. Not shown are periods of limited backscatter, which occurred when the radars entered the nightside region at ∼00:30 UT (see Section 3.2).

The time periods when the DMSP F16, F17 and F18 satellites were above 70° magnetic latitude (MLAT) are shown as green bars in Figure 5.3. The DMSP satellites cross the northern hemisphere approximately every 1.5 hours. The F17 and F18 satellites have nearly simultaneous crossings, while the F16 satellite crosses the northern hemisphere ∼30 minutes earlier. This leads to ∼1 hour intervals without DMSP coverage.

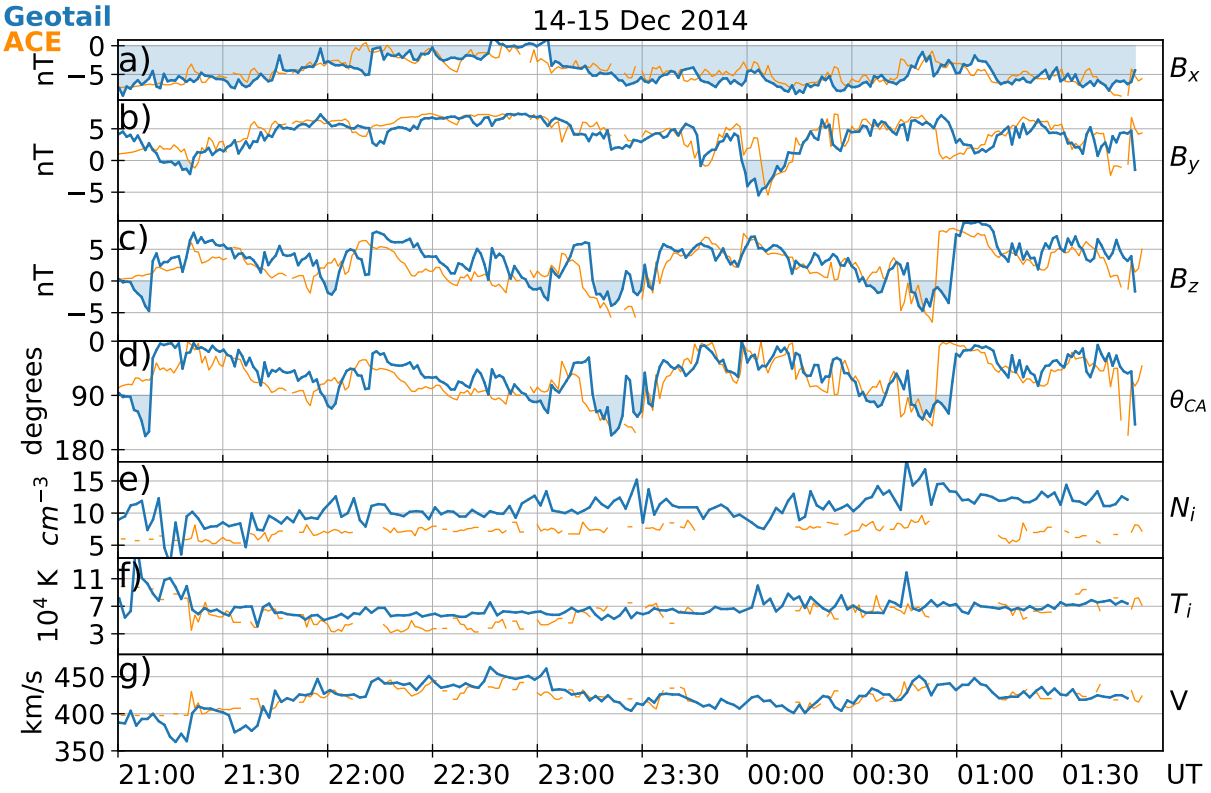

Figure 5.2: Solar wind data from ACE (orange) and Geotail (blue) for 14-15 December 2014. The ACE data has been time-shifted to the predicted bow shock nose. (a, b and c) B_X, B_Y and B_Z IMF components. Negative values from Geotail are indicated with shading. (d) The absolute value of the clock angle. $|\theta_{\mathrm{CA}}|$ >90° from Geotail is indicated with shading. (e) solar wind ion density, N_i. (f) solar wind ion temperature, T_i. (g) solar wind velocity, V.

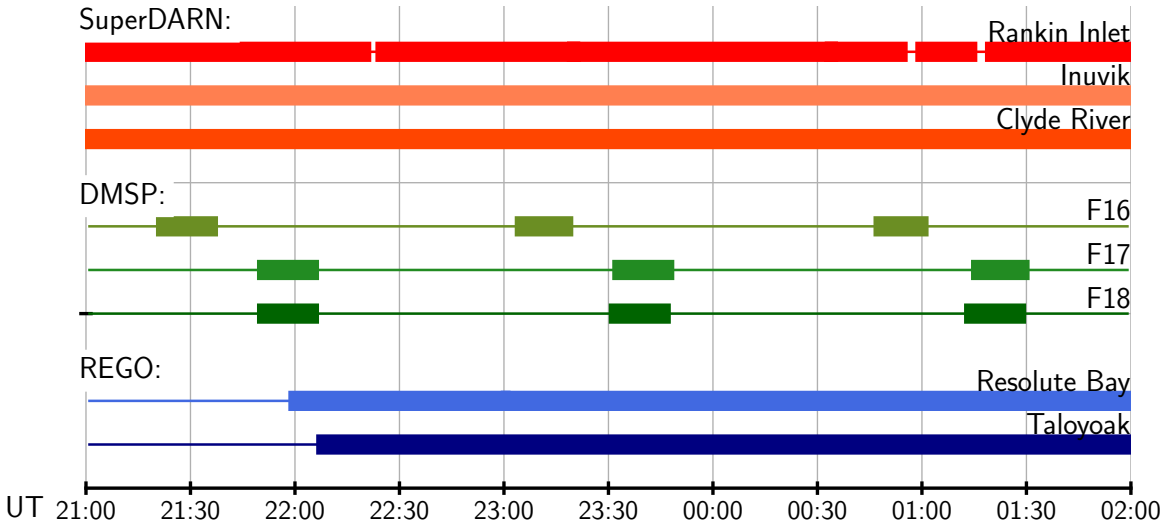

Figure 5.3: Temporal coverage of SuperDARN radars (orange colour), REGO all-sky imagers (blue colour), and DMSP satellite crossings >70° MLAT (green colour) during the 14-15 December 2014 auroral arc event. Thick lines indicate that observational data is available.

The blue bars in Figure 5.3 show the REGO all-sky imager coverage. The imager at Resolute Bay starts operating at 22:00 UT with a small data gap at 23:00-23:02 UT (not visible in Figure 5.3). The Taloyoak imager operates continuously from 22:09 UT. The ground-based SuperDARN radars and all-sky imagers move in magnetic local time (MLT) as the Earth rotates and enter different MLT sectors during the observation period. The satellite crossings also cover different northern hemisphere regions depending on their trajectory, but their northern hemisphere passes are roughly aligned dusk to dawn due to their sun-synchronous orbit.

5.2 Turbulent mesoscale convection in SuperDARN data

During the observation period, where variable SW/IMF is seen, SuperDARN radars observe frequent instances of turbulent convection in the F-region plasma. Some of the mesoscale flows are not compatible with the traditional large-scale convection patterns (see Section 2.6). In this thesis, the mesoscale flows can be studied in great detail as there are simultaneous observations from three SuperDARN radars in northern Canada. The radars have overlapping fields of view (FOV) and are operating nearly continuously. In order to distinguish the turbulent flow from noise, all flow structures presented in this section were visible for at least five consecutive radar scans (5 minutes).

This section introduces the mesoscale flow structures through three examples. To put the local SuperDARN observations into a global context, they are compared to map potential plots (global convection patterns) from Virginia Tech (VT) (downloaded from `https://www.vt.superdarn.org`; discussed further in Section 6.2). The global convection maps are obtained for times corresponding to the radar scan times.

Depending on the direction of the convection, the different radars will observe different flow structures. Of the three radars used in this thesis, the Clyde River (CLY) radar is east-west aligned and most convenient for detecting reversed flow events (RFE), as they tend to be zonally-oriented (*Rinne et al.*, 2007). This zonal orientation is also typical for polar cap (PC) flow channels (FC) (*Herlingshaw et al.*, 2019). The Inuvik (INV) radar can also observe parts of the zonal flows but is angled slightly northwards. The Rankin Inlet (RKN) radar has look-direction into the PC and mainly observes the convection structures in its azimuthal direction.

Example 1 - 22:45 UT

Figure 5.4 presents data from 14 December 2014 at 22:45 UT. Panel a shows a map potential plot for 22:44-22:46 UT. The SuperDARN radar FOVs are overlaid with dashed lines to compare the individual radar observations to the global pattern. The curves in the global pattern are equipotential contours (interpreted as convection streamlines) with contour intervals of 6 kV. The convection along the contours are in the clockwise direction for the blue colour and in the counter-clockwise direction for the red colour. The green line indicates the lower latitude of the convection (Heppner-Maynard boundary (HMB); *Shepherd and Ruohoniemi*, 2000). The SW/IMF and dipole tilt parameters (left) and other relevant parameters (right) for the map potential plots are shown at

the top of the panel. The MLT sectors and colour scale for the (fitted) velocity vectors are also included.

Individual SuperDARN scans at 22:45 UT are shown as fan plots in panels b, c, and d. The panels show line-of-sight (LOS) Doppler-velocities from the RKN, CLY, and INV radars, respectively. Blue colour is LOS velocities of plasma convection towards the radar site, while red colour is valocities away from the radar site. The SuperDARN radars were operating in common mode at one-minute resolution on channel A. The radar transmitter frequency is written below each radar scan. Labels for the

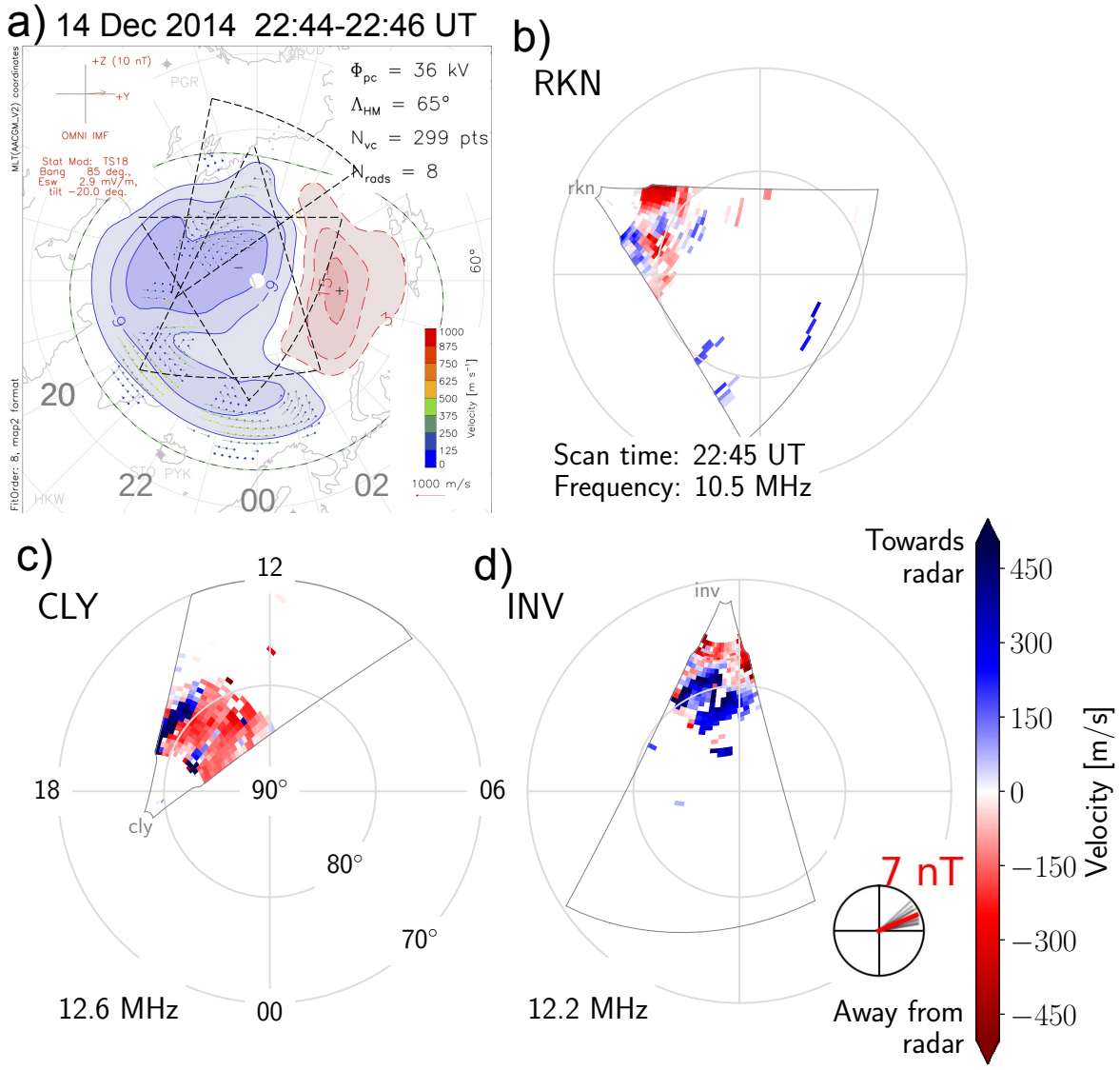

Figure 5.4: SuperDARN data from 14 December 2014 at 22:45 UT. The data are projected on an MLAT/MLT grid. (a) Map potential plot for 22:44-22:46 UT. The black dashed lines are radar fields of view. (b, c and d) Doppler velocity observations from individual radars at 22:45-22:46 UT. Blue (red) colours are line-of-sight velocities towards (away from) each radar site. The panels show fan plots from Rankin Inlet, Clyde River and Inuvik, respectively. The dial in panel d shows the IMF clock angle and magnitude of the IMF transverse component observed from Geotail. See text for details.

MLAT/MLT grid are included in panel c.

In the lower right-hand corner of panel d, a dial shows the IMF clock angle as observed from Geotail. 15 minutes of IMF observations prior to the scan is included in order to show the IMF that is possibly driving the dayside convection. The grey lines are all θ_{CA} observed during the 15 minutes, and the red arrow is the mean value. The length of the arrows is the magnitude of the IMF transverse component, B_T, and the red number is the mean B_T. The clock angle dial shows a slightly northward, B_Y+ dominated IMF, with the mean values $\theta_{\mathrm{CA}} = 67^\circ$ and $B_T = 7$ nT.

Quite surprisingly, there are structured flows observed within the radar FOVs at this time. In the RKN fan plot (panel b), convection speeds are generally low. Still, four regions of flows in opposing directions (alternating red and blue colours) are observed. The largest velocities observed by RKN are the flows away from the radar on the westward edge of the FOV ($\sim$400 m/s) shown as a dark red colour. In panel c, the CLY FOV shows most of the flow at speeds of $\sim$150 m/s away from the radar (red colour), corresponding to sunward convection inside the PC. Embedded in the sunward flows are two channels of anti-sunward flows with velocities $\sim$500 m/s towards the radar (blue). One of the channels is only $\sim$100 km wide and does not extend all the way towards the dayside. The INV radar in panel d also observes sunward flow within the PC (blue), seemingly in two main regions that are separated by lower velocities. There are also structured anti-sunward flows further towards the dayside shown in red in the INV FOV.

The sunward flow at high latitudes is visible in the map potential plot in panel a, and the anti-sunward flow on the equatorward edge of the CLY FOV seems to be in the same direction as the large-scale convection. However, the narrower flow channel observed at $\sim 82^\circ$ MLAT is not accounted for in the large-scale convection map. This area of reversed flow has developed from a location near the radar site and is visible as a narrow feature only for a few minutes. The SuperDARN map potential plot is unable to resolve the many areas of opposing flows seen in the individual radars.

Example 2 - 23:59 UT

The SuperDARN observations at 23:59 UT are presented in Figure 5.5. The map potential plot in panel a is for 23:56-23:58 UT. The clock angle dial in panel d shows mean values of $\theta_{\mathrm{CA}} = 30^\circ$ and $B_T = 5$ nT. This is a more northward oriented IMF than for *Example 1*. The warped global pattern in panel a reflects turbulent F-region flows but the global pattern is not able to resolve the detailed mesoscale flows observed by the individual radars.

A mesoscale flow region at $\sim 81^\circ$ MLAT is evident in the fan plots in panels b-d. CLY and INV both observe a flow channel of high velocity ($\geq$500 m/s) in the anti-sunward direction. The flow channel is a couple of 100 km wide, and it is clearly distinguishable from the background of significant sunward flows with velocities of $\sim$300 m/s. INV observes a region of slow anti-sunward flows on the westward edge of its FOV in addition to the main flow channel. The RKN radar observes a narrow azimuthal area of convection with velocities of $\geq$400 m/s in the equatorward direction at $\sim 81^\circ$ MLAT (dark blue colour). On the equatorward side of the flow channel, RKN observes poleward flows with velocities of $\sim$200 m/s. There is also poleward convection to the north of the equatorward flow region which has low velocities of $\sim$75 m/s.

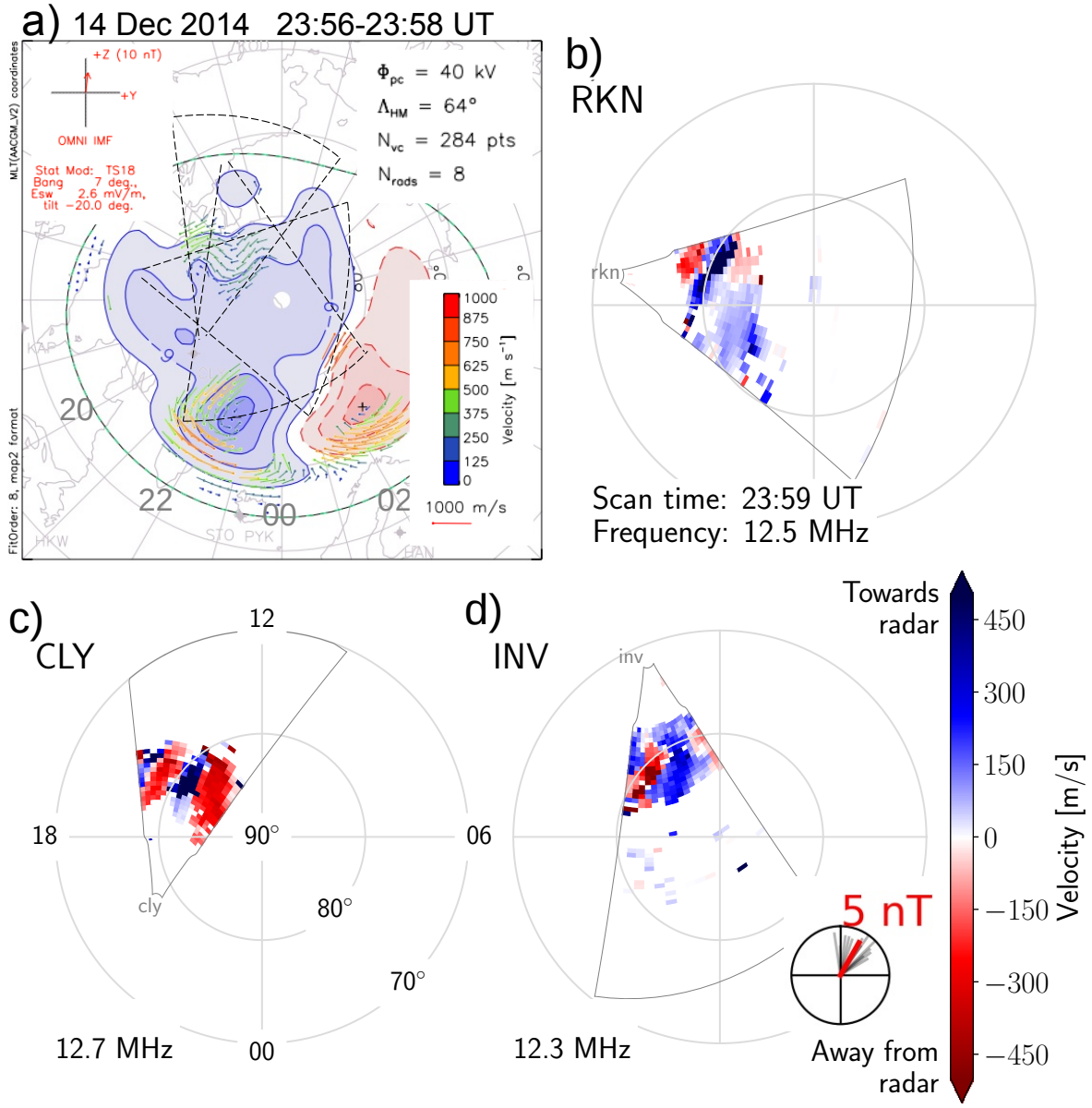

Figure 5.5: SuperDARN data from 14 December 2014 at 23:59 UT, and map potential plot for 23:56-23:58 UT. The figure is in the same format as Figure 5.4. See text for details.

The main flow channel at ∼81° MLAT is embedded in a background sunward flow for ∼18 minutes. CLY also observes a second region of anti-sunward flow at ∼75° MLAT, which is within its FOV for ∼13 minutes. The sunward flows separating the two anti-sunward flow channels at ∼75° MLAT and ∼81° MLAT disappears at ∼00:08 UT.

Example 3 - 00:44 UT

In Figure 5.6, observations from 00:44 UT is presented. The map potential plot in panel a is for 00:44-00:46 UT. At this time, Geotail observes a B_Y+ dominated IMF with mean values of $\theta_{\mathrm{CA}} = 83°$ and $B_T = 5$ nT.

At this time, the RKN radar in panel b observes structured flows in the azimuthal direction. Towards the eastern half of the FOV, the convection is polewards (blue) at

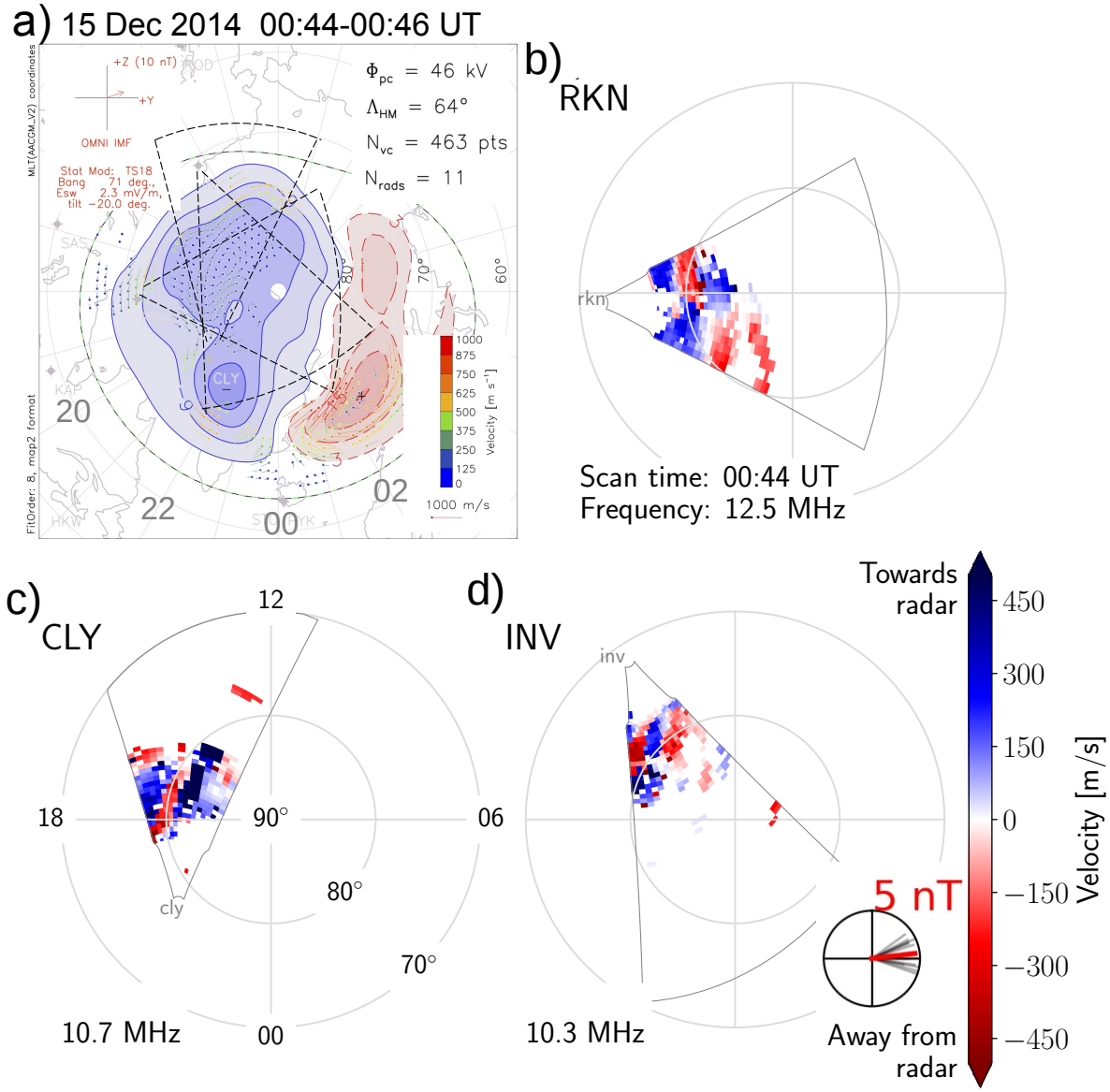

Figure 5.6: SuperDARN data from 15 December 2014 at 00:44 UT, and map potential plot for 00:44-00:46 UT. The figure is in the same format as Figure 5.4. See text for details.

low latitudes, and equatorwards (red) at higher latitudes. On the western half of the FOV, a region of poleward convection is embedded in a background of equatorward flows. The channel at ∼80° MLAT is a couple of 100 km wide and has velocities of ∼300 m/s. Along this same latitude, the CLY radar observes a ∼150 km wide channel of sunward flow. The channel is embedded in a background of anti-sunward convection with velocities ≥300 m/s. The anti-sunward flows on the immediate poleward side of the sunward channel have velocities of ≥500 m/s that are confined to a narrow area. Further poleward, a region of slower anti-sunward flows with velocities ≤100 m/s and even some slow sunward flows are observed. Multiple channels of convection matching the CLY observations are also observed by INV. In the INV FOV up to four channels of opposing flows are clearly distinguishable as alternating regions of red and blue colour.

The map potential plot in panel a is unable to resolve the detailed convection of the

multiple mesoscale flow channels. Some signatures of complex convection are, however, observed approximately the centre of the dusk convection cell. It is hard to see the background convection in the global pattern, but the convection within the collective radar FOVs appears to be in the anti-sunward direction. The sunward channel at $\sim$81° MLAT is therefore identified as a candidate channel of reversed flow. The channel starts out very narrow and widens to more than 100 km. It extends over 14−19 MLT, to a net length >400 km.

Summary

It is difficult to interpret the detailed morphology of convection based on single radar LOS observations, but the three examples presented in this section showed convection that is surprisingly turbulent and different from the expected global patterns (see Section 2.6.1). Although the map potential plots show some evidence of complex convection, they could not resolve the full mesoscale features seen in the individual radar scans.

In the following sections, we will investigate the more detailed characteristics of the flow channels using the regional model of the SECS technique, but first, we will put the observations into a global context based on DMSP satellite observations, followed by ground-based all-sky images.

5.3 DMSP observations of auroral emissions and convection

Structured ionospheric convection on scales similar to the SuperDARN observations is observed by the DMSP spacecraft. In this section, space-based observations of ion drifts and auroral emissions are used to establish a global context for the regional observations.

Figures 5.7 and 5.8 present observations from all northern hemisphere DMSP F16 (a, d, and g), F17 (b, e, and h) and F18 (c, f, and i) passes during the observation period. Figure 5.7 shows auroral emissions, and Figure 5.8 shows plasma convection. Both figures are in the same format. The timestamps in the upper left hand corner of each panel is the UT when the satellite is approximately at the centre of the pass. The satellites have dusk to dawn trajectories, meaning they are going from left to right in the panels. The labels of the MLAT/MLT grid are included in panel i.

The far-ultraviolet (FUV) auroral emissions in Figure 5.7 are in the Lyman-Birge-Hopfield short (LBHS) wavelength range and are observed by SSUSI (see Section 3.3.3). The dashed lines show the spacecraft trajectories.

In Figure 5.8, the horizontal cross-track ion drift velocities measured in-situ by SSIES are shown as black vectors. The vectors are perpendicular to the spacecraft trajectory and the scale is given in panel i. Note that the ion drifts are presented in Earth's rotating system (they have been corrected for corotation; see Section 3.3.1).

Auroral emissions

The PCA can be recognised in the F18/F17 passes at $\sim$21:57 UT in Figures 5.7b and c. These are the earliest observations where the PCA is visible. The PCA location

is indicated with red arrows in the panels. The thin arc has width <100km, and is observed on the dusk-side, poleward of a weak main oval. The main oval emissions have intensities $\lesssim$170 Rayleigh (R). The PCA is connected to the main oval at ∼22/23 MLT. From there, it reaches towards the dayside approximately parallel with the main oval. The PCA has a similar location in the successive F18/F17 passes at ∼23:39 UT (panels e and f), though the main oval emissions have shifted slightly equatorward. In panel f, a spot of enhanced emissions is observed on the dayside (∼75° MLAT and 13:30 MLT), consistent with the expected footprint of subsolar dayside reconnection for a B_Y+ IMF orientation (*Frey et al.*, 2019). At ∼01:21 UT (panels h and i), the PCA is connected to the main oval in both ends and has shifted to lower latitudes. It is slightly bent towards the nightside end, connecting to the main oval at ∼19 MLT. The main oval and the PCA emissions have higher intensities with main oval emissions of $\gtrsim$400 R. Panels i and h show the last SSUSI images where the PCA is observable. The PCA is also visible on the nightside edge of F16 SSUSI images but is smeared out and distorted due to the viewing angle. Red arrows in panels d and g indicate emissions that may be the PCA.

Convection

Significant convection structure above ∼79.5° MLAT, with sunward drifts at lower latitudes is seen at ∼21:30 UT in Figure 5.8a. Panels b and c show the convection 30 minutes later, at ∼21:57 UT. At this time, sunward convection is seen inside the PC with two narrower regions of anti-sunward convection on either side, related to northward IMF orientation. We refer to Section 2.6.1 for a description of global convection patterns for different IMF orientations. The F18 pass in panel b shows a small enhancement of the sunward convection on the equatorward side of the flow reversal at ∼78° MLAT as indicated by the red arrow. This flow reversal is colocated with where SSUSI observes the PCA in Figure 5.7b. In Figure 5.8c, multiple convection reversals on the dusk-side are indicated by an orange arrow. These convection reversals are possibly related to multiple weak auroral arc emissions that are just barely visible in Figure 5.7c. Fast anti-sunward flows are seen on the dawn-side (outside the region of interest) and have locations that are consistent with the fast flow channels for B_Y+ studied by *Herlingshaw et al.* (2020) (see Section 2.6.2). A blue arrow in Figure 5.8c indicates the location of such a channel. In general, fast anti-sunward flows are expected on the dawn-side in the global convection patterns for IMF B_Y+.

Figure 5.8d shows three convection reversals at ∼12 MLT with a generally anti-sunward flow inside the PC for the F16 crossing at ∼23:11 UT. Below ∼76° MLAT on the dawn-side, a region of sunward return flow is observed. Panels e and f show fast anti-sunward flows inside the PC, with higher velocities on the dawn-side. These observations are consistent with global two-cell convection during IMF B_Y+. Some exceptions from the traditional pattern are the small regions of sunward convection around 13 MLT in panel e and the multiple convection reversals on the dawn-side seen in panels e and f. In panel e, the red arrow is pointing to the flow reversal at ∼80° MLAT that is related to the PCA seen in Figure 5.7e. Enhanced anti-sunward flows are observed on the poleward side of the reversal.

Figures 5.8g, h, and i all show cross-track drifts with substantial mesoscale structure. Most interesting for this study is the narrow channel of sunward flow with velocities

>1500 m/s observed at ∼79° MLAT by F18 at ∼23:39 UT. Panel h shows how the channel is embedded in a region of anti-sunward convection. The PCA seen in Figure 5.7h is located on the poleward side of this channel. The red arrow in Figure 5.8h points to the flow reversal at the PCA location.

The along-track ion velocities are not shown in Figure 5.8, but are available in the DMSP data set. All six satellite passes show significant variation in this component as

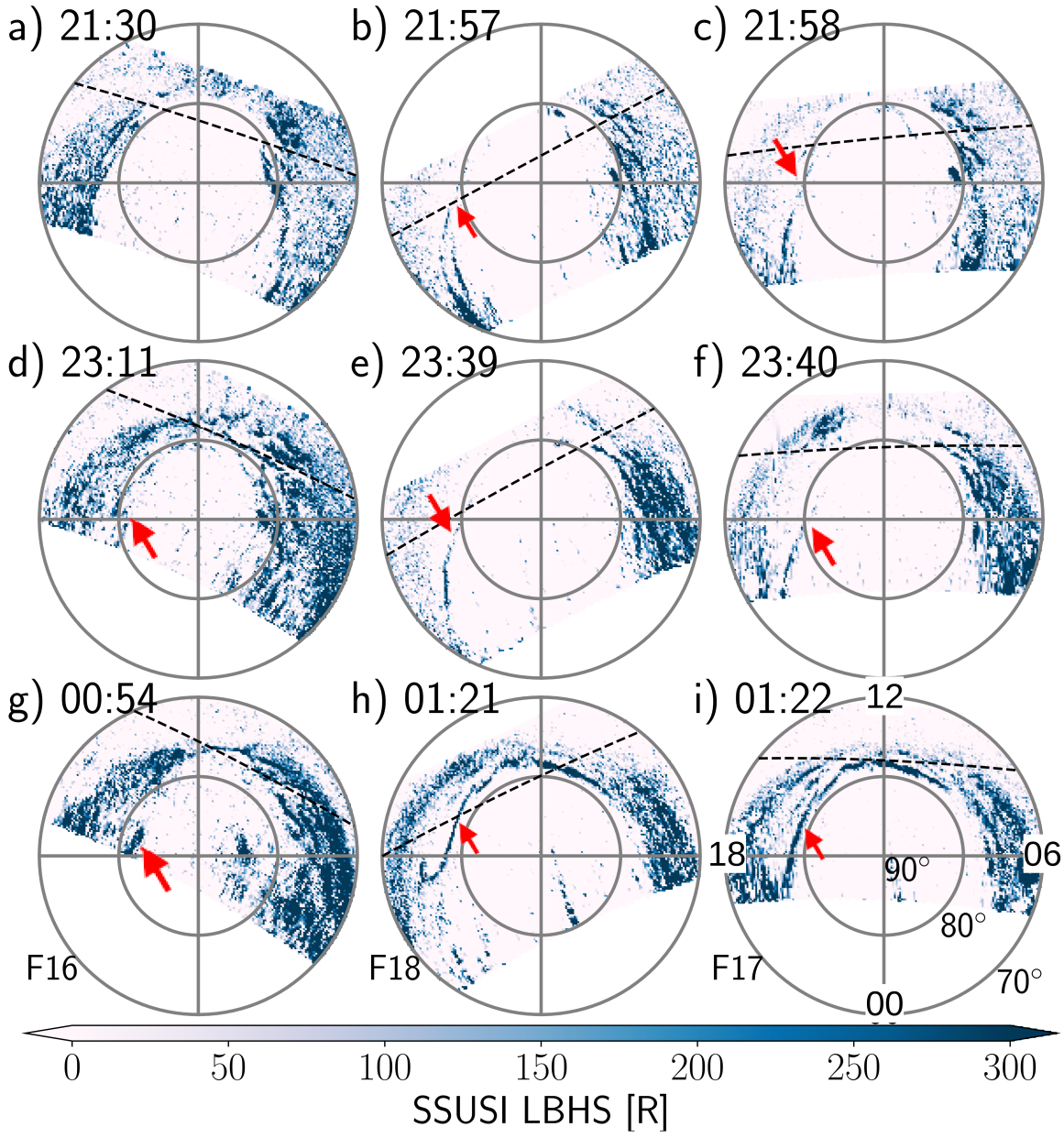

Figure 5.7: Far-ultraviolet (LBHS) images from three DSMP satellites on 14-15 December 2014. The time indicated on the plot is the approximate midpoint of the northern hemisphere polar pass. The emission intensities are given in the colour bar. The red arrows indicate a polar cap auroral arc. The dashed lines are the (dusk to dawn) spacecraft trajectories. The images are projected on an MLAT/MLT grid. Axis labels are written in panel i. (a, d, and g) F16 passes. (b, e, and h) F18 passes. (c, f, and i) F17 passes.

well, except for the F17 pass at 21:58 UT (Figure 5.8c), where the along-track velocities are generally towards the dusk-side.

The DMSP F18 passes over the PCA will be revisited in more detail in Section 5.8.

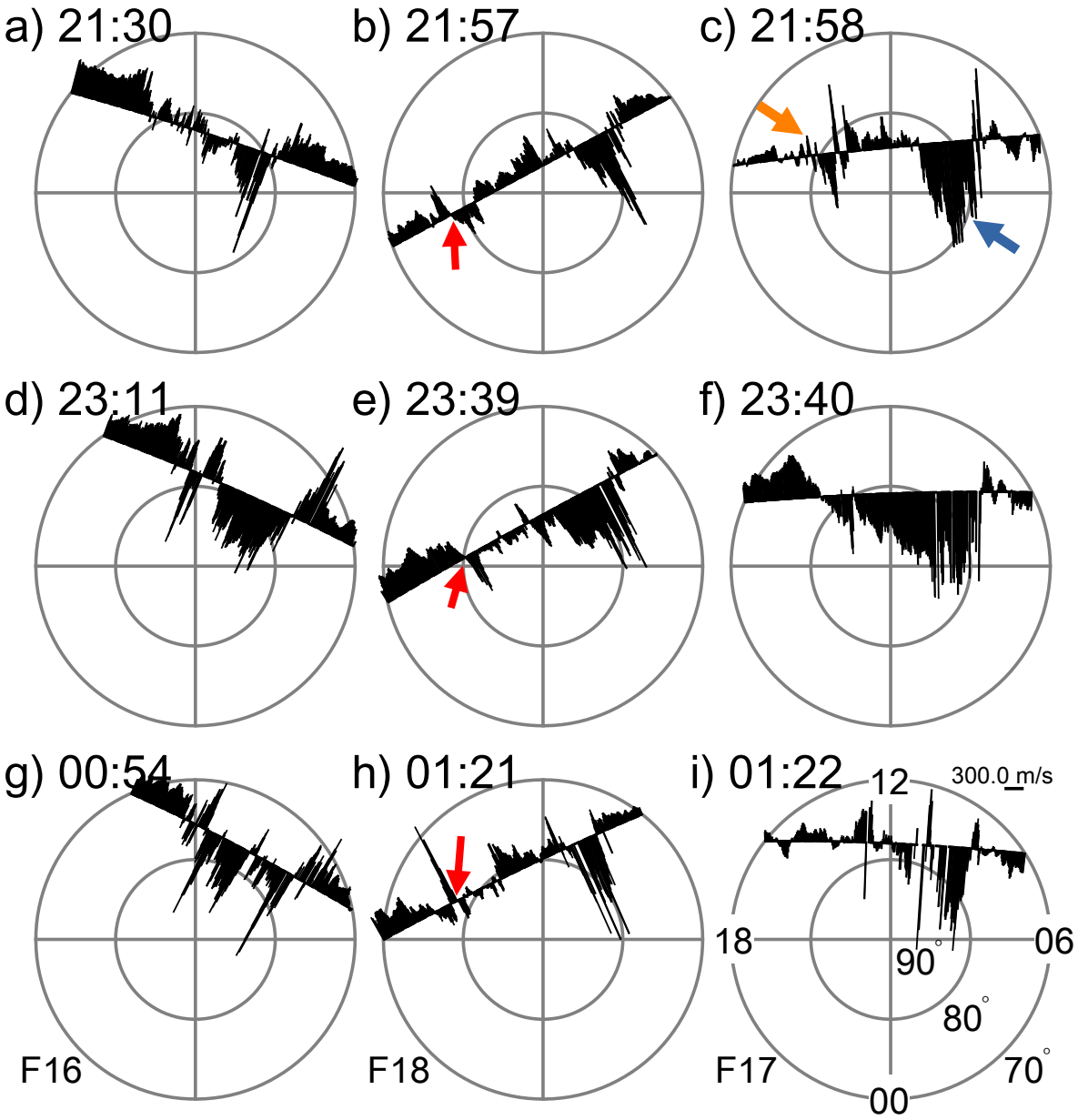

Figure 5.8: Horizontal cross-track ion drifts (black vectors) from three DMSP satellites on 14-15 December 2014. These are the same northern hemisphere passes as presented in Figure 5.7. The scale for the velocity vectors is shown in panel i. The red arrows indicate convection reversals associated with the polar cap auroral arc. The orange arrow in panel c indicates multiple convection reversals in the dusk-side F17 observations. The blue arrow in the same panel indicates a possible fast flow channel of the type studied by *Herlingshaw et al.* (2020). (a, d, and g) F16 passes. (b, e, and h) F18 passes. (c, f, and i) F17 passes.

5.4 Global context of the auroral arc observed by all-sky imagers

The DMSP satellites are suitable for providing a large-scale overview of the aurora and convection, but the space-based observations are spaced far apart in time. The ground-based observational methods have more continuous coverage of the ionosphere, and all-sky imagers are better suited for following the movement of the PCA with time. The all-sky imagers do, however, have limited FOVs and can only observe parts of the PCA. Images from the DMSP spacecraft are needed to put the auroral emissions observed from the ground into a global context.

In Figure 5.9, the ground-based all-sky images of 630.0 nm (red-line) emissions are overlaid FUV images from the DMSP satellites. Images from the satellites and all-sky imagers that have the best viewing geometry of the PCA are selected. The SSUSI images in panels a, b, and c are close-ups of Figures 5.7c, f, and h, respectively. The all-sky images are from the REGO imagers at Resolute Bay (RESU) and Taloyoak (TALO). Note that the intensity of the emissions is different for the all-sky imagers, possibly because of a calibration issue, different viewing angle, or atmospheric conditions (see Section 3.4).

In Figure 5.9a, the first available all-sky image from RESU at 22:00 UT is overlaid an image taken from F17 at ∼21:55 UT. The two images are taken 4 minutes apart and are not expected to match completely. Still, the location and orientation of the auroral form in the all-sky image seem consistent with the large-scale view of the PCA in the SSUSI image.

The all-sky image in panel b is from RESU and is taken at 23:37 UT, almost sim-

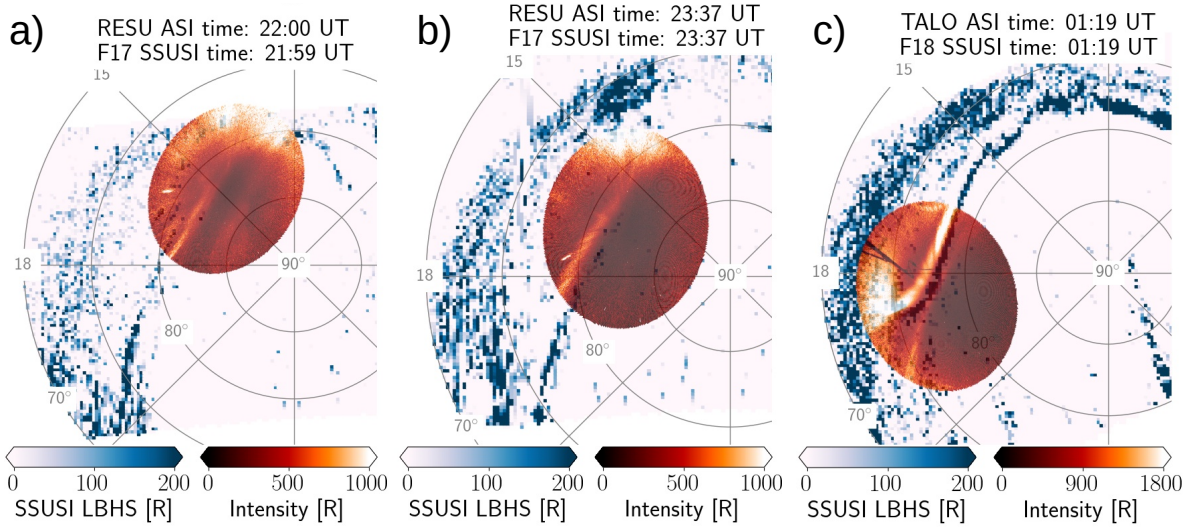

Figure 5.9: Ground-based observations of red-line emissions by REGO all-sky imagers compared to space-based observations of far-ultraviolet (LBHS) emissions by DMSP SSUSI on 14-15 December 2014. (a) A Resolute Bay (RESU) all-sky image at 22:00 UT overlaid an F17 SSUSI image taken at ∼21:56 UT. (b) Same as for panel a, but for images at 23:37 UT. (c) A Taloyoak (TALO) all-sky image overlaid a F18 SSUSI image. Images taken at 01:19 UT.

ultaneous to when the F17 satellite passes over the all-sky imager FOV. The bright emissions across the centre of the all-sky imager FOV must be related to the PCA emissions observed by F17. However, the locations of the emissions do not overlap completely. The inconsistency can be attributed to mapping effects and distortion due to viewing geometry (see Section 3.4.1). It could also be due to a slight movement of the PCA at this time. Note how the location of a brightening on the dayside in the all-sky image matches the bright spot in the F17 SSUSI image.

An all-sky image from TALO at 00:19 UT is shown in panel c. The SSUSI image is from the F18 spacecraft that passes over the all-sky imager FOV at ∼00:19 UT. Both observational methods show brighter PCA emissions than observed in panels a and b. The shape of the aurora observed by TALO is similar to the slightly bent auroral form observed by F18 SSUSI. The small difference in the location of the emissions could be explained by the same arguments as for the two previous conjunctions.

Despite the two observational methods observing different emission wavelengths, the all-sky imagers and DMSP spacecraft likely observe the same auroral arc form. In the following sections, the all-sky images are used to examine the PCA's north-south movement and determine the location of the PCA with respect to east-west convection structures.

5.5 Time evolution of the auroral arc and its related convection

Although they have a limited FOV, the ground-based images fill in and compliment the space-based images between the DMSP northern hemisphere passes. In this section, the PCA migration and F-region plasma motion in the north-south (dawn-dusk) direction will be investigated using observations presented in Figure 5.10. Figure 5.11 supplements Figure 5.10, and shows all-sky images from selected times during the observation period.

The movement of the PCA and the surrounding F-region plasma convection can be related to the concurrent IMF observations. Figures 5.10a and b show the IMF B_Y and B_Z components during the observation period. The observations are not time-lagged. The light blue shading indicates negative values.

The keogram in Figure 5.10c is aligned in time with the IMF observations in panels a and b. It shows a cut of the centre pixels in the 630.0 nm all-sky images from RESU (top) and TALO (bottom) stitched together at the latitudes where their FOVs overlap. The cut is taken along ∼265° geographic longitude, and the geographic (left) and magnetic (right) latitude is shown on the y-axes. The plot is a continuous time series showing the latitudinal (north-south) movement of the PCA during the observation period. Some streaks of high intensity are seen as bright vertical lines in the bottom part of the keogram and are attributed to artificial light from headlights or lamps in the vicinity of TALO. The MLT sectors of the imagers are written in white at the top of the keogram emphasise that they move towards the nightside during the observation period.

In order to relate the motion of the PCA to the ionospheric plasma convection, a range-time (RT) plot from the RKN SuperDARN radar is included in Figure 5.10d. An RT plot is a cut along the radar FOV showing a time series of radar observations

from a single beam (here: beam 6), and is like a keogram for LOS Doppler-velocity observations. The MLT sectors of the central RKN FOV are written at the top of the panel, and the location of beam 6 in the FOV is shown in the lower left-hand corner. The RKN radar is oriented in such a way that it observes plasma flow in the north-south direction. Plasma cannot move across the OCB (unless reconnection takes place; see Section 2.4), and a bulk motion of the plasma in the poleward or equatorward direction will correspond to motion of the OCB or redistribution of the plasma within the PC.

Figure 5.11 shows a selection of all-sky images. The yellow lines in Figure 5.11r show the latitudinal cut of the FOVs that are used for the keogram in Figure 5.10c and the white arrows on top of the keogram indicate the UT of the selected images. Note that brightness and shape of the aurora observed from ground will vary depending on where it is located in the imager FOV, as discussed in Section 3.4.

The approximate location of the PCA based on the keogram in Figure 5.10c is plotted as a black curve on top of the RT plot in Figure 5.10d. The plot shows an overall compliance between the plasma motion in the poleward (red colour) and equatorward (blue colour) direction and the north-south migration of the PCA. The following description details the movement of the PCA.

In the first all-sky image from RESU at 22:00 UT, an auroral arc is spotted at the eastward edge of the FOV. Multiple thin curtains of emissions in the arc are seen, just barely visible at the start of the observation period. A slight poleward shift of the arc is observed, as indicated by the white arrow in Figure 5.11a. At 22:13 UT, a brightening of the main oval emissions is observed on the on the westward edge of the imager FOVs (at ∼13 MLT). The bright region expands towards the dusk-side as indicated by the blue arrow in Figures 5.11b and c. This coincides with the first IMF polarity change at ∼22:00 UT. Figure 5.10b shows a brief period of ∼4 minutes where $B_Z < 0$ nT. Such a small departure from the northward orientation could be interpreted as noise, but the auroral brightening indicates that dayside reconnection probably occurred (*Frey et al.*, 2019).

After the dayside brightening, the arc starts moving slightly poleward from ∼82° to ∼83° MLAT. The movement is too slow to be marked by arrows in Figure 5.11. The slight poleward movement of the aurora after the brightening is consistent with observations of the bulk flow of the F-region plasma away from the RKN radar site seen in Figure 5.10d. The poleward movement subsides after a few minutes, and both the bulk plasma and the auroral form starts drifting equatorward.

A new dayside brightening is observed at 23:08 UT at the eastward edge of the imager FOVs (∼14 MLT). The brightening spreads duskward as indicated by the blue arrow in Figure 5.11g. The brightening coincides with a period of B_Y+ dominated IMF with $B_Z < 0$ nT at ∼23:00-23:30 UT. The imagers and radar are located at ∼16 MLT and the dayside brightening is not as noticeable as during the previous IMF B_Z polarity change at 22:13 UT. Fortunately, a space-based image from DMSP F17 is available at this time, giving us an overview of the aurora. As noted in Section 5.3, the FUV image in Figure 5.7f shows a spot of bright aurora on the dayside (most likely within the main oval) at ∼76° MLAT and ∼14 MLT. In Section 5.4, we saw that these emissions were consistent with the all-sky imager observations of the brightening (Figure 5.9b).

After the brightening, an equatorward movement of the PCA is observed (white arrows in Figure 5.11g and h). The PCA follows the fairly fast ∼350 m/s flow of

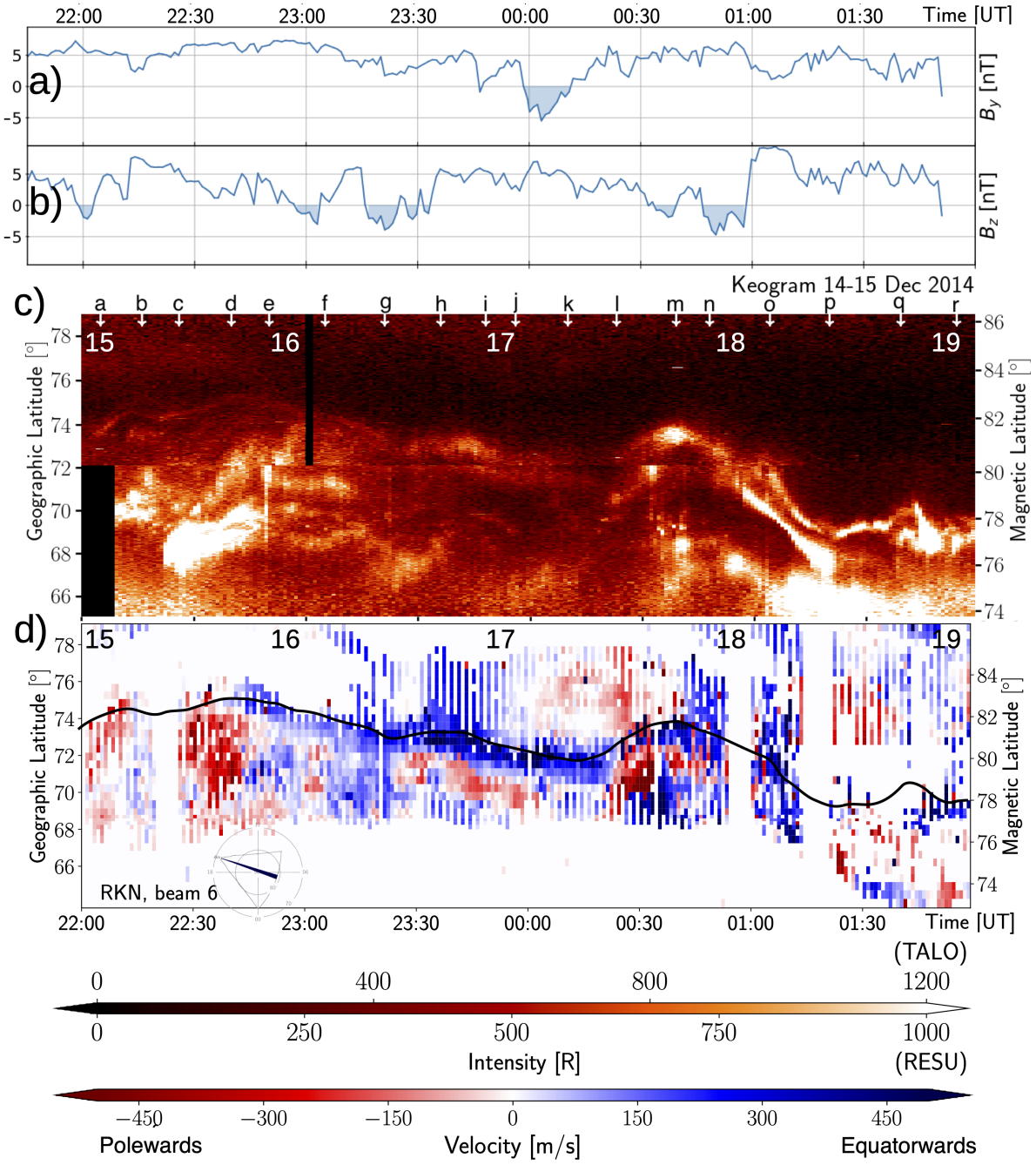

Figure 5.10: Observations of IMF, red-line aurora and plasma convection on 14-15 December 2014 at 21:45-02:00 UT. (a and b) IMF B_Y and B_Z component observed from Geotail. Shading indicates negative values. (c) Keogram from REGO all-sky imagers at Resolute Bay (RESU) and Taloyoak (TALO). The intensity of the 630.0 nm emissions is given in the colour bar at the bottom of the figure. The letters a-r at the top correspond to the panels in Figure 5.11. (d) Range-time plot for beam 6 of the SuperDARN Rankin Inlet radar. The line-of-sight Doppler velocities are given in the colour bar at the bottom of the figure. The black line is the location of a polar cap arc identified in the keogram in panel c. See text for details.

F-region plasma towards the RKN radar site. There is a short interruption in the equatorward movement at ∼23:25 UT that could be due to a short period of northward oriented IMF at ∼23:15 UT. The PCA equatorward motion subsides at ∼00:20 UT, at which point it is located at ∼79° MLAT.

An IMF B_Y polarity change is observed at ∼00:00 UT. The PCA starts moving poleward at ∼00:20 UT (white arrow in Figure 5.11l). The PCA also appears brighter after ∼00:30 UT. The speed of the poleward motion of the PCA is estimated based on the time it takes to move the distance 79°−82° MLAT (∼400 km). The PCA moves poleward for ∼20 minutes, leading to an estimated poleward velocity of ∼330 m/s. The speed is similar to the poleward velocity of the F-region plasma convection seen in Figure 5.10d. The sign of B_Y has been related PCA dawn-dusk motion (see Section 2.7.1), and this response will be further discussed in Section 6.3. Note that the observations of the PCA and the plasma flow at this time is done far into the dusk-side, at a location where both dayside and nightside processes control the ionospheric convection (see Section 2.6.1).

The B_Y component has negative values for ∼15 minutes, before gradually turning back to positive values. The PCA starts moving equatorwards at 00:40 UT (white arrows in Figures 5.11m-o), which is ∼25 minutes after the B_Y turns back to a positive orientation. The equatorward migration of the PCA is fairly rapid, and the arc moves from ∼82° MLAT to ∼78° MLAT in 40 minutes. During the equatorward movement,

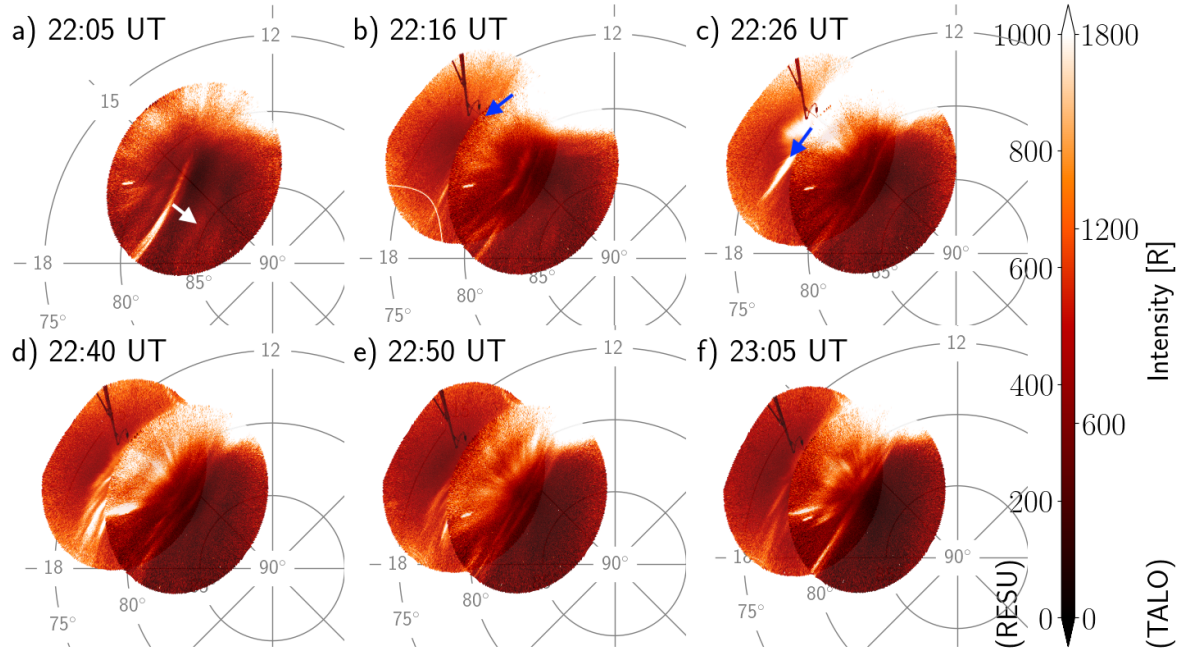

Figure 5.11: All-sky images of 630.0 nm auroral emissions from imagers located at Resolute Bay (RESU) and Taloyoak (TALO). The panels a-r show a selection of times during 14-15 December 2014. The time of the images is written at the top of each panel. The images have been projected on an MLAT/MLT grid where noon is up and dusk is to the left. White arrows indicate north-south motion of the auroral arc form, and the blue arrows in panels b, c, and g show how brightening of the dayside-aurora expands towards the dusk-side.

TALO observes a splitting of the PCA into two arcs, seen both in Figure 5.10c after 01:00 UT and in Figures 5.11o-r. Unfortunately, the SuperDARN radar receives little backscatter at this time and multiple gaps are observed in the RT plot in Figure 5.10d. Still, the radars seem to observe a bulk equatorward motion of the plasma surrounding the PCA.

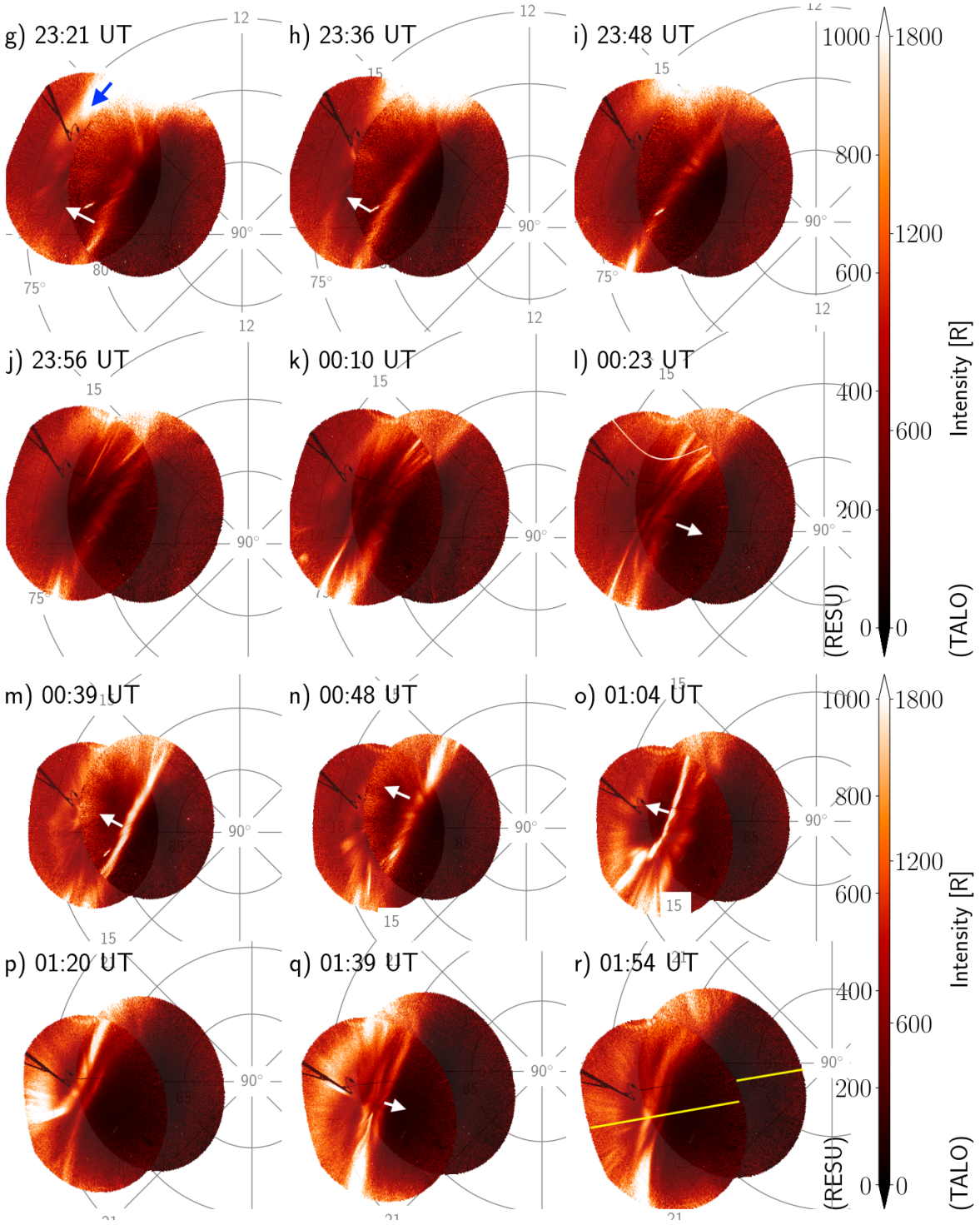

Figure 5.11: Continued.

The last IMF polarity changes are observed during ∼00:30-01:00 UT where IMF B_Z has departures towards negative values. At this time, the imagers are located too far on the nightside to see clear optical signatures of dayside reconnection. However, the aurora in the space-based image from DMSP F16 at ∼00:54 UT (Figure 5.7g) shows emissions that are generally brighter than during the previous passes (even if comparing with the same satellite in Figure 5.7d).

In summary, the north-south movement of the PCA is overall similar to the bulk movement of the F-region plasma and the observations can be related to the IMF orientation.

5.6 Time evolution of the mesoscale convection pattern

As seen through the examples in Section 5.2, the mesoscale convection is highly dynamic during the observation period. This section outlines the main features of the local two-dimensional F-region convection surrounding the PCA through the time series presented in Figure 5.12. The figure shows regional models constructed from the convection data from SuperDARN and DMSP through the SECS technique as described in Chapter 4. The models are selected to show features that are consistent over several minutes. Figures 5.12g-x have times corresponding to the all-sky images from Section 5.5 (Figure 5.11).

The model time of the selected models in Figure 5.12 is written at the top of each panel. The black contours are electric equipotential lines with contour intervals of 1 kV. The equipotential lines can be interpreted as plasma convection streamlines. The black arrows are selected unit vectors of the model $\mathbf{E} \times \mathbf{B}$ drift velocity. The blue and red colour contours are SECS node amplitudes.

How to interpret the model plots will be revisited in Section 5.7, but can be summarised as:

- Positive SECS node amplitudes (red) mark regions of positive flow vorticity, corresponding to shears or reversals in the counter-clockwise direction.
- Negative SECS node amplitudes (blue) mark regions negative flow vorticity, or shears or reversals in the clockwise direction. These are associated with upwards FAC and auroras (see Section 4.6 and Section 2.7).
- The potential contours are convection streamlines with flows in the direction indicated by the $\mathbf{E} \times \mathbf{B}$ drift velocity unit vectors. Closely spaced contours indicate strong convection.

The number below the model region indicates the coverage quality, as defined in Section 4.8.1. Models with good coverage are selected when possible (coverage quality >0.84; see Section 4.8.2). The brown stars in panels u-x indicate model solutions that should be treated cautiously as the total number of observations is low (<2800). Models with DMSP driftmeter observations as additional data input are marked by satellite icons (panels c, f, n, and v).

Figure 5.13 shows the coverage plots corresponding to the panels in Figure 5.12 (see Section 4.8.1). The brown to white colour scale shows the density of observations across

the region. The total number of observations that contribute to the model solution and the coverage quality is written in the lower left-hand corner of each panel. Note how the very poleward and equatorward edges of the model region generally have a lower density of observations. The models are subsequently less reliable in those areas. In panels c, f, n, and v, marked with satellite icons, DMSP satellite crossings are visible as white streaks across the region as there is a high density of observations along their trajectory. Even though the observations are evenly distributed in panels u-x as reflected in the high coverage qualities, they are sparse. Brown stars mark the panels.

Time evolution

The model at 21:09 UT in Figure 5.12a shows an anti-sunward flow of plasma towards the pole at 12 MLT. The plasma flows westward (sunward) below ∼75° MLAT and eastward (anti-sunward) at higher latitudes. The convection is consistent with global convection patterns for IMF B_Y+ (see Section 2.6.1 for large-scale patterns sorted on IMF clock angle). By 21:15 UT (panel b), the convection speed has increased, with significant plasma convection around 12 MLT. The convection speed gradually decreases by 21:25 UT (panel c). A circular convection pattern starts to develop by 21:32 UT (panel d) and grows into a counter-clockwise convection cell covering most of the model region with a centre at ∼81° MLAT and ∼14 MLT. The convection cell is seen at 21:42 UT (panel e). This convection pattern is similar to the plasma drifts observed by DMSP (Figures 5.8b and c) and can be related to a northward IMF.

At 21:55 UT (Figure 5.12f), a structured convection is observed on the northeastward part of the model region at ∼80° MLAT, ∼18 MLT. The blue colour indicates a clockwise flow shear/reversal associated with a localised channel of anti-sunward flows. At 22:05 UT (panel g), these blue contours have migrated poleward to ∼82° MLAT. At ∼22:05 UT, a reconfiguration starts, and by ∼22:16 UT, the counter-clockwise convection cell is no longer visible (panel h). At this time, flows consistent with a southward IMF convection pattern are observed, with anti-sunward convection at higher latitudes, sunward convection on lower latitudes, and a reversal at ∼81° MLAT. The time of this reconfiguration coincides with the dayside brightening linked to a southward turning of the IMF described in Section 5.5 (blue arrow in Figure 5.11b). There is still evidence of the localised area of anti-sunward flow at ∼83° MLAT and 17 MLT (blue and red colour contours).

At 22:18 UT, the flows consistent with two-cell convection decrease, and sunward flows develop at higher latitudes. The signature of the enhanced anti-sunward flow persists, and by 22:26 UT (panel i), four flow reversals are seen along the eastward edge of the model region (alternating blue and red colours). At this time, the convection is mainly sunward around 12 MLT (similar to the convection in panels e-g). This sunward convection persists for >30 minutes (panels j-l), while dynamic mesoscale flow structures are observed on the southeastward part of the model region. On the northeastward part of the model region, the channel of anti-sunward flow remains.

By 23:21 UT (panel m), the pattern resembling southward IMF convection returns; sunward flow is seen at latitudes below ∼79° MLAT, and anti-sunward flows are seen at the higher latitudes. In Section 5.5, a dayside brightening was observed at this time and related to a southward turning of the IMF (blue arrow in Figure 5.11g).

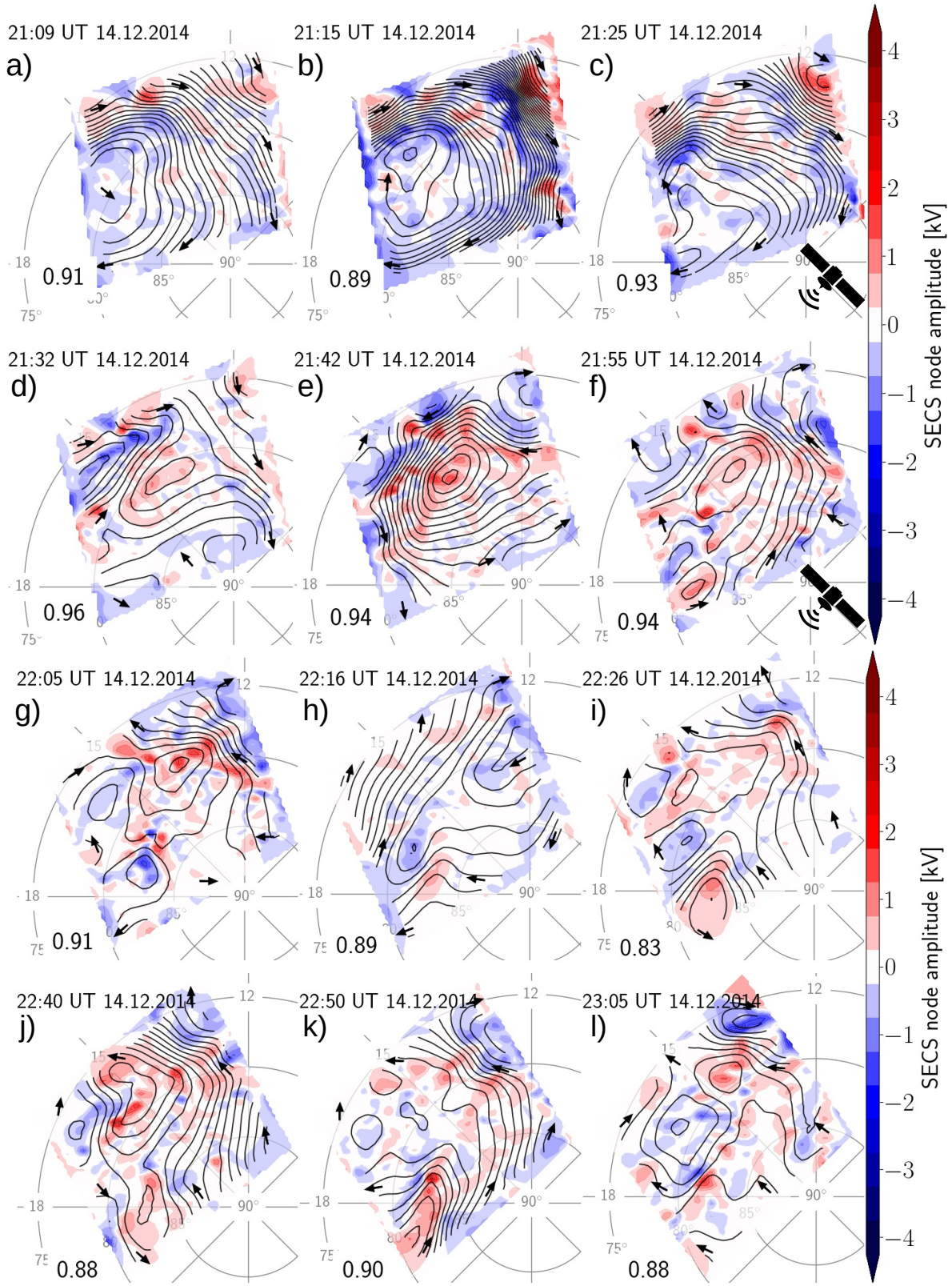

Figure 5.12: Model solution of electrostatic potential and plasma drift in a local region for a selection of times on the 14-15 December 2014 at 21:00-02:00 UT. The coverage quality for each panel is written in the lower right hand corner. Solutions marked with brown stars (panels u-x) should be treated with caution. Solutions marked with a black satellite icon are constructed with driftmeter satellite data as additional input. See text for details.

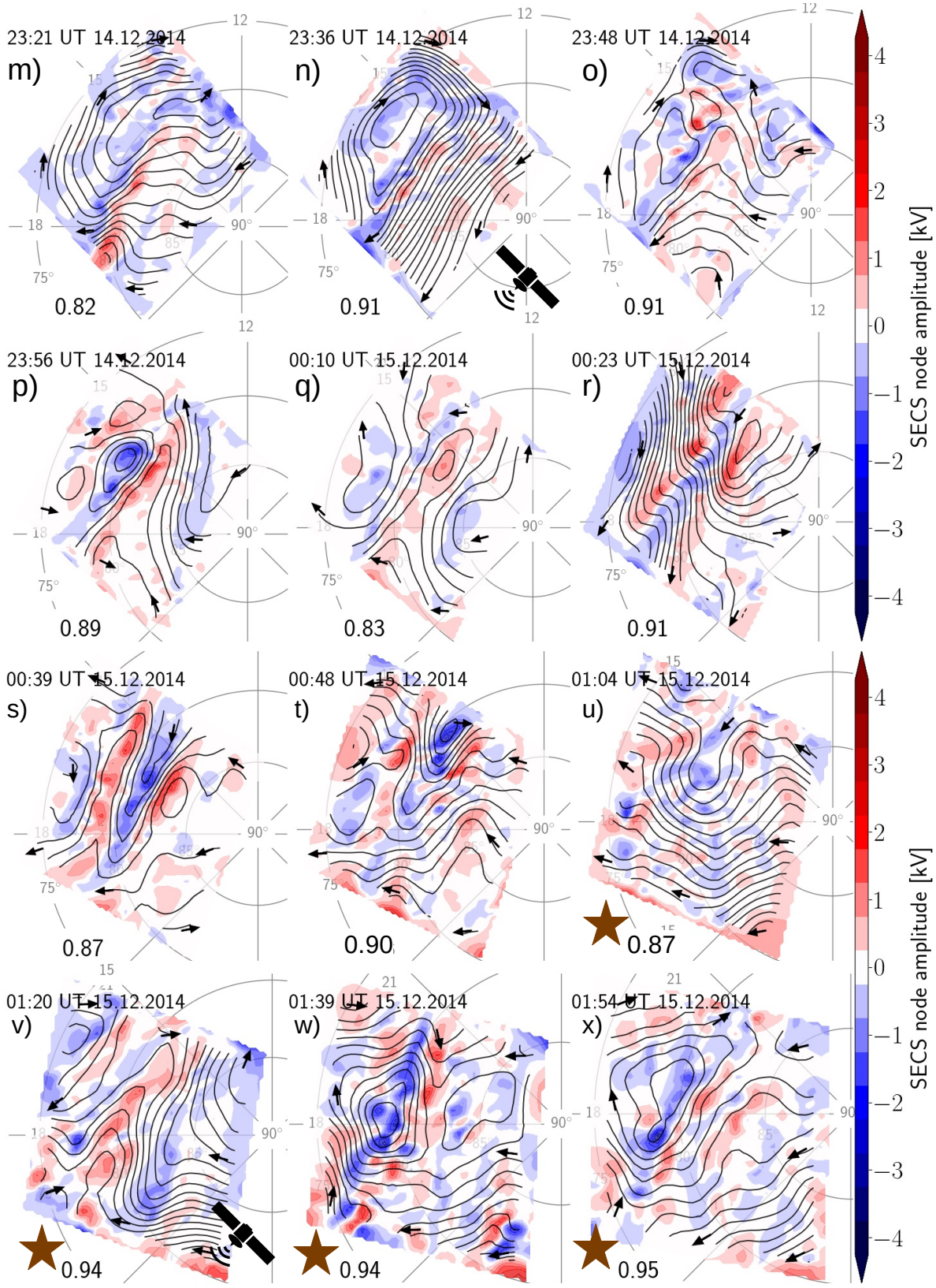

Figure 5.12: Continued.

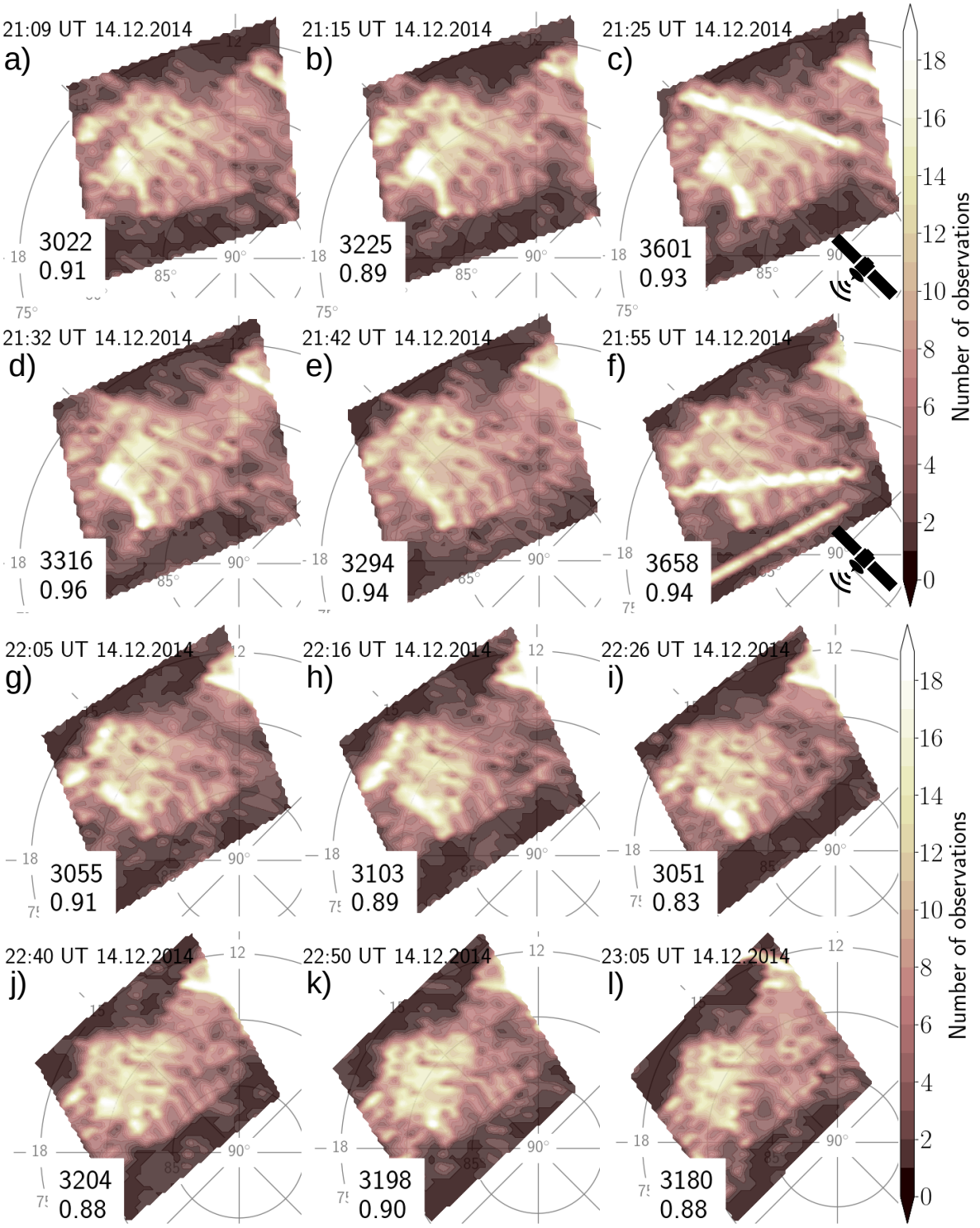

Figure 5.13: Data coverage of the model region for a selection of times on the 14-15 December 2014 at 21:00-02:00 UT corresponding to the plots in Figure 5.12. Solutions marked with brown stars have total number of observations <2800 (panels u-x). Panels marked with a black satellite icon contain driftmeter observation points from the DMSP satellites. See text for details.

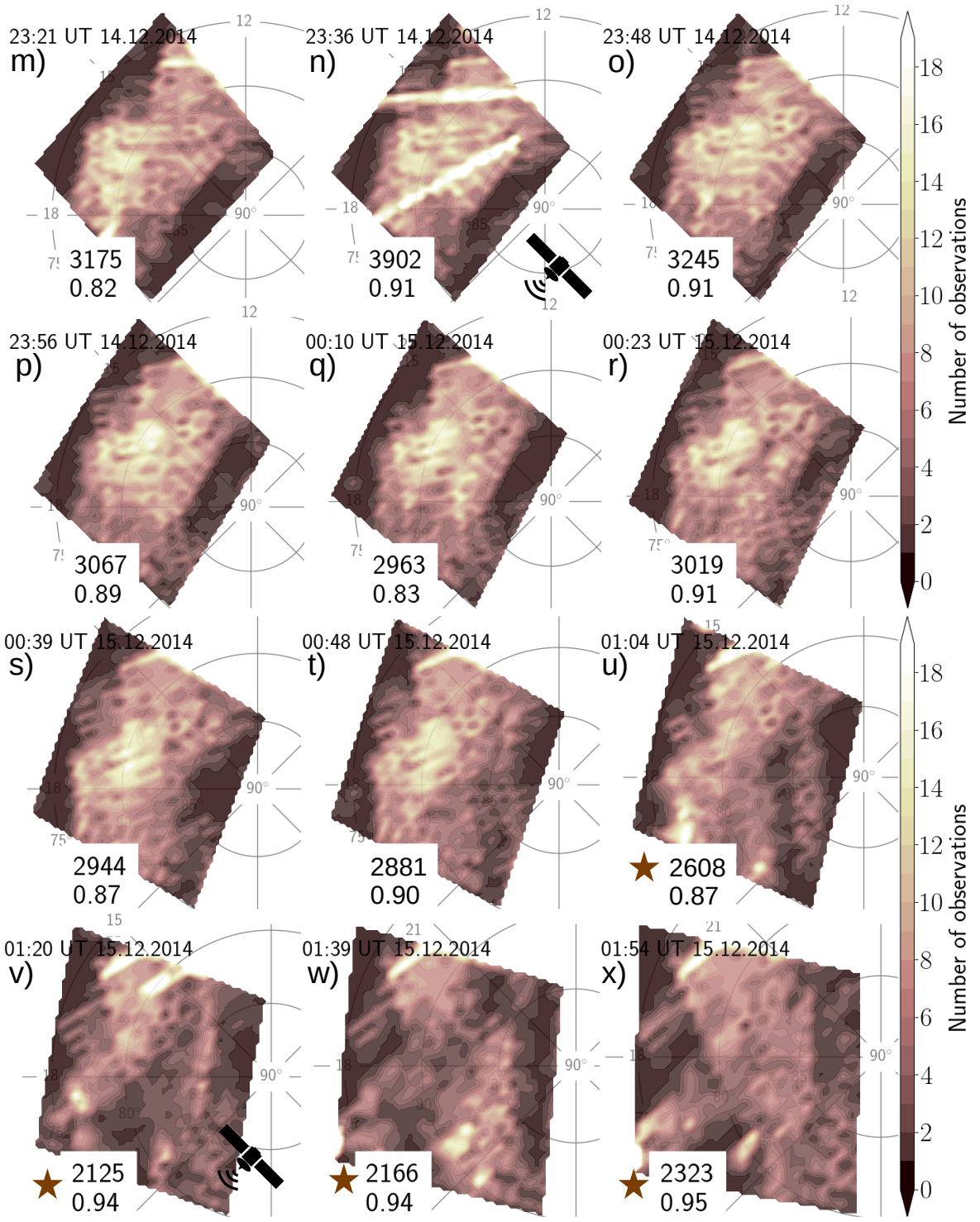

Figure 5.13: Continued.

The convection has a component in the equatorward direction, moving the region of blue contours associated with the channel anti-sunward flow slightly towards the equator. Some sunward flow is observed at higher latitudes for a brief period at ∼23:22-23:30 UT but disappears as the anti-sunward convection speeds increase by ∼23:36 UT (panel n). This coincides with the pause in the poleward migration of the PCA emissions described in Section 5.5.

Sunward convection develops on higher latitudes by ∼23:48 UT (panel o), as expected for a northward IMF orientation. Turbulent convection is observed on lower latitudes, but the anti-sunward flow channel is still observed at ∼80° MLAT. By 23:56 UT (panel p), the channel of anti-sunward flow is surrounded by two regions of convection that are generally sunward. The flow channel almost traverses the entire model region at this time. After 00:00 UT, the sunward flow at lower latitudes weakens as significant turbulent convection disrupts the flow. In general, the convection at latitudes below ∼80° MLAT turns anti-sunward (panel q). At 00:18 UT, the convection speeds increase, and the convection gets a poleward component. The channel of anti-sunward flows shifts towards higher latitudes. This movement is similar to the PCA motion described in Section 5.5, where it was associated with a B_Y polarity change. A second region of fast anti-sunward flows is seen on the equatorward edge of the model region at 00:23 UT (panel r). Sunward flows at high latitudes persist on the northwestern side of the model region.

A sunward flow starts to develop between the two fast anti-sunward flow regions at ∼00:26 UT. This time coincides with an apparent increase in PCA luminosity at ∼00:30 UT as described in Section 5.5. The multiple channels of opposing flow are clearly visible by 00:39 UT (panel s). Areas of darker reds and blues indicate strong flow shears or reversals. The poleward motion has stopped at this time, and the convection has components towards the equator again. The equatorward flows are even more prominent by 00:48 UT (panel t), though the multiple reversals from panels r and s are still seen on the westward edge of the region.

After 00:48 UT, the model solution becomes less and less reliable due to a decreasing total number of observations (marked by a brown star). Though the model solutions have large variations after 00:52 UT (panels u-x), reflecting the effect of poor coverage, a slight equatorward shift of the region of multiple flow reversals is distinguishable between 00:48 UT and 01:04 UT (panel t and panel u). This is similar to the equatorward movement of the PCA described in Section 5.5.

Summary

Table 5.2 summarises the main convection features detailed in this section. The sign of the IMF (B_X, B_Y, B_Z) components are from 5−15 minutes before the convection pattern is first observed. ACE observations are used to determine the IMF for the first row, and the entry is written in red. Periods identified as reconfiguration between large-scale patterns are not included but are generally characterised by turbulent flows.

Regional convection that resembles part of a two-cell pattern is identified for four time periods during the observation period. Each of these is associated with IMF B_Z- prior to the model time and have throughout the section been related to the auroral observations presented in Section 5.5. In between most of the two-cell time intervals, there are intervals where the regional convection is identified as part of a three/four-cell

Table 5.2: Summary of regional convection from model on 14-15 December 2014. The columns contain the model times of the convection configuration, corresponding panels in Figure 5.12, IMF (B_X, B_Y, B_Z), possible large-scale convection pattern, and number of region of opposing convection (Nr. of FC) resolved in the regional convection pattern.

UT	Figure 5.12	IMF	Convection	Nr. of FC
21:00-21:23	a, b	(-, +, -)	Two-cell	-
21:38-22:05	e, f, g	(-, +, +)	Three/four-cell (Lobe-cell)	3
22:14-22:18	h	(-, +, -)	Two-cell	1
22:26-23:05	i, j, k, l	(-, +, +)	Three/four-cell	3
23:14-23:22	m	(-, +, -)	Two-cell	1
23:31-23:42	n	(-, +, -)	Two-cell	1
23:48-00:39	o, p, q, r, s	(-, +, +)	Three/four-cell	3
00:40-02:00	t, u, v, w, x	N/A	Unclear	3 (?)

pattern. These times are characterised by sunward convection at high latitudes. However, the convection at lower latitudes and towards later MLTs is turbulent and does not entirely match the traditional patterns. A minimum of three regions of opposing convection is observed during the three/four-cell convection periods and are characterised as FC in Table 5.2. The lobe-cell convection period at 21:38-22:05 UT will be further described in Section 5.9. The convection at the very end of the observation period is included in the table for completeness, but we cannot distinguish patterns in the modelled convection with confidence due to the insufficient data coverage.

5.7 Comparison of mesoscale convection and optics

Section 5.5 and 5.6 described a similar meridional (north-south) migration of both the PCA and F-region convection structures. In this section, the ground-based images and modelled convection is used to showcase the mesoscale convection surrounding the PCA in more detail. Through five examples, we focus on identifying the PCA location with respect to zonal (east-west) flows. The examples will also show how well the regional model can resolve the turbulent convection seen in the observational data from SuperDARN.

The five examples are presented in Figures 5.14-5.18 using the following layout:

panel a shows SuperDARN fan plots of LOS Doppler-velocities. This panel has the same format as the fan plots shown in Figure 5.4, and contains an IMF clock angle dial showing observations from the 15 minutes preceding the time of the radar scan.

panel b shows a regional model solution in the same format as in Figure 5.12. Each model solution is based on four minutes of observational data starting at the *model time* written below the model region (see Section 4.5). Note that the observations in panel a are part of the input data for the model, and the all-sky image in panel d is obtained within the model time. The coverage plots corresponding to the models are given Figure 5.19 at the end of this section. They are in the same format as Figure 5.13.

panel c shows a repeat of the model in panel b. The coverage quality defined in Section 4.8.1 is written below the region. The green contour is auroral emissions with high intensities observed by the REGO imagers. The intensity threshold of the contour is different for each example, and is selected to best display PCA emissions.

panel d shows 630.0 nm all-sky images in the same format as in Figure 5.11.

Example 1 - 23:26-23:30 UT

The models in Figure 5.14 are constructed from data from 23:26-23:30 UT. Panel a depicts SuperDARN observations within this time period. There is a structure in the F-region convection that could be related to the PCA. Up to four regions of opposing flows in the zonal direction are observed, most prominently visible as alternating regions of red and blue colours in the INV fan plot. Note the channel of >500 m/s anti-sunward flow with width <100 km seen at ∼81° MLAT in both the CLY and INV fan plots. The channel is located on the equatorward side of a broader region of anti-sunward flow.

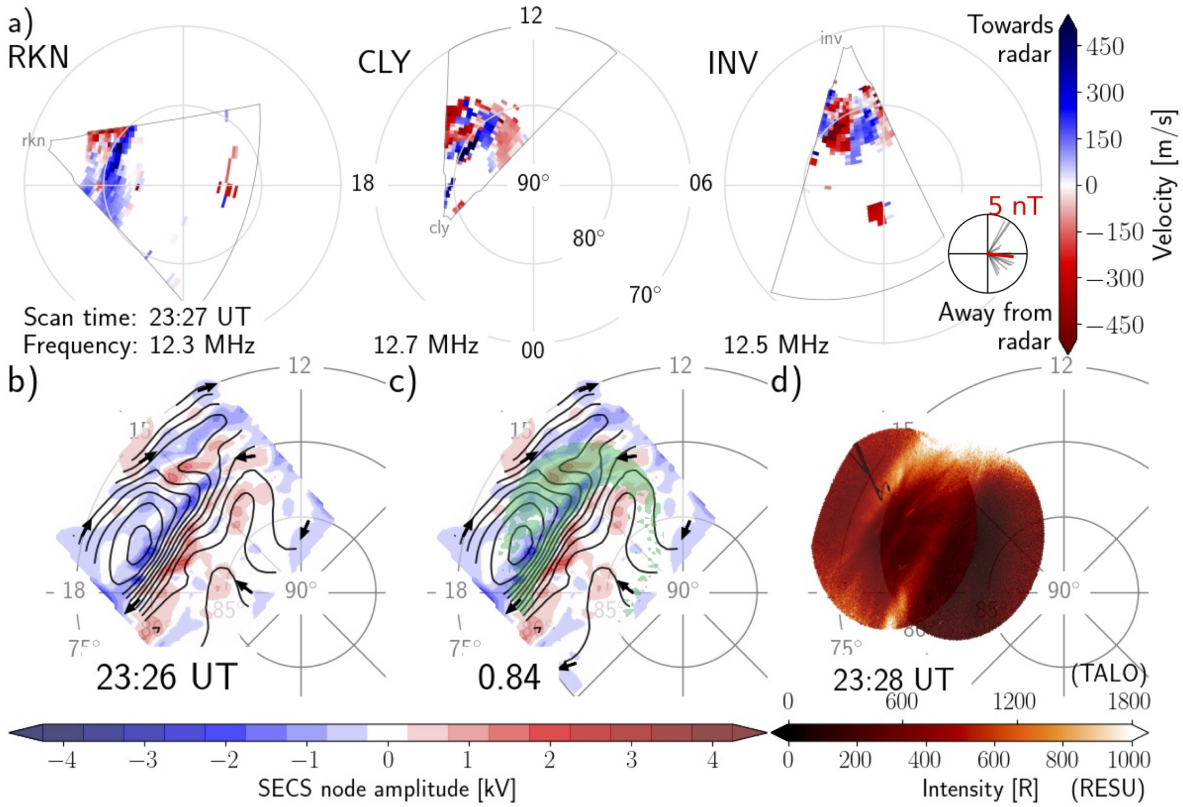

Figure 5.14: Data from 14 December 2014 at ∼23:26-23:30 UT. (a) SuperDARN fan plots for radars at Rankin Inlet (RKN), Clyde River (CLY), and Inuvik (INV) at 23:27 UT. Same format as in, e.g. Figure 5.4. (b) Model solution at 23:26-23:30 UT. See text for details. (c) Same as panel b but with a green contour on top showing red-line emissions >350 R observed by the REGO imager at Resolute Bay (RESU). The number at the bottom is the coverage quality for the model. (d) REGO all-sky images of 630.0 nm aurora at 23:28 UT from RESU and Taloyoak (TALO).

The model solution in panel b has a coverage quality of 0.84 and the corresponding Figure 5.19a shows that the total number of observations is >2800. These are good coverage conditions, and the regional model should perform well in reproducing the ionospheric convection at this time (see Section 4.8.1). We take this opportunity to discuss how to interpret the model plots compared to the more familiar SuperDARN fan plots.

In panel b, the model plot depicts the narrow anti-sunward flow channel at ∼81° MLAT as closely spaced equipotential lines (black curves). The flow reversal between the narrow anti-sunward channel and the relatively fast sunward flows on its equatorward side (observed to the left in the CLY FOV) is reflected in the blue colour contours aligned with ∼80° MLAT in the model plot. On the poleward side of the narrow anti-sunward channel, slower sunward convection is observed (seen to the right in both the CLY and INV FOVs). This shear is reflected in the red colour contours in the model plot. More substantial reversals can also be seen as kinks in the potential contours (convection streamlines). At ∼85° MLAT in the model, the contours are spaced far apart, reflecting the slower convection speed, and the magnitude of the SECS node amplitudes is small, indicating that the flow shears in the area are weak.

This comparison shows that the regional model can resolve the mesoscale convection observed by the SuperDARN radars in two dimensions. The overall convection pattern depicted by the model does not seem to fit any traditional global pattern. The model time is between two periods identified as in the two-cell category in Section 5.6. The model seems to depict part of a transition period, where the convection at high latitudes turns anti-sunward, consistent with the clock angle plot from panel a, which shows a large spread in the IMF orientation and magnitude in the 15 minutes preceding this example. The IMF turns from being strongly northward to having a southward orientation at ∼10 minutes prior to the model time.

The anti-sunward channel and the PCA emissions have the same orientation in the MLAT/MLT grid. In panel c, the PCA emissions are seen as a green contour near 80° MLAT. It is located slightly poleward of where the model shows significant clockwise flow reversal. Still, the small displacement from the predicted location can be explained by viewing geometry and smearing (see Section 3.4). The PCA is likely located within or on the equatorward side of a narrow anti-sunward flow channel.

Example 2 - 23:55-23:59 UT

In Figure 5.15, data from 23:55-23:59 UT is shown. The example is close to the time of *Example 2* in Section 5.2, and the SuperDARN fan plots in Figure 5.15a depicts the same convection structures as in Figure 5.5. We refer to Section 5.2 for a description of the SuperDARN fan plots and focus here on the convection seen in the regional model.

Strong sunward convection is observed at high latitudes in the model shown in panel b. The sunward flow is disrupted by a channel of fast anti-sunward flow a little poleward of 80° MLAT. On the equatorward side of the channel, the convection is in the sunward direction. Strong flow reversals are observed on either side of the channel, as indicated by the large magnitudes of the SECS node amplitudes most clearly seen at the centre of the model region. There is some structured flows located farther towards the southeastern area of the model region where low-velocity anti-sunward convection is observed.

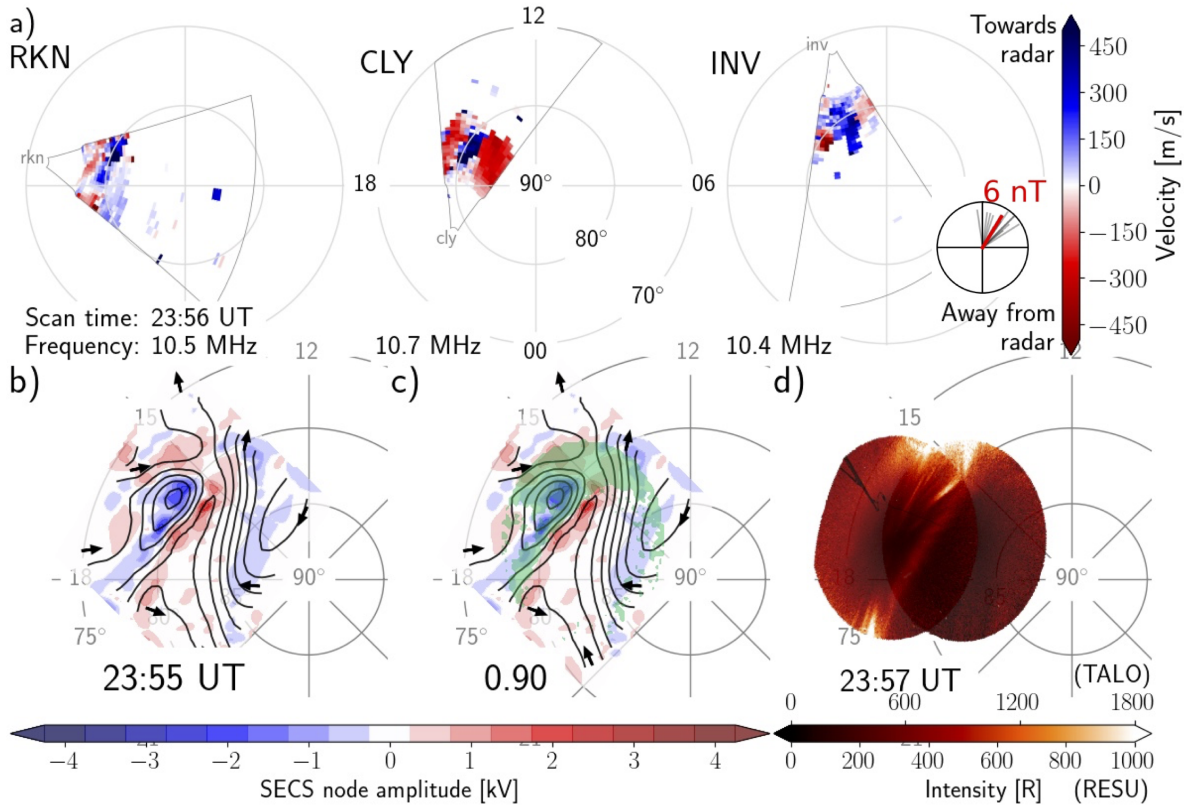

Figure 5.15: Data on 14 December 2014 at 23:55-23:59 UT. Same format as Figure 5.14. (a) Fan plots at 23:56 UT. (b) Regional model at 23:55-23:59 UT. (c) Green contour is red-line emissions >300 R observed by Resolute Bay imager. (d) All-sky images from 23:57 UT.

The IMF clock angle dial in panel a shows that the concurrent IMF was northward oriented. The sunward convection at high latitudes could fit such an IMF configuration, and the model time falls under the three/four-cell category from the overview in Section 5.6.

Panel c shows that the PCA emissions are located at ∼80° MLAT, which is at the area of the strong, clockwise flow reversal in the model. As in the previous *Example 1*, this corresponds to the PCA being located on the equatorward side of the anti-sunward flow channel.

Example 3 - 00:25-00:29 UT

Figure 5.16 depicts data from 00:25-00:29 UT. At this time, the SuperDARN observations in panel a show high-speed anti-sunward convection over a large portion of their combined FOV. The anti-sunward convection is seen at latitudes below ∼82° MLAT. The zonal flow is mainly visible in the CLY and INV fan plots, where it is clear that there is some structure within the anti-sunward convection. At ∼80° MLAT, a small area of lower velocity convection of ∼200 m/s in the same direction as the background flow is observed, separating the >500 m/s anti-sunward convection into two channels. CLY and INV fan plots also show some signs of sunward convection within the region of decreased anti-sunward flow. Sunward flow on high latitudes is observed to the right in the CLY and INV fan plots. RKN observes convection mainly in the poleward dir-

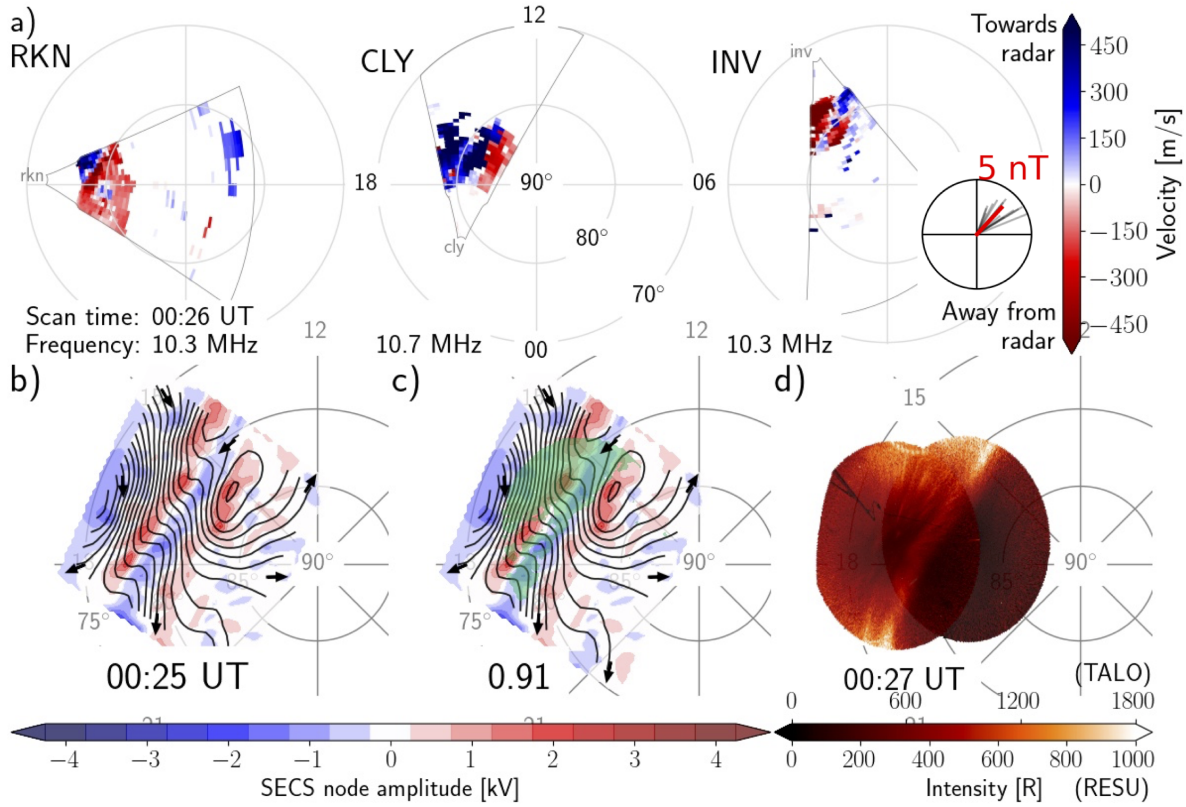

Figure 5.16: Data on 15 December 2014 at 00:25-00:29 UT. Same format as Figure 5.14. (a) Fan plots at 00:26 UT. (b) Regional model at 00:25-00:29 UT. (c) Green contour is red-line emissions >350 R observed by Resolute Bay imager. (d) All-sky images from 00:27 UT.

ection, with the strongest poleward flows observed at ∼79° MLAT. Some equatorward flows are seen close to the RKN radar site at ∼17 MLT and locally at ∼80° MLAT and 18 MLT.

The model in panel b reflects the high-speed anti-sunward convection by closely spaced contours. The shears surrounding the lower velocity anti-sunward channel at ∼80° MLAT is visible as high magnitude SECS node amplitudes (darker red and blue colour). The convection is, in general, more substantial on the equatorward side of the model region than on the poleward side. Similar to the previous *Example 2*, the sunward convection on high latitudes matches the northward orientation of the IMF shown in the clock angle dial in panel a, and falls under tge three/four-cell category in Section 5.6. The convection is, however, dominated by a poleward component and the clockwise shear at ∼80° MLAT migrates towards the north (also described in Section 5.6).

In panel c, the green PCA contours are located directly at the region of clockwise flow shear in the model. In the previous two examples, the PCA was located at a flow reversal on the equatorward side of the anti-sunward flow channel. In this example, the PCA is located at the shear between the strong anti-sunward flow channel and the slower velocity anti-sunward flow on its equatorward side.

Example 4 - 00:39-00:43 UT

In Figure 5.17, data from 00:39-00:43 UT is shown. In the 14 minutes between *Example 3* and this example, the convection has changed significantly, and a strong sunward channel now separates the two areas of anti-sunward convection. The flow channel at ∼81° MLAT is <200 km wide and has speeds of ∼900 m/s. The anti-sunward convection at lower latitudes and the sunward flow channel have speeds of ∼500 m/s. In panel a, the RKN and CLY radars see three opposing flow channels, while the INV radar is missing backscatter in the location of the anti-sunward flow channel closest to the pole. This example is close in time to *Example 3* in Section 5.2, where the SuperDARN observations are described in more detail. The sunward flow observed between the two anti-sunward channels was identified as a reversed flow channel.

The model in panel b shows the multiple flow reversals matching the radar observations. The dark colour contours traversing the model region in the zonal direction mark the high clockwise and counter-clockwise velocity reversals on either side of the reversed flow channel. The dial in panel a shows an IMF that is B_Y+ dominated, but the convection pattern showcased by the model is inconsistent with the predicted global patterns for such an IMF orientation. Still, a slight low-velocity sunward convection is observed at high latitudes near magnetic noon, and the model was included in the three/four-cell category in Section 5.6 (the same model time is shown in Figure 5.12r).

The PCA emissions have increased in intensity from the previous examples, as seen

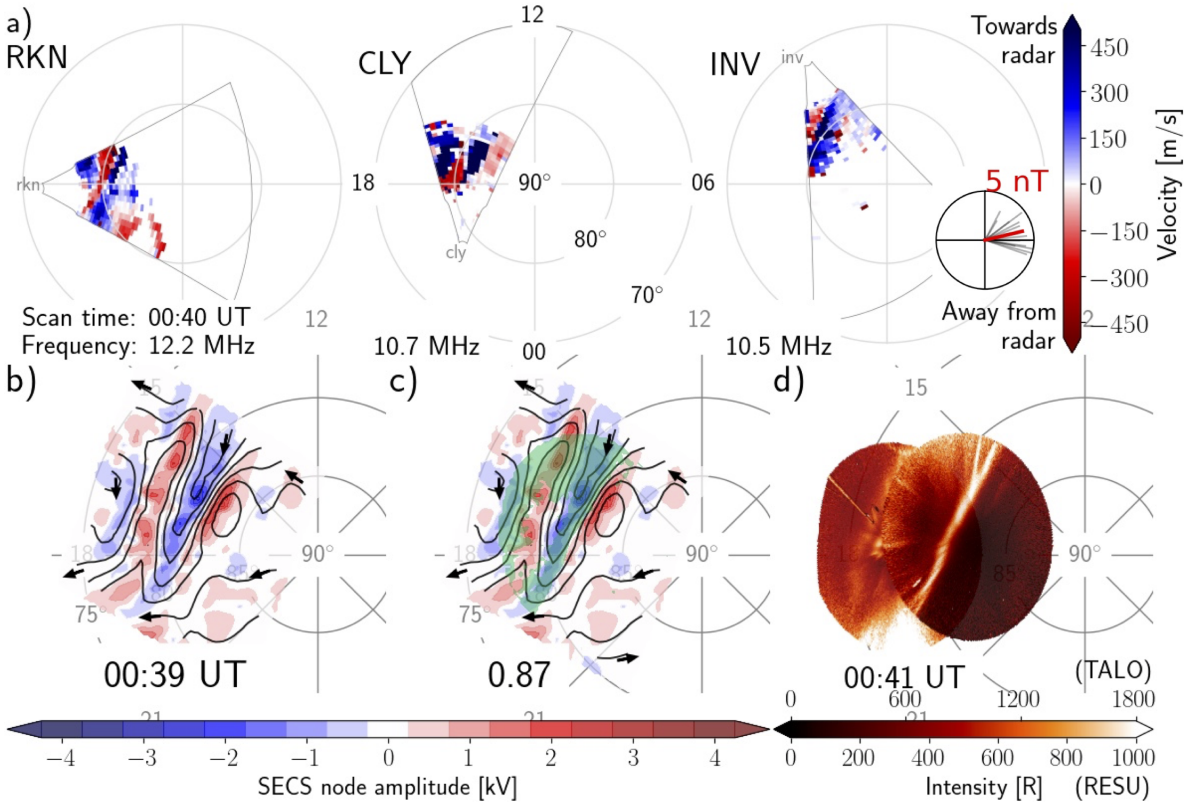

Figure 5.17: Data on 15 December 2014 at 00:39-00:43 UT. Same format as Figure 5.14. (a) Fan plots at 00:40 UT. (b) Regional model at 00:39-00:43 UT. (c) Green contour is red-line emissions >400 R observed by the Resolute Bay imager. (d) All-sky images at 00:41 UT.

in Figure 5.17d. Panel c shows that the PCA emissions are located where the model shows a distinct clockwise flow reversal at 80°−81° MLAT, at the reversal between the anti-sunward flow channel and the reversed flow channel.

Example 5 - 01:05-01:09 UT

Figure 5.18 shows data from 01:05-01:19 UT. At this time, the amount of SuperDARN backscatter is very inconsistent. Despite this, the RKN fan plot in panel a mainly shows equatorward convection speeds of ∼400 m/s. The CLY radar observes sunward flows with varying speeds on latitudes below ∼80° MLAT and anti-sunward convection on higher latitudes. The INV radar also sees a region of anti-sunward flows directly poleward of ∼80° MLAT. There is equatorward convection on the western part of the INV fan plot, though some poleward flows are still seen at lower latitudes.

The model for this time has a total number of observations <2800, and a brown star marks the model plot in panel c. From the coverage plot in Figure 5.19e, it is clear that large areas of the model region, especially in the northeast, have a low density of observations even though the coverage quality is high at 0.87. Interpreting the model plot must be done with this in mind. The model also shows a significant structure in the SECS node amplitudes that could be an artefact of the modelling technique (see Section 4.9). The model in Figure 5.18b shows significant equatorward

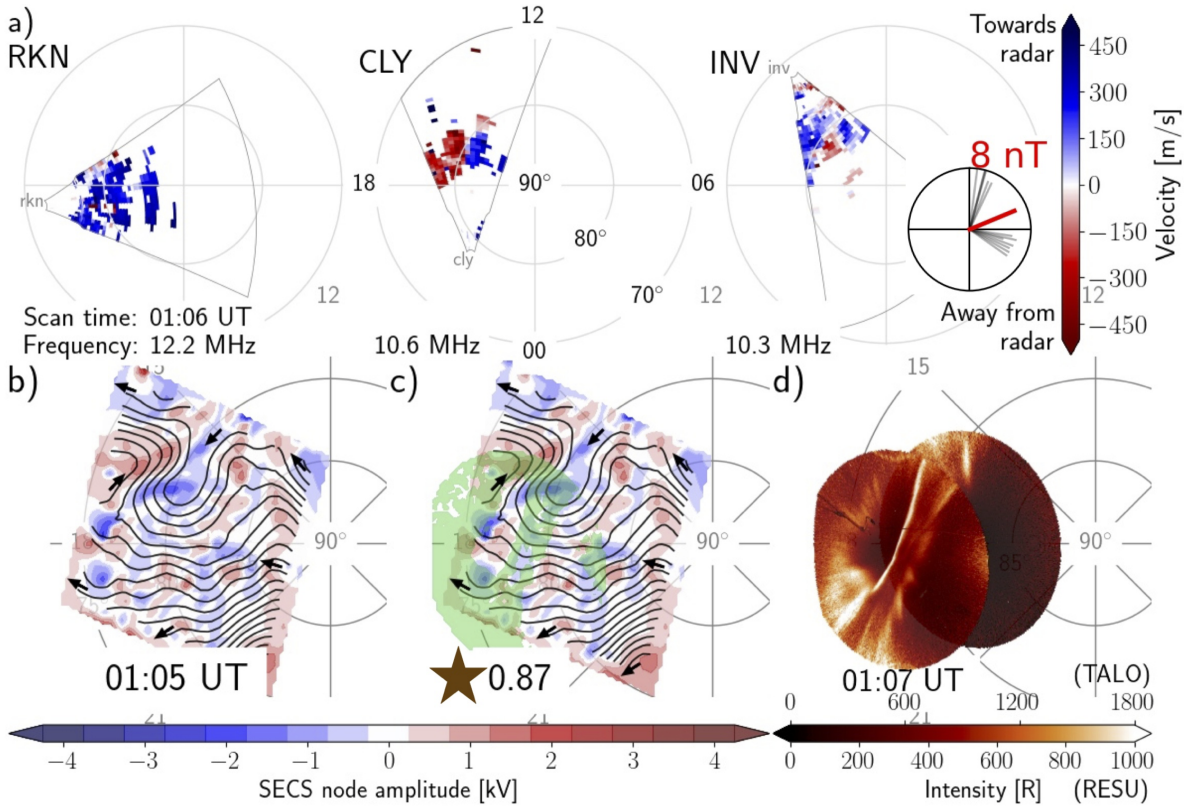

Figure 5.18: Data on 15 December 2014 at 01:05-01:09 UT. Same format as Figure 5.14. (a) Fan plots at 01:06 UT. (b) Regional model at 01:05-01:09 UT. (c) Green contour is red-line emissions >800 R observed by the Taloyoak imager. The brow star indicates <2800 observations. (d) All-sky images at 01:07 UT.

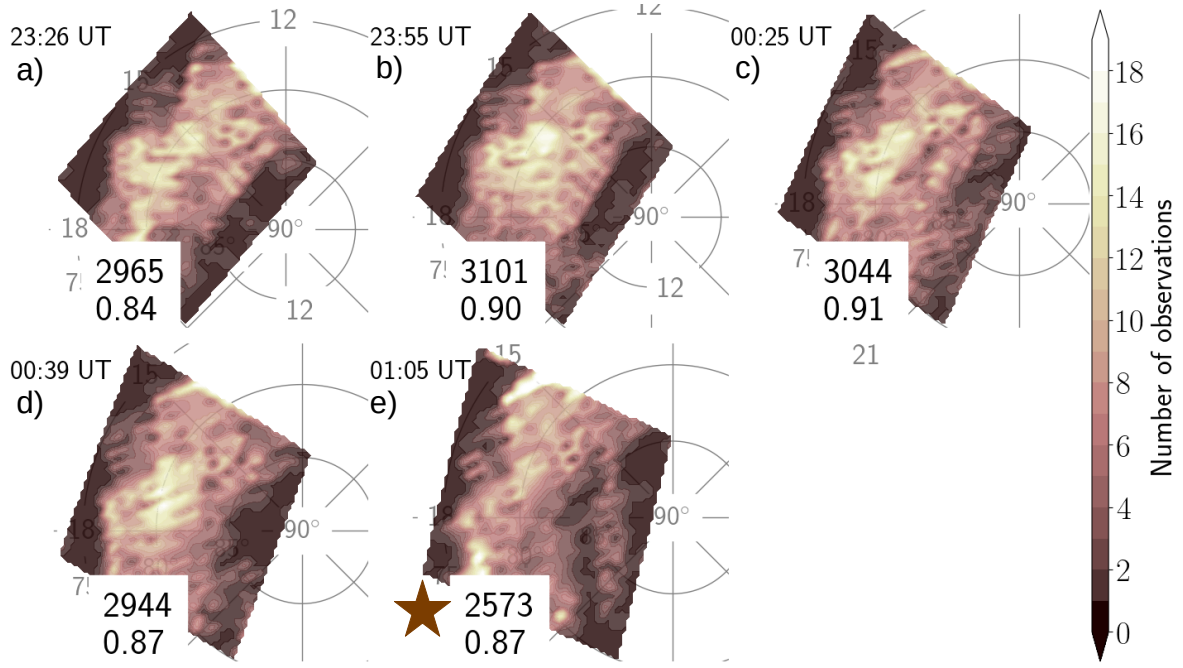

Figure 5.19: Data coverage of the model region corresponding to Figures 5.14-5.18. In the same format at Figure 5.13. (a) Coverage at model time 23:26 UT. (b) Coverage at model time 23:55 UT. (c) Coverage at model time 00:25 UT. (d) Coverage at model time 00:39 UT. (e) Coverage at model time 01:05 UT. A brown star marks the panel to indicate the low number of total observations (<2800).

convection. Zonal structure is mainly observed in the western side of the model region. The pattern reflects the distribution of LOS observations, as there is a lack of CLY and INV observations on the eastern side of the model region.

Due to the unreliability of the model, it is hard use panel c to determine the PCA location with respect to the convection. It is possible that the clockwise reversal observed on the western side of the model region would traverse the entire region if observations with a zonal component were more evenly distributed. Still, the PCA seems to be colocated with the reversal between lower latitude sunward flows and higher latitude anti-sunward flows on the eastern side of the model region. The images in panel d also show that the PCA emissions are pretty intense and that the arc form has split in two.

Summary

Overall, the model plots show mesoscale structure on scales comparable to the SuperDARN observations. The figures show examples of turbulent flows, similar to the examples presented in Section 5.2. The modelled convection patterns are generally more structured than statistical global patterns expected from the IMF orientation but some convection features are recognisable as part of a large-scale convection pattern.

Table 5.3 summarises the five examples from this section. The IMF (B_X, B_Y, B_Z), number of regions of opposing flow (Nr. of FC), and the PCA location with respect to the modelled convection is included. The PCA is generally observed towards the centre of the model region, where many observations constrain the model. Panel c in Figures 5.15-5.17 display a good correlation between the predicted location of the PCA

Table 5.3: Summary of five examples on 14-15 December 2014 showing the IMF orientation (B_X, B_Y, B_Z) prior to the examples, the number of channels of opposing convection and the location of polar auroral arc (PCA) emissions with respect to modelled shear/reversal.

	UT	**IMF**	**Nr. of FC**	**Flow shear and PCA**
1	23:26-23:30	$(-,+,0)$	4	Clockwise reversal
2	23:55-23:59	$(-,+,+)$	3	Clockwise reversal
3	00:25-00:29	$(-,+,+)$	2−3	Clockwise shear
4	00:39-00:42	$(-,+,0)$	3−4	Clockwise reversal
5	01:05-01:09	$(-,+,+)$	3 (?)	N/A

at a clockwise flow shear/reversal and the independent observations of PCA emissions in the all-sky images. All examples show the PCA as approximately located on the equatorward side of a narrow channel of anti-sunward convection.

The findings presented in this section are consistent with the driftmeter observations from DMSP F18 presented in Section 5.3. Figures 5.8b, e, and h all showed how the PCA was located at the reversal of sunward to anti-sunward flow. The DMSP observations will be revisited next.

5.8 DMSP passes over the auroral arc

When the DMSP spacecraft passes over the PCA, it observes in-situ particle precipitation associated with the auroral emissions, and ion drifts directly above the PCA. Simultaneously, FUV images are obtained. In this section, these space-based observations are used to study the PCA and surrounding ionospheric convection in more detail, and the regional model is compared to the FUV images.

The DMSP F18 spacecraft passes directly over the PCA at ∼21:55 UT, ∼23:37 UT, and ∼01:19 UT. The F16 and F17 spacecraft do not have any clear passes over the PCA. Observations during the DMSP F18 passes are presented in Figures 5.20-5.22. The figures all share the same layout:

panel a is a close up of the dusk-side region of the DMSP F18 FUV images from Figure 5.7. The spacecraft trajectory is shown as a dotted line with time stamps. An IMF clock angle dial is included at the bottom, and shows values from when the F18 trajectory is above 70° MLAT and the preceding 15 minutes. The red arrow and number is the mean clock angle and transverse component magnitude, B_T.

panel b shows the electron energy-versus-time spectrogram for the northern hemisphere pass. The y-axis shows the particle energies in electron volts (eV), and the colour scale shows the particle energy flux. The spectrograms are downloaded from the JHU/APL website (see Section 3.3.2).

panel c shows the same as panel b, but for precipitating ions.

panel d shows the horizontal cross-track ion drifts. Positive (negative) values is plasma flow in the sunward (anti-sunward) direction, i.e. observations to the left (right)

of the dusk to dawn spacecraft trajectory. The ion drift observations are the same as presented in Section 5.3.

panel e shows a close up of the two minute time period inside the dashed box in panel b. During this two minute interval the satellite passes over the PCA.

panel f shows a close up of the two minute time period inside the dashed box in panel c.

panel g shows a close up of the two minute time period inside the dashed box in panel d.

panel h shows the modelled convection surrounding the PCA. The model plot is in the same format as the panels in Figure 5.12, and the corresponding coverage plots are marked by a black satellite symbols in Figure 5.13 (panels f, n and v). The SSUSI FUV image is the same as in panel a, shown with a grey to black colour scale.

Pass 1 - DMSP F18 at 21:51-22:06 UT

Data from the DMSP F18 pass at ∼21:57 UT is presented in Figure 5.20. The spacecraft passes from dusk to dawn over the northern hemisphere and crosses through two regions of diffuse auroral emissions. The dusk and dawn precipitation regions are separated by an interval of low energy fluxes in the PC, as seen in panels b and c. The image in panel a shows that the spacecraft passes over PCA emissions at ∼21:55-21:56 UT. Directly under the spacecraft trajectory, the PCA FUV emission intensity is ∼150 R, comparable to the main oval emission intensities.

The spectrograms in panels e and f show a region of enhanced electron energy flux centred at ∼21:55:10 UT. This precipitation is likely the cause of the PCA emissions, and some ion precipitation is also observed. Poleward of the PCA precipitation are two similar areas of enhanced, although a little weaker, electron energy flux centred at ∼21:55:30 UT and ∼21:55:50 UT. Although the PCA appears detached from the dusk-side auroral oval in the FUV images, the PCA precipitation signature is not clearly separated from the rest of the dusk-side precipitation.

The characteristics of the particle precipitation can be applied to determine a magnetospheric source region for the precipitation. The dayside automated identifications in the JHU/APL database (see Section 3.3.2) classifies the precipitation over the PCA at this time as having boundary plasma sheet (*BPS*) origin, shown by a red bar on top of panel e. The BPS precipitation region starts at ∼70° MLAT, and the precipitation observed further equatorward is classified as central plasma sheet (*CPS*). The region of enhanced energy flux observed at ∼21:55:50 UT is *unclassified*, and the low energy fluxes further poleward are identified as *void*.

The electron precipitation associated with the PCA resembles an inverted-V (see Section 2.7.1), though the precipitation characteristics are somewhat ambiguous. The enhanced electron fluxes are seen in a monoenergetic band that increases to a peak and subsequently decreases as the satellite passes through it. Average electron energies over the PCA are ∼300 eV, but the enhanced energy fluxes are seen in the $0.1-1$ keV range. In contrast to the more intense precipitation over the PCA, the precipitation equatorward of the region in the dashed box in panel b generally has low electron energy fluxes distributed over a broad energy range.

Panels e-g show that the PCA precipitation is located in a region where the sunward convection speeds decrease from a peak of 650 m/s. There is a flow reversal at ∼78° MLAT before the satellite enters a region of anti-sunward ∼100 m/s cross-track ion drifts. In the region of PCA precipitation, the cross-track velocity changes $\Delta \mathbf{v} = 570$ m/s over a distance of ∼50 km, and the cross-track velocity shear (vorticity) is ∼0.011 s^{-1}. The two small regions of enhanced precipitation on the poleward side of the PCA precipitation are located within the region of anti-sunward flow, in locations where decreased convection speeds are observed. The negative slope of the graph in panel g corresponds to a clockwise flow shear/reversal.

In panel h, the modelled convection surrounding the PCA is presented. The model time is 21:55 UT, matching the timing of the DMSP pass over the model region. As described in Section 5.6 (Figure 5.12f), the modelled convection resembles a lobe cell and is consistent with a northward IMF orientation. The clock angle dial in panel a shows an IMF that is B_Y+ dominated. On average, IMF had a slight northward orientation, with $\theta_{CA} \approx 64°$ and $B_T = 6$ nT. The red arrow in panel h indicates where the PCA seen in the FUV image enters the model region. The location corresponds to a modelled clockwise flow shear (blue contours) at ∼80° MLAT.

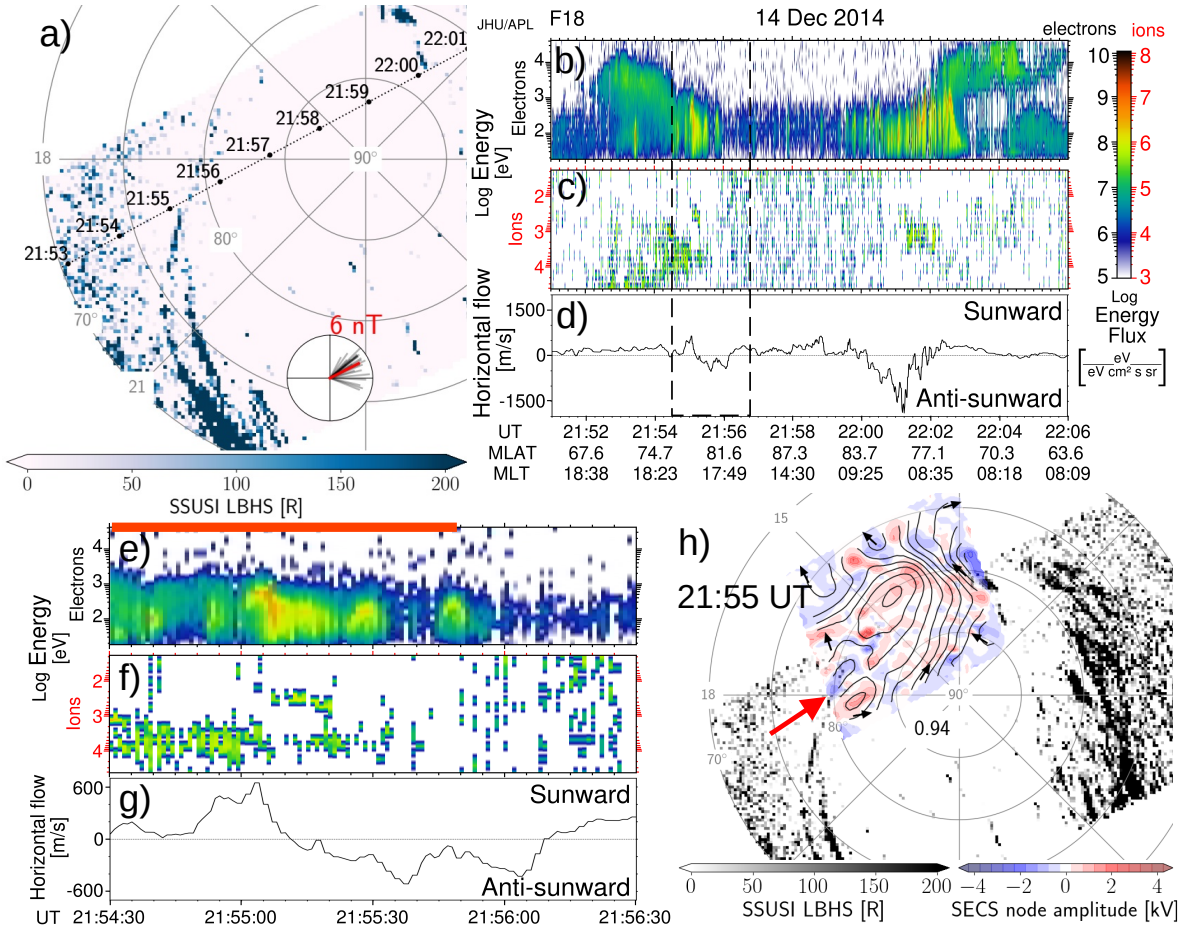

Figure 5.20: Observations from the DMSP F18 spacecraft over the northern hemisphere on 14 December 2014 at 21:51-22:06 UT. See text for details. The coverage plot in Figure 5.13f corresponds to the the model in panel h.

Pass 2 - DMSP F18 at 23:33-23:45 UT

Data from the second DMSP F18 pass is shown in Figure 5.21. Panel a shows that the spacecraft passes over the PCA emissions at ∼23:37-23:38 UT. The PCA LBHS emission intensities below the satellite trajectory are ∼150 R, comparable to the main oval intensities. Similar to *Pass 1*, panels b and c show that a region of low energy flux separates the dusk and dawn precipitation regions. There is generally more ion precipitation observed in the two main precipitation regions during this pass than for *Pass 1*.

The spectrograms in panels e and f show a relatively wide region of enhanced electron energy flux centred at ∼23:37:10 UT, which is associated with the PCA. Its width can be attributed to the spacecraft passing over the PCA at an angle and thus spending more time observing the PCA precipitation. Very little ion precipitation is observed over the PCA. The electron precipitation over the PCA has a less ambiguous inverted-V signature than observed in *Pass 1*. The electron precipitation is concentrated in a monoenergetic beam, though the electron energies are low at ∼200 eV. The inverted-V energy is slightly higher than the average electron energy over the PCA, which is 170 eV.

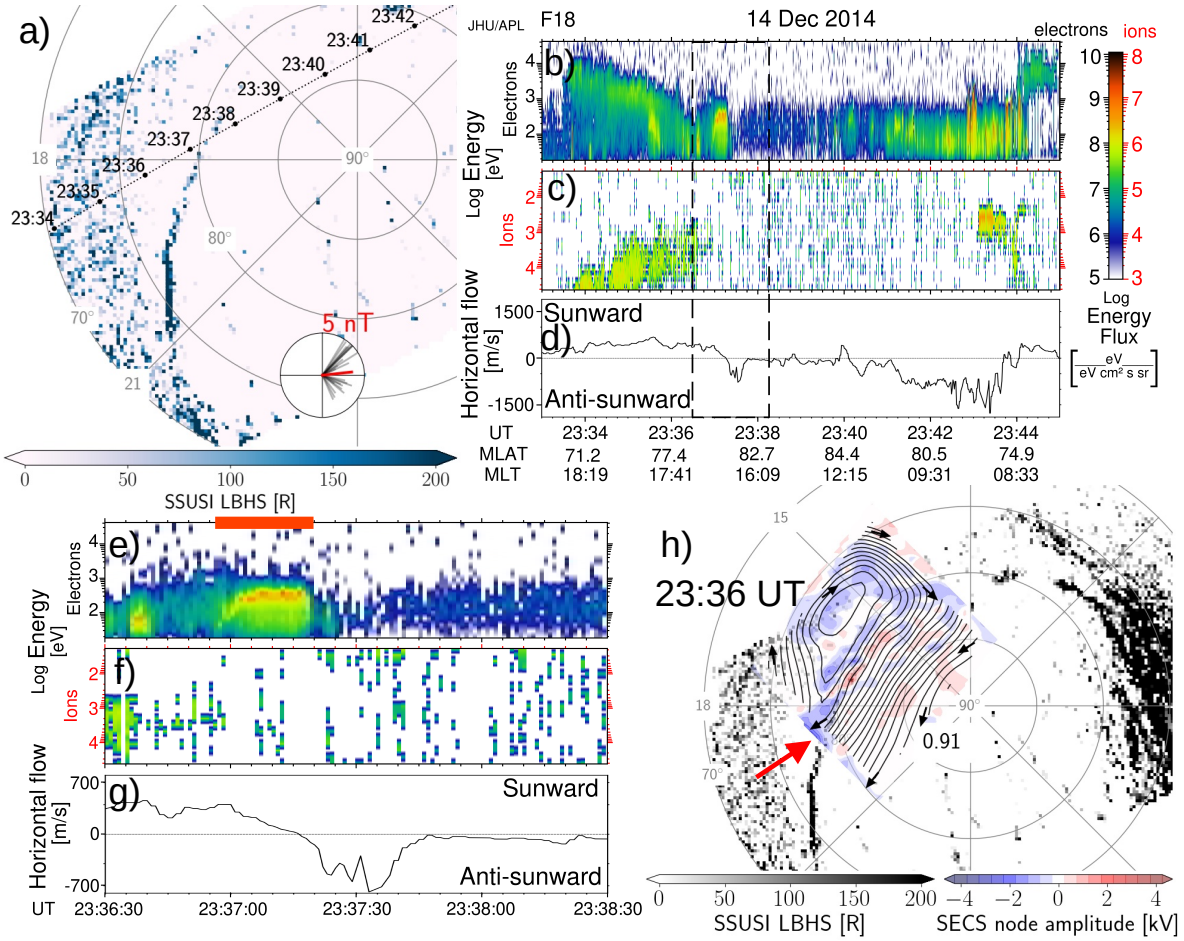

Figure 5.21: Same format as Figure 5.20, but for 14 December 2014 at 23:33-23:45 UT. The coverage plot in Figure 5.13n corresponds to the the model in panel h.

Similar to *Pass 1*, the particle data shows that the PCA precipitation is not entirely detached from the rest of the dusk-side precipitation. As seen from the red bar at the top of panel e, the PCA precipitation is identified as *BPS*. There is also a region of BPS precipitation further towards the equator, but a small area of *unclassified* precipitation separates the two BPS regions. On the immediate poleward side of the PCA, the precipitation is identified as *void*.

Panels e-g show that the PCA precipitation is on the equatorward side of a convection reversal in the cross-track ion drifts. The PCA precipitation is located in a region where sunward convection decreases from a local peak of ∼400 m/s. The flow reversal is observed at ∼80° MLAT, slightly further poleward than observed for *Pass 1*. The anti-sunward convection seen poleward of the reversal also has slightly higher velocities at ∼700 m/s, and fast anti-sunward flow is concentrated over a narrow area of ∼200 km. At the region of PCA precipitation, $\Delta \mathbf{v} \approx 550$ m/s over a distance of ∼150 km, and the cross-track velocity shear is low at ∼0.0037 s^{-1}.

The arrow in panel h shows that the PCA observed by SSUSI enters the model region in an area of clockwise flow shear/reversal (blue colour contours). The modelled convection speeds are overall high, and the pattern does not show too much structure. The model was categorised as two-cell in Section 5.6 but as discussed in *Example 1* (∼23:26 UT) in Section 5.7, the ionospheric convection likely reflects a transition period. There is a large spread in both clock angles and B_T during the pass. The average IMF during the pass was $\theta_{\mathrm{CA}} \approx 84°$ and $B_T = 5$ nT.

Pass 3 - DMSP F18 at 01:15-01:27 UT

The third DMSP pass over the PCA is presented in Figure 5.22. The figure shows significant differences between this pass en the previous two northern hemisphere passes. Panel a shows that the FUV emissions are overall more intense. The spacecraft passes over the PCA at ∼01:19-01:20 UT, and the PCA emission intensity below the spacecraft trajectory is >700 R. These are strong emissions compared to the main oval emissions at ∼400 R. Overall, higher energy fluxes in the precipitation are observed, as can be seen in panels b and c. Still, the energies of the precipitating particles are in the same range as for *Pass 1* and *Pass 2*.

Panel e shows a narrow region of high electron energy flux centred at 01:19:10 UT that corresponds to the location of the PCA emissions. Significant ion precipitation is observed on the poleward side of the enhanced electron precipitation. The precipitation resembles inverted-V, but enhanced energy fluxes at lower characteristic energies are also observed. The PCA precipitation has the most substantial electron energy fluxes in a narrow energy range around 1 keV, but the average electron precipitation energy above the PCA is 500 eV.

Over the PCA, the precipitation is identified as *BPS*, indicated by the red bar on top of panel e. On its equatorward side, the precipitation is classified as *void*, i.e. no significant precipitation, and the PCA is separate from the broad dusk-side region of precipitation (classified as low latitude boundary layer and BPS). The precipitation on the poleward side of the BPS classification is *unclassified* but the electron precipitation observed after 01:20 UT is classified as *polar rain*.

The first dusk-side reversal from sunward to anti-sunward convection is observed by the spacecraft at ∼76° MLAT. Close to the PCA, a channel of ∼1500 m/s sunward

convection is observed as embedded in the region of anti-sunward flows, similar to the convection seen in *Example 4* in Section 5.7. Panels e-g show that the PCA precipitation is observed on the poleward edge of the sunward channel, where the sunward convection speeds are rapidly decreasing. The PCA flow reversal is at ∼78° MLAT, on lower latitudes than during *Pass 2*. On the poleward side of the reversal, ∼350 m/s anti-sunward convection is observed. Across the region of PCA precipitation, $\Delta\mathbf{v}$ ≈1500 m/s over ∼45 km, and the shear in the cross-track ion drifts is ∼0.033 s^{-1}. The strong electron energy fluxes over the PCA are consistent with the large flow shear.

The regional model at 01:20 UT is shown in panel h for completeness, but the model should not be trusted and is marked with a brown star. The corresponding coverage plot in Figure 5.13v shows a low density of observations across the model region and a low number of total observations. The IMF clock angle dial in panel a shows a strongly northward oriented IMF, with the average values $\theta_{CA} \approx 34°$ and $B_T = 8$ nT. Sunward convection on high latitudes is expected from such an orientation (see Section 2.6.1).

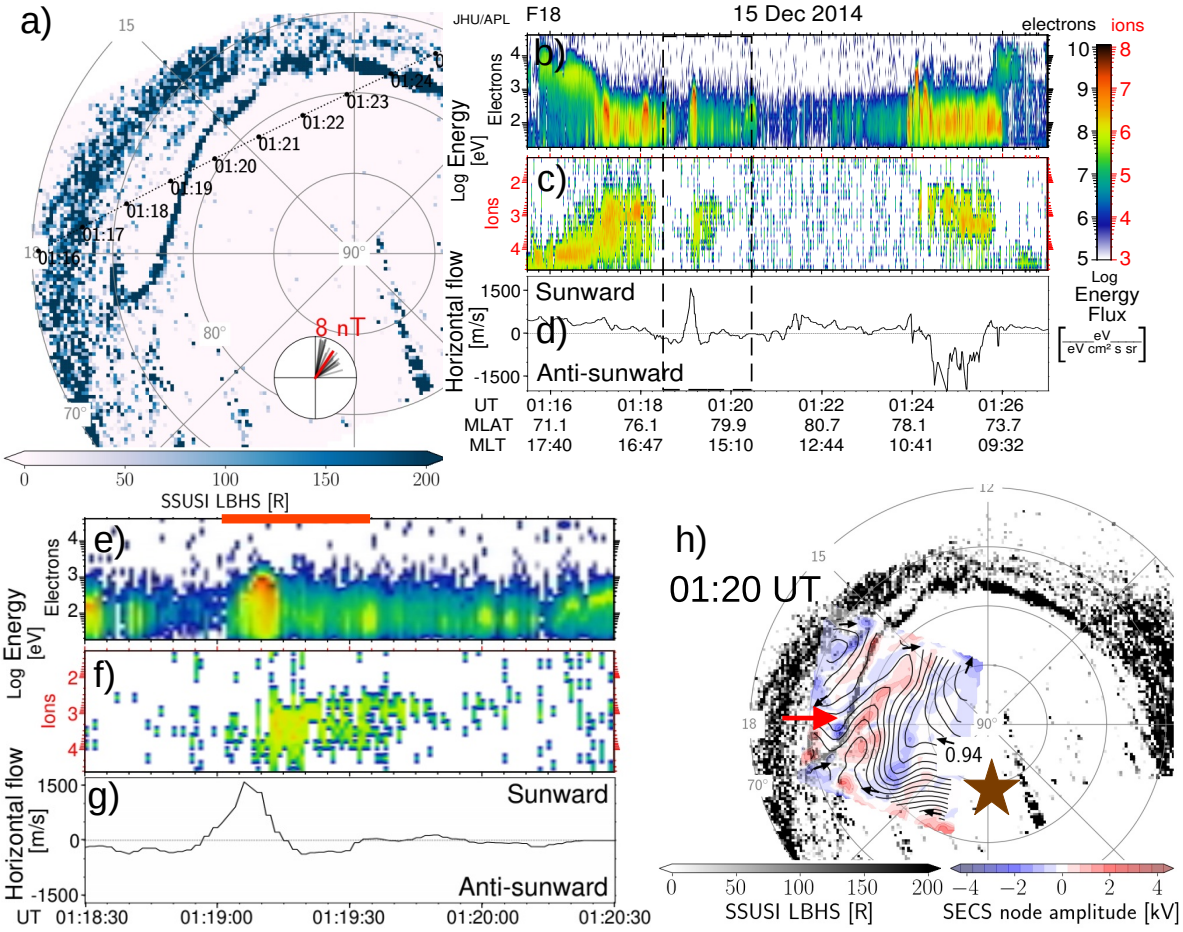

Figure 5.22: Same format as Figure 5.20, but for 15 December 2014 at 01:15:30-01:27:00 UT. The regional model in panel h is for 01:20 UT with corresponding coverage plot given in Figure 5.13v. This model should be treated with caution and is marked by a brown star.

Summary

Table 5.4 summarises some of the main PCA features for each pass. The PCA precipitation is consistently classified as BPS and the electron precipitation resembles inverted-Vs. *Pass 3* stands out as the PCA precipitation has higher electron energy fluxes and is separated from the rest of the dusk-side precipitation. Both PCA emission intensity and cross-track shear is higher for this pass.

Table 5.4: Table summarising the DMSP F18 observations of a polar cap arc from the northern hemisphere passes on 14-15 December 2014 at 21:57 UT, 23:39 UT, and 01:21 UT.

DMSP F18 northern hemisphere	**Pass 1**	**Pass 2**	**Pass 3**
Time over PCA	21:55:10 UT	23:37:10 UT	01:19:10 UT
Average electron energy over PCA	310 eV	170 eV	500 eV
Maximum energy over PCA	1 keV	200 eV	1 keV
Inverted-V	Possibly	Yes	Possibly
Identified source region	BPS	BPS	BPS
Separation from main oval	No	Unclear	Yes
PCA emission intensity (LBHS)	∼150 R	∼150 R	>700 R
DMSP cross-track shear, $\Delta\mathbf{v}/\Delta x$	0.011 s^{-1}	0.0037 s^{-1}	0.033 s^{-1}

Overall, the Figures 5.20-5.22 show a correlation between negative slopes in the horizontal ion convection (clockwise flow shears/reversals) and enhanced precipitation related to the PCA. The PCA precipitation is located on the equatorward side of an anti-sunward flow, in a region where sunward convection speeds are falling off (equatorward of a flow reversal). In Figures 5.20h and 5.21h, the PCA FUV emissions coincide with regions of clockwise shears/reversals in the regional model, though this is not as clear for the model in *Pass 3*.

5.9 Time response of the ionospheric convection to a northward turning

Before summarising the observations and model results, the lobe-cell pattern observed at the start of the observation period is investigated. The time series in Section 5.6 (Figures 5.12a-f) showed a reconfiguration of the ionospheric convection from local convection consistent with a B_Y+ two-cell pattern to convection consistent with a four-cell morphology (a lobe cell is observed within the model region; see Section 2.6.1). The model allows for determination of the time response of the ionosphere to a northward turning of the IMF.

Three regional models depicting the change in convection are presented in the left-hand column of Figure 5.23 (panels a, c, and e). They are in the same format as Figure 5.12 (1 kV contour intervals), but without the colour contours for SECS node amplitudes. The model time is written on top of the panels. The orange markers indicate the location of the maximum and minimum potential values, and the maximum potential difference, $\Delta\Phi$, is written in the lower left-hand corner. Panel e shows an example where $\Delta\Phi$ is measured across the lobe cell. The IMF clock angle is presented

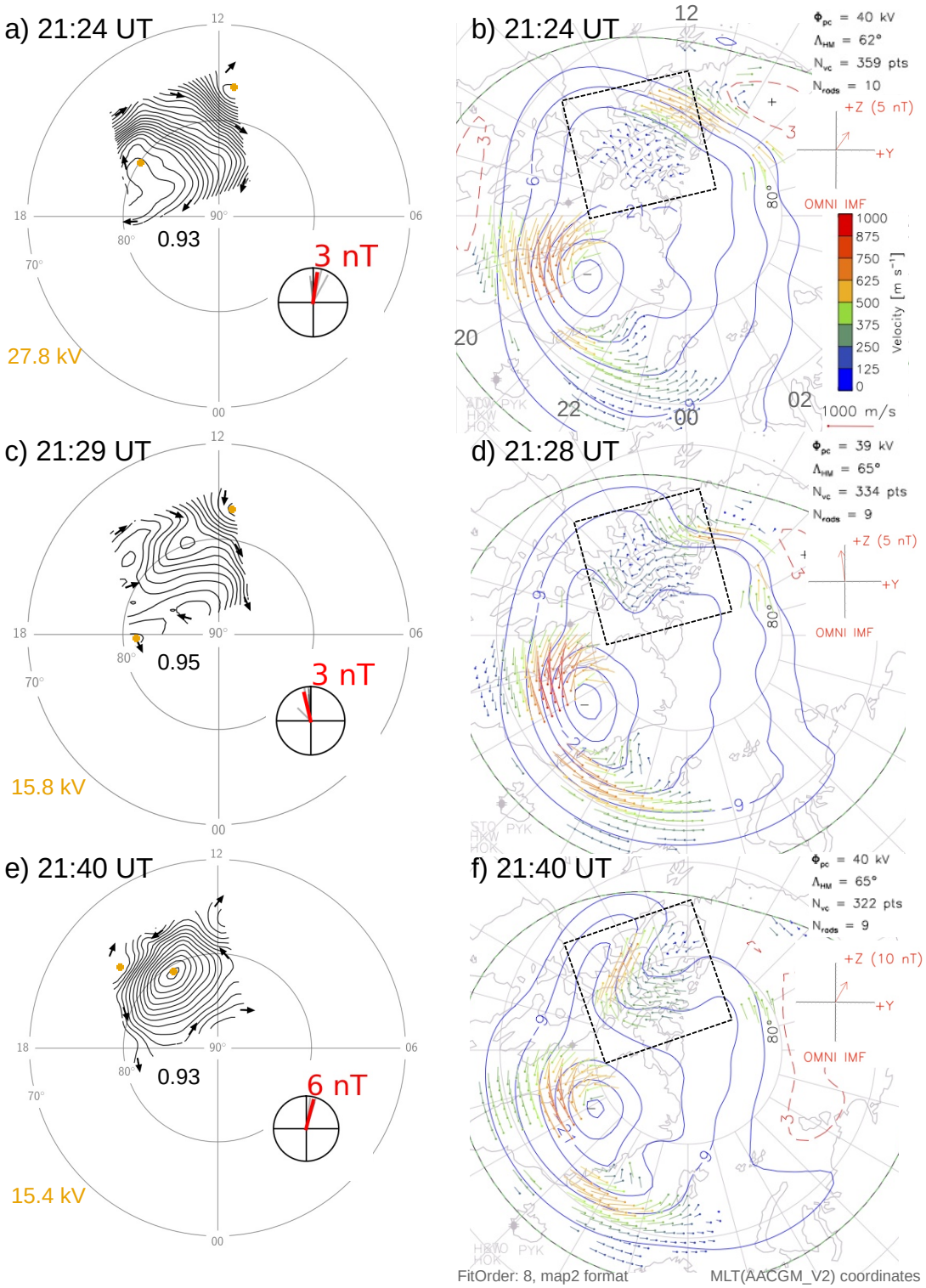

Figure 5.23: Selected times showing the ionospheric response to a northward turning of the IMF on 14 December 2014. (a, c and e) Regional models with the same format as in Figure 5.12, but without the SECS node amplitude colour contours. The orange crosses are the locations of maximum and minimum electric potential, and the text is the difference between the two. The dial at the bottom shows the IMF clock angle and magnitude of the IMF transverse component observed from Geotail. (b, d and f) Map potential plots for the selected times. The black dashed square is the location of the corresponding model region. See text for details.

in the dial to the lower right of the model region. The grey arrows are all values observed during the 10−15 minutes before the model time, and the red arrow is the mean value.

The right-hand column of Figure 5.23 shows map potential plots for times corresponding to the regional models. The map potential plots have the same format as seen in Section 5.2 (e.g. Figure 5.4a), but the potential contours are not filled. The map potentials have contour intervals of 6 kV. The MLT sectors and scale of the fitted velocity vectors are included in panel b, and model information is given in each panel's top right-hand corner. A dashed square marks the model region from the corresponding left-hand panel.

The regional model shows a change in the two-cell B_Y+ convection pattern starting at ∼21:23 UT (Figure 5.23a). The reconfiguration starts with a decrease in the convection speed before the direction of convection changes. The directional change is first seen at around 80° MLAT and 13 MLT. At 21:29 UT, a small vortex of reverse convection is seen (Figure 5.23c). By ∼21:38 UT, the lobe cell covers nearly the entire modelling region as shown in Figure 5.23e. The entire reconfiguration takes ∼15 minutes, after which the lobe cell is observed for ∼27 minutes before the model shows signs of a new change at ∼22:05 UT.

The corresponding map potential plots in panels b, d, and f show a similar reconfiguration. The potential contours in the map potential plots are spaced further apart, and the circulation is not as easily discernible as in the regional models. The responses are also seen slightly later in the map potential plots than in our regional model. Note that the map potential plots include predictions from the *Thomas and Shepherd* (2018) statistical model to construct the convection patterns and use solar wind data as input. The implications of this will be discussed in Section 6.2.

The IMF clock angle during the time interval 21:00-22:30 UT is shown in Figure 5.24. The grey lines correspond to the model times shown in Figure 5.23. Figure 5.24a shows ACE observations (orange) and panel b shows Geotail observations (blue). Southward IMF ($|\theta_{\mathrm{CA}}| > 90°$) is indicated by shading. The IMF B_Y is generally positive. Panel c shows the $\Delta\Phi$ across the model region for the same time interval. Panels a and b have a blue shading in the period 21:23-22:05 UT when the model first showed evidence of change towards a lobe-cell pattern to when signs of a new change were seen. The light orange shading in Panel c at 21:34-22:08 UT indicates where $\Delta\Phi$ is measured across the lobe cell (i.e. between a point at the centre of the lobe cell and some location on the edge of the model region). It is a measure of the strength of the lobe-cell convection. Note that the values outside the orange shading are the potential differences between other locations in the model region and do not measure the strength of the lobe-cell convection.

The response of the modelled ionospheric convection matches the sharp northward IMF turning seen in the Geotail data at 21:10 UT. Although ACE also observes a slow northward turning where $|\theta_{\mathrm{CA}}| > 90°$ after 21:05 UT, the ionospheric response is abrupt, something that is likely more consistent with the sudden IMF polarity change observed by Geotail. The change towards a lobe-cell convection (the blue shaded region) is detected at the model time ∼13 minutes after Geotail observes a northward IMF turning. The modelled convection starts to change away from the lobe-cell pattern (end of the blue shaded region) at the model time 6 minutes after Geotail observes a southward IMF turning at 21:59 UT.

A red arrow in Figure 5.24 links a period strongly southward IMF observed from Geotail at ∼21:08 UT to a local maxima in $\Delta\Phi$ at ∼21:18 UT (10 minutes delay) which could be the ionospheric response to an increased coupling on the dayside (subsolar reconnection). Geotail observes a rapid increase in B_T from 2−8 nT at 21:21 UT (note the difference between the clock angle dials in Figures 5.23c and e). After this, some slight fluctuations in B_T are observed, though the orientation of the IMF remains northward. The variations in IMF B_T could be related to the fluctuation in the $\Delta\Phi$ across the lobe cell (orange shaded region in Figure 5.24c). It is, however, possible that the variations are due to slight differences in the accuracy of the modelling method. Another red arrow connects the southward IMF turning at 21:59 UT to an increased $\Delta\Phi$ at ∼22:13 UT (13 minutes delay). This peak is seen after the lobe-cell convection has ceased, and the model shows sunward convection at lower latitudes and anti-sunward convection at higher latitudes (similar to Figure 5.12h).

Summary

The response and reconfiguration times to the strong northward IMF turning are summarised in Table 5.5. The model is constructed from four minutes of observational data starting at the *model time*, and the response times cannot be determined with an accuracy better than ±2 minutes.

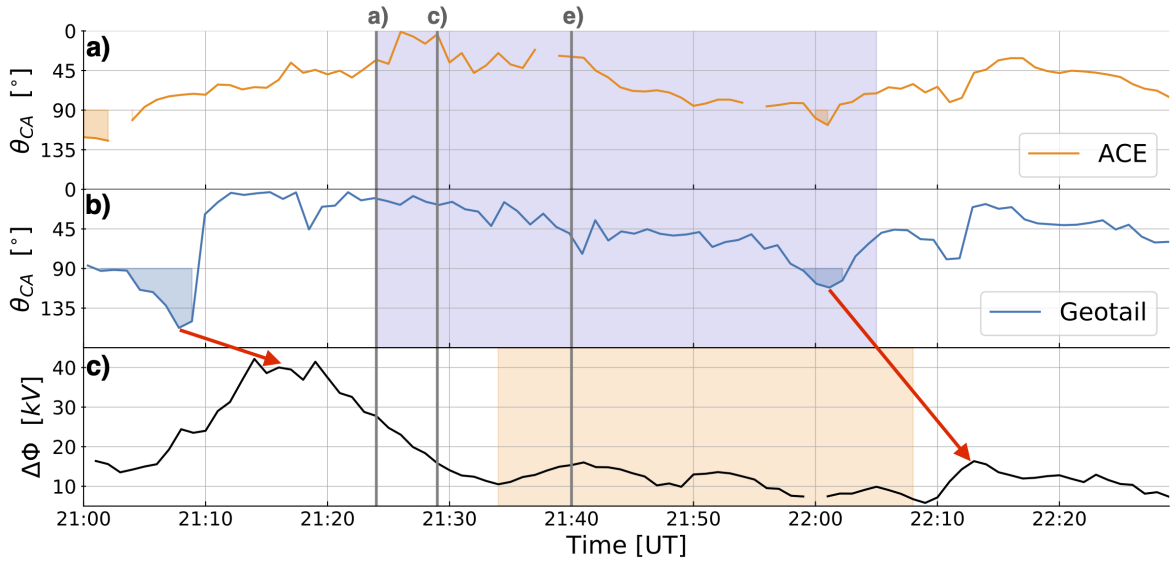

Figure 5.24: (a and b) The IMF clock angle from ACE (orange) and Geotail (blue) on 14 December 2014 at 21:00-22:30 UT. Shading indicates $|\theta_{\mathrm{CA}}|$ >90°. B_Y is generally positive for the time period. The blue shaded region is the time interval when the modelled convection has a pattern consistent with a lobe cell. (c) Modelled maximum potential difference across the region. The orange shaded region in panel c is where the potential difference is measured across the lobe cell. The grey vertical lines correspond panels in Figure 5.23.

Table 5.5: Times of ionospheric response and reconfiguration to a northward IMF turning on 14 December 2014.

IMF	**Ionospheric**	**Time**
Northward IMF turning	Response	15 ± 2 minutes
Northward IMF	Reconfiguration	13 ± 2 minutes
Southward IMF turning	Response	8 ± 2 minutes

5.10 Summary of observations and modelling results

This section summarises the main findings presented in this chapter. There was low geomagnetic activity during the observation period on 14-15 December 2014 at 21:00-02:00 UT. The IMF was generally characterised by positive B_Y and B_Z but had significant and sudden variations where the IMF turned southward and one B_Y polarity change. Before the observation period, there had been a prolonged period of southward IMF. The ionospheric observations before and after ∼00:20 UT showed significant differences in convection features, auroral emission intensities, and particle precipitation characteristics.

Convection

In the individual SuperDARN radar scans, the ionospheric convection was more structured and dynamic than the global convection maps could resolve. Between one and four areas of zonal flows in opposing directions were frequently observed. The modelled mesoscale convection patterns also underwent several changes linked to IMF polarity changes, one of which was related to a sharp northward IMF turning at the start of the observation period. Turbulent convection was most frequently observed at times identified as transition periods, while multiple channels of opposing flow were most often observed during periods where the IMF was northward oriented. An anti-sunward flow channel was observed around 80° MLAT for large parts of the observation period, and a channel of reversed flow on its equatorward side was identified after ∼00:20 UT.

Regional model

The regional model was made to represent the convection in the F-region ionosphere and did indeed capture most mesoscale convection features (given sufficient data coverage). The model was also, in general, able to predict the location of the PCA in regions of high vorticity - at clockwise flow shears/reversals. The model was used to determine that the ionospheric convection responded to a northward IMF turning after 15 ± 2 minutes and that a full reconfiguration of the local convection pattern took 13 ± 2 minutes.

Polar cap arc

A PCA was observed close to the dusk-side auroral oval for >3 hours in both ground-based and space-based imaging. The PCA migrated in the north-south direction with

the bulk plasma, seemingly responding to IMF polarity changes. A similar motion for the consistent channel of anti-sunward flow was observed, and the PCA seemed to be located on the equatorward side of the channel. The PCA had emission intensities comparable to the main oval emissions at the start of the observation period but intensified at ∼00:30 UT, after an IMF B_Y polarity change was observed. At the start of the observation period, the PCA also appeared as separated from the main oval in space-based imaging but not in the in-situ particle precipitation data. During a DMSP F18 pass at ∼01:19 UT, the PCA was separate from the dusk-side main oval in both space-based imaging and particle precipitation data. A relationship between the vorticity of the ionospheric convection and the intensity of the PCA emissions was observed. Stronger cross-track vorticity corresponded to enhanced emission intensity.

Chapter 6

Discussion

In this chapter, the results and choices made throughout this study are discussed. The regional model developed in this thesis is discussed in Section 6.1, emphasising discovered limitations and areas of improvement. Section 6.2 discusses how reliable the solar wind and interplanetary magnetic field (IMF) observations are when looking at the ionospheric context. In Section 6.3, the existing theories for possible production mechanisms for the polar cap auroral arc (PCA) are discussed in light of the observations and model results presented in Chapter 5. The convection related to the PCA and other mesoscale features are discussed in Section 6.4.

6.1 Model limitations

See Chapter 4 for a description of the fundamental advantages and limitations of the SECS technique for regional modelling.

Compliance with independent observations

As summarised in Section 5.10, the regional modelling technique proved useful in reproducing the mesoscale convection features (Section 5.7). The regional model showed convection features that matched the location and motion of auroral emissions observed by ground and space-based imagers (Sections 5.7 and 5.8). Section 5.6 showed that the model exhibited convection patterns compatible with the global climatological patterns expected for the observed solar wind and IMF conditions. Additionally, the modelled patterns identified as convection for southward IMF were observed after evidence of subsolar reconnection was detected in the auroral imaging presented in Section 5.5 (brightening on the dayside; *Frey et al.*, 2019). There was also evidence of reconfiguration due to northward turnings (also see Section 5.9). The modelled ionospheric responses to solar wind driving are discussed further in Section 6.2. Neither the auroral emissions or the solar wind/IMF conditions are used as input data to the model. The fact that the model is generally consistent with these independent observations validates the methodology.

Vorticity and field-aligned currents

As shown in Sections 5.7 and 5.8, the model generally showed flow shears/rotations that were consistent with the location of the most intense PCA emissions. The prediction of

auroral emissions relies on the assumption that gradients in the ionospheric conductances are negligible (see Section 4.6). This assumption is best in a sunlit hemisphere, where the ionisation by sunlight causes a nearly uniform conductance, and variable auroral precipitation can lead to conductance gradients in a dark ionosphere (*Chisham et al.*, 2009). Although the conductance has not been investigated in this thesis, the low energies of particle precipitation ($\leq$1 keV) and low-intensity emissions make it unlikely that precipitation caused any strong conductance gradients, at least before the intensification of the emissions observed after 00:30 UT. Therefore, the vorticity is likely a good proxy for the field-aligned currents (FACs) during this event.

To better predict the FACs in a future application, the modelling method can be expanded to include conductance maps over the region, either through a model or from observations. Conductances can be derived from auroral images or obtained from observations by incoherent scatter radars (ISR). Conversely, a comparison of the current regional model with FAC measurements from, e.g. low-Earth orbit (LEO) spacecraft could be applied to study the effect of conductance gradients in the ionosphere.

Curl-free assumption

One of the most fundamental assumptions in the modelling technique is that the convection electric field is curl-free. This steady-state assumption is widespread when constructing maps of convection and a reasonable assumption on our modelling timescales (see Section 4.2). However, it also means that convection due to rapid variations in magnetic perturbations ($\frac{\partial \mathbf{B}}{\partial t}$) cannot be described.

Uncertainties and weights

Reducing the uncertainties in the observation locations, specifically better determination of the location of the backscatter volume in the SuperDARN observations, would improve the model's ability to reproduce the observed electrodynamics accurately. Likely, the uncertainty in range-gate location discussed in Section 3.2 is one of the largest sources of error in the current modelling technique.

Accounting for observational uncertainties or statistical errors in the input data more robustly would also improve the model. As described in Section 4.7, observations with significant error estimates are not included as input data. A more thorough approach could be to apply weights to the data depending on their uncertainties. With such an approach, the largest challenge would be to determine what the error of each measurement is, as multiple aspects can affect the accuracy of an observation (e.g. the ones outlined in Chapter 3). This error measure would also have to include the uncertainties in the location of the observation points.

Magnetic field line mapping

In this work, a common altitude of 300 km for all SuperDARN observations is assumed. As discussed in Section 3.2, there is possible contamination from lower altitude (E-region) backscatter at range gates close to the radar site. Some studies that use SuperDARN observations for empirical modelling avoid the E-region contamination by

omitting observations within a certain distance from the site (e.g. *Thomas and Shepherd*, 2018) but as the modelling method is dependent on a high density of observations, removing them could lead to poor model quality.

Section 4.7 described how the DMSP convection measurements are mapped along magnetic field lines to 300 km altitude. The horizontal DMSP ion drift observations are assumed to be perpendicular to the geomagnetic field when doing the mapping since the field is assumed to be vertical (radial) at the latitudes of the model region. Accounting for the inclination of the geomagnetic field could be an improvement to the model technique. The SSIES system has ion drift measurements in three dimensions (see Section 5.3), and it is possible to calculate the perpendicular component of the observed ion drifts before mapping. Still, this correction would likely not change the model results noticeably, as other sources of error are currently more dominating.

Data coverage

The reliability of the model depends on the data coverage. The test in Section 4.8.2 showed that the model was able to reproduce a simulated scenario with a maximum relative error of 13.12% (for a coverage quality of 0.65 and a total of 1476 observations). This result is similar to the results by *Amm et al.* (2010), who with a similar method found that their SECS model was able to reproduce the observed velocities with an error <12%, even for a low coverage scenario. The simulated model that was reproduced in Section 4.8.2 did, however, not exhibit significant mesoscale convection structure and was a relatively smooth situation. The model techniques ability to reproduce a real scenario would likely be reduced if the observed convection had substantial variation and noise.

The coverage quality defined in Section 4.8 was made for easy identification of models that are unreliable due to inadequate observational coverage. As has been shown throughout Chapter 5, a high coverage quality measure did not guarantee a good model solution. The coverage quality does not include the total number of observations or where the data are sparse in the region, and coverage plots must be consulted before interpreting the model results. Referring to the coverage plots is not an optimal solution since it makes the model plots harder to understand. An improvement for a future application is a new way of determining the coverage quality that accounts for variations in the total number of observations.

The model is largely determined by local observations, which is generally an advantage, especially when the observations are evenly distributed over the model region. It can, however, lead to regions of high data coverage dominating the solution. This behaviour was briefly discussed when studying *Example 5* in Section 5.7, where the eastern half of the model region appeared to be dominated by observations from only one SuperDARN radar (one line-of-sight direction). The technique should be adjusted for a future application so that areas in the model region that are constrained by observations in multiple line-of-sight directions dominate the solution. The adjustment could for instance be implemented by weighting.

Temporal resolution

Four minutes of observations were used to construct each regional model (see Section 4.5). This time window limits the temporal resolution of the current modelling technique, making it unsuitable for studying phenomena on time scales shorter than the four minutes. This aspect of the model may cause it to underestimate the response times of ionospheric convection, ad introduced uncertainties in the determination of ionospheric response times presented in Section 5.9.

In situations of excellent data coverage, a shorter time window could be chosen. The model would then be able to resolve transient features in the ionosphere with higher accuracy. Additionally, the constraint on observation density limits the size of the model region that can be used, as there is no point in expanding the model region into areas void of observational data. Adding other observational data as inputs to the SECS model (e.g. convection measurements from LEO satellites or ISR) may provide the required observation density to both improve the temporal resolution and expand the area of the model region.

6.2 Solar wind driving

Ionospheric response times

The ionospheric dynamics seen during the observation period showed changes on time scales of a few minutes. The ionospheric convection is often related to solar wind data, and the timing of the solar wind observations is critical. The uncertainties of solar wind propagation times inherent in the HRO time-lag (see Section 3.1) were in this work reduced by mainly relying on observations from Geotail (see Section 5.1). A propagation delay is still seen before the solar wind observed at the Geotail location interacts with the magnetopause, and some minutes of additional delay is expected before the response is communicated to the ionosphere (see Section 2.6.1; *Freeman et al.*, 1990a). According to *Samsonov et al.* (2017), the total time from a southward IMF turning at the bow shock nose is detected in the ionosphere is estimated to be 10−16 minutes.

Ground-based observations of the ionosphere are a method for calibrating the transition time (*Samsonov et al.*, 2017). The modelling technique shows promise for future use in investigations of ionospheric response times to solar wind driving. Section 5.6 described frequent changes in the modelled convection patterns that coincided with northward and southward IMF turnings. The southward turnings had ionospheric responses within ∼10−14 minutes, while northward turnings had slightly longer response times at ∼12−17 minutes (the model region was located at ∼12−19 MLT). The trend in the time delay of modelled ionospheric responses was further supported by the case studied in Section 5.9. Still, the number of IMF turnings and regional models with sufficient data coverage were limited in the period of focus of this work.

Comparison with global models

Similar to the regional modelling technique developed in this thesis, the map potentials used for global context in Sections 5.2 and 5.9 utilises data assimilation where Su-

perDARN observations are used to construct the 'real-time' convection patterns. The map potential method does, however, also use an empirical model from *Thomas and Shepherd* (2018) (TS18) to constrain the model in regions where observational data is lacking. It is common to use statistical models for fill-in data. The global convection maps are thus based on time-lagged solar wind and IMF observations (see Section 2.6.1). The effect of a fill-in model on the final convection pattern can be significant, as the measured velocity and the convection predicted by the statistical patterns are combined to find the optimal fit (*Chisham et al.*, 2007). Sorting the global patterns on solar wind observations has some inherent assumptions, and using these patterns as a basis for real-time diagnostics is not straightforward.

One main weakness of solar wind-based fill-in models is related to the determination of solar wind time delay discussed in the previous paragraphs. A single time delay for all solar wind driving cannot be accurately determined (*Samsonov et al.*, 2017). Despite this, most global real-time convection maps assume that the delay from the solar wind observation time to an ionospheric response is known. It is also assumed that the solar wind observed at, e.g. the L1 point, is the same conditions that are interacting with the magnetosphere (*Gjerloev et al.*, 2018). Such an assumption implies that the solar wind observations by ACE and Geotail presented in Section 5.1 should exhibit the same structure, which the results show is not always the case.

Gjerloev et al. (2018) also note that the global real-time convection maps often do not account for prior driving conditions and inertia in the magnetosphere-ionosphere (M-I) system. The global dynamics are, in reality, determined by both dayside and nightside activity (see Section 2.6), and the amount of nightside activity will depend on prior solar wind conditions. Disregarding flows in the M-I system set up by an earlier driver or other internal M-I processes such as tail reconnection can lead to abrupt changes in the global convection patterns that are not realistic. Abrupt changes are especially prominent when the solar wind is variable, as seen during the observation period studied in this thesis.

Despite these limitations of the map potentials, the global patterns presented in Section 5.9 seemed to reproduce the lobe-cell reconfiguration reasonably well, mainly due to a high density of convection measurements constraining the model in that area. Still, Section 5.2 showed that the global map potentials were not great for resolving mesoscale convection structures. Because of the fill-in model technique, mesoscale variation that is highly incompatible with the anticipated large-scale convection from the model may be suppressed. In addition, the global maps use spherical harmonic basis functions to construct the patterns and need to be restrained by boundary conditions (*Chisham et al.*, 2007).

The SECS modelling technique used in this thesis is solely based on observational data from the ionosphere and the curl-free SECS basis function, and no fill-in model or solar wind data is used. There is no need to determine boundary conditions as a local region is modelled. Unlike the global models, the regional model contains no assumption on what processes are driving the observed convection and only depicts the ground truth. The trade-off is that the regional modelling method only works in regions where observational data is available.

The map potential plots use gridded observational data with 2 minute averages within grid cells with ∼100 km resolution (*Ruohoniemi and Baker*, 1998). The map

potential plots can thus not be expected to resolve convection features on spatial scales smaller than 100 km. The grid resolution used for the SECS model is 70 km, and the regional model is naturally able to resolve finer details in the ionospheric convection than the map potentials. The regional model is thus better suited for studies of electrodynamics where there is a desire to resolve mesoscale convection details.

6.3 The polar cap auroral arc

Comment on polar cap arc intensities

The PCA is connected to the nightside main oval and narrows as it reaches towards the dayside. The space-based images could not resolve a continuous auroral arc on the dayside for large parts of the observation period. The lack of far-ultraviolet (FUV) emissions does not necessarily mean that there are no PCA emissions sunward of 18 MLT at this time. In fact, in Section 5.4 it was shown that weak red-line PCA emissions were observed on the dayside. In addition to observing different wavelengths, the observational methods have different sensitivity thresholds (see Section 3.4.1). The PCA emissions at FUV wavelengths were too weak to appear in the space-based images, while the red-line emissions observed from the ground had higher emission intensities. This inconsistency could be due to low precipitation energies over the PCA, as red-line emissions are more sensitive to low energy precipitation than the FUV emissions (see Sections 2.7). A similar explanation could be used to explain why space-based images observed a lack of emissions between the main oval and PCA, while the particle precipitation data showed no significant separation (for *Pass 1* at 21:57 UT and *Pass 2* at 23:39 UT in Section 5.8).

Type of polar cap arc

The PCA studied in this thesis is observed during a period of northward IMF ($|\theta_{CA}| < 90°$ for the majority of the time) and quiet geomagnetic conditions, consistent with the majority of other reported PCA (*Hosokawa et al.*, 2020). This subsection compares the characteristics of the PCA to the polar arc categories introduced in Section 2.7.1.

The IMF control of the PCA's initial location can indicate the type of PCA (e.g. *Fear and Milan*, 2012a) but as discussed in Section 6.2, determining the time delay between the solar wind observations and their effect on the M-I system is not straightforward. As some theories for PCA formation are related to activity on the magnetosphere flanks or tail, determining a time delay for the IMF becomes even more difficult. Different studies also show different statistical correlations between the IMF B_Y and the PCA's initial location. *Kullen et al.* (2015) estimates that the best correlation is 1−2 hours prior to the PCA, while *Fear and Milan* (2012a) find the correlation to be 3−4 hours (for transpolar arcs).

The PCA was first observed in global images at 21:57 UT but had likely formed at an earlier time. If the PCA belongs to the arc category of *transpolar arcs* (TPA), it is likely to have developed from a bulge on the nightside auroral oval. Whether or not this is the case is unclear. The PCA may have started developing before or during the DMSP F16 pass at 21:30 UT presented in Section 5.3, as the nightside auroral oval

was outside of the imager FOV at that time. Insufficient observational coverage also limits the ability to determine how the PCA disappeared. The PCAs long lifetime is consistent with the statistical properties of TPA (average lifetimes of 2 hours; *Kullen et al.*, 2002). However, the PCA was generally narrow and had low luminosity, an uncommon characteristic for TPA, which are usually bright features.

Global images of the aurora can provide the temporal resolution needed for studying the global development of the PCA. However, no such instrumentation has been available on High Earth orbit spacecraft since the IMAGE spacecraft ceased to operate in 2007. There is also doubt as to whether or not global FUV imagers would be able to observe the thin arc due to their high luminosity thresholds and lower spatial resolution (*Zhu et al.*, 1997).

Based on the space-based FUV images from DMSP, it seems likely that if the PCA developed from a bulge on the nightside, it would have developed at a pre-midnight MLT. In the TPA framework introduced by *Milan et al.* (2005) this would correspond to an IMF B_Y+ in the 3−4 hours before the PCA development. Due to the difficulties in determining the start-time of the PCA, it is hard to determine the IMF orientation preceding the PCA formation with certainty. Still, the IMF B_Y in the period 3−4 hours before the observation period was variable but on average positive. *Milan et al.* (2005) also predict tail reconnection during IMF northward non-substorm intervals (TRINNI) in the nightside ionosphere before the arc formation (*Fear and Milan*, 2012b), but despite good observational coverage in the region of interest, no such flows were seen in the VT map potential plots. It is unlikely that a TRINNI occurred before the PCA. There was also no conjugate PCA observations discernible in the southern hemisphere DMSP FUV images which would have suggested a closed field-line topology (*Zhu et al.*, 1997).

It is unlikely that the PCA is in the *bending arc* category. Firstly, the PCAs temporal evolution is inconsistent with the definition of bending arcs. The PCA was connected to the main oval at ∼22/23 MLT, which is further towards the nightside than for typical bending arcs (*Kullen et al.*, 2015), and had more or less the same shape for at least 1.5 hours (two subsequent DMSP passes). It did not exhibit the characteristic detachment and subsequent bending motion into the polar cap (PC) of bending arcs, and the PCA lifetime was significantly longer than usual bending arc lifetimes (tens of minutes *Kullen et al.*, 2002). Secondly, the bending arcs are associated with dayside reconnection and are often observed after a southward turning of the IMF, or for IMF $B_Z \approx 0$ nT (*Kullen et al.*, 2002; *Carter et al.*, 2015). The IMF observed prior to the arc formation exhibited the opposite behaviour, turning towards a northward orientation.

The emissions of the PCA were quite faint (generally <1 kR), and the PCA thus resembles the *sun-aligned arcs*. Sun-aligned arcs are also associated with lower energy particle precipitation (0.5−2 keV; *Zhu et al.*, 1997), matching the precipitation energies of ≤1 keV observed over the PCA. The PCA particle precipitation was classified as boundary plasma sheet (*BPS*), and accelerated polar rain on open field lines due to flow shears is an unlikely source of the PCA precipitation (*Carlson and Cowley*, 2005; *Newell et al.*, 2009). Still, the particle precipitation classification is not free of errors, and precipitation in some regions adjacent to the PCA precipitation were *unclassified*, which could suggest that the automated identification is struggling to classify the particle precipitation. In addition, BPS precipitation on the dayside can be explained

as being on open field lines (*Lockwood*, 1998). Kelvin-Helmholtz instabilities (KHI) or interchange instabilities on the low latitude magnetopause flanks could cause flow shears on both open and closed field lines (*Zhang et al.*, 2016). KHI on the dusk-side flank may fit the location of the PCA but cannot necessarily explain the movement of the PCA in the north-south direction.

The shape of the large-scale auroral configuration and the fluctuating IMF during the observation period makes *horse-collar auroras* an unlikely candidate for the PCA. The *Milan et al.* (2020) dual-lobe reconnection theory for horse-collar auroras requires IMF northward with $B_Y \approx 0$ nT, but the IMF was generally B_Y+ dominated during the observation period, and evidence of dayside reconnection was observed.

Motion of the polar cap arc

The PCA's movement can be explained in terms of reconfiguration of the large-scale convection. In Section 5.5, the PCA movement in the north-south direction showed evidence of responding to IMF polarity changes. The slow equatorward motion of the PCA observed after the southward IMF turnings can be attributed to convection excited by dayside reconnection for B_Y+ IMF. Evidence of the dayside reconnection was seen both as localised brightening of aurora on the dayside and in the modelled convection. In Section 5.6 convection patterns consistent with subsolar dayside reconnection were identified after the southward turnings (Figures 5.12h, m and n). The opening of magnetic flux on the dayside leads to an expansion of the PC, and as the PCA followed the motion of the bulk plasma, it responded to the redistribution of plasma in the PC.

The dawnward motion of the PCA that occurred ∼15 minutes after the B_Y polarity change from positive to negative at ∼00:00 UT is consistent with PCA statistical properties (see Section 2.7.1; *Hosokawa et al.*, 2020). *Milan et al.* (2005) suggested that movement of a TPA in the dawn-dusk direction is due to the changing size of the lobe cells for different signs of IMF B_Y. Note that they describe the motion in terms of the TRINNI TPA framework. A similar explanation may be used for a PCA located at the open-closed boundary (OCB), as the PC has been found to shift as the stirring due to single-lobe reconnection alters the large-scale distribution of open magnetic flux in the PC (e.g. *Stubbs et al.*, 2005).

Polar cap arc at the open-closed boundary

The particle precipitation over the PCA attests to the auroral form possibly being located at the poleward boundary of the auroral oval, at the OCB, similar to the auroral arcs observed in horse-collar aurora. *Newell et al.* (2009) discussed how some PCA that appear to be separated from the main oval in optical observations are connected to the main oval when looking at particle precipitation data. This was observed for the PCA in comparison of FUV emissions and particle spectrograms in Section 5.8.

Kullen and Janhunen (2004) used magnetohydrodynamic (MHD) simulations to show how the OCB can get strongly displaced towards the pole due to tail twisting for B_Y dominated IMF and suggest that an oval-aligned arc similar to the PCA studied in this thesis could occur at the OCB. MHD simulations were not performed for the case studied in this thesis but could be applied to investigate if a poleward displacement of the OCB is likely for the interplanetary conditions seen during the observation period.

In the DMSP F18 *Pass 1* at 21:57 UT and *Pass 2* at 23:39 UT the PCA was located on what appeared to be the main convection reversal at the OCB (see Sections 5.3 and 5.8). If the PCA was located at the edge of a poleward contracted PC, i.e. the OCB, the convection on the equatorward side of the PCA emissions must be located within the main oval. An anti-sunward channel of ionospheric convection was also consistently observed on the poleward side of the PCA. In between the satellite passes, ground-based observations revealed both sunward and anti-sunward convection on the equatorward side of the PCA flow channel (in Sections 5.2, 5.6, and 5.7). Instability processes at the low latitude magnetopause that may cause flow shears on closed field lines could explain structured convection within the main oval (interchange instability or local injection of magnetosheath plasma; *Kozlovsky et al.*, 2009).

In observations from the DMSP F18 *Pass 3* at 01:21 UT, the PCA did not seem to be located at the OCB. The PCA was separated from the main oval in both particle precipitation data and FUV emissions. Additionally, the enhanced reversed (sunward) flow channel observed equatorward of the PCA flow channel seems incompatible with structured convection within the main oval. It seems likely that some process causes the PCA to separate from the main oval between the DMSP F18 pass at 23:39 UT and the pass at 01:21 UT. This relates to the discussion of the ionospheric convection surrounding the PCA in the following Section 6.4.

6.4 Mesoscale convection

Turbulent flows

As presented in Sections 5.2, 5.6, and 5.7, the ionospheric convection was quite turbulent, with convection features on spatial scales of a few 100 km. The more stable mesoscale convection features were zonal flow channels, often occurring in multiples. The most stable convection feature was the channel of anti-sunward flow consistently located on the poleward side of the PCA. The most transient convection features were not described in detail in Chapter 5, as noisy measurements may have compromised them. However, turbulent flows were typically located on latitudes <70° MLAT and on spatial scales of only a few SuperDARN grid cells. This turbulent convection was most frequently observed at times identified as transition periods in Section 5.6, which suggests that turbulent flows are most common as the ionospheric convection reconfigures.

PCA flow channel

The anti-sunward flow channel associated with the PCA had speeds ∼900 m/s for parts of the observation period, and its width also varied. The channel does not fit any of the fast flow channel categories presented in Section 2.6.2. The channel is situated on the dusk-side, inconsistent with the statistical properties of flow channels for B_Y+ (*Herlingshaw*, 2021). Additionally, flow channel events on the dayside are most commonly observed for southward IMF conditions, but the observation period is characterised by northward IMF (*Sandholt and Farrugia*, 2009).

The presence of a localised channel of anti-sunward flow on the poleward edge of the dusk-side PCA is consistent with previous studies of convection surrounding polar auroral arcs (see Section 2.8). Due to the coupled motion of the PCA and the

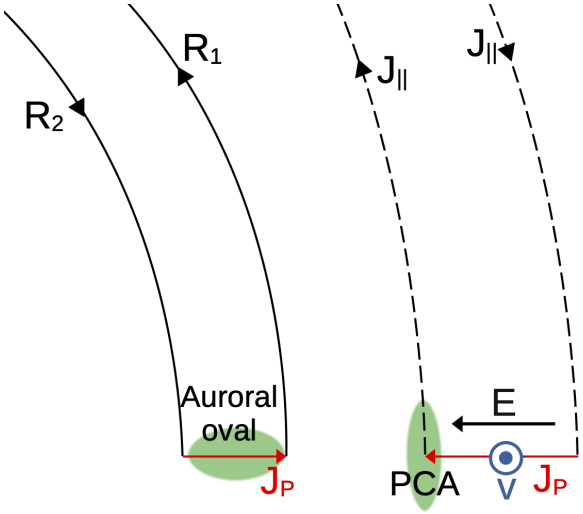

Figure 6.1: Schematic of proposed current system and ionospheric features for 14-15 December 2014. The dusk-side polar cap arc (PCA) is seen in conjunction with an anti-sunward flow channel (blue dotted circle). The associated pair of field-aligned currents ($J_{||}$) are poleward of Regions 1 and 2 field-aligned currents (R1 and R2). $\mathbf{J}_P$ are the ionospheric Pedersen currents and **E** is the convection electric field. Auroral emissions are highlighted in green.

anti-sunward flow channel described in Sections 5.5 and 5.6, they are likely a coupled ionospheric responses to a common system driver. Section 5.8 also showed a coupled relationship between shears in the ionospheric convection and PCA, as more intense FUV emissions and electron precipitation were observed for a high vorticity.

Figure 6.1 shows a schematic of a possible current geometry over the PCA (green highlight) and anti-sunward flow channel (blue). The black arrow is the convection electric field over the flow channel. The red arrows are horizontal Pedersen currents. In this example, the PCA is poleward of the Region 1 and 2 FAC system of the main oval and has a related FAC system marked with $J_{||}$. Such a geometry places the PCA on open magnetic field lines in the polar cap but could still explain why the PCA is located adjacent to the main oval. The driver of the PCA-related FAC system remains to be resolved.

A reversed flow channel

As introduced in Section 2.6.2, reversed flow channel events (RFEs) have mainly been studied as a cusp-phenomenon and have been linked to transient subsolar dayside reconnection. All RFEs in the statistical work by *Rinne et al.* (2007) were on the dayside, constrained in the 10:30−13:30 MLT sector (though it must be noted that their data set only contained observations in the 09−15 MLT region). Other studies of RFEs (*Moen et al.*, 2008; *Oksavik et al.*, 2004, 2005, 2011; *Spicher et al.*, 2016) all focus on the cusp-region and thus try to explain the RFE in the context of dayside processes. These studies also focus on northern hemisphere winter events only. RFE-like convection signatures were identified on the nightside (9%) in the statistical work of *Reed* (2017), which he suggested were related to processes in the magnetotail.

Flows opposing the main background convection were frequently seen during the

observation period, but they rarely met the RFE criteria defined by *Rinne et al.* (2007). The RFE criteria were fulfilled only for the reverse flow channel described in *Example 3* in Section 5.2 and *Example 4* in Section 5.7. The reverse flow channel was first observed at ∼00:22 UT as a suppression of the anti-sunward background convection around ∼80° MLAT and ∼18 MLT. No evidence of subsolar reconnection was observed at the time of formation. The channel appeared to develop from the nightside towards the dayside during a period where the PCA was moving rapidly towards the pole after an IMF B_Y sign change. The reversed flow channel is visible in the radar observations for >20 minutes. Likely, the 1500 m/s reversed convection structure observed by DMSP F18 during *Pass 3* at 01:21 UT in Section 5.8 is the same reversed flow channel as observed from the ground. If this is the case, the reversed flow channel persisted for >1 hour.

Based on the location of the reversed flow channel and the northward IMF orientation prior to the development of the flow signature, it seems unlikely that the reversed flow channel was caused by (subsolar) dayside reconnection. The long lifetime of the reversed flow channel also suggests a different driving mechanism. An alternative mechanism was proposed by *Moen et al.* (2008), who separated RFE into two categories. They suggest that some RFE are driven by the closure of current loops from independent voltage generators, *drivers*, through a low conducting ionosphere. This formation mechanism could account for longer RFE lifetimes and does not limit the RFE location to the footprint of transient dayside reconnection. This alternative formation mechanism relies on low Pedersen conductance in the ionosphere and thus suggests a seasonal asymmetry for RFE occurrence. The reverse flow channel identified in this work is seen during winter and at night in an area void of strong auroral emissions. This suggests a low plasma density at both E and F-region altitudes, hence a low Pedersen conductance. *Moen et al.* (2008) also predicts inverted-V arc precipitation associated with this type of RFE, which is consistent with the PCA particle precipitation presented in Section 5.8.

The lack of precipitation on the equatorward side of the PCA seen during *Pass 3* in Section 5.8, also suggests a low Pedersen conductance close to the reversed flow channel. There is enhanced particle precipitation over the PCA with energies as high as 1 keV, as well as more intense FUV aurora, that could suggest localised plasma production at the PCA location and therefore increased Pedersen conductance. Applying the *Moen et al.* (2008) mechanism to our channel of reversed flow requires two independent voltage generators to be located within the PC.

If the reversed flow channel is not linked to dayside activity, other formation mechanisms must be explored. For instance, KHI at the magnetosphere flanks may cause regions of opposing convection and could explain why the RFE appears to develop from the nightside towards the dayside (*Zhang et al.*, 2016). Another possibility is that the reversed flow channel results from nightside reconnection in a twisted magnetotail for B_Y+. No strong geomagnetic activity was observed during the observation period, and any possible nightside reconnection would have to be a TRINNI. However, the VT map potential plots do not show any evidence of B_Y+ TRINNI flows before the reversed flow channel was observed.

An intriguing idea is that some RFE events might be related to nightside activity rather than dayside activity. The DMSP SSUSI observations in Figure 5.7 showed

several examples where the PCA extended all the way to the dayside noon sector. In principle, a similar situation may have occurred for some of the RFE cases that have been published in literature (e.g. *Rinne et al.*, 2007; *Moen et al.*, 2008; *Oksavik et al.*, 2011). One example is the RFE seen by *Oksavik et al.* (2011) that extended quite far into the afternoon sector. But limited data coverage at that time prevented any information on whether it reached all the way to the nightside or not. The study conducted in this thesis nicely illustrates the robustness of combined multi-instrument observations, advanced regional modelling, and a global perspective on the dynamics and processes involved. In that regard, it seems relevant to revisit previous theories on RFE formation related to subsolar dayside reconnection. However, that has to be left out for future work.

Specific limitations of SuperDARN observations

Lastly, it should be emphasised that while the SuperDARN radars can resolve narrow flow channels, the convection features must have scale sizes larger than the SuperDARN spatial resolution to be detected. Narrow channels located in between the beams will not be resolved. Similarly, opposing flows on spatial scales smaller than the SuperDARN resolution may result in observations being interpreted as low-velocity regions, since the SuperDARN observations are averages over the backscatter volume. This means that very narrow reversed flow channels may be misinterpreted as reductions in the background flow rather than actual opposing flow channels. The spectral width parameter of the backscatter may be used to reveal turbulence within a SuperDARN observation volume.

Uncertainties in determining the location of SuperDARN observations lead to difficulties interpreting the observed ionospheric convection with respect to thin auroral forms like the PCA. As both flow channels and auroral arcs are usually narrow features, an accuracy of a few 10 km may be necessary to compare the two ionospheric signatures, such as can be obtained from, e.g. ISR. The DMSP spacecraft also obtain ion drift measurements at this scale (see Section 5.3). As noted in Section 5.7 (and Section 3.4), there are additional challenges in determining the location of red-line emissions observed from the ground. Still, Section 5.7 showed a good relatively correlation between the clockwise flow reversals/shears observed by the radars (regional model) and PCA location.

Chapter 7

Conclusion

Through an event study with an exceptionally high density of observational data, we obtained a good picture of the ionospheric dynamics in a local region during a period of highly variable solar wind driving and otherwise quiet geomagnetic conditions. We developed an assimilative modelling technique for studying local ionospheric convection at the mesoscale using ionospheric measurements of convection and curl-free SECS basis functions. By applying the modelling technique in the event study, we have tested its applicability and explored its limitations.

The modelling technique shows great promise for studying ionospheric convection in two-dimensions and on small spatial scales of $\sim$100 km. With sufficient data coverage, it performs well in reproducing the ionospheric convection and can be applied to study several aspects relating to external driving, M-I coupling and other details of the ionospheric electrodynamics without any a priori assumptions of the system other than that it is in steady-state. We have demonstrated how the model can be used to quantify the ionospheric convection response to a northward IMF turning. It took 15 ± 2 minutes from the IMF turning northward near the bow shock before reconfiguration became visible in the convection in the polar ionosphere. Another 13 ± 2 minutes passes before the northward IMF reconfiguration is complete and a lobe cell is fully developed. We suggest that the model also can be used to study the temporal response and reconfiguration of the ionosphere to both solar wind discontinuities or internal processes in the magnetosphere.

The extensive study of convection surrounding the PCA confirms earlier reports of mesoscale anti-sunward flow on the dawnward side of the arc. The PCA and anti-sunward channel migrate in the north-south direction with the bulk plasma motion. Due to limitations of the observational methods, we cannot conclude on a likely formation mechanism. However, we suggest that the PCA originally was at, or adjacent to, the open-closed boundary before separating from the oval after a B_Y sign change was observed. We find a clear relationship between PCA emission intensity and flow vorticity in the ionosphere.

The convection data and model presented in this work deviate from the average statistical picture of the polar ionosphere, as it is highly structured and dynamic. We saw that the most turbulent convection was observed in response to changes in IMF clock angle and during periods of northward IMF. We show an example of a flow channel that has similar characteristics to a reversed flow event (RFE). The RFE is a convection phenomenon that previously was identified on the dayside. Our observations suggest that some flow channels with surprisingly similar characteristics to RFEs can also be

driven by processes at MLTs far away from magnetic noon. It opens up the intriguing question of whether all RFEs are generated on the dayside, or if some RFEs can map to processes at the magnetospheric flanks or further into the nightside, as may be suggested by the analysis where we have put the flow channels into a global perspective.

Chapter 8

Future Perspectives

The assimilative regional model developed in this thesis can be applied to both case studies and statistical studies of mesoscale convection features. The location and size of the model region can be adjusted to fit other regions and instrumentation with good observational coverage such as the upcoming EISCAT_3D (European Incoherent Scatter 3D; *McCrea et al.*, 2015). The radar array will be able to obtain three-dimensional plasma drift vectors and maps of ionospheric conductivities with high spatial and temporal resolution. The model from this thesis is an important first step in developing a technique for assimilative modelling that, with further development, can be applied to EISCAT_3D. Incoherent scatter radars have better spatial resolution than the SuperDARN radars used for data input in this thesis, allowing for a finer SECS node grid and better model resolution. EISCAT_3D is predicted to be operational in early 2023. Applying the regional model technique to existing incoherent scatter radars such as Poker Flat ISR (PFISR) and Resolute Bay ISR (RISR) may facilitate studies with EISCAT_3D data.

Continuous global or near-global imaging of the polar ionosphere will help resolve the temporal evolution of auroral features within the polar cap. There are currently no satellites in high Earth orbit that are equipped for global imaging. The upcoming Solar wind Magnetosphere Ionosphere Link Explorer (SMILE; *Raab et al.*, 2016) mission is expected to have imaging capabilities of the global auroral oval in the northern hemisphere. The images may also be used for deriving ionospheric conductances that can be applied to improve the ability of the regional model to predict field-aligned currents (see Section 6.1).

At least two projects follow naturally from the work conducted in this thesis:

Project 1 - Ionospheric response times to a northward IMF turning. This project would quantify the response and reconfiguration times of the ionospheric convection to a northward IMF turning based on results from Section 5.9. Adjustments to improve the modelling method should be implemented, specifically improvements to the temporal resolution. The modelling technique would be used to quantify the response and reconfiguration time to northward IMF turnings observed close to the Earth's bow shock (observations from Geotail). The project could be expanded to using the method for quantifying responses of the ionospheric convection to other solar wind discontinuities.

Project 2 - Statistical study of reversed flow channels. A statistical study of reversed flow channels can resolve questions about the occurrence, distribution,

seasonal dependence, and IMF dependence of the convection feature. The SuperDARN data sets contain almost three decades of observational data, which are suited for this study. This project involves developing a detection algorithm for reversed flow channels and applying it to the available data from mid, high and polar latitude radars. The detection algorithm may also be used to identify case study candidates. The project can be of help in resolving questions about possible formation mechanisms and could be used to assess the role of reversed flow events in the structuring of ionospheric plasma.

Appendix A

Magnetic Reference Frames

International Geomagnetic Reference Field (IGRF)

The International Geomagnetic Reference Field (IGRF) is a mathematical description of Earth's main magnetic field (see Section 2.2) which is valid on and above the Earth surface. It is a set of spherical harmonic coefficients that defines a magnetic scalar potential function that describes the geomagnetic field (*Alken et al.*, 2021). The IGRF has observation-based coefficients that can be put into a mathematical model and only depict the large-scale field. IGRF cannot predict disturbances on short time scales like those seen during enhanced geomagnetic activity. It is, however, an excellent approximation to the realistic main field and is updated every five years with new and revised coefficients. The current generation of the model is IGRF-13 (*Alken et al.*, 2021).

Magnetic coordinate systems

Geocentric solar magnetic system (GSM)
When describing interplanetary magnetic field (IMF) and solar wind parameters close to the Earth, it is convenient to use a coordinate system that is fixed with respect to the Sun-Earth line, where the geomagnetic dipole field is in one of the planes. The geocentric solar magnetic (GSM) coordinate system fits this description. The coordinate system is shown in Figure A.1, with the Earth's centre in its origin. The X-axis points from the Earth towards the Sun (along the Sun-Earth line). The Z-axis points up through magnetic north. The Y-axis completes the right-hand system, pointing perpendicular to the Earth's magnetic dipole in a direction approximately opposite the Earth's orbital motion (*Laundal and Richmond*, 2017).

Magnetic Apex coordinates
When comparing ionospheric scalar and vector quantities, it is useful to use a coordinate system oriented with respect to the geomagnetic field as ionospheric phenomena like aurora and plasma motion are strongly organised by the magnetic field lines. Magnetic Apex coordinates (*VanZandt et al.*, 1972) is one of several coordinate systems proposed for working with phenomena in the F-region ionosphere. A magnetic Apex coordinate, latitude and longitude, is constant along geomagnetic field lines of a realistic geomagnetic field model (like the IGRF).

The Modified Apex coordinate system (*Richmond*, 1995) is a version of the magnetic Apex system where coordinates are defined by mapping to a reference altitude

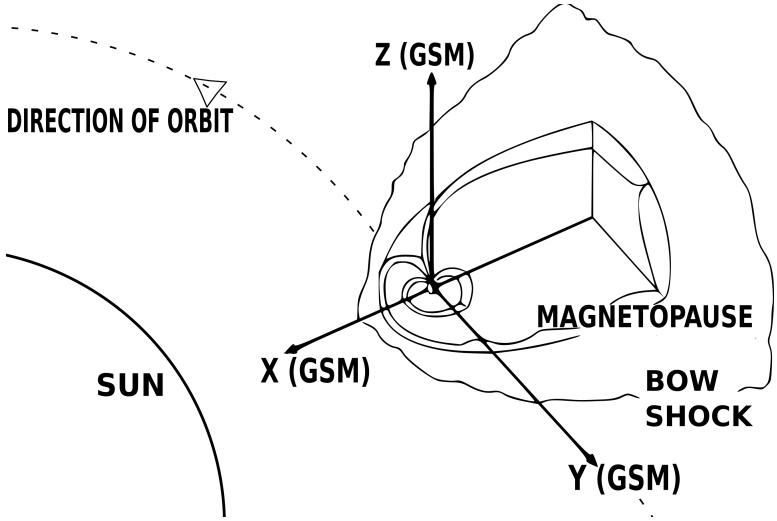

Figure A.1: The geocentric solar magnetic (GSM) coordinate system (adapted from *Tanskanen*, 2002).

(in contrast to the original magnetic Apex system where the coordinates are mapped to the equatorial radius of an ellipsoidal Earth). In a multi-instrument study like the one conducted in this thesis, Modified Apex is especially useful as observations can be mapped along the field lines to a common reference altitude for comparison. This is the coordinate system used throughout this thesis for presenting observational data in magnetic coordinates. Altitude-adjusted corrected geomagnetic (AACGM) coordinates are also a common system used for this purpose. AACGM and Modified Apex coordinates are nearly identical at high latitudes, as illustrated in Figure A.2 (*Laundal and Richmond*, 2017).

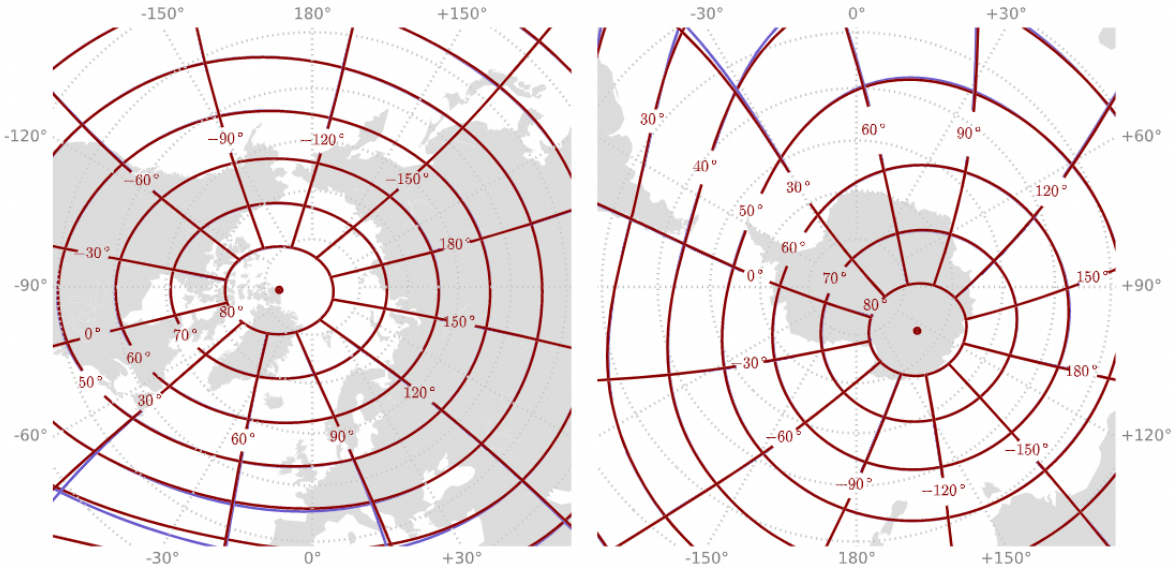

Figure A.2: Comparison of Modified Apex (blue) and AACGM (red) coordinates (at height zero). Northern hemisphere is to the left, and southern hemisphere is to the right. The coordinates are nearly identical at high latitudes. (from *Laundal and Richmond*, 2017).

Magnetic local time (MLT)

It is also useful to visualise polar ionospheric phenomena with respect to the Sun-Earth line, as many of them are driven by interactions with the Sun. It is therefore common to replace the magnetic longitude with the magnetic local time (MLT) (*Laundal and Richmond*, 2017). A magnetic latitude/MLT coordinate system is shown in Figure A.3. The magnetic latitudes are shown as concentric circles with the geomagnetic pole (90° magnetic latitude) in the centre (red dot), and the MLTs are written along the edge of the outer circle. Magnetic noon (12 MLT, sunward direction) is at the top, and magnetic midnight (24 MLT, anti-sunward/tailward direction) is at the bottom. The dawn-side (06 MLT) is to the right, and the dusk-side (18 MLT) is to the left. This coordinate system stays fixed with respect to the Sun while the Earth rotates below it. Note that Earth's rotational axis is offset from the geomagnetic pole.

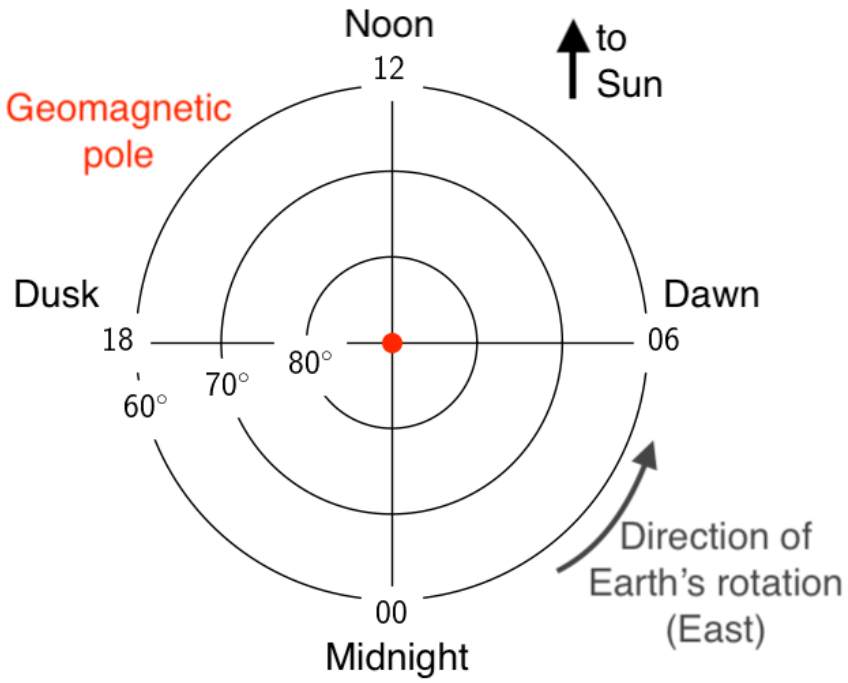

Figure A.3: The magnetic latitude and magnetic local time (MLT) axis. The Earth rotates (eastward arrow) below while the system is fixed with respect to the direction towards the Sun (upwards arrow). Midnight (00/24 MLT) is down, dawn (06 MLT) is to the right, noon (12 MLT) is up, and dusk (18 MLT) is to the left. The geomagnetic pole (red) is in the centre of the grid.

References

Akasofu, S.-I. (1981), Auroral Arcs and Auroral Potential Structure, in *Geophysical Monograph Series: Physics of Auroral Arc Formation*, vol. 25, edited by S.-I. Akasofu and J. R. Kan, chap. 1, American Geophysical Union, Washington D. C., doi:10.1029/GM025p0001.

Alfvén, H. (1942), Existence of Electromagnetic-Hydrodynamic Waves, *Nature*, *150*, 405–406, doi:10.1038/150405d0.

Alken, P., E. Thébault, C. D. Beggan, H. Amit, J. Aubert, J. Baerenzung, T. N. Bondar, W. J. Brown, S. Califf, A. Chambodut, A. Chulliat, G. A. Cox, C. C. Finlay, A. Fournier, N. Gillet, A. Grayver, M. D. Hammer, M. Holschneider, L. Huder, G. Hulot, T. Jager, C. Kloss, M. Korte, W. Kuang, A. Kuvshinov, B. Langlais, J.-M. Léger, V. Lesur, P. W. Livermore, F. J. Lowes, S. Macmillan, W. Magnes, M. Mandea, S. Marsal, J. Matzka, M. C. Metman, T. Minami, A. Morschhauser, J. E. Mound, M. Nair, S. Nakano, N. Olsen, F. J. Pavón-Carrasco, V. G. Petrov, G. Ropp, M. Rother, T. J. Sabaka, S. Sanchez, D. Saturnino, N. R. Schnepf, X. Shen, C. Stolle, A. Tangborn, L. Tøffner-Clausen, H. Toh, J. M. Torta, J. Varner, F. Vervelidou, P. Vigneron, I. Wardinski, J. Wicht, A. Woods, Y. Yang, Z. Zeren, and B. Zhou (2021), International Geomagnetic Reference Field: the thirteenth generation, *Earth, Planets and Space*, *73*(49), doi:10.1186/s40623-020-01288-x.

Amm, O. (1997), Ionospheric Elementary Current Systems in Spherical Coordinates and Their Application, *Journal of geomagnetism and geoelectricity*, *49*(7), 947–955, doi:10.5636/jgg.49.947.

Amm, O., and A. Viljanen (1999), Ionospheric disturbance magnetic field continuation from the ground to the ionosphere using spherical elementary current systems, *Earth Planets and Space*, *51*(6), 431–440, doi:10.1186/BF03352247.

Amm, O., A. Grocott, M. Lester, and T. K. Yeoman (2010), Local determination of ionospheric plasma convection from coherent scatter radar data using the SECS technique, *Journal of Geophysical Research: Space Physics*, *115*(A03304), doi:10.1029/2009ja014832.

Andalsvik, Y. L., P. E. Sandholt, and C. J. Farrugia (2011), Dayside and nightside contributions to cross-polar cap potential variations: The 20 March 2001 ICME case, *Annales Geophysicae*, *29*(11), 2189–2201, doi:10.5194/angeo-29-2189-2011.

Anderson, B. J., H. Korth, C. L. Waters, D. L. Green, and P. Stauning (2008), Statistical Birkeland current distributions from magnetic field observations by the Iridium constellation, *Annales Geophysicae*, *26*, 671–678.

Aster, R. C., B. Borchers, and C. H. Thurber (2013), Generalized Cross-Validation, in *Parameter estimation and inverse problems*, pp. 115–117, Academic Press.

Bates, D. R. (1950), Dissociative Recombination, *Physical Review*, *78*(4), 492–493, doi:10.1103/PhysRev.78.492.

Baumjohann, W., and R. A. Treumann (2012), *Basic Space Plasma Physics: Revised Edition*, Imperial College Press, London.

Birkeland, K. (1908), *The Norwegian Aurora Polaris Expedition 1902–1903*, vol. 1, H. Aschehoug, New York and Christiania.

Borovsky, J. (2017), The Magnetosphere and Its Problems, Retrieved from `https://event.cwi.nl/spaceweather2017/talks/borovsky_talk.pdf`, [Online; last accessed 20-Jan-2021].

Borovsky, J. E., and J. A. Valdivia (2018), The Earth's Magnetosphere: A Systems Science Overview and Assessment, *Surveys in Geophysics*, *39*(5), 817–859, doi:10.1007/s10712-018-9487-x.

Buchvarova, M., H. Ruder, P. I. Y. Velinov, and P. Tonev (2003), Ionization by galactic cosmic rays in the ionosphere and atmosphere depending on the solar activity, in *Solar variability as an input to the Earth's environment. International Solar Cycle Studies (ISCS) Symposium*, edited by A. Wilson, pp. 351–354, ESA Publications Division, publ. ESTEC, Noordwijk, The Netherlands.

Burch, J., and J. Drake (2009), Reconnecting Magnetic Fields, *American Scientist*, *97*(5), 392–399, doi:10.1511/2009.80.392.

Carlson, H. C., and S. W. Cowley (2005), Accelerated polar rain electrons as the source of Sun-aligned arcs in the polar cap during northward interplanetary magnetic field conditions, *Journal of Geophysical Research: Space Physics*, *110*(A05302), doi:10.1029/2004JA010669.

Carter, J. A., S. E. Milan, R. C. Fear, A. Kullen, and M. R. Hairston (2015), Dayside reconnection under interplanetary magnetic field By-dominated conditions: The formation and movement of bending arcs, *Journal of Geophysical Research: Space Physics*, *120*, 2967–2978, doi:10.1002/2014JA020809.

Carter, J. A., S. E. Milan, A. R. Fogg, H. Sangha, M. Lester, L. J. Paxton, and B. J. Anderson (2020), The Evolution of Long-Duration Cusp Spot Emission During Lobe Reconnection With Respect to Field-Aligned Currents, *Journal of Geophysical Research: Space Physics*, *125*(e2020JA027922), doi:10.1029/2020JA027922.

Chisham, G., and M. Pinnock (2002), Assessing the contamination of SuperDARN global convection maps by non-F-region backscatter, *Annales Geophysicae*, *20*, 13–28, doi:10.5194/angeo-20-13-2002.

Chisham, G., M. Lester, S. E. Milan, M. P. Freeman, W. A. Bristow, A. Grocott, K. A. McWilliams, J. M. Ruohoniemi, T. K. Yeoman, P. L. Dyson, R. A. Greenwald, T. Kikuchi, M. Pinnock, J. P. S. Rash, N. Sato, G. J. Sofko, J.-P. Villain, and A. D. M. Walker (2007), A decade of the Super Dual Auroral Radar Network (SuperDARN): scientific achievements, new techniques and future directions, *Surveys in Geophysics*, *28*(1), 33–109, doi:10.1007/s10712-007-9017-8.

Chisham, G., T. K. Yeoman, and G. J. Sofko (2008), Mapping ionospheric backscatter measured by the SuperDARN HF radars 1: A new empirical virtual height model, *Annales Geophysicae*, *26*(4), 823–841, doi:10.5194/angeo-26-823-2008.

Chisham, G., M. P. Freeman, G. A. Abel, W. A. Bristow, A. Marchaudon, J. M. Ruohoniemi, and G. J. Sofko (2009), Spatial distribution of average vorticity in the high-latitude ionosphere and its variation with interplanetary magnetic field direction and season, *Journal of Geophysical Research: Space Physics*, *114*(A09301), doi:10.1029/2009JA014263.

Cottin, H., J. M. Kotler, D. Billi, C. Cockell, R. Demets, P. Ehrenfreund, A. Elsaesser, L. d'Hendecourt, J. J. van Loon, Z. Martins, S. Onofri, R. C. Quinn, E. Rabbow, P. Rettberg, A. J. Ricco, K. Slenzka, R. delaTorre, J. P. de Vera, F. Westall, N. Carrasco, A. Fresneau, Y. Kawaguchi, Y. Kebukawa, D. Nguyen, O. Poch, K. Saiagh, F. Stalport, A. Yamagishi, H. Yano, and B. A. Klamm (2017), Space as a Tool for Astrobiology: Review and Recommendations for Experimentations in Earth Orbit and Beyond, *Space Science Reviews*, *209*(1-4), 83–181, doi:10.1007/s11214-017-0365-5.

Cowley, S. W. (1976), Comments on the Merging of Nonantiparallel Magnetic Fields, *Journal of Geophysical Research*, *81*(19), 3455–3458, doi:10.1029/JA081i019p03455.

Cowley, S. W. H. (2000), Magnetosphere-ionosphere interactions: A tutorial review, in *Geophysical Monograph Series*, vol. 118, pp. 91–106, Blackwell Publishing Ltd, doi:10.1029/GM118p0091.

Cowley, S. W. H., and M. Lockwood (1992), Excitation and Decay of solar wind-driven flows in the magnetosphere-ionosphere system, *Annales Geophysicae*, *10*(1-2), 103–115.

Cowley, S. W. H., J. A. Davies, A. Grocott, H. Khan, M. Lester, K. A. McWilliams, Milan S. E., G. Provan, P. E. Sandholt, J. A. Wild, and T. K. Yeoman (2003), Solar-wind-magnetosphere-ionosphere interactions in the Earth's plasma environment, *Philosophical Transactions of the Royal Society A-Mathematical Physical and Engineering Sciences*, *361*(1802), 113–126, doi:10.1098/rsta.2002.1112.

Craven, P., and G. Wahba (1978), Smoothing Noisy Data with Spline Functions: Estimating the Correct Degree of Smoothing by the Method of Generalized Cross-Validation, *Numerische Mathematik*, *31*, 377–403, doi:10.1007/BF01404567.

Crooker, N. U. (1979), Dayside merging and cusp geometry, *Journal of Geophysical Research*, *84*(A3), 951–959, doi:10.1029/ja084ia03p00951.

Dungey, J. W. (1961), Interplanetary Magnetic Field and the Auroral Zones, *Physical Review Letters*, *6*(2), 47–48, doi:10.1103/PhysRevLett.6.47.

Eckhart, C., and G. Young (1939), A principal axis transformation for non-Hermitian matrices, *Bulletin of the American Mathematical Society*, *45*(2), 118–121, doi:10.1090/S0002-9904-1939-06910-3.

Emmert, J. T., A. D. Richmond, and D. P. Drob (2010), A computationally compact representation of Magnetic-Apex and Quasi-Dipole coordinates with smooth base vectors, *Journal of Geophysical Research: Space Physics*, *115*(A08322), doi:10.1029/2010JA015326.

Fairfield, D. H. (1971), Average and unusual locations of the Earth's magnetopause and bow shock, *Journal of Geophysical Research*, *76*(28), 6700–6716, doi:10.1029/ja076i028p06700.

Farris, M. H., and C. T. Russell (1994), Determining the standoff distance of the bow shock: Mach number dependence and use of models, *Journal of Geophysical Research*, *99*(A9), 17,681–17,689, doi:10.1029/94JA01020.

Fear, R. C., and S. E. Milan (2012a), The IMF dependence of the local time of transpolar arcs: Implications for formation mechanism, *Journal of Geophysical Research: Space Physics*, *117*(A03213), doi:10.1029/2011JA017209.

Fear, R. C., and S. E. Milan (2012b), Ionospheric flows relating to transpolar arc formation, *Journal of Geophysical Research: Space Physics*, *117*(A09230), doi:10.1029/2012JA017830.

Feldstein, Y. I., and G. V. Starkov (1967), Dynamics of auroral belt and polar geomagnetic disturbances, *Planetary and Space Science*, *15*, 209–229, doi:10.1016/0032-0633(67)90190-0.

Förster, M., and S. Haaland (2015), Interhemispheric differences in ionospheric convection: Cluster EDI observations revisited, *Journal of Geophysical Research: Space Physics*, *120*(7), 5805–5823, doi:10.1002/2014JA020774.

Frank, L. A., J. D. Craven, J. L. Burch, and J. D. Winningham (1982), Polar views of the Earth's aurora with Dynamics Explorer, *Geophysical Research Letters*, *9*(9), 1001–1004, doi:10.1029/GL009i009p01001.

Freeman, M. P., C. J. Farrugia, S. W. Cowley, and A. Etemadi (1990a), The response of dayside ionospheric convection to the Y-component of the magnetosheath magnetic field: A case study, *Planetary and Space Science*, *38*(1), 13–41, doi:10.1016/0032-0633(90)90003-9.

Freeman, M. P., D. J. Southwood, M. Lester, and J. A. Waldock (1990b), Measurement of Field-aligned Currents by the SABRE Coherent Scatter Radar, *Physics of Magnetic Flux Ropes, Geophysical Monograph Series*, *58*, 575–580, doi:10.1029/GM058p0575.

Frey, H. U., D. Han, R. Kataoka, M. R. Lessard, S. E. Milan, Y. Nishimura, R. J. Strangeway, and Y. Zou (2019), Dayside Aurora, *Space Science Reviews*, *215*(51), doi:10.1007/s11214-019-0617-7.

Friis-Christensen, E., Y. Kamide, A. D. Richmond, and S. Matsushita (1985), Interplanetary Magnetic Field Control of High-Latitude Electric Fields and Currents Determined From Greenland Magnetometer Data, *Journal of Geophysical Research*, *90*(A2), 1325–1338, doi:10.1029/JA090iA02p01325.

Gabrielse, C., Y. Nishimura, L. Lyons, B. Gallardo-Lacourt, Y. Deng, and E. Donovan (2018), Statistical Properties of Mesoscale Plasma Flows in the Nightside High-Latitude Ionosphere, *Journal of Geophysical Research: Space Physics*, *123*, 6798–6820, doi:10.1029/2018JA025440.

Gallardo-Lacourt, B., Y. Nishimura, L. R. Lyons, S. Zou, V. Angelopoulos, E. Donovan, K. A. McWilliams, J. M. Ruohoniemi, and N. Nishitani (2014), Coordinated SuperDARN THEMIS ASI observations of mesoscale flow bursts associated with auroral streamers, *Journal of Geophysical Research: Space Physics*, *119*, 142–150, doi:10.1002/2013JA019245.

Geotail CPI Definitive Solar Wind Moments and three-dimensional velocity distribution function. Version: 2.3.0 (ed. 2021), Retrieved from `https://hpde.io/JAXA/NumericalData/Geotail/CPI/SWMD/PT48S`, [Online; last accessed 25-May-2021].

Geotail KP Magnetic Field Data (64s). Version: 2.3.0 (ed. 2021), Retrieved from `https://hpde.io/JAXA/NumericalData/Geotail/MGF/PT64S`, [Online; last accessed 25-May-2021].

Gillies, D. M., D. Knudsen, E. Donovan, B. Jackel, R. Gillies, and E. Spanswick (2017), Identifying the 630 nm auroral arc emission height: A comparison of the triangulation, FAC profile, and electron density methods, *Journal of Geophysical Research: Space Physics*, *122*, 8181–8197, doi:10.1002/2016JA023758.

Gillies, R. G., G. C. Hussey, G. J. Sofko, K. A. McWilliams, R. A. Fiori, P. Ponomarenko, and J. P. St.-Maurice (2009), Improvement of SuperDARN velocity measurements by estimating the index of refraction in the scattering region using interferometry, *Journal of Geophysical Research: Space Physics*, *114*(A07305), doi:10.1029/2008JA013967.

Gjerloev, J. W., C. L. Waters, and R. J. Barnes (2018), Deriving Global Convection Maps From SuperDARN Measurements, *Journal of Geophysical Research: Space Physics*, *123*(4), 2902–2915, doi:10.1002/2017JA024543.

Greenwald, R. A., K. B. Baker, J. R. Dudeney, M. Pinnock, T. B. Jones, E. C. Thomas, J. P. Villain, J. C. Cerisier, C. Senior, C. Hanuise, R. D. Hunsucker, G. Sofko, J. Koehler, E. Nielsen, R. Pellinen, A. D. M. Walker, N. Sato, and H. Yamagishi (1995), DARN/SuperDARN, *Space Science Reviews*, *71*(1-4), 761–796, doi:10.1007/BF00751350.

Hadamard, J. (2003), *Lectures on Cauchy's Problem in Linear Partial Differential Equations*, Dover Phoenix Editions, Dover Publications.

Hardy, D. A., E. G. Holeman, W. J. Burke, L. C. Gentile, and K. H. Bounar (2008), Probability distributions of electron precipitation at high magnetic latitudes, *Journal of Geophysical Research*, *113*(A06305), doi:10.1029/2007JA012746.

Harris, C. R., K. J. Millman, S. J. van der Walt, R. Gommers, P. Virtanen, D. Cournapeau, E. Wieser, J. Taylor, S. Berg, N. J. Smith, R. Kern, M. Picus, S. Hoyer, M. H. van Kerkwijk, M. Brett, A. Haldane, J. F. del Río, M. Wiebe, P. Peterson, P. Gérard-Marchant, K. Sheppard, T. Reddy, W. Weckesser, H. Abbasi, C. Gohlke, and T. E. Oliphant (2020), Array programming with NumPy, *Nature*, *585*(7825), 357–362, doi:10.1038/s41586-020-2649-2.

Herlingshaw, K. (2021), Characterising Mesoscale Fast Flow Channels in the Polar Cap Ionosphere, Ph.D. thesis, University of Bergen, `https://hdl.handle.net/11250/2724001`.

Herlingshaw, K., L. J. Baddeley, K. Oksavik, D. A. Lorentzen, and E. C. Bland (2019), A Study of Automatically Detected Flow Channels in the Polar Cap Ionosphere, *Journal of Geophysical Research: Space Physics*, *124*(11), 9430–9447, doi:10.1029/2019JA026916.

Herlingshaw, K., L. J. Baddeley, K. Oksavik, and D. A. Lorentzen (2020), A Statistical Study of Polar Cap Flow Channels and Their IMF By Dependence, *Journal of Geophysical Research: Space Physics*, *125*(e2020JA028359), doi:10.1029/2020JA028359.

Hones, E. W., J. D. Craven, L. A. Frank, D. . Evans, and P. T. Newell (1989), The Horse-Collar Aurora: A Frequent Pattern of the Aurora in Quiet Times, *Geophysical Research Letters*, *16*(1), 37–40, doi:10.1029/GL016i001p00037.

Hosokawa, K., A. Kullen, S. Milan, J. Reidy, Y. Zou, H. U. Frey, R. Maggiolo, and R. Fear (2020), Aurora in the Polar Cap: A Review, *Space Science Reviews*, *216*(15), doi:10.1007/s11214-020-0637-3.

Ieda, A., S. Oyama, H. Vanhamäki, R. Fujii, A. Nakamizo, O. Amm, T. Hori, M. Takeda, G. Ueno, A. Yoshikawa, R. J. Redmon, W. F. Denig, Y. Kamide, and N. Nishitani (2014), Approximate forms of daytime ionospheric conductance, *Journal of Geophysical Research: Space Physics*, *119*(12), 397–415, doi:10.1002/2014JA020665.

Iijima, T., and T. A. Potemra (1976), The Amplitude Distribution of Field-Aligned Currents at Northern High Latitudes Observed by Triad, *Journal of Geophysical Research*, *81*(13), 2165–2174, doi:10.1029/ja081i013p02165.

Iyemori, T., M. Takeda, M. Nose, Y. Odagi, and H. Toh (2010), Mid-latitude Geomagnetic Indices "ASY" and "SYM", Retrieved from `http://wdc.kugi.kyoto-u.ac.jp/aeasy/asy.pdf`, [Online; last accessed 10-May-2021].

Kelley, M. C. (2009), *The Earth's Ionosphere: Plasma Physics and Electrodynamics*, vol. 96, 2nd ed., 1–556 pp., Academic Press, San Diego.

Kilcommons, L. M., R. J. Redmon, and D. J. Knipp (2017), A new DMSP magnetometer and auroral boundary data set and estimates of field-aligned currents in dynamic auroral boundary coordinates, *Journal of Geophysical Research: Space Physics*, *122*, 9068–9079, doi:10.1002/2016JA023342.

King, J., and N. Papitashvili (2021), One min and 5-min solar wind data sets at the Earth's bow shock nose, Retrieved from `https://omniweb.gsfc.nasa.gov/html/omni_min_data.html`, [Online; last accessed 23-June-2021].

King, J. H., and N. E. Papitashvili (2005), Solar wind spatial scales in and comparisons of hourly Wind and ACE plasma and magnetic field data, *Journal of Geophysical Research: Space Physics*, *110*(A02104), doi:10.1029/2004JA010649.

Kozlovsky, A., T. Turunen, and S. Massetti (2009), Field-aligned currents of postnoon auroral arcs, *Journal of Geophysical Research*, *114*(A03301), doi:10.1029/2008JA013666.

Kullen, A., and P. Janhunen (2004), Relation of polar auroral arcs to magnetotail twisting and IMF rotation: A systematic MHD simulation study, *Annales Geophysicae*, *22*(3), 951–970, doi:10.5194/angeo-22-951-2004.

Kullen, A., M. Brittnacher, J. A. Cumnock, and L. G. Blomberg (2002), Solar wind dependence of the occurrence and motion of polar auroral arcs: A statistical study, *Journal of Geophysical Research: Space Physics*, *107*(A11), 1362, doi:10.1029/2002JA009245.

Kullen, A., R. C. Fear, S. E. Milan, J. A. Carter, and T. Karlsson (2015), The statistical difference between bending arcs and regular polar arcs, *Journal of Geophysical Research: Space Physics*, *120*(12), 10,443–10,465, doi:10.1002/2015JA021298.

Laundal, K. M. (2021), secsy, GitHub repository, Retrieved from `https://github.com/klaundal/secsy`, [Online; last accessed 30-June-2021].

Laundal, K. M., and A. D. Richmond (2017), Magnetic Coordinate Systems, *Space Science Reviews*, *206*(1-4), 27–59, doi:10.1007/s11214-016-0275-y.

Laundal, K. M., J. H. Yee, V. G. Merkin, J. W. Gjerloev, H. Vanhamäki, J. P. Reistad, M. Madelaire, K. Sorathia, and P. J. Espy (2021), Electrojet Estimates From Mesospheric Magnetic Field Measurements, *Journal of Geophysical Research: Space Physics*, *126*(e2020JA028644), doi:10.1029/2020ja028644.

Lee, C. N., K. W. Min, J. J. Lee, G. K. Parks, M. O. Fillingim, D. Lummerzheim, K. S. Cho, K. H. Kim, Y. H. Kim, Y. D. Park, W. Han, J. Edelstein, and E. Korpela (2010), Spectral observations of FUV auroral arcs and comparison with inverted-V precipitating electrons, *Journal of Geophysical Research: Space Physics*, *115*(A09223), doi:10.1029/2009JA015071.

Lente, G., and K. Ősz (2020), Barometric formulas: various derivations and comparisons to environmentally relevant observations, *ChemTexts*, *6*(2), 13, doi:10.1007/s40828-020-0111-6.

Li, K. J., J. Zhanng, and W. Feng (2016), A statistical analysis of 50 years of daily solar wind velocity data, *The Astronomical Journal*, *151*, 128, doi:10.3847/0004-6256/151/5/128.

Li, W., J. Raeder, M. F. Thomsen, and B. Lavraud (2008), Solar wind plasma entry into the magnetosphere under northward IMF conditions, *Journal of Geophysical Research: Space Physics*, *113*, A04,204, doi:10.1029/2007JA012604.

Liang, J., E. Donovan, B. Jackel, E. Spanswick, and M. Gillies (2016), On the 630 nm red-line pulsating aurora: Red-line Emission Geospace Observatory observations and model simulations, *Journal of Geophysical Research: Space Physics*, *121*, 7988–8012, doi:10.1002/2016JA022901.

Lin, C. S., and R. A. Hoffman (1982), Observations of inverted-V electron precipitation, *Space Science Reviews*, *33*, 415–457, doi:10.1007/BF00212420.

Liu, L. B., W. X. Wan, Y. D. Chen, and H. J. Le (2011), Solar activity effects of the ionosphere: A brief review, *Chinese Science Bulletin*, *56*(12), 1202–1211, doi:10.1007/s11434-010-4226-9.

Lockwood, M. (1998), *Identifying the Open-Closed Field Line Boundary*, pp. 73–90, Springer Netherlands, Dordrecht, doi:10.1007/978-94-011-5214-3_7.

Lockwood, M., and M. F. Smith (1993), Comment on "Mapping the dayside ionosphere to the magnetosphere according to particle precipitation characteristics" by Newell and Meng, *Geophysical Research Letters*, *20*(16), 1739–1740, doi:10.1029/93GL01967.

Lockwood, M., P. E. Sandholt, S. W. Cowley, and T. Oguti (1989), Interplanetary magnetic field control of dayside auroral activity and the transfer of momentum across the dayside magnetopause, *Planetary and Space Science*, *37*(11), 1347–1365, doi:10.1016/0032-0633(89)90106-2.

Lockwood, M., S. W. H. Cowley, and M. P. Freeman (1990), The excitation of plasma convection in the high-latitude ionosphere, *Journal of Geophysical Research*, *95*(A6), 7972, doi:10.1029/ja095ia06p07961.

Loewe, C. A., and G. W. Prölss (1997), Classification and mean behavior of magnetic storms, *Journal of Geophysical Research A: Space Physics*, *102*(A7), 14,209–14,213, doi:10.1029/96JA04020.

Luhmann, J. G., R. J. Walker, C. T. Russell, N. U. Crooker, J. R. Spreiter, and S. S. Stahara (1984), Patterns of Potential Magnetic Field Merging Sites on the Dayside Magnetopause, *Journal of Geophysical Research*, *89*(A3), 1739–1742, doi:10.1029/JA089iA03p01739.

Lühr, H., M. Rother, W. Köhler, P. Ritter, and L. Grunwaldt (2004), Thermospheric up-welling in the cusp region: Evidence from CHAMP observations, *Geophysical Research Letters*, *31*(L06805), doi:10.1029/2003GL019314.

Lyons, L. R., Y. Nishimura, and Y. Zou (2016), Unsolved problems: Mesoscale polar cap flow channels' structure, propagation, and effects on space weather disturbances, *Journal of Geophysical Research: Space Physics*, *121*(4), 3347–3352, doi:10.1002/2016JA022437.

Ma, X., K. Nykyri, A. Dimmock, and C. Chu (2020), Statistical Study of Solar Wind, Magnetosheath, and Magnetotail Plasma and Field Properties: 12+ Years of THEMIS Observations and MHD Simulations, *Journal of Geophysical Research: Space Physics*, *125*(10), doi:10.1029/2020JA028209.

Matzka, J., C. Stolle, Y. Yamazaki, O. Bronkalla, and A. Morschhauser (2021a), The geomagnetic Kp index and derived indices of geomagnetic activity, *Space Weather*, *19*(e2020SW002641), doi:10.1029/2020SW002641.

Matzka, J., O. Bronkalla, K. Tornow, K. Elger, and C. Stolle (2021b), Geomagnetic Kp index. V. 1.0. GFZ Data Services., doi:10.5880/Kp.0001.

McCrea, I., A. Aikio, L. Alfonsi, E. Belova, S. Buchert, M. Clilverd, N. Engler, B. Gustavsson, C. Heinselman, J. Kero, M. Kosch, H. Lamy, T. Leyser, Y. Ogawa, K. Oksavik, A. Pellinen-Wannberg, F. Pitout, M. Rapp, I. Stanislawska, and J. Vierinen (2015), The science case for the EISCAT_3D radar, *Progress in Earth and Planetary Science*, *2*(21), doi:10.1186/s40645-015-0051-8.

Milan, S. E. (2013), Modeling Birkeland currents in the expanding/contracting polar cap paradigm, *Journal of Geophysical Research: Space Physics*, *118*(9), 5532–5542, doi:10.1002/jgra.50393.

Milan, S. E. (2015), Sun et Lumière: Solar Wind-Magnetosphere Coupling as Deduced from Ionospheric Flows and Polar Auroras., in *Magnetospheric Plasma Physics: The Impact of Jim Dungey's Research. Astrophysics and Space Science Proceedings*, vol. 41, edited by Cowley F. R. S., W. H. Stanley, D. Southwood, and S. Mitton, pp. 33–64, Springer International Publishing, Cham, doi:10.1007/978-3-319-18359-6_2.

Milan, S. E., M. Lester, S. W. H. Cowley, and M. Brittnacher (2000), Convection and auroral response to a southward turning of the IMF: Polar UVI, CUTLASS, and IMAGE signatures of transient magnetic flux transfer at the magnetopause, *Journal of Geophysical Research: Space Physics*, *105*(A7), 15,741–15,755, doi:10.1029/2000JA900022.

Milan, S. E., B. Hubert, and A. Grocott (2005), Formation and motion of a transpolar arc in response to dayside and nightside reconnection, *Journal of Geophysical Research: Space Physics*, *110*(A01212), doi:10.1029/2004JA010835.

Milan, S. E., T. A. Evans, and B. Hubert (2010), Average auroral configuration parameterized by geomagnetic activity and solar wind conditions, *Annales Geophysicae*, *28*(4), 1003–1012, doi:10.5194/angeo-28-1003-2010.

Milan, S. E., L. B. N. Clausen, J. C. Coxon, J. A. Carter, M.-T. Walach, K. Laundal, N. Østgaard, P. Tenfjord, J. Reistad, K. Snekvik, H. Korth, and B. J. Anderson (2017), Overview of Solar Wind–Magnetosphere–Ionosphere–Atmosphere Coupling and the Generation of Magnetospheric Currents, *Space Science Reviews*, *206*(1-4), 547–573, doi:10.1007/s11214-017-0333-0.

Milan, S. E., J. A. Carter, G. E. Bower, S. M. Imber, L. J. Paxton, B. J. Anderson, M. R. Hairston, and B. Hubert (2020), Dual-Lobe Reconnection and Horse-Collar Auroras, *Journal of Geophysical Research: Space Physics*, *125*(10), doi:10.1029/2020JA028567.

Mironova, I. A., K. L. Aplin, F. Arnold, G. A. Bazilevskaya, R. G. Harrison, A. A. Krivolutsky, K. A. Nicoll, E. V. Rozanov, E. Turunen, and I. G. Usoskin (2015), Energetic Particle Influence on the Earth's Atmosphere, *Space Science Reviews*, *194*, 1–96, doi:10.1007/s11214-015-0185-4.

Moen, J., Y. Rinne, H. C. Carlson, K. Oksavik, R. Fujii, and H. Opgenoorth (2008), On the relationship between thin Birkeland current arcs and reversed flow channels in the winter cusp/cleft ionosphere, *Journal of Geophysical Research: Space Physics*, *113*(A09220), doi:10.1029/2008JA013061.

Ness, N. F. (1965), The Earth's magnetic tail, *Journal of Geophysical Research*, *70*(13), 2989–3005, doi:10.1029/jz070i013p02989.

Neudegg, D. A., S. W. H. Cowley, S. E. Milan, T. K. Yeoman, M. Lester, G. Provan, G. Haerendel, W. Baumjohann, B. Nikutowski, J. Buè Chner, U. Auster, K.-H. Fornacon, and E. Georgescu (2000), A survey of magnetopause FTEs and associated flow bursts in the polar ionosphere, *Annales Geophysicae*, *18*, 416–435, doi:10.1007/s00585-000-0416-0.

Newell, P. T., and C.-I. Meng (1992), Mapping the dayside ionosphere to the magnetosphere according to particle precipitation characteristics, *Geophysical Research Letters*, *19*(6), 609–612, doi:10.1029/92GL00404.

Newell, P. T., W. J. Burke, E. R. Sánchez, C.-I. Meng, M. E. Greenspan, and C. R. Clauer (1991), The Low-Latitude Boundary Layer and the Boundary Plasma Sheet at Low Altitude: Prenoon Precipitation Regions and Convection Reversal Boundaries, *Journal of Geophysical Research*, *96*(A12), 21,013–21,023, doi:10.1029/91JA01818.

Newell, P. T., J. M. Ruohoniemi, and C. I. Meng (2004), Maps of precipitation by source region, binned by IMF, with inertial convection streamlines, *Journal of Geophysical Research: Space Physics*, *109*(A10), doi:10.1029/2004JA010499.

Newell, P. T., K. Liou, and G. R. Wilson (2009), Polar cap particle precipitation and aurora: Review and commentary, *Journal of Atmospheric and Solar-Terrestrial Physics*, *71*, 199–215, doi:10.1016/j.jastp.2008.11.004.

Niehof, J., S. Morley, Jnlanl, Spacecataz, J. Haiducek, B. Larsen, A. Merrill, P. Killick, A. Reimer, M. Engel, A. Stricklan, A. Hendry, and Mghenderson64 (2020), SpacePy/SpacePy: 0.2.2, doi:10.5281/zenodo.4472086.

Nishida, A. (1994), The GEOTAIL Mission, *Geophysical Research Letters*, *21*(25), 2871–2873, doi:10.1029/94GL01223.

Nishimura, Y., L. R. Lyons, Y. Zou, K. Oksavik, J. I. Moen, L. B. Clausen, E. F. Donovan, V. Angelopoulos, K. Shiokawa, J. M. Ruohoniemi, N. Nishitani, K. A. McWilliams, and M. Lester (2014), Day-night coupling by a localized flow channel visualized by polar cap patch propagation, *Geophysical Research Letters*, *41*(11), 3701–3709, doi:10.1002/2014GL060301.

Nishitani, N., J. M. Ruohoniemi, M. Lester, J. Benjamin, H. Baker, A. V. Koustov, S. G. Shepherd, G. Chisham, T. Hori, E. G. Thomas, R. A. Makarevich, A. Marchaudon, P. Ponomarenko, J. A. Wild, S. E. Milan, W. A. Bristow, J. Devlin, E. Miller, R. A. Greenwald, T. Ogawa, and T. Kikuchi (2019), Review of the accomplishments of mid-latitude Super Dual Auroral Radar Network (SuperDARN) HF radars, *Progress in Earth and Planetary Science*, *6*(27), doi:10.1186/s40645-019-0270-5.

Oksavik, K., J. Moen, and H. C. Carlson (2004), High-resolution observations of the small-scale flow pattern associated with a poleward moving auroral form in the cusp, *Geophysical Research Letters*, *31*(11), doi:10.1029/2004GL019838.

Oksavik, K., J. Moen, H. C. Carlson, R. A. Greenwald, S. E. Milan, M. Lester, W. F. Denig, and R. J. Barnes (2005), Multi-instrument mapping of the small-scale flow dynamics related to a cusp auroral transient, *Annales Geophysicae*, *23*(7), 2657–2670, doi:10.5194/angeo-23-2657-2005.

Oksavik, K., J. I. Moen, E. H. Rekaa, H. C. Carlson, and M. Lester (2011), Reversed flow events in the cusp ionosphere detected by SuperDARN HF radars, *Journal of Geophysical Research: Space Physics*, *116*(A12303), doi:10.1029/2011JA016788.

Olsen, N., G. Hulot, and T. J. Sabaka (2010), *Sources of the Geomagnetic Field and the Modern Data That Enable Their Investigation*, pp. 105–124, Springer, Berlin, Heidelberg, doi:10.1007/978-3-642-01546-5_5.

Østgaard, N., S. B. Mende, H. U. Frey, J. B. Sigwarth, and J. M. Weygand (2007), Auroral conjugacy studies based on global imaging, *Journal of Atmospheric and Solar-Terrestrial Physics*, *69*, 294–255, doi:10.1016/j.jastp.2006.05.026.

Parker, E. N. (1958), Dynamics of the interplanetary gas and magnetic fields, *Astrophysical Journal*, *128*(3), 664–676, doi:10.1086/146579.

Paxton, L. J., C.-I. Meng, G. H. Fountain, B. S. Ogorzalek, E. H. Darlington, S. A. Gary, J. O. Goldsten, D. Y. Kusnierkiewicz, S. C. Lee, L. A. Linstrom, J. J. Maynard, K. Peacock, D. F. Persons, and B. E. Smith (1992), Special sensor ultraviolet spectrographic imager: an instrument description, in *Instrumentation for planetary and terrestrial atmospheric remote sensing*, edited by S. Chakrabarti and A. B. Christensen, pp. 2–15, International Society for Optics and Photonics, San Diego, doi:10.1117/12.60595.

Pedregosa, F., G. Varoquaux, A. Gramfort, V. Michel, B. Thirion, O. Grisel, M. Blondel, P. Prettenhofer, R. Weiss, V. Dubourg, J. Vanderplas, A. Passos, D. Cournapeau, M. Brucher, M. Perrot, and E. Duchesnay (2011), Scikit-learn: Machine learning in Python, *Journal of Machine Learning Research*, *12*, 2825–2830.

Pinnock, M., A. S. Rodger, J. R. Dudeney, K. B. Baker, P. T. Newell, R. A. Greenwald, and M. E. Greenspan (1993), Observations of an enhanced convection channel in the cusp ionosphere, *Journal of Geophysical Research: Space Physics*, *98*(A3), 3767–3776, doi:10.1029/92JA01382.

Provan, G., T. K. Yeoman, and S. E. Milan (1998), CUTLASS Finland radar observations of the ionospheric signatures of flux transfer events and the resulting plasma flows, *Annales Geophysicae*, *16*, 1411–1422, doi:10.1007/s00585-998-1411-0.

Raab, W., G. Branduardi-Raymont, C. Wang, L. Dai, E. Donovan, G. Enno, P. Escoubet, A. Holland, L. Jing, D. Kataria, L. Li, A. Read, D. Rebuffat, J. Romstedt, C. Runciman, S. Sembay, E. Spanswick, J. Sykes, J. Thornhill, A. Wielders, A. Zhang, and J. Zheng (2016), SMILE: a joint ESA/CAS mission to investigate the interaction between the solar wind and Earth's magnetosphere, in *Space Telescopes and Instrumentation 2016: Ultraviolet to Gamma Ray*, *Society of Photo-Optical Instrumentation Engineers (SPIE) Conference Series*, vol. 9905, edited by J.-W. A. den Herder, T. Takahashi, and M. Bautz, p. 990502, doi:10.1117/12.2231984.

Redmon, R. J., W. F. Denig, L. M. Kilcommons, and D. J. Knipp (2017), New DMSP database of precipitating auroral electrons and ions, *Journal of Geophysical Research: Space Physics*, *122*(8), 9056–9067, doi:10.1002/2016JA023339.

Reed, K. (2017), Study of meso-scale reversed flow events in the polar ionosphere by SuperDARN radars, Master's thesis, University of Bergen, Bergen, Norway, `https://hdl.handle.net/1956/16148`.

Rees, M. H. (1989), *Physics and Chemistry of the Upper Atmosphere*, Cambridge University Press, doi:10.1017/CBO9780511573118.

REGO Calibration Method to Correct Images (2015), Retrieved from `https://data.phys.ucalgary.ca/sort_by_project/GO-Canada/REGO/calibration/documentation/rego_calibration_method_to_correct_images.pdf`, [Online; last accessed 10-Jan-2021].

Reistad, J. P., K. M. Laundal, N. Østgaard, A. Ohma, S. Haaland, K. Oksavik, and S. E. Milan (2019), Separation and Quantification of Ionospheric Convection Sources: 1. A New Technique, *Journal of Geophysical Research: Space Physics*, *124*(7), 6343–6357, doi:10.1029/2019JA026634.

Richmond, A. D. (1995), Ionospheric Electrodynamics Using Magnetic Apex Coordinates, *Journal of Geomagnetism and Geoelectricity*, *47*(2), 191–212, doi:10.5636/jgg.47.191.

Richmond, A. D. (2007), *Ionosphere*, pp. 452–454, Springer Netherlands, Dordrecht, doi:10.1007/978-1-4020-4423-6_159.

Rinne, Y., J. Moen, K. Oksavik, and H. C. Carlson (2007), Reversed flow events in the winter cusp ionosphere observed by the European Incoherent Scatter (EISCAT) Svalbard radar, *Journal of Geophysical Research: Space Physics*, *112*(A10313), doi:10.1029/2007JA012366.

Ronchi, C., R. Iacono, and P. S. Paolucci (1996), The "Cubed Sphere": A New Method for the Solution of Partial Differential Equations in Spherical Geometry, *Journal of Computational Physics*, *124*(1), 93–114, doi:10.1006/jcph.1996.0047.

Ruohoniemi, J. M., and K. B. Baker (1998), Large-scale imaging of high-latitude convection with Super Dual Auroral Radar Network HF radar observations, *Journal of Geophysical Research: Space Physics*, *103*(A9), 20,797–20,811, doi:10.1029/98JA01288.

Russell, C. T. (1972), The Configuration of the Magnetosphere, in *Critical Problems of Magnetospheric Physics*, edited by E. R. Dyer, National Academy of Sciences, Madrid.

Russell, C. T., and R. C. Elphic (1978), Initial ISEE Magnetometer Results: Magnetopause Observations, *Space Science Reviews*, *22*, 681–715, doi:10.1007/BF00212619.

Russell, C. T., M. Ginskey, and S. M. Petrinec (1994), Sudden impulses at low latitude stations: Steady state response for southward interplanetary magnetic field, *Journal of Geophysical Research*, *99*(A7), 13,403–13,408, doi:10.1029/94ja00549.

Samsonov, A. A., D. G. Sibeck, N. P. Dmitrieva, and V. S. Semenov (2017), What Happens Before a Southward IMF Turning Reaches the Magnetopause?, *Geophysical Research Letters*, *44*(18), 9159–9166, doi:10.1002/2017GL075020.

Sandholt, P. E., and C. J. Farrugia (2009), Plasma flow channels at the dawn/dusk polar cap boundaries: momentum transfer on old open field lines and the roles of IMF By and conductivity gradients, *Annales Geophysicae*, *27*(4), 1527–1554, doi:10.5194/angeo-27-1527-2009.

Sandholt, P. E., H. Carlson, and A. Egeland (2002), *Dayside and Polar Cap Aurora*, vol. 270, Kluwer Academic Publishers, Dordrecht, doi:10.1007/0-306-47969-9.

Shepherd, S. G., and J. M. Ruohoniemi (2000), Electrostatic potential patterns in the high-latitude ionosphere constrained by SuperDARN measurements, *Journal of Geophysical Research: Space Physics*, *105*(A10), 23,005–23,014, doi:10.1029/2000ja000171.

Shue, J. H., J. K. Chao, H. C. Fu, C. T. Russell, P. Song, K. K. Khurana, and H. J. Singer (1997), A new functional form to study the solar wind control of the magnetopause size and shape, *Journal of Geophysical Research: Space Physics*, *102*(A5), 9497–9511, doi:10.1029/97JA00196.

Sinnhuber, M., H. Nieder, N. Wieters, Á. H. Nieder, and N. Wieters (2012), Energetic Particle Precipitation and the Chemistry of the Mesosphere/Lower Thermosphere, *Surveys in Geophysics*, *33*(6), 1281–1334, doi:10.1007/s10712-012-9201-3.

Skoug, R. M., J. T. Gosling, J. T. Steinberg, D. J. McComas, C. W. Smith, N. F. Ness, Q. Hu, and L. F. Burlaga (2004), Extremely high speed solar wind: 29-30 October 2003, *Journal of Geophysical Research: Space Physics*, *109*(A09102), doi:10.1029/2004JA010494.

Sofko, G. J., R. Greenwald, and W. Bristow (1995), Direct determination of large-scale magnetospheric field-aligned currents with SuperDARN, *Geophysical Research Letters*, *22*(15), 2041–2044.

Spicher, A., A. A. Ilyasov, W. J. Miloch, A. A. Chernyshov, L. B. Clausen, J. I. Moen, T. Abe, and Y. Saito (2016), Reverse flow events and small-scale effects in the cusp ionosphere, *Journal of Geophysical Research: Space Physics*, *121*(10), 10,466–10,480, doi:10.1002/2016JA022999.

SSUSI Data Products Algorithms, Version 1.13 (2013), Retrieved from `https://ssusi.jhuapl.edu/docs/algorithms/SSUSI_DataProductAlgorithms_V1_13.doc`, [Online; last accessed 5-Mar-2021].

Stone, E. C., A. M. Frandsen, R. A. Mewaldt, E. R. Christian, D. Margolies, J. F. Ormes, and F. Snow (1998), The Advanced Composition Explorer, *Space Science Reviews*, *86*, 1–22, doi:10.1023/A:1005082526237.

Stubbs, T. J., R. R. Vondrak, N. Østgaard, J. B. Sigwarth, and L. A. Frank (2005), Simultaneous observations of the auroral ovals in both hemispheres under varying conditions, *Geophysical Research Letters*, *32*(L03103), doi:10.1029/2004GL021199.

SuperDARN Data Analysis Working Group, E. Thomas, M. Schmidt, E. Bland, A. Burrell, P. Ponomarenko, A. Reimer, K. Sterne, and M.-T. Walach (2021a), SuperDARN Radar Software Toolkit (RST) 4.5, doi:10.5281/zenodo.4435297.

SuperDARN Data Analysis Working Group, M. Schmidt, D. Billett, C. Martin, D. Huyghebaert, E. Bland, A. Burrell, M. Detwiller, K. Herlingshaw, K. Krieger, D. Peters, A. Reimer, J. Reistad, C. Roberston, and K. Sterne (2021b), SuperDARN/pydarn: pyDARNio v2.0.1, doi:10.5281/zenodo.4558130.

Tanskanen, E. I. (2002), Terrestrial substorms as a part of global energy flow, Ph.D. thesis, Finnish Meterological Institute, Helsinki, Finland, `https://www.researchgate.net/publication/34974646_Terrestrial_substorms_as_a_part_of_global_energy_flow`.

Thomas, E. G., and S. G. Shepherd (2018), Statistical Patterns of Ionospheric Convection Derived From Mid-latitude, High-Latitude, and Polar SuperDARN HF Radar Observations, *Journal of Geophysical Research: Space Physics*, *123*(4), 3196–3216, doi:10.1002/2018JA025280.

Thorne, K. S., and R. D. Blandford (2017), *Modern Classical Physics: Optics, Fluids, Plasmas, Elasticity, Relativity, and Statistical Physics*, pp. 998–1001, Princeton and Oxford Princeton University Press.

ThoughSF (2020), Interplanetary magnetic field, Retrieved from `https://twitter.com/ToughSf/status/1256976812351066114?s=20`, [Online, Tweet; last accessed 23-Jul-2021].

Tonks, L., and I. Langmuir (1929), A General Theory of the Plasma of an Arc, *Physical Review*, *34*(6), 876–922, doi:10.1103/PhysRev.34.876.

van der Meeren, C., K. M. Laundal, A. G. Burrell, G. Starr, A. S. Reimer, and A. Morschhauser (2021), aburrell/apexpy: ApexPy Version 1.1.0, doi:10.5281/zenodo.4585641.

Vanhamäki, H., and L. Juusola (2020), Introduction to Spherical Elementary Current Systems, in *Ionospheric Multi-Spacecraft Analysis Tools. ISSI Scientific Report Series*, vol. 17, edited by M. W. Dunlop and H. Lühr, chap. 2, pp. 5–33, Springer International Publishing, Cham, doi:10.1007/978-3-030-26732-2_2.

VanZandt, T. E., W. L. Clark, and J. M. Warnock (1972), Magnetic apex coordinates: A magnetic coordinate system for the ionospheric F2 layer, *Journal of Geophysical Research*, *77*(13), 2406–2411, doi:10.1029/ja077i013p02406.

Weimer, D. R. (2005), Improved ionospheric electrodynamic models and application to calculating Joule heating rates, *Journal of Geophysical Research: Space Physics*, *110*(A05306), doi:10.1029/2004JA010884.

Wild, J. A., S. W. H. Cowley, J. A. Davies, H. Khan, M. Lester, S. E. Milan, G. Provan, T. K. Yeoman, A. Balogh, M. W. Dunlop, K.-H. Fornacon, and E. Georgescu (2001), First simultaneous observations of flux transfer events at the high-latitude magnetopause by the Cluster spacecraft and pulsed radar signatures in the conjugate ionosphere by the CUTLASS and EISCAT radars, *Annales Geophysicae*, *19*, 1491–1508, doi:10.5194/angeo-19-1491-2001.

Wurz, P. (2005), Solar wind composition, in *Proceedings of the 11th European Solar Physics Meeting "The Dynamic Sun: Challenges for Theory and Observations" (ESA SP-600)*, edited by D. Danesy, S. Poedts, A. De Groof, and J. Andries, Leuven, Belgium.

Yeoman, T. K., D. M. Wright, A. J. Stocker, and T. B. Jones (2001), An evaluation of range accuracy in the Super Dual Auroral Radar Network over-the-horizon HF radar systems, *Radio Science*, *36*(4), 801–813, doi:10.1029/2000RS002558.

Zhang, H., Q. Zong, H. Connor, P. Delamere, G. Facskó, D. Han, H. Hasegawa, E. Kallio, Á. Kis, G. Le, B. Lembòge, Y. Lin, T. Liu, K. Oksavik, N. Omidi, A. Otto, J. Ren, Q. Shi, D. Sibeck, and S. Yao (2021a), Dayside transient phenomena and their impact on the magnetosphere and ionosphere, *Space Science Reviews*, (Submitted).

Zhang, Q.-H., Y.-L. Zhang, C. Wang, M. Lockwood, H.-G. Yang, B.-B. Tang, Z.-Y. Xing, K. Oksavik, L. R. Lyons, Y.-Z. Ma, Q.-G. Zong, J. I. Moen, and L.-D. Xia (2020), Multiple transpolar auroral arcs reveal insight about coupling processes in the Earth's magnetotail, *Proceedings of the National Academy of Sciences of the USA*, *117*(28), 16,193–16,198, doi:10.1073/pnas.2000614117.

Zhang, Q.-H., Y.-L. Zhang, C. Wang, K. Oksavik, L. R. Lyons, M. Lockwood, H.-G. Yang, B.-B. Tang, J. I. Moen, Z.-Y. Xing, Y.-Z. Ma, X.-Y. Wang, Y.-F. Ning, and L.-D. Xia (2021b), A space hurricane over the Earth's polar ionosphere, *Nature Communications*, *12*(1207), doi:10.1038/s41467-021-21459-y.

Zhang, S. R., J. M. Holt, and M. McCready (2007), High latitude convection based on long-term incoherent scatter radar observations in North America, *Journal of Atmospheric and Solar-Terrestrial Physics*, *69*(10-11), 1273–1291, doi:10.1016/j.jastp.2006.08.017.

Zhang, Y., L. J. Paxton, Q. Zhang, and Z. Xing (2016), Polar cap arcs: Sun-aligned or cusp-aligned?, *Journal of Atmospheric and Solar-Terrestrial Physics*, *146*, 123–128, doi:10.1016/j.jastp.2016.06.001.

Zhu, L., R. W. Schunk, and J. J. Sojka (1997), Polar cap arcs: a review, *Journal of Atmospheric and Solar-Terrestrial Physics*, *59*(10), 1087–1126, doi:10.1016/S1364-6826(96)00113-7.